

DESIGN, FABRICATION, AND APPLICATIONS OF
SILICON ELECTROOSMOTIC MICROPUMPS

A DISSERTATION

SUBMITTED TO THE DEPARTMENT OF MECHANICAL ENGINEERING

AND THE COMMITTEE ON GRADUATE STUDIES

OF STANFORD UNIVERSITY

IN PARTIAL FULFILLMENT OF THE REQUIREMENTS

FOR THE DEGREE OF

DOCTOR OF PHILOSOPHY

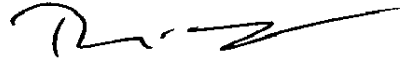
Daniel J. Laser

June 2005

© Copyright by Daniel J. Laser 2005

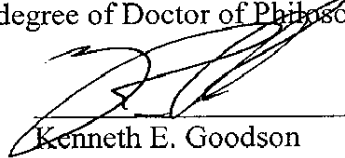
All Rights Reserved

I certify that I have read this dissertation and that, in my opinion, it is fully adequate in scope and quality as a dissertation for the degree of Doctor of Philosophy.



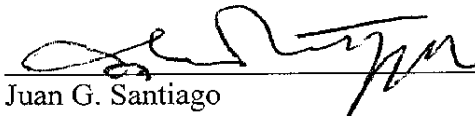
Thomas W. Kenny, Principal Advisor

I certify that I have read this dissertation and that, in my opinion, it is fully adequate in scope and quality as a dissertation for the degree of Doctor of Philosophy.



Kenneth E. Goodson

I certify that I have read this dissertation and that, in my opinion, it is fully adequate in scope and quality as a dissertation for the degree of Doctor of Philosophy.



Juan G. Santiago

Approved for the University Committee on Graduate Studies.

ABSTRACT

A new class of micropumps based on electroosmotic flow has been developed. These micropumps are fabricated through silicon micromachining and incorporate electroosmotic flow elements consisting of parallel arrays of hundreds of narrow, deep trenches designed to enhance the transfer of momentum into the fluid phase. A comprehensive model of silicon electroosmotic micropump operation has been developed by adapting and extending the Burgreen-Nakache model of electroosmotic flow in slit capillaries. The newly developed model takes into account deviations from the ideal slit capillary geometry arising from silicon etch and thin film processes, as well as factors such as pressure losses and potential gradients within the micropump but external to the electroosmotic flow element.

Over sixty prototype silicon electroosmotic micropumps have been fabricated and tested. Prototype silicon electroosmotic micropumps with 1.5 cm³ package sizes generate flow rates up to 170 $\mu\text{L min}^{-1}$ and pressures of nearly 10 kPa. Using the newly developed micropump model to compare data for micropumps with different electroosmotic flow element geometries and for a range of operating voltages, micropump flow rate is seen to scale in proportion to the magnitude of the electric field in the electroosmotic flow element, while pressure scales in proportion to the total voltage drop across the electroosmotic flow element—findings consistent with established models of electroosmotic flow and electric double layers. The effect on micropump performance of dielectric thin film composition has been characterized, with zeta potentials found to be approximately -20 mV for nitride films and -40 mV for oxide-on-nitride films.

Abstract

Critical processing steps in the silicon electroosmotic micropump fabrication process have been characterized in detail. Dielectric thin film deposition processes have been developed which mitigate substrate current sufficiently to permit micropump operation at up to 500 V. Trap-controlled hole conduction in the silicon nitride layer is proposed as the current-limiting mechanism in these films. Transient pressure response data has been obtained by laser vibrometry measurement of the deflection of integrated pressure-sensing diaphragms. Silicon electroosmotic micropumps have been evaluated for applications in integrated circuit thermal management and biological fluids analysis.

PREFACE AND ACKNOWLEDGEMENTS

In many respects, generating electroosmotic flow in silicon-based devices is inherently problematic. Thanks to silicon's relatively narrow bandgap, silicon structures act all too readily as electrodes when strongly biased in the presence of an aqueous medium. Fixturing requirements drive up die sizes, mitigating one of silicon micromachining's production advantages. Worst of all, the electrical properties of that famously insulating thin film, silicon oxide, are thoroughly compromised by the alkali ions which are all but unavoidable in electroosmotic flow systems.

Yet the intersection of a powerful set of technologies with an equally powerful physical phenomenon is almost always fertile territory for engineering research. With silicon micromachining and electroosmotic flow, just such an intersection occurs at a particular lengthscale, one micron—nearly the lower limit for conventional photolithography, just thicker than a thick Gouy-Chapman layer. This intersection is mapped in great detail in the following chapters. Parallel arrays of hundreds of trenches, each a few microns wide and etched deep into a silicon substrate, are seen to be well suited to electroosmotic flow generation. These silicon slit capillary arrays are easily interfaced with manifolds, ports, and electrodes to produce working micropumps. Micropump operation hinges on coating the silicon with a dielectric thin film resistant to ionic penetration; near-stoichiometric silicon nitride affords the necessary properties.

With judicious choices for the slit capillary geometry and a special process for increasing the dielectric film zeta potential, silicon electroosmotic micropumps can pump a volume of fluid equivalent to their package size every minute—a respectable rate even by the standards of macroscopic pumps. Low operating voltages bring the ancillary

benefit of simplifying the electrical apparatus needed to operate the pumps, expanding the realm of potential applications. Challenges with silicon electroosmotic micropumps undoubtedly remain, with the issue of substrate current in particular offering grist for abundant academic research in years to come. At the same time, the transition of silicon electroosmotic micropumps toward real-world applications is well underway, with patents filed and commercial entities evaluating the technology for a variety of uses.

The organization of this dissertation is as follows. Chapter 1 is a cursory introduction to a few key topics. Major applications of micropumps are surveyed to establish the context surrounding the development of silicon electroosmotic micropumps; a classification system for micropumps is introduced and figures of merit discussed. Electrokinetics, the broad category of phenomena which includes electroosmotic flow, is also introduced in Chapter 1, as are electrolytic cells. In Chapter 2, the development of micropumps over the past twenty-five years is traced in some detail. Chapter 3 focuses on the electrochemical phenomena relevant to the operation of silicon electroosmotic micropumps: interface electrification, electroosmotic flow generation, and silicon-electrolyte interfaces. A basic model of silicon electroosmotic micropump operation is developed, in the context of the micromachining technologies available for micropump fabrication, in Chapter 4. Chapter 5 presents a particular prototype design, with development of a comprehensive operational model. Operational data for silicon electroosmotic micropumps with this design is set forth and analyzed. In Chapter 6, the challenging issue of substrate current is addressed. Silicon electroosmotic pumps are considered in the context of specific applications and compared to other micropumps

(and to other types of electroosmotic pumps) in Chapter 7. Conclusions and a discussion of future work are set out in chapter 8.

The work presented here was supported by a vast array of individuals and institutions. My graduate studies were funded by a Stanford University Mechanical Engineering departmental fellowship and a Semiconductor Research Corporation Graduate Fellowship, as well as research funding from the Defense Advanced Research Projects Agency. I benefited from numerous discussions with colleagues in the Stanford community, particularly in the research groups of Prof. Tom Kenny and Prof. Juan Santiago. I was fortunate to share a lab with fellow researchers Shuhuai Yao and Chuan-Hua Chen, experts on electroosmotic pumping, and with a talented visiting scholar working on electroosmotic pumping with silicon substrates, Dr. Alan Myers of Intel Corp.

Prof. William Perry of the Center for International Security and Cooperation at Stanford and Dr. Hal Jerman of Iolon Inc. took time out of their busy schedules serve on my defense committee, with Prof. Perry the chairman. My reading committee was a trio of professors with whom I had the good fortune to work closely throughout my time at Stanford. Prof. Ken Goodson was instrumental in focusing the initial silicon electroosmotic micropump work on IC thermal management; targeting such a demanding application early on undoubtedly drove the work to a higher level of achievement. I have always counted Prof. Juan Santiago as a de facto co-advisor; he introduced me to the field of electrokinetics and continually spurred me to conduct my research with greater rigor and ambition. My principal advisor, Prof. Kenny, embodies all that makes Stanford an outstanding place to be a graduate student. In addition to a keen intellect and a warm

sense of humor, he has an uncanny knack for knowing exactly when to offer a gentle word of support to his graduate students; when to prod them along with a choicely worded late-night email; and when to leave them alone. Working with Tom has truly been a privilege.

I owe a tremendous debt of gratitude to my father, my mother, and my brother Dave for their support and encouragement over the years. And my heartfelt thanks, of course, to my magnificent wife Cindy, who makes every day bright and keeps me from taking myself too seriously.

CONTENTS

Abstract.....	iv
Preface and Acknowledgements	vi
Contents	x
List of Figures.....	xiii
Chapter 1: Background and Introduction.....	1
1.1. APPLICATIONS OF MICROPUMPS	1
1.2. THE STUDY OF MICROPUMPS	5
<i>Micropump classification</i>	5
<i>Figures of merit</i>	9
1.3. ELECTROOSMOTIC PUMPING BASICS.....	11
<i>Electrolytic cells with aqueous salt solutions</i>	11
<i>Electrokinetic phenomena</i>	14
<i>Electroosmotic pumps and silicon micromachining</i>	15
1.4. NOMENCLATURE.....	17
Chapter 2: Review of Micropump Technologies.....	22
2.1 RECIPROCATING DISPLACEMENT MICROPUMPS	22
<i>Structure and operation</i>	22
<i>Diaphragm mechanical properties</i>	25
<i>Diaphragm geometry and flow rate</i>	27
<i>Diaphragm geometry and pressure generation</i>	30
2.2. PERFORMANCE AND DESIGN OF REPORTED RECIPROCATING DISPLACEMENT MICROPUMPS.....	33
<i>Chamber configuration</i>	33
<i>Materials and fabrication techniques</i>	35
<i>Diaphragm geometry</i>	38
<i>Drivers</i>	38
<i>Valves</i>	50
<i>Dynamic effects</i>	52
2.3. OTHER DISPLACEMENT MICROPUMPS	55
<i>Rotary Displacement Micropumps</i>	55
<i>Aperiodic Displacement Micropumps</i>	56
2.4. DYNAMIC MICROPUMPS	58
<i>Electrohydrodynamic micropumps</i>	59
<i>Electroosmotic micropumps</i>	62

	<i>Magnetohydrodynamic micropumps</i>	64
	<i>Other dynamic micropumps</i>	65
Chapter 3: Established Models of Electrified Interfaces and Electroosmotic Flow		67
3.1.	THE GOUY-CHAPMAN-GRAHAME-STERN ELECTRIFIED INTERFACE MODEL.....	67
	<i>Qualitative description of the silicon oxide-electrolyte interface</i>	68
	<i>Modeling ionic concentration and electrical potential in the liquid phase of the EDL</i>	70
	<i>The Debye-Hückel approximation</i>	76
3.2.	ELECTROOSMOTIC FLOW IN SLIT CAPILLARIES.....	78
	<i>Modeling electroosmotic flow</i>	78
	<i>The Burgreen-Nakache model</i>	82
	<i>Zeta potential</i>	87
3.3.	MODELS OF EQUILIBRIUM AND NONEQUILIBRIUM PROCESSES IN SILICON- ELECTROLYTE INTERFACES.....	89
	<i>Single-crystal silicon and bare silicon-electrolyte interfaces</i>	90
	<i>Non-equilibrium charge transfer at semiconductor-electrolyte interfaces</i>	92
	<i>Effect of an intermediate insulating layer</i>	94
Chapter 4: Core Design Considerations		98
4.1	SILICON ELECTROOSMOTIC MICROPUMP COMPONENTS AND MODELING.....	98
	<i>Internal pressure losses</i>	99
	<i>Electromigration current</i>	100
4.2	FORMING SLIT CAPILLARY ARRAYS IN SILICON.....	101
	<i>Silicon trench etching techniques</i>	102
	<i>Thin film dielectric deposition</i>	104
	<i>Slit capillary array formation</i>	106
4.3	PROCESS YIELD.....	112
	<i>Thin film dielectric failure</i>	112
	<i>Slit capillary wall fracture during processing</i>	115
Chapter 5: Detailed Modeling and Operational Data		118
5.1	STANDARD SILICON ELECTROOSMOTIC MICROPUMP DESIGN.....	118
5.2	EXPERIMENTAL METHODS.....	120
	<i>Micropump operational testing apparatus</i>	120
	<i>Working fluids</i>	123
5.3	PRESSURE, FLOW RATE, AND POWER CONSUMPTION.....	124
	<i>Thin EDL silicon electroosmotic micropump model</i>	125
	<i>Minimal-back-pressure data</i>	126
	<i>Zeta potential, buffer chemistry, and surface composition</i>	130
	<i>Pressure vs. flow rate</i>	131
5.4	TRANSIENT RESPONSE.....	133
	<i>Micropump design for measurement of fast transient response</i>	133
	<i>Fast transient response data</i>	136

Slow transients—EOF retardation due to electrolytic gas generation..... 140

Chapter 6: Substrate Current..... **141**

Equivalent circuit model..... 141

Discussion of substrate current mechanisms..... 146

Chapter 7: Silicon Electroosmotic Micropumps in Practice..... **152**

7.1 COMPARISON WITH OTHER REPORTED MICROPUMPS 152

Comparison with other dynamic micropumps 152

Comparison with reciprocating displacement micropumps 154

7.2 SILICON ELECTROOSMOTIC MICROPUMPS FOR INTEGRATED CIRCUIT THERMAL
MANAGEMENT..... 155

7.3 AUTOMATING BIOLOGICAL FLUIDS ANALYSIS 157

Chapter 8: Conclusions **160**

Appendix A: Design and Operational Parameters of Reported Micropumps..... **162**

Appendix B: Micropump Fabrication Process Details..... **170**

Process flow for two-layer thin film dielectric, backside inlet/outlet ports 170

Silicon nitride deposition recipe 171

Polysilicon deposition recipe..... 178

Wet oxidation recipe 182

References..... **185**

LIST OF FIGURES

Figure 1.1: System for classifying pumps and micropumps; after Krutzch and Cooper [47]. Unshaded boxes are pump categories of which operational micropumps have been reported.	8
Figure 1.2: Schematic of a simple electrolytic cell with an aqueous electrolyte. A battery forces electrons from the electrode at right to the electrode at left through an external current path. This charge transport drives oxidation processes at the right electrode (the anode) and reduction processes at the left electrode (the cathode). Ions in solution carry charge between the electrodes. The reactions shown are applicable to borate buffers, a common electroosmotic pump working fluid.	12
Figure 1.3: Butler-Volmer model (eqn 1.5) of current density i for platinum electrode reactions in an aqueous solution with $\alpha = 0.5$	14
Figure 2.1: Schematic showing the structure and operation of a generic reciprocating displacement micropump. (a) Top view and section. (b) Discharge and suction strokes. During the discharge stroke, the driver acts to reduce the pump chamber volume, expelling working fluid through the outlet valve. During the suction stroke, the pump chamber is expanded, drawing working fluid in through the inlet valve.	23
Figure 2.2: Diametric dependence of pump diaphragm mechanical properties. A spatially uniform, circular diaphragm clamped at its perimeter is assumed. Centerline displacement y_0 is calculated for the driver pressures shown using eqn 2.1; centerline displacement at the yield point of the diaphragm using eqns 2.1 and 2.2; diaphragm resonant frequency using eqn 2.3. (a) 100 μm thick silicon diaphragm; (b) 10 μm thick silicon diaphragm.	29
Figure 2.3: Stroke length vs. diaphragm diameter for reported RD micropumps with planar, circular diaphragms.	30
Figure 2.4: Theoretical scaling with diaphragm diameter d_d of maximum generated pressure Δp_{max} for reciprocating displacement micropumps. As shown in eqn 2.4, Δp_{max} is generally a function of compression ratio ε_C and of the compressibility κ of the fluid in the pump chamber. For $\varepsilon_C = \text{constant}$ and $\kappa = \text{constant}$, pressure generation is independent of diaphragm diameter. As the diaphragm diameter is scaled down, the impact of a bubble of a given volume V_b in the pump chamber on κ —and therefore on Δp_{max} —increases. When the bubble fills the entire pump chamber, Δp_{max} reaches its minimum. The pump dead volume is taken to be $V_0 = 0.001d_d^3$	32
Figure 2.5: Reciprocating displacement micropump with three pump chambers in series developed by Smits [16]. The micropump is made from an etched silicon substrate bonded between two glass plates. Piezoelectric disks are bonded to the glass above each of the three pump chambers etched in the silicon. Applying a voltage to a piezoelectric actuator causes the glass to bow away from the pump chamber beneath, drawing in fluid. Staggered actuation as shown results in net fluid flow from the inlet at left to the outlet at right.	34

Figure 2.6: Drivers for reciprocating displacement micropumps. (a) Piezoelectric driver in the lateral-strain configuration. The bottom surface of the piezoelectric disk is bonded to the pump diaphragm; the top surface is unconstrained. During operation, the pump diaphragm deflects under a bending moment produced by radial strain in the piezoelectric disk. An axial electric field is applied to the disk. (b) Piezoelectric driver in the axial-strain configuration, where a piezoelectric disk is mounted between the pump diaphragm and a rigid frame. During operation, the pump diaphragm deflects primarily as a result of axial strain in the piezoelectric disk. As in (a), an axial electric field is applied to the disk. (c) Thermopneumatic driver, in which a thin-film resistive element heats fluid in a secondary chamber above the pump chamber. The heated fluid expands, exerting pressure on the pump diaphragm. (d) Electrostatic driver, in which the pump diaphragm deflects upward when an electric potential difference is applied between parallel electrodes. Electrostatically-driven reciprocating displacement micropumps typically have a powered suction stroke and an unpowered discharge stroke. Insulating coatings prevent shorting. (e) External pneumatic driver, in which active valves alternately pressurize and vent a secondary chamber above the pump diaphragm. Illustrations capture key features of reported micropumps with each type of driver; see text for specific examples and citations..... 39

Figure 2.7: IBM ink jet printhead schematic. To eject an ink droplet, a piezoelectric disk actuator deflects the plate sealing the back side of the chamber, decreasing the chamber volume. Surface tension at the ejector orifice acts as a check valve, rectifying the flow. From U.S. patent no. 4,266,232 [121]. 40

Figure 2.8.: Dynamic effects in reported reciprocating displacement micropumps. The product of the Reynolds number Re and the Strouhal number Sr indicates the importance of fluid inertia in low Re flows. The ratio of the operating frequency f and the diaphragm resonant frequency f_r indicates the extent to which dynamic effects are relevant in the membrane mechanical response. Higher values of ff_r and lower $Re*Sr$ is indicative of a micropump performance-limited by the mechanical time constant of the pump driver and/or diaphragm. Lower values of ff_r and higher $Re*Sr$ are associated with micropumps where fluid inertia is particularly important. Multiple data points shown for micropumps tested with more than one working fluid and/or at more than one operating frequency. . 54

Figure 2.9: One type of traveling-wave (induction) electrohydrodynamic pump. Arrays of electrodes capacitively induce mirror charges at the interface between two fluids. Sequential switching of the electrode arrays results in net fluid flow. After Ahn and Kim [243]..... 60

Figure 2.10: Top view (a) and section view (b) schematics of a simple magnetohydrodynamic micropump. A transverse magnetic field exerts a Lorentz force on current-carrying ions flowing across the channel, producing net flow in the axial direction. After Jang and Lee [271] 65

Figure 3.1: Perspective schematic illustration of an oxide surface with paired hydroxyl groups. After Furlong et al. [288]..... 69

Figure 3.2: Schematic of the Gouy-Chapman-Grahame-Stern model of the electric double layer (EDL) at the interface between a silicon oxide surface and a pH-neutral or basic aqueous electrolyte. Interface equilibrium is characterized by charge buildup at the

oxide surface and adsorption of ions and water molecules. The outer Helmholtz plane is defined by the point of closest approach to the interface of hydrated ions. Beyond the outer Helmholtz plane is the diffuse Gouy-Chapman layer, where counterions are found at greater concentration than in the bulk and co-ions at lesser concentration.	70
Figure 3.3: Flat-plate geometry showing coordinate axes used in EDL model.....	71
Figure 3.4: Electrical potential and ionic concentration in the Gouy-Chapman layer for common chemistries and ζ values of -10 mV and -50 mV. (a) The electrical potential φ_{DL} decays with increasing y to zero in the bulk. (b) Counterion and co-ion concentrations approach their bulk values over the same lengthscale. Values calculated using the Hunter solution (eqn. 3.11) to the Poisson-Boltzmann equation assuming a room-temperature univalent, symmetrical electrolyte with $c_{i,\infty} = 0.2$ mM.	75
Figure 3.5: Electrical potential and ionic concentration in the Gouy-Chapman layer for a range of bulk concentrations ($c_{i,\infty} = 0.1, 0.2, 0.4$ mM) – (a) potential φ_{DL} ; (b) counterion and co-ion concentration, normalized by dividing by the bulk concentration $c_{i,\infty}$. Values calculated from the Hunter solution (eqn. 3.11) to the Poisson-Boltzmann equation assuming a room-temperature univalent, symmetrical electrolyte and $\zeta = -50$ mV.	76
Figure 3.6: Debye-Hückel approximation for the exponential term in the Poisson-Boltzmann equation. The error in this term grows rapidly as the zeta potential increases past a few millivolts.....	77
Figure 3.7: Error in concentration values determined by using the Debye-Hückel approximation for the exponential term in the Poisson-Boltzmann equation. Values calculated for a symmetrical, univalent electrolyte at room temperature, where the argument of the exponential term equals 1 at $\varphi_{DL} = 25.7$ mV.	78
Figure 3.8: Schematic of electroosmotic flow in a capillary. An externally-applied electric field exerts force on ions near the charged wall. Ion drag forces the fluid to flow against a pressure gradient.....	79
Figure 3.9: A rectangular cross-section fluid conduit in which one cross-sectional dimension is much larger than the other is referred to as a slit capillary. (a) Notation and coordinate axes used in slit capillary EOF analysis. The dimension a_l is one-half of the smaller of the two cross-sectional dimensions; it is referred to as the slit half-width. (b) Top view, showing the spatially constant one-dimensional electric field E_x and the pressures at left and right ends of slit, p_1 and p_2	81
Figure 3.10: Variation of the finite EDL correction factor with double layer thickness relative to slit capillary half-width a_l	86
Figure 3.11: Scaling relations for electroosmotic flow in slit capillaries. Back pressure at zero net flow Δp_{\max} and mean flow velocity at negligible back pressure \bar{v}_{\max} are calculated for Debye lengths $\lambda_D = 10$ nm and 100 nm assuming working fluid properties similar to those of water and a modest value for zeta potential, $\zeta = -10$ mV. Δp_{\max} and \bar{v}_{\max} are linear functions of applied potential and applied field strength, respectively; the values shown are per 100 V and per 10^5 V m ⁻¹ , respectively. \bar{v}_{\max} is independent of a_l for	

$a_1 \gg \lambda_D$ and decreases with decreasing a_1 in the finite EDL regime. Δp_{\max} is proportional to the inverse square of a_1 for $a_1 \gg \lambda_D$ 87

Figure 3.12: Comparison of unbiased silicon-metal and silicon-electrolyte interfaces using energy band diagrams. (a) At a semiconductor-metal interface, the Fermi energies of the two materials are matched through band bending (space charge layer formation) in the semiconductor; in the case shown here, the metal workfunction is greater than the semiconductor workfunction and the space charge region is a depletion layer. (b) At a semiconductor-electrolyte interface with an equivalent energetic relation ($E_{redox}^0 < E_{FS}$), band bending is partially mitigated by ionization of surface states and by double layer effects. Note that the x -axis in the electrolyte-side profiles is the density of states, not the spatial location. Energy bands shown are for n -type silicon. After Pierret [306] and Morrison [287]. 91

Figure 3.13: Effect of biasing a semiconductor-electrolyte interface (n -type shown). (a) A strong anodic bias (of the electrolyte relative to the semiconductor) drives the semiconductor into a degenerate (deep depletion) state near the interface, leading to metallic behavior and the movement of electrons from reducing agent in the electrolyte into the semiconductor valence band. (b) With the semiconductor at cathodic bias, an inversion layer forms in the semiconductor. After Morrison [287]. 92

Figure 3.14: Energy band diagrams for a silicon-insulator-electrolyte interface, unbiased (a) and with the silicon at cathodic potential (b). As in the uninsulated silicon case (fig 3.12), band bending occurs in the silicon. After Morrison [287]. 94

Figure 3.15: Energy band diagram illustrating mechanisms of charge transport into and through dielectric films. After Campbell and Morley [311] 95

Figure 4.1: Schematic (section view) of a basic silicon electroosmotic micropump design. The EOF element is a structure with features conducive to generating electroosmotic flow, such as an array of fine pores. Biasing the electrodes on either side of the EOF element causes an axial electric field to develop in the EOF element. Fluid manifolds connect the EOF element with inlet and outlet ports. Silicon surfaces exposed to the electrolyte are coated with dielectric thin films. 99

Figure 4.2: Schematic of approximate pressure gradients within silicon electroosmotic micropumps. 100

Figure 4.3: TMICP etch rate dependence on trench width and depth. After Chow [332]. 104

Figure 4.4: Scanning electron micrograph of a slit capillary array. The trenches are 3 μm wide and spaced at a pitch of 10 μm 106

Figure 4.5: Dependence of trench depth b^*b on photolithographically patterned trench width: (a) $2a' = 3 \mu\text{m}$; (b) $2a' = 4 \mu\text{m}$ 109

Figure 4.6: Trench depth variation as a function of trench width. Standard deviation is approximately 1.6 μm ($N = 9$) for both the $2a = 3 \mu\text{m}$ and $2a = 4 \mu\text{m}$ trenches. 109

Figure 4.7: Deviation of TMICP-etched high-aspect-ratio silicon trenches from ideal slit capillary geometry. Trench width varies slightly as a function of distance from the

substrate surface, bulging slightly near the top of the trench and contracting toward the trench bottom. The in-plane trench wall curvature is a mask feature.	110
Figure 4.8: Trench width variation as a function of distance from substrate surface. Mean and standard deviation shown; $N = 9$	111
Figure 4.9: Yield data for dielectric thin films, taking into account both dielectric breakdown and anodic bonding failure. (a) Low-stress nitride films tend to fail at all thicknesses evaluated. (b) Dielectric failure is rare with near-stoichiometric nitride films, but anodic bonding can be inhibited. Consistently high yields were realized with near-stoichiometric films with thickness between 400-600 μm	114
Figure 4.10: Slit capillary walls resemble slab cantilevers and are susceptible to mechanical failure when subjected to a transverse load, as shown, during processing. .	116
Figure 4.11: Mechanical integrity of microfabricated slit capillary arrays. Test arrays were 1 cm wide, with slots spaced at 20 μm intervals and etched for 80 minutes. For over half of the test arrays with 50 μm long slots, one or more walls broke during processing. Test array yield with an oxide-on-nitride coating is slightly higher than with a nitride coating only.	117
Figure 5.1. Standard silicon electroosmotic micropump design. The EOF element is an array of n narrow, deep trenches, each of which resembles a slit capillary. Platinum wires are inserted on either side of the slit capillary array causes an axial electric field to develop in the slit capillaries. The micropump is sealed with a glass cover (not shown).	119
Figure 5.2: Silicon electroosmotic micropump, fixtured for testing. (a) Showing glass cover and platinum electrodes. (b) Showing fluid interconnects.	120
Figure 5.3: Schematic of standard experimental setup used for silicon electroosmotic micropump testing.	121
Figure 5.4: Schematic of test apparatus for measuring silicon EO micropump transient response.	122
Figure 5.5: Pressure scaling factor γ (calculated using eqn 5.2) as a function of slit half-width a_l for various manifold depths b . Assumptions: $A_2 = 0.25 \times b \times w$; $l_1/l_3 = 0.1$. .	126
Figure 5.6: Minimal-back-pressure flow rate for seven micropumps with three different slit capillary lengths. Each data point is the mean Q_{max} value for several tests of a particular micropump with each working fluid (7 pumps total). All micropumps have oxide-on-nitride surfaces. Working fluid is borate buffer ($\text{Na}_2\text{B}_4\text{O}_7$, pH=9.2) with concentrations (based on Na^+) as shown. The operating voltage is $V_2 = 200 \text{ V}$	127
Figure 5.7: Normalized minimal-back-pressure flow rates Q'_{max} for the oxide-on-nitride flow rate data in figure 5.6 and comparable data (not shown) for nitride-only micropumps. The normalization collapses Q_{max} to a single value across all l_1 for each surface composition/buffer chemistry combination.	129
Figure 5.8: Measured current drawn during operation of micropumps with oxide-on-nitride surfaces. Working fluid is borate buffer ($\text{Na}_2\text{B}_4\text{O}_7$, pH=9.2) with concentrations	

(based on Na^+) as indicated in figure; test conditions as described in text. Error bars show standard deviation..... 129

Figure 5.9: Pressure-flow rate data for an oxide-on-nitride micropump with $l_f = 100 \mu\text{m}$. Working fluid is borate buffer ($\text{Na}_2\text{B}_4\text{O}_7$, $\text{pH}=9.2$), concentrations (based on Na^+) 0.2 mM; operating voltage as shown. 132

Figure 5.10: Silicon electroosmotic micropump design with an integrated pressure-sensitive diaphragm. 134

Figure 5.11: (a) Scanning electron micrograph of the top side of the silicon substrate (prior to bonding of the glass cover) showing a portion of etched annular pump structure. (b) SEM showing the released circular diaphragm. 135

Figure 5.12: Predicted static response of silicon nitride pressure sensing diaphragms. Full-model curves calculated using eqn 2.1; linear small-displacement model curves calculated using a linearized form of eqn 2.1. 136

Figure 5.13: Flow rate-back pressure curve (quasistatic operation), $V_2 = 400 \text{ V}$. Maximum back pressure for this micropump is approximately 5.5 kPa 137

Figure 5.14: Measured diaphragm amplitude (centerline deflection) as a function of driving frequency. 137

Figure 5.14: Micropump response (500 μm diaphragm) for a 25 Hz, 400 volt square-wave input with a duty cycle of 20%. Data is ensemble averaged over 1,280 cycles. Plots show (a) diaphragm velocity and (b) diaphragm displacement (found by integrating velocity). Curves shown for both positive and negative center electrode bias. Positive velocities and displacements correspond to outward deflection of the membrane..... 138

Figure 6.1: Proposed silicon electroosmotic micropump equivalent circuit model..... 142

Figure 6.2: Estimated error in slit capillary conductance calculations based on assuming the EDL to be negligibly thin. EDL ionic concentration calculated using eqn 3.11; symmetric electrolyte with $\nu_i = 5.4 \times 10^{-13} \text{ mol N}^{-1} \text{ m s}^{-1}$ assumed. 143

Figure 6.3: Current unaccounted for by liquid phase ionic conduction during operation of micropumps with oxide-on-nitride surfaces. Working fluid is borate buffer ($\text{Na}_2\text{B}_4\text{O}_7$, $\text{pH}=9.2$) with concentrations (based on Na^+) as indicated in figure; test conditions as described in text. 143

Figure 6.4: Micropump current with step voltage bias input. 144

Figure 6.5: Visualization of micropump operation. Direction of flow is left to right. . 146

Figure 6.6: Proposed conduction models for an electrolyte-oxide-nitride-silicon system. With the silicon at cathodic potential (left), holes are the dominant carrier in the nitride and are injected from the oxide/electrolyte. Sodium ions tend to migrate through the oxide toward the oxide-nitride interface, where they may sediment. With the silicon at anodic potential (right), holes are injected into the nitride from the silicon and migrate toward the oxide interface, where they recombine with electrons released during oxidation processes. Such processes could include anodic oxide (oxynitride) formation on the surface of the silicon-rich nitride. 147

List of Figures

Figure 6.7: Schematic of accumulation, depletion, and inversion regions in an insulated *n*-type semiconducting substrate subjected to a linear electrical potential gradient (represented by a voltage divider). Filled and open circles represent electrons and holes, respectively. Similar effects can be expected to occur in electrolytic cells with thin-film-insulated silicon walls. 149

Figure 6.8: Field dependence of conduction in silicon nitride thin films, believed to limit substrate conduction in silicon electroosmotic micropumps. The high-field regime is associated with either Poole-Frenkel conduction or multiphonon-assisted tunneling.... 150

Figure 7.1: Q_{max} for reported electrohydrodynamic and electroosmotic micropumps, plotted as a function of operating voltage V 153

Figure 7.2. Comparison of several reported micropumps based on maximum volumetric flow rate, Q_{max} , maximum pressure Δp_{max} , and package size S_p 154

Figure 7.3. (a) Thermal management system for ICs based on integrated electroosmotic micropumps and microchannels. Single-phase, micropump-driven forced-convective cooling supplements heat conduction from high-power-density regions. In a two-layer 3-D IC, forced convection cools regions on the layer furthest from the heat sink. (b) Estimated flow rate required for single-phase forced-convective cooling of a 1 mm x 1 mm hot spot with a local microchannel heat sink. The pressure drop in the microchannel heat sink is also shown. 156

Figure 7.4: Schematic of sandwich assay automation using silicon electroosmotic micropumps. 158

Figure 7.5: Measured pressure vs. flow rate for removing a lysed and labeled biological fluid sample from a porous sample pad. 159

Figure B.1: Standard process flow for fabrication of silicon electroosmotic micropumps with oxide-on-nitride thin film dielectrics, backside inlet/outlet ports, anodically bonded glass covers, post-cleanroom electrode insertion. 171

CHAPTER 1: BACKGROUND AND INTRODUCTION

When studying a class of devices, an understanding of target applications is almost always helpful. Among the many possible uses of micropumps, four application categories are particularly prominent: implantable medical devices, microelectronics cooling, miniature biochemical analysis systems, and space exploration. In this chapter, these applications are introduced and micropump specifications relevant to each are estimated. This survey of micropump applications is followed by an overview of how micropumps are classified and a discussion of micropump figures of merit. Electroosmotic pumping is then introduced in section 1.3, with brief discussions of electrolytic cells, electrokinetic phenomena, and special considerations for combining electrokinetics with silicon micromachining. Finally, nomenclature used in the text is tabulated in section 1.4.

1.1. Applications of micropumps

From biology and medicine to space exploration and microelectronics cooling, volumes of fluids on the order of a milliliter—the volume contained in a cube 1 cm on a side—and below figure prominently in an increasing number of engineering systems. The small fluid volumes in these systems are often pumped, controlled, or otherwise manipulated during operation: liquid-phase biological samples are moved through miniaturized assay systems [1-4], coolant is forced through micro heat exchangers [5-7], etc. Passive mechanisms, most notably surface tension, are sometimes adequate for transporting fluids within microscale systems [8-11]. When active fluid transport is required, interfacing macroscale pumps, pressure/vacuum chambers, and/or valves to a

microfluidic system is sometimes an acceptable solution [12-15]. Yet the availability of self-contained, active pumps, with package sizes comparable to the volume of fluid to be pumped, is critical to the viability of many microfluidic systems. In this section, a few applications of microfluidic systems are considered briefly to gain insight into when micropumps are required and which micropump design parameters are most relevant.

Controlled, temporally varying administration of pharmaceutical compounds and other therapeutic agents can lead to improved therapeutic outcomes. The prospect of dispensing solutions into the human body has long motivated micropump researchers. Micropump-based systems—either implanted or with a catheter—might be used for insulin delivery, allowing diabetics to control their blood sugar levels without frequent needle injections [16]. Micropumps might also be used to dispense engineered macromolecules into tumors or the bloodstream [17, 18]. High volumetric flow rates are not likely to be required of implanted micropumps (the amount of insulin required by a diabetic per day, for example, is less than a milliliter) but precise metering is of great importance [17, 19-21]. The pressure generation requirements for implantable micropumps are not insignificant, as the back pressure encountered *in vivo* can be as high as 25 kPa. Reliability, power consumption, cost, and biocompatibility are critical [17, 20, 22]. To date, deficiencies in these areas have precluded widespread implantation of micropumps. For example, currently available implanted insulin delivery systems employ static pressure reservoirs metered by solenoid-driven valves, rather than micropumps, even though these systems are over 50 cm³ in size [12, 22, 23]. Physiological integration of microdevices is further discussed by Richards Grayson et al. [24].

A number of researchers have sought to develop micropumps for use in single- or two-phase cooling of microelectronic devices [5-7]. Microelectronics cooling is highly demanding with respect to flow rate. For instance, Tuckerman and Pease's seminal paper on single-phase chip cooling contemplated flow rates of several hundred milliliters per minute [5]. Recent studies indicate that two-phase convective cooling of a 100 W microchip will require flow rates of order 10 milliliters per minute or more, while single-phase fluid cooling will require flow rates of 100-1000 milliliters per minute [6, 25, 26]. The fundamental scaling associated with pressure-driven flow dictates that high pressures (100 kPa or greater) will be required to force such high flow rates through microchannels and/or jet structures found in micro heat sinks. In the laminar regime, an order-of-magnitude decrease in the hydraulic diameter of a channel increases by two orders of magnitude the pressure difference required to maintain a constant average flow velocity. Beyond pressure and flow rate, working fluid phase dependence (for two-phase cooling), cost, and (particularly for mobile units) power consumption are important considerations for microelectronics cooling. Micropumps might also be built directly into integrated circuits to cool transient hot spots, in which case fabrication methods and temporal response are likely to be particularly important [27].

Much attention has been focused recently on miniature systems for chemical and biological analysis [1-4, 28-31]. Miniaturization of these micro total analysis systems (μ TAS) can yield improvements both in terms of performance (e.g. by allowing assays to be completed more quickly) and cost (e.g. through lessened manual intervention, decreased sample and reagents quantities, and the use of disposable substrates). Miniaturization can also make systems easier to transport, which is advantageous in some

instances. Portability is a critical attribute of a chemical analysis system under development at Sandia National Labs; it is expected to require fluid pumping with flow rates on the order of 100 mL min^{-1} and pressures greater than 28 kPa [32].

Despite the ubiquitousness of fluid transport in μ TAS operation, micropumps are found in very few current-generation systems, with fluid transport instead accomplished through manual pipetting, with external pneumatic sources, or through non-pump electroosmotic flow. Compatibility with the range of fluid volumes of interest is a prerequisite for greater use of micropumps in micro total analysis systems. Monitoring single cells may require manipulation of fluid volumes on the order of one picoliter—the volume contained in a cube ten microns on a side [33-35]. Microchip-based systems used in drug discovery amplify DNA, separate species through capillary electrophoresis, and/or interface with mass spectrometers with sample volumes ranging from hundreds of picoliters to hundreds of microliters [1-3, 36-38]. Patient pain considerations have prompted manufacturers of *in vitro* blood glucose monitors for diabetics to minimize sample sizes; current systems need only a one-third microliter blood sample [39]. Detecting microbes in human body liquids often requires somewhat larger sample volumes; for example, a common immunoassay-based blood test for malaria uses a sample volume of ten microliters [40, 41]. Besides fluid volume, other important considerations for μ TAS include working fluid properties such as pH, viscosity, viscoelasticity, and temperature, as well as the presence of cells, dust, or other particles or (for liquid phase systems) gas bubbles which may disrupt operation of pumps and valves. Secondary effects associated with reliability and corrosion include the impact of

mechanically shearing the sample, chemical reactions, adsorption of analytes, and wear of moving parts.

Space exploration is another exciting area for micropump technologies. Miniature roughing pumps are needed for use in mass spectrometer systems to be transported on lightweight spacecraft [42]. Such pumps would likely be required to achieve a vacuum of approximately 0.1 Pa, the level at which high vacuum pumps typically become effective [43]. Miniature roughing pumps have been sought for other applications as well [44]. Micropropulsion is another potential application of micropumps in space. For example, ion-based propulsion systems proposed for future 1-5 kg “microspacecraft” may require delivery of compressed gases at 1 mL min^{-1} flow rates [45, 46]. Higher compression ratios are generally required for pumping gases than for pumping liquids, making these space exploration applications particularly challenging.

1.2. The study of micropumps

As with any collection of complex engineering systems, the study of micropumps is facilitated by establishing a system of classification. Categorizing micropumps based on the manner and means by which fluid flow and pressure is produced—the approach adopted in this text—affords both cogency and flexibility. Also presented in this section is a set of parameters useful for drawing comparisons among dissimilar micropumps.

Micropump classification

Figure 1.1 illustrates the micropump classification system used in this text. This system is applicable to pumps generally and is essentially an extension of the system set forth by Krutzch and Cooper for traditional pumps [47]. Pumps generally fall into one of

two major categories: (1) **displacement pumps**, which exert pressure forces on the working fluid through one or more moving boundaries; and (2) **dynamic pumps**, which continuously add energy to the working fluid in a manner that increases either its momentum (as in the case of centrifugal pumps) or its pressure directly (as in the case of electroosmotic and electrohydrodynamic pumps). Momentum added to a fluid in a dynamic pump is converted into pressure by the action of an external fluidic resistance. Many displacement pumps operate in a periodic manner, incorporating some means of rectifying periodic fluid motion to produce net flow. Such periodic displacement pumps can be further broken down into pumps that are based on reciprocating motion, as of a piston or a diaphragm, and pumps that are based on rotary elements such as gears or vanes. The majority of reported micropumps are reciprocating displacement pumps in which the moving surface is a diaphragm. These are sometimes called membrane pumps or diaphragm pumps. Another subcategory of displacement pumps are aperiodic displacement pumps, the operation of which does not inherently depend on periodic movement of the pressure-exerting boundary. Aperiodic displacement pumps typically pump only a limited volume of working fluid; a syringe pump is a common macroscale example. Dynamic pumps include centrifugal pumps, which are typically ineffective at low Reynolds numbers and have only been miniaturized to a limited extent, as well as pumps in which an electromagnetic field interacts directly with the working fluid to produce pressure and flow (electrohydrodynamic pumps, electroosmotic pumps, and magnetohydrodynamic pumps) and acoustic-wave micropumps. (Krutzh and Cooper refer to noncentrifugal dynamic pumps as “special effect” pumps, a practice that is

abandoned here in favor of identifying the specific physical mechanism that imparts momentum to the working fluid.)

In figure 1.1, open boxes represent pump categories of which operational micropumps have been reported. The term *micropump* is used according to the convention for microelectromechanical systems, with the prefix *micro* considered to be appropriate for devices with prominent features having length scales of order 100 μm or smaller. Many pumps that meet this criterion are micromachined, meaning that they are fabricated using tools and techniques originally developed for the integrated circuit industry or resembling such tools and techniques (e.g., tools involving photolithography and etching). Techniques such as plastic injection molding and precision machining have also been used to produce micropumps. In keeping with the nomenclature associated with nanotechnology, the term nanopump is here considered to be appropriate only for devices with prominent features having length scales of order 100 nm or smaller (so pumps that pump nanoliter volumes of liquid are not necessarily nanopumps). Terms that more accurately describe the operation of a nanoscale device are used instead of nanopump when appropriate. Of course, subcontinuum effects may be important in nanopumps and some micropumps, particularly in the case of devices that pump gases [48]. As an aside, it is noted that electric-motor-driven miniature reciprocating displacement pumps that are compact relative to most macroscopic pumps (but large relative to most micropumps) are commercially available. The performance of several such pumps is reviewed by Wong et al. [32].

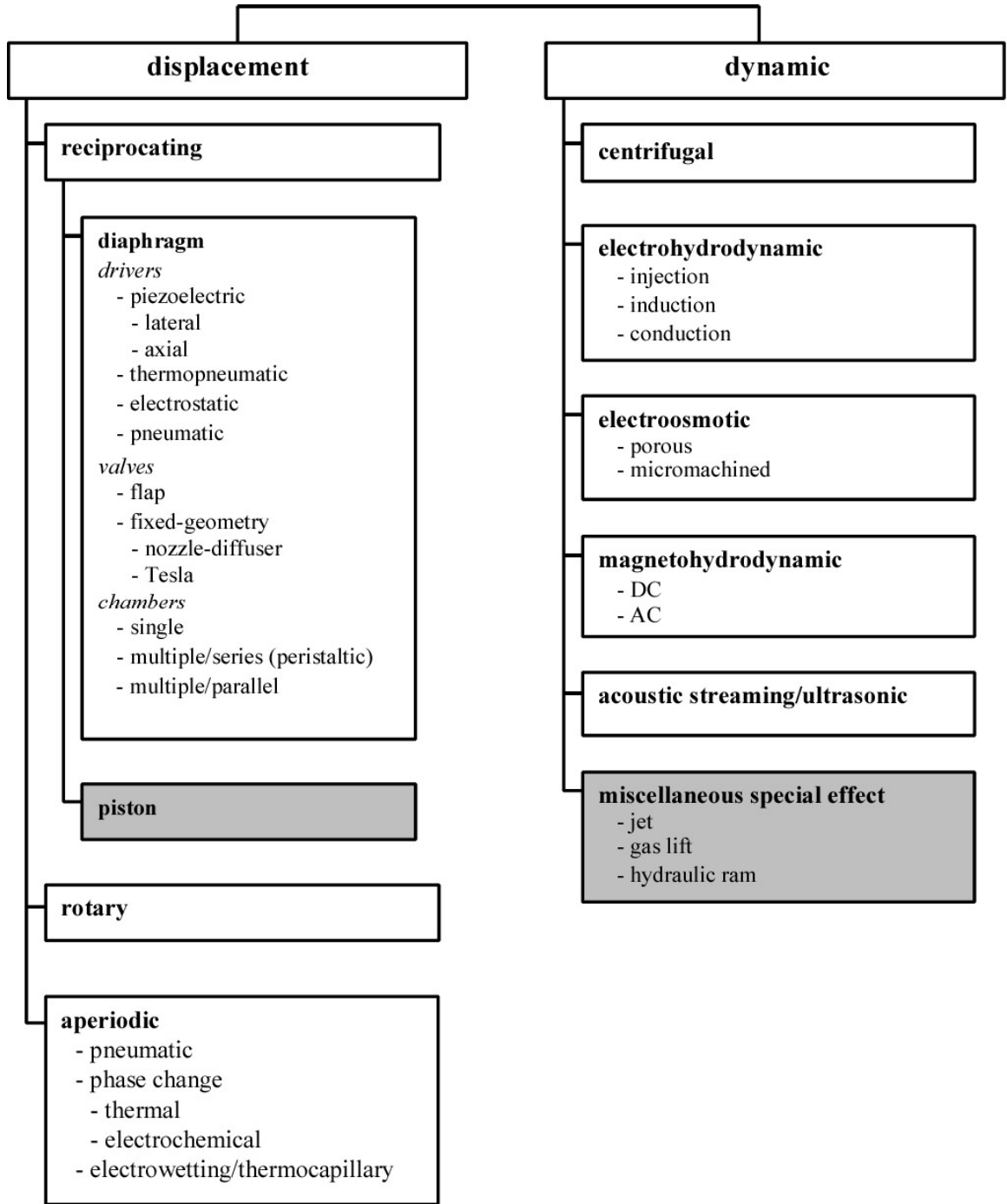


Figure 1.1: System for classifying pumps and micropumps; after Krutzch and Cooper [47]. Unshaded boxes are pump categories of which operational micropumps have been reported.

Figures of merit

The most obvious operational metrics for micropumps—as for pumps generally—are the rate at which fluid is pumped and the pressure against which it is being pumped. Where a micropump is used to pump a liquid, the flow rate Q most often reported is the volumetric flow rate; it is usually expressed in mL min^{-1} or $\mu\text{L min}^{-1}$. When a gas phase is pumped, mass flow rate is usually reported; common gas flow units are standard cubic centimeters per minute, or sccm. The back pressure Δp is the pressure difference sustained between the micropump inlet and outlet. Flow rate Q and back pressure Δp are almost always interdependent, so it is appropriate to report both parameters for a given set of operating conditions. Describing the operation of a micropump over a range of operating conditions is simplified by recognizing that, in many cases, the functional relationship between Q and Δp is reasonably well described by an equation of the form

$$Q = Q_{\max} \left(1 - \frac{\Delta p}{\Delta p_{\max}} \right) \quad (1.1)$$

Here Q_{\max} is the volumetric flow rate when the pressure difference between the pump inlet and outlet is negligible:

$$Q_{\max} = Q|_{\Delta p=0}.$$

The parameter Δp_{\max} is the back pressure when the net flow through the micropump is zero:

$$\Delta p_{\max} = \Delta p|_{Q=0}.$$

Q_{\max} and Δp_{\max} are used in this text and elsewhere as shorthand for the complete pressure-flow rate curve. However, it should be recognized that (i) actual micropump flow rate-pressure curves can deviate significantly from the linear model of eqn 1.1 and

(ii) since Q_{\max} and Δp_{\max} are limit values, they usually can not be realized simultaneously (i.e. most micropumps can not pump their Q_{\max} against a back pressure equal to their Δp_{\max}).

Since many micropumps are explicitly targeted for applications where compactness is important, overall package size S_p must be considered a micropump figure of merit. A related, and particularly interesting, micropump metric is the ratio of maximum flow rate Q_{\max} to package size S_p . This ratio is referred to as the self-pumping frequency, f_{sp} . In this text, S_p of reported micropumps has been estimated when necessary. Estimations of S_p are based on published micropump images, by making inferences from known dimensions, etc.

Also relevant in evaluating micropumps are power consumption P , operating voltage V , and (for devices with periodic operation) operating frequency f . These parameters partially determine the electronics and other components needed to operate a micropump—important considerations for size- and/or cost-sensitive applications. P generally includes the total power consumed by the pump (including power consumed by motors and other actuators, voltage conversion, power transmission, etc.). Lastly, thermodynamic efficiency η is an important parameter for any device which converts energy from one form to another. The most useful definition of thermodynamic efficiency η for a micropump producing a flow rate Q against a back pressure Δp while consuming power at a rate P is [49]

$$\eta = \frac{Q\Delta p}{P}$$

For the purpose of comparing micropumps, it is convenient to estimate maximum thermodynamic efficiency from reported values of Q_{\max} , Δp_{\max} , and P by assuming that eqn 1.1 holds, such that

$$\eta_{est} = 0.25 \frac{Q_{\max} \Delta p_{\max}}{P} \quad (1.2)$$

1.3. Electroosmotic pumping basics

A device which uses electroosmotic flow—one of a class of physicochemical phenomena known as *electrokinetic effects*—to drive a fluid through an external fluidic resistance is an electroosmotic pump. Electroosmotic pumps comprise, at a minimum, two electrodes, a voltage source, a quantity of working fluid, a fluid chamber with inlet and outlet ports, and a structure (or a set of structural features) conducive to electroosmotic flow. All but the last of these components are shared with electrolytic cells—electrochemical systems in which the flow of ionic current through an electrolyte is supported by oxidation and reduction reactions at electrodes. As such, an electroosmotic pump can be considered essentially a special case of an electrolytic cell. Electrolytic cells and electrokinetic phenomena are introduced very briefly in this section, followed by an overview of special considerations for combining electroosmotic pumping and silicon micromachining.

Electrolytic cells with aqueous salt solutions

Electrochemical reactions at phase interfaces give rise to such familiar phenomena as metal oxidation and current generation by dry-cell batteries. Such reactions also underpin the operation of electroosmotic pumps in that the ionic current which flows through the liquid phase during pump operation is sourced and sunk at

electrodes, where applied electrical potentials drive entergonic reactions. Electrode/electrolyte systems driven in this manner are generally referred to as electrolytic cells. Important parameters for electrolytic cells include the magnitude of the applied electrical potential difference, the electrode material, and the composition of the working fluid. Consider a generic electrolytic cell, illustrated schematically in figure 1.2, with two platinum electrodes and an aqueous salt solution as the electrolyte.

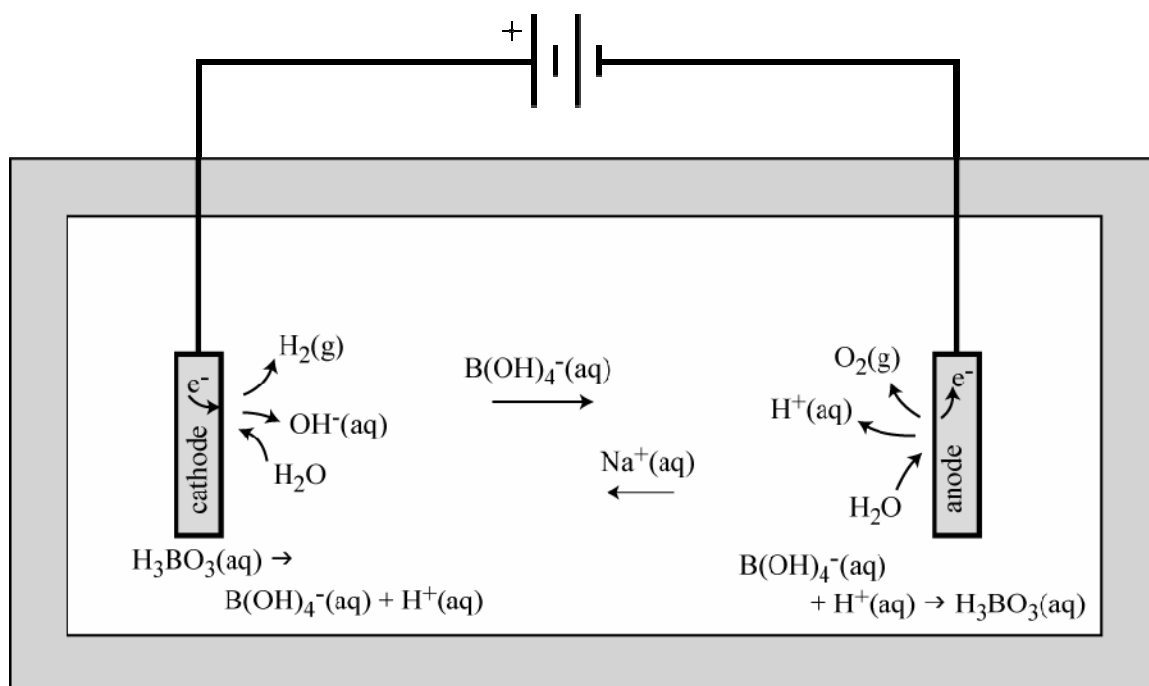
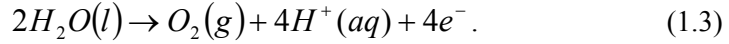
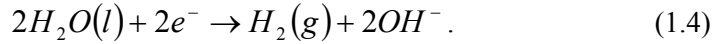


Figure 1.2: Schematic of a simple electrolytic cell with an aqueous electrolyte. A battery forces electrons from the electrode at right to the electrode at left through an external current path. This charge transport drives oxidation processes at the right electrode (the anode) and reduction processes at the left electrode (the cathode). Ions in solution carry charge between the electrodes. The reactions shown are applicable to borate buffers, a common electroosmotic pump working fluid.

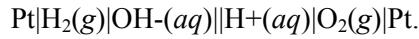
Applying a potential difference greater than 1.8 V across the electrodes drives the oxidation of water at the anode, producing oxygen gas [50, 51]:



At the cathode, water is reduced to produce hydrogen gas:



The required 1.8 V overpotential includes the cell potential and overpotentials of approximately 0.1 V and 0.5 V, respectively, required for the evolution of hydrogen and oxygen gas. Other reactions may occur at the electrodes as well, depending on the composition of the electrolyte and the magnitude of the applied voltage. An electrolytic cell in which the reactions shown in eqns 1.3 and 1.4 are dominant is described by the expression



Electrolytic cell current can be limited by electrode processes or by mass transport. The maximum rate of charge transfer across an electrode-solution interface per unit electrode area (the electrode current density i) as a function of the overpotential η ($\eta = \Delta\phi - \Delta\phi_e$) is described by the Butler-Volmer equation [51, 52]:

$$i = i_0 \left\{ \exp \left[(1 - \alpha) \frac{F}{RT} \eta \right] - \exp \left[-\alpha \frac{F}{RT} \eta \right] \right\} . \quad (1.5)$$

Here F is the Faraday constant, equal to Avogadro's number N_A times the electron charge e ; R is the gas constant; and T is the solution temperature. The constant multiplier i_0 is the rate at which charge moves in both directions across an electrode-solution interface absent a net current (i.e. with the cell potential, if any, balanced by an externally imposed interfacial potential $\Delta\phi_e$). The parameter α is the (cathodic) transfer coefficient, the value

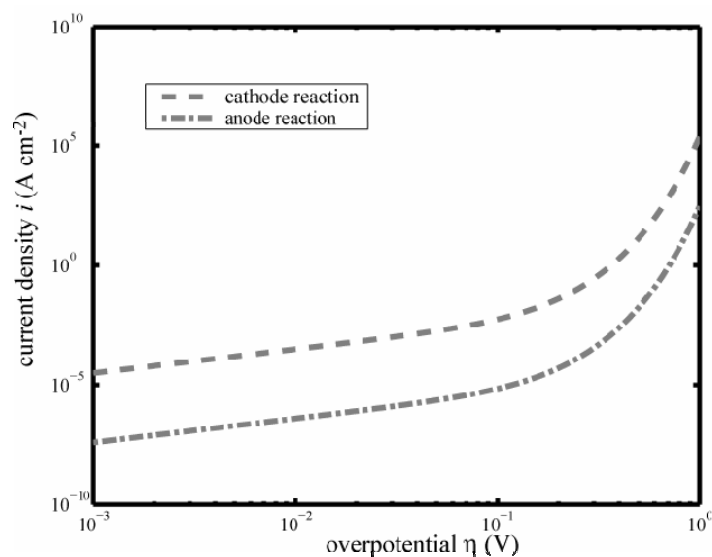


Figure 1.3: Butler-Volmer model (eqn 1.5) of current density i for platinum electrode reactions in an aqueous solution with $\alpha = 0.5$.

of which is typically around 0.5. Calculated values of i for the reaction $2H_2O + 2e^- \rightarrow H_2(g) + 2OH^-$ at a platinum cathode ($i_0 = 0.79 \text{ mA cm}^{-2}$) and for $2H_2O \rightarrow O_2(g) + H_3O^+ + 2e^-$ at a platinum anode ($i_0 \approx 10^{-3} \text{ mA cm}^{-2}$) over a range of η are plotted in figure 1.3. At $T = 298 \text{ K}$, the value of the constant term F/RT appearing in both parts of eqn 1.5 is 38.94. For η on the order of 100 millivolts or larger, therefore, the second term in eqn 1.5 is nearly zero and i grows exponentially with increasing η , exceeding $10^5 i_0$ for $\eta \geq 0.6 \text{ V}$. Electrolytic cells are discussed in detail in texts such as Bard and Faulkner [53].

Electrokinetic phenomena

Electrochemical equilibrium at a phase interface generally entails accumulation of net charge in both phases at or near the interface. The reciprocal charge layers in the two phases are collectively referred to as the electric double layer (EDL). The charge which

accumulates in the liquid phase of the electric double layer underlies a collection of physicochemical effects referred to as electrokinetic phenomena. Electroosmotic flow (EOF, also called electroosmosis), is one such phenomena; it is EDL-based motion of a fluid phase relative to a stationary solid phase under the influence of an electric field. Applications of EOF range from soil remediation to transporting liquids in micro chemical and biological analysis systems. EOF's use in chemical and biological analysis dates back to at least 1974 [54] and has grown to encompass on-chip flow injection analysis [55], electrophoretic separations [1, 56, 57], and liquid chromatography [58].

Three other electrokinetic phenomena, besides electroosmotic flow, have been identified: electrophoresis, streaming potential, and sedimentation potential. Electrophoresis is motion of a solid phase (such as a particle) relative to a fluid phase under the influence of an electric field. Streaming potential is an electrical potential difference generated by pressure-driven flow past a stationary solid phase. Sedimentation potentials, analogously, arise when charged particles move relative to stationary liquid phases. A detailed model of electroosmotic flow in a particular geometry, the slit capillary, is developed in chapter 3; further discussion of electroosmotic flow and of the other electrokinetic phenomena can be found in Probstein [59].

Electroosmotic pumps and silicon micromachining

A prominent source of variety among electroosmotic pumps is the choice of the material which comprises the electroosmotic flow structure. Electroosmotic pumps have been reported with EOF structures made of beads, either packed between frits [60] or sintered [61]; and with an EOF structure consisting of one or more channels etched into a glass plate [62, 63]. Photolithography-based processing of single-crystal silicon presents further options for producing EOF structures. Over the past half-century, an extensive

global infrastructure has been developed for producing integrated circuits from single-crystal silicon wafers. More recently, photolithography-based tools and techniques used to make integrated circuits have been adapted for the production of structures which are interesting for their mechanical properties, rather than (or in addition to) their electrical properties. Producing mechanical structures using IC industry-based tools and techniques is often referred to as *micromachining*, with the prefix *micro* indicating that the devices typically have feature sizes on the order of 100 μm and below. Unlike traditional machining, in which spinning cutters, reciprocating blades, etc. are used to physically shape a part from a block of material, micromachining largely relies on physicochemical and electrochemical means of removing and depositing material. At moderate volumes, micromachining supports relatively low unit costs (typically below \$10 and often much less).

Among other capabilities, silicon micromachining can be used to produce fine pores and capillaries—the types of geometries inherently well suited to EOF generation. Complicating the use of silicon in high-electric-field electrokinetic devices, however, is the prospect of significant substrate leakage current. Silicon surface films are critical for minimizing charge transfer between the silicon substrate and the electrolyte. Silicon oxides have excellent properties for solid-state applications, but permit diffusion of water and alkalis from aqueous solutions with which they are in contact. Silicon nitride—also widely used in solid-state devices—is a more effective dielectric where an aqueous solution is present. The properties of these films are discussed in chapter 3.

1.4. Nomenclature

Table 1.1 sets forth the nomenclature used throughout this text. Where the same symbol is used for more than one parameter (e.g. σ for both stress and electrical conductivity), the appropriate meaning is readily discerned from the context.

Table 1.1: Nomenclature

<u>symbol</u>	<u>definition</u>	<u>SI units</u>
A_d	diaphragm area	m^2
A_1	capillary array flow cross-sectional area	m
A_2	electroosmotic pump manifold cross-sectional area	m
A^*	manifold-capillary contraction parameter	—
a_1	slit capillary half-width	m
a_1^*	slit capillary half-width scaling factor	—
a_1'	photolithographically defined slit capillary half-width	m
α	Butler-Volmer transfer coefficient	—
B	magnetic flux density	wb m^{-2}
b	manifold depth	m
b_1	slit capillary depth	m
b^*	slit capillary depth scaling factor	m
C	capacitance	F
c	molar concentration	mol m^{-3}
D	diffusion constant	$\text{m}^2 \text{s}^{-1}$
D_h	hydraulic diameter	m
d_d	diaphragm diameter	m
E	electric field	V m^{-1}
E_c	electrolytic cell potential	

<u>symbol</u>	<u>definition</u>	<u>SI units</u>
E_y	material Young's modulus	Pa
ε	permittivity	F m ⁻¹
ε_C	compression ratio	—
ζ	zeta potential	V
η	thermodynamic efficiency	—
η_{est}	estimated thermodynamic efficiency	—
η	electrode overpotential	V
F_e	electrostatic force	N
f_r	diaphragm resonant frequency	s ⁻¹
f_{sp}	self-pumping frequency	s ⁻¹
f	operating frequency	s ⁻¹
G	electrical conductivity	S m ⁻¹
i	current density	A m ⁻²
i_0	electrolytic cell exchange current density	A m ⁻²
I	current	A
\bar{j}_i	molar flux of ionic species i	mol s ⁻¹ m ⁻²
\bar{j}_i	mass flux of ionic species i	kg s ⁻¹ m ⁻²
κ	fluid compressibility	m ² N ⁻¹
l_1	slit capillary (or pore or microchannel) length	m
l_2	electrode separation distance	m
λ_D	Debye shielding length	m
λ_i	contribution of species i to molar conductivity	S m ² mol ⁻¹
μ	viscosity	N sec m ⁻²
N	number of species	—

<u>symbol</u>	<u>definition</u>	<u>SI units</u>
n	number of pores/capillaries/channels	—
n_i	number density of species i	m^{-3}
ν	material Poisson ratio	—
P	power	W
p_a	applied driver pressure	Pa
Δp	pressure differential	Pa
Δp	entrance-to-exit capillary pressure increase	Pa
Δp_{\max}	back pressure at zero net flow	Pa
p^*	pressure scaling factor	—
Q	volumetric flow rate	$\text{m}^3 \text{ sec}$
Q_{\max}	volumetric flow rate at negligible back pressure	$\text{m}^3 \text{ sec}$
q	charge density	m^{-3}
ρ	density	kg m^{-3}
ρ_E	charge density	C m^{-3}
Re	Reynolds number	—
S_p	package size	m^3
s	electrode separation distance	m
s_{cc}	centerline-to-centerline spacing of slit capillaries	m
Sr	Strouhal number	—
σ_{ij}	material stress tensor	N m^{-2}
σ	electrical conductivity	S m^{-1}
σ_Y	yield stress	Pa
T	temperature	K
t_d	diaphragm thickness	m

<u>symbol</u>	<u>definition</u>	<u>SI units</u>
t_i	solid film thickness – film material i	m
\bar{u}	flow velocity	m s^{-1}
v_i	mobility in solution of species i	$\text{mol N}^{-1} \text{m s}^{-1}$
V	electrical potential difference	V
V_1	electrical potential drop through a conduit	V
V_2	electroosmotic micropump electrode bias	V
V_0	dead volume	m^3
ΔV	stroke volume	m^3
\bar{v}	mean velocity (= normalized flow rate)	m s^{-1}
\bar{v}_{max}	mean EOF velocity, zero back pressure limit	m s^{-1}
y_0	diaphragm centerline displacement	m
y_s	effective stroke length	m
w	manifold effective width	m
z_i	valence number of species i	—
φ	electrical potential difference	V
φ_{DL}	double layer electrical potential difference	V

Table 1.2: Physical constants

e	electron charge	$1.602 \times 10^{-19} \text{ C}$
F	Faraday constant	$9.65 \times 10^4 \text{ C mol}^{-1}$
N_A	Avogadro number	$6.022 \times 10^{23} \text{ mol}^{-1}$
k	Boltzmann constant	1.381 J K^{-1}
R	gas constant	$8.314 \text{ J K}^{-1} \text{ mol}^{-1}$

CHAPTER 2: REVIEW OF MICROPUMP TECHNOLOGIES

In this chapter, the various categories of micropumps delineated in section 1.2 are considered individually. Important features are reviewed, micropump operation is analyzed, prominent examples are described, and applications are discussed. As a supplement to the discussion of micropumps here, the reader may wish to refer to other reviews of micropump technologies [64-67] and to surveys of micro total analysis systems [28, 29, 68, 69], as well as to general surveys of microfluidics [70-74] and of microelectromechanical systems [75-79].

Much of the material in this chapter first appeared in *A Review of Micropumps* by Laser and Santiago, published in the Journal of Micromechanics and Microengineering in 2004 [80].

2.1 Reciprocating displacement micropumps

As discussed in section 1.2, displacement micropumps use moving surfaces to apply pressure to a working fluid. The vast majority of reported micropumps are reciprocating displacement micropumps—micropumps in which moving boundaries or surfaces does periodic pressure work on the working fluid.

Structure and operation

Pistons are the moving boundaries in many macroscale reciprocating displacement pumps, but micromachined, sealed piston structures have not been used in micropumps. In most reciprocating displacement micropumps, the force-applying moving surface is instead a deformable plate with fixed edges—the pump diaphragm. Common pump diaphragm materials include silicon, glass, and plastic. Figure 2.1

depicts the structure and operation of a generic diaphragm-based reciprocating displacement micropump. The basic components are a pump chamber (bounded on one side by the pump diaphragm), an actuator mechanism or driver, and two passive check

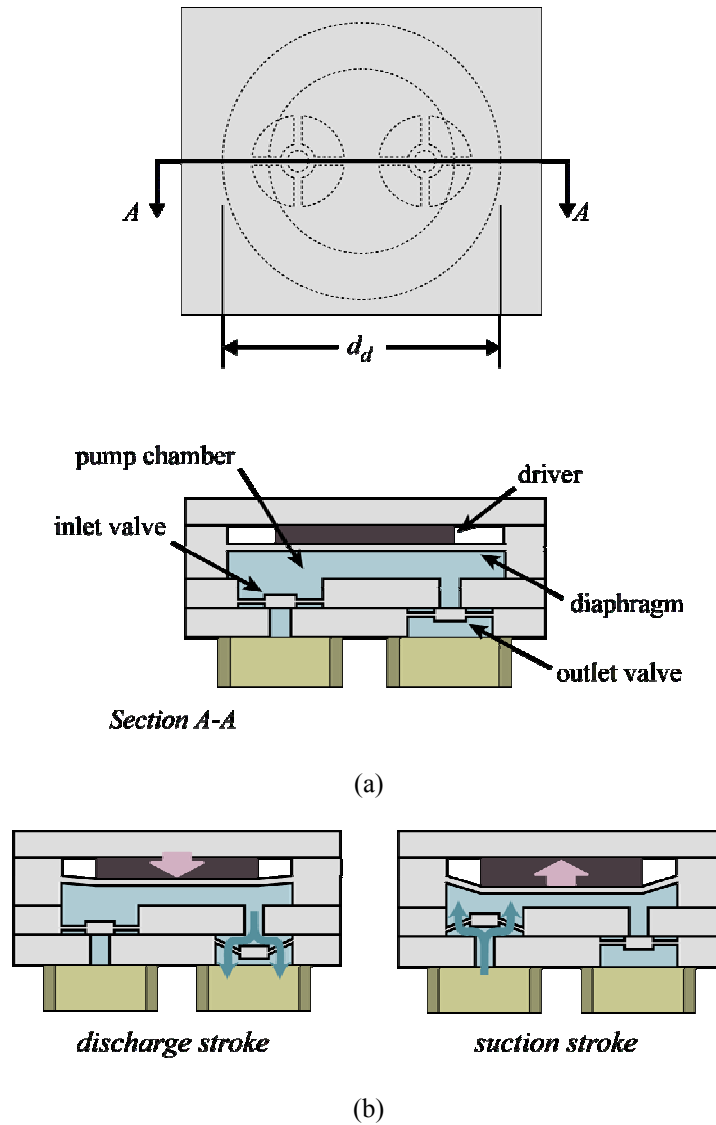


Figure 2.1: Schematic showing the structure and operation of a generic reciprocating displacement micropump. (a) Top view and section. (b) Discharge and suction strokes. During the discharge stroke, the driver acts to reduce the pump chamber volume, expelling working fluid through the outlet valve. During the suction stroke, the pump chamber is expanded, drawing working fluid in through the inlet valve.

valves—one at the inlet (or suction side) and one at the outlet (or discharge side). The generic reciprocating displacement micropump shown in figure 2.1 is constructed from four layers of material. Micropumps made from as few as two and as many as seven layers of material have been reported.

During operation, the driver acts on the pump diaphragm to alternately increase and decrease the pump chamber volume. Fluid is drawn into the pump chamber during chamber expansion/suction stroke and forced out of the pump chamber during the contraction/discharge stroke. The check valves at the inlet and outlet are configured to favor flow into and out of the pump chamber, respectively, rectifying the flow over a two-stroke pump cycle. The basic design illustrated in figure 2.1 is perhaps most directly attributable to Harald van Lintel and coworkers, who reported a micromachined two-valve, single-chamber reciprocating displacement micropump in the journal *Sensors and Actuators* in 1988 [81]. Van Lintel et al.'s micropump comprises an entire 2 inch silicon wafer bonded between two glass plates. The pump chamber is a 12.5 mm diameter, 130 μm deep cavity etched in the silicon wafer using an ethylene diamine/pyrocatechol/pyrazine solution (EDP) with a silicon oxide mask. Diaphragm-like check valves and connecting channels are also etched into the silicon. A 0.19 mm thick glass plate seals the pump chamber side of the device; a thicker piece of glass seals the other side. The portion of the thin glass plate above the pump chamber is the pump diaphragm. A piezoelectric disk actuator is affixed to this glass diaphragm; lateral strain induced in this piezoelectric disk causes the diaphragm to deflect, driving the micropump. This design was patented in 1992 [82, 83]. Operating at $f = 1$ Hz and $V = 125$ V, this

micropump pumps water with $Q_{\max} = 8 \mu\text{L min}^{-1}$ and $\Delta p_{\max} = 10 \text{ kPa}$. With $S_p \cong 4 \text{ cm}^3$, self-pumping frequency is $f_{sp} \cong 0.002 \text{ min}^{-1}$.

Diaphragm mechanical properties

The operation of reciprocating displacement micropumps often involves the interaction of several types of mechanics including electromechanical forces, solid mechanics, and fluid mechanics. Because of this complexity, accurate, tractable, broadly applicable analytical models of reciprocating displacement micropump operation are not readily available. Low-order lumped-parameter models provide significant insight on key aspects of micropump operation [84-86]. Finite element analysis is also a useful tool in studying reciprocating displacement micropumps. Commercial packages such as ANSYS and ALGOR have been used to analyze the response of micropump diaphragms subjected to actuator forces [86-88]. A variety of numerical and semi-analytical approaches have been taken in the study of fluid flows in reciprocating displacement micropumps [89-91]; commercial packages suitable for such analysis include CFDRC, Coventor, FEMLAB, and ANSYS [92].

By assuming quasi-static flow and ideal valve operation, simple models of reciprocating displacement micropump operation can be readily developed. These models provide a starting point for micropump design and elucidate certain aspects of reported micropump performance. Quasi-static flow models are particularly useful for reciprocating displacement micropumps operating in flow regimes characterized by both very low Reynolds number ($Re = \rho U D_h / \mu$) and low Reynolds number and Strouhal number ($St = f D_h / U$) product [48, 59, 93].

For reciprocating displacement pumps, Q and Δp primarily depend on (1) stroke volume ΔV , the difference between the maximum and minimum volumes of the pumping chamber over the course of the pump cycle; (2) dead volume V_0 , the minimum fluid volume contained between the inlet and outlet check valves at any point during the pump cycle; (3) pump operating frequency, f ; (4) inlet and outlet valve properties; and (5) working fluid properties. For ideal valves ($\Delta p_{\text{forward}} = 0$ and $\Delta p_{\text{reverse}} \rightarrow \infty$) and an incompressible working fluid, conservation of mass dictates that the flow rate is simply the product of the stroke volume ΔV and the operating frequency f . Stroke volume ΔV depends strongly on the characteristics of the micropump driver. Piezoelectric drivers in micropumps sometimes function as nearly ideal displacement sources, while other drivers are well modeled as pressure sources. For displacement source-like drivers, diaphragm displacement (and therefore ΔV) is limited by the driver's range and by the mechanical failure criteria of the diaphragm. For pressure source-like drivers, the diaphragm stiffness and dynamic response limit ΔV and f .

In light of the dependence of Q and Δp on the pump diaphragm mechanical response, an understanding of how the mechanical properties of a generic pump diaphragm depend on geometry and material properties is useful. For a circular pump diaphragm of uniform thickness t_d with diameter d_d clamped at its perimeter and subjected to a spatially uniform applied driver force per unit cross-sectional area p_a , the centerline displacement y_0 is [94]

$$\frac{p_a d_d^4}{16E_y t_d^4} = \frac{5.33}{(1-\nu^2)} \frac{y_0}{t_d} + \frac{2.6}{(1-\nu^2)} \left(\frac{y_0}{t_d} \right)^3, \quad (2.1)$$

where E_y and ν are the Young's modulus and Poisson ratio, respectively, of the diaphragm material. The maximum stress σ in the diaphragm is given by

$$\frac{\sigma d_d^2}{4E_y t_d^2} = \frac{4}{(1-\nu^2)} \frac{y_0}{t_d} + 1.73 \left(\frac{y_0}{t_d} \right)^2. \quad (2.2)$$

The first mechanical resonance f_r of a “dry” diaphragm (i.e., one not subject to significant pressure forces from a liquid) is [95]

$$f_r = 2\pi \left(\frac{1.015}{d_d} \right)^2 \sqrt{\frac{E_y t_d^2}{12\rho(1-\nu^2)}} \quad (2.3)$$

where ρ is the density of the diaphragm material.

Eqns 2.1 and 2.2, taken together, can be used to estimate the absolute upper limit on y_0 —and therefore on ΔV —for a given diaphragm geometry and driver properties. Eqn 2.2 defines the diaphragm-yield-limited maximum y_0 for a driver resembling a displacement source, while eqn 2.1 provides pressure-dependent y_0 for drivers resembling pressure sources. Eqn 2.3 can be used to estimate the range of operating frequencies over which the diaphragm mechanical response is expected to be quasi-static. Dynamic effects are relevant in micropumps operated at or near the diaphragm resonant frequency, potentially increasing performance but also making pump performance more dependent on valve characteristics and external conditions. Dynamic effects are discussed further below.

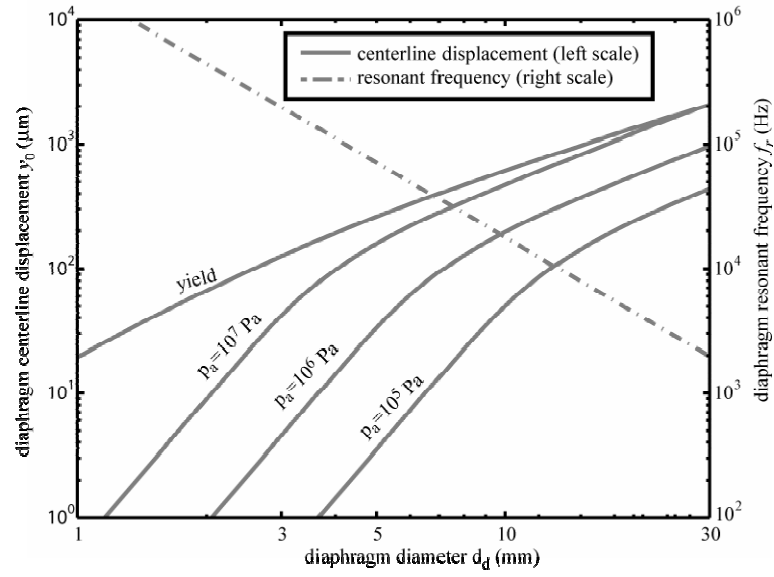
Diaphragm geometry and flow rate

Minimizing S_p is a high priority for many micropump applications. Most reciprocating displacement micropumps are roughly planar structures, with the pump diaphragm located in-plane and occupying a sizable portion of the in-plane area.

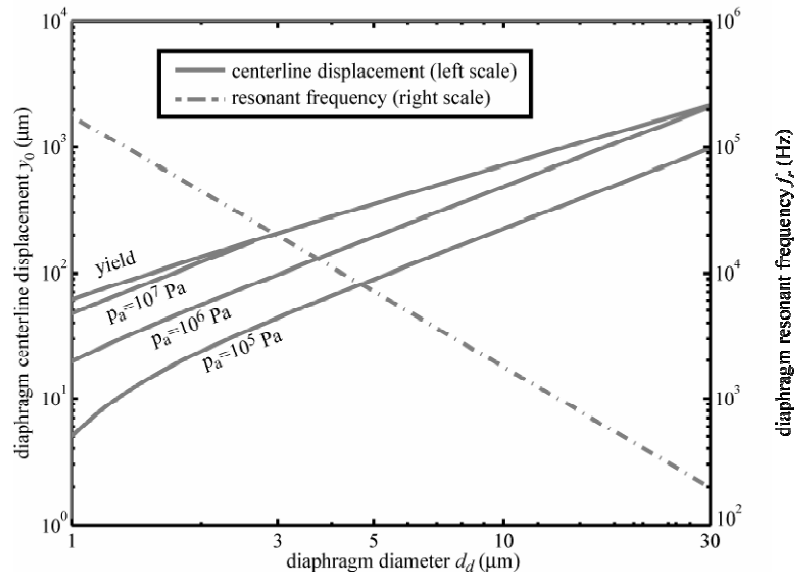
Minimizing S_p , therefore, often depends on minimizing the diaphragm area A_d . The above equations for diaphragm mechanical response provide a means for evaluating tradeoffs associated with minimizing A_d . This analysis is subject to the caveats set forth earlier in this section regarding quasi-static operation and ideal valve operation.

In figure 2.2, calculated values of y_0 at yield, pressure-dependent y_0 , and f_r are plotted for silicon diaphragms ($\sigma_y = 7.0$ GPa [75]) with thickness $t_d = 100$ μm and 10 μm . For $y_0 \ll t_d$, y_0 scales with the fourth power of d_d . High-force drivers are therefore generally required to produce moderate ΔV for small d_d . Even with a driver capable of supplying effectively unlimited force, displacement is limited by the diaphragm's failure criteria—which also scale unfavorably with decreasing d_d . Note that, for sinusoidal forcing functions, resonance frequencies that are large compared to the frequency of operation imply that the inertia of the diaphragm can be neglected and its mechanical response considered quasi-static (although the inertia of the fluid may still be important).

The relationship between diaphragm in-plane dimensions and stroke length suggested by this simple analysis is borne out in the operation of reported micropumps. For a reported micropump with diaphragm area A_d operating with stroke volume ΔV , an effective stroke length can be defined as $y_s = \Delta V/A_d$. In figure 2.3, y_s is plotted as a function of diaphragm diameter d_d for a type of reciprocating displacement micropump of which a large number of comparable examples have been reported, those with planar circular diaphragms to which a piezoelectric disk actuator is directly attached (the lateral-strain driver configuration, described in section 2.2 below). Effective stroke length



(a)



(b)

Figure 2.2: Diametric dependence of pump diaphragm mechanical properties. A spatially uniform, circular diaphragm clamped at its perimeter is assumed. Centerline displacement y_0 is calculated for the driver pressures shown using eqn 2.1; centerline displacement at the yield point of the diaphragm using eqns 2.1 and 2.2; diaphragm resonant frequency using eqn 2.3. (a) 100 μm thick silicon diaphragm; (b) 10 μm thick silicon diaphragm.

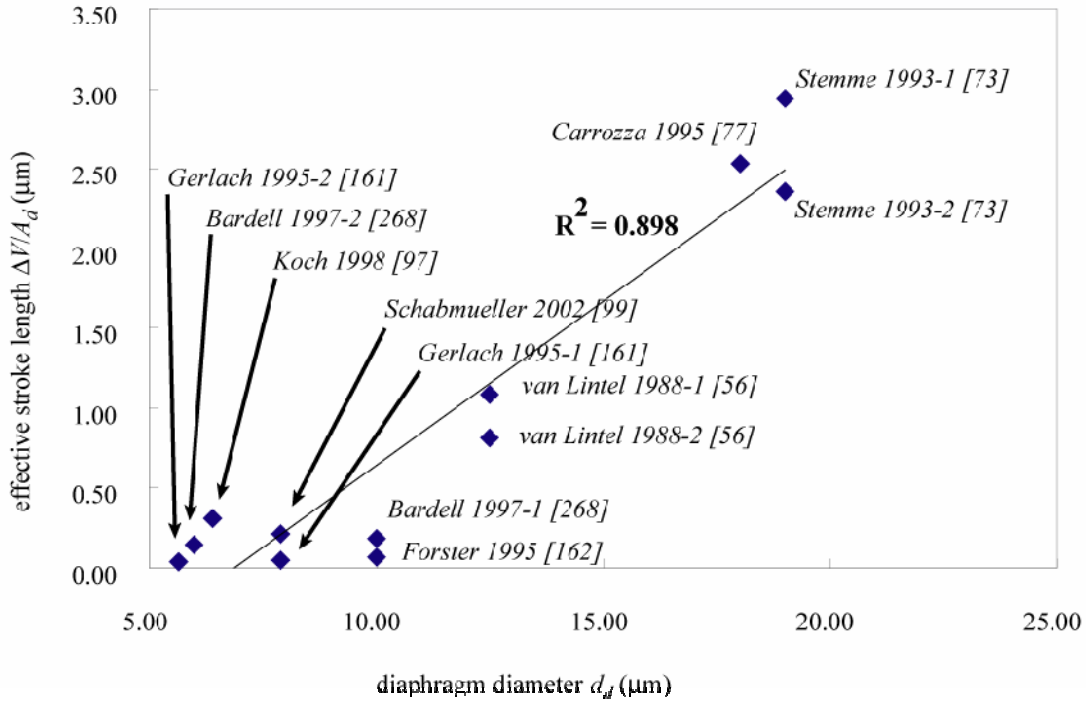


Figure 2.3: Stroke length vs. diaphragm diameter for reported RD micropumps with planar, circular diaphragms.

decreases with decreasing d_d , in part because of diaphragm stiffness dependencies reflected in eqn 2.1.

Diaphragm geometry and pressure generation

For physical reciprocating displacement micropumps, Δp_{\max} is ultimately limited by driver force and valve characteristics. In the operating regime where the driver pressure is much greater than the back pressure and the valve behavior is nearly ideal, the compressibility κ of the working fluid limits pressure generation. For a reciprocating displacement pump with ideal valves, theoretical Δp_{\max} is [96]:

$$\Delta p_{\max} = \frac{1}{\kappa} \varepsilon_c = \frac{1}{\kappa} \left(\frac{\Delta V}{V_0} \right), \quad (2.4)$$

where ε_C is the pump compression ratio, the ratio between the stroke volume ΔV and the dead volume V_0 . Eqn 2.4 dictates that micropumps intended to pump gases against high back pressures must be designed such that ε_C is very large.

For working fluids with low, uniform compressibility, Δp_{\max} on the order of tens of kPa or higher is feasible with a high-force driver and a design which minimizes V_0 . Engineering of micropumps intended to pump liquid phases is complicated, however, by the very real possibility that bubbles might be present in the working fluid. Among micropumps with the same compression ratio ε_C , bubbles of a given size disproportionately affect micropumps with smaller V_0 . Smaller micropumps tend to have smaller V_0 , so the scaling of bubble-dependent Δp_{\max} with V_0 is a further challenge for reciprocating displacement micropump designers wishing to minimize package size. Figure 2.4 shows Δp_{\max} , as a function of diaphragm diameter d_d , for bubble-laden working fluids. V_0 is taken as $0.001 d_d^3$, which approximately describes the relationship between these two parameters for many reported reciprocating displacement micropumps. Exclusive of bubbles, the working fluid is assumed to be a typical liquid, with very low compressibility ($\kappa = 0.5 \text{ m}^2 \text{ N}^{-1}$). When no bubbles are present in the working fluid, Δp_{\max} is given by eqn 2.4 and is independent of d_d for a given compression ratio ε_C . However, Δp_{\max} decreases rapidly with decreasing d_d when a bubble of volume comparable to V_0 is present.

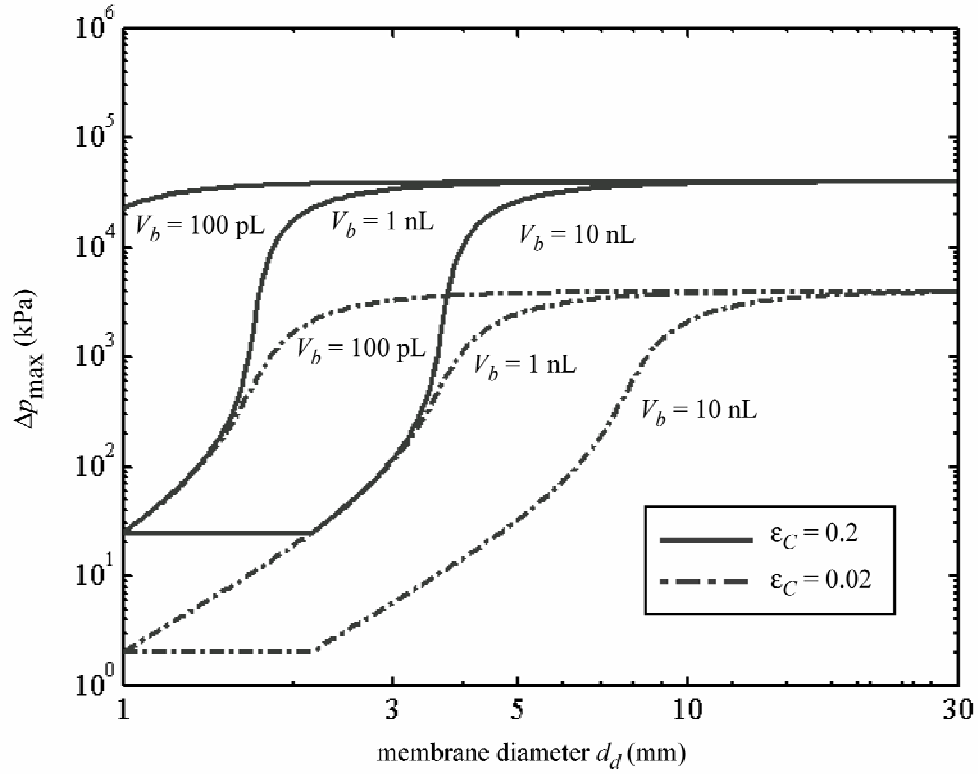


Figure 2.4: Theoretical scaling with diaphragm diameter d_d of maximum generated pressure Δp_{\max} for reciprocating displacement micropumps. As shown in eqn 2.4, Δp_{\max} is generally a function of compression ratio ε_C and of the compressibility κ of the fluid in the pump chamber. For $\varepsilon_C = \text{constant}$ and $\kappa = \text{constant}$, pressure generation is independent of diaphragm diameter. As the diaphragm diameter is scaled down, the impact of a bubble of a given volume V_b in the pump chamber on κ —and therefore on Δp_{\max} —increases. When the bubble fills the entire pump chamber, Δp_{\max} reaches its minimum. The pump dead volume is taken to be $V_0 = 0.001d_d^3$.

Richter et al. [96] and Linnemann et al. [97] studied the relationship between ε_C and bubble tolerance experimentally. Three micropumps very similar to one another, but with different compression ratios, were tested under similar conditions. A micropump with $\varepsilon_C = 0.002$ was found to pump water effectively, but stalled when an 8 μL bubble entered the pump chamber. A micropump with $\varepsilon_C = 0.017$ exhibited limited bubble tolerance, stalling after two bubbles entered the chamber in succession. A micropump with $\varepsilon_C = 0.085$ consistently passed bubbles that entered the chamber. Other recent

papers have discussed pressure generation by reciprocating displacement micropumps [98, 99].

2.2. Performance and design of reported reciprocating displacement micropumps

Reciprocating displacement micropumps with a wide range of designs have been reported. While most pump designs have a single pump chamber, a few micropumps have multiple pump chambers arranged either in series or in parallel. Driver types and configurations vary widely; reciprocating displacement micropumps with piezoelectric, electrostatic, thermopneumatic, and pneumatic drivers, among others, have been reported. Various valve designs based on flaps or other moving structures have been developed, as have fixed-geometry structures that rectify flow using fluid inertial effects. Variations among reciprocating displacement micropumps, with representative reported examples, are discussed further below. Key features and measured performances characteristics of reported reciprocating displacement micropumps are summarized (and referenced) in appendix A.

Chamber configuration

The micropump reported by Smits [16] introduced a multi-chamber design shown in figure 2.5. Channels leading to the first and from the third chambers function as the pump's inlet and outlet. Additional channels link the pump chambers in series. Piezoelectric actuators drive each of the three pump chamber diaphragms individually. Actuating the three piezoelectric disks 120° out of phase with one another produces net flow through the pump. Operating in this manner, the micropump requires no valves to

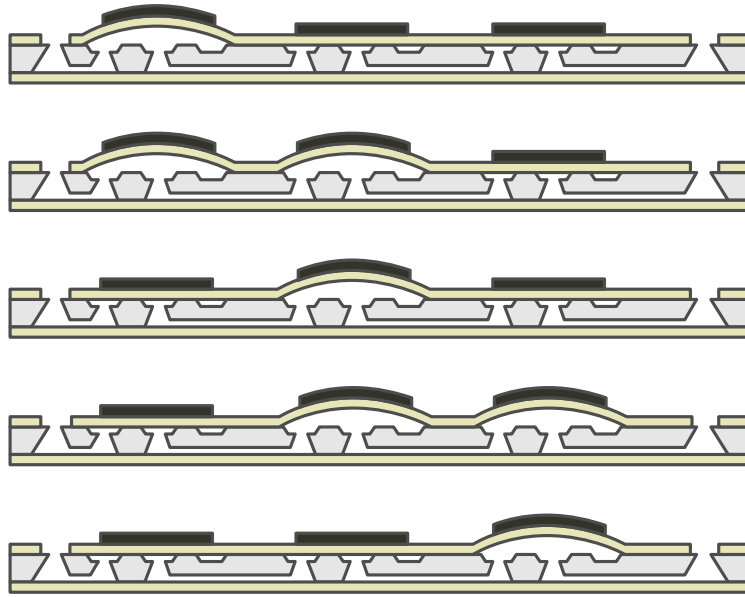


Figure 2.5: Reciprocating displacement micropump with three pump chambers in series developed by Smits [16]. The micropump is made from an etched silicon substrate bonded between two glass plates. Piezoelectric disks are bonded to the glass above each of the three pump chambers etched in the silicon. Applying a voltage to a piezoelectric actuator causes the glass to bow away from the pump chamber beneath, drawing in fluid. Staggered actuation as shown results in net fluid flow from the inlet at left to the outlet at right.

rectify the flow. Micropumps with multiple chambers in series and no valves operate in a manner somewhat similar to macroscale peristaltic pumps, and accordingly are sometimes referred to as peristaltic micropumps. Smits' micropump, which is fabricated from a single etched silicon substrate with two anodically-bonded glass covers, was patented in the U.S. in 1990 [100]. It is relatively large ($S_p \cong 1.5 \text{ cm}^3$) and pumps water with $Q_{\max} = 100 \mu\text{L min}^{-1}$ and $\Delta p_{\max} = 600 \text{ Pa}$ operating at $f = 15 \text{ Hz}$ and $V = 100 \text{ V}_{\text{p-p}}$.

In 1990, Shoji et al. reported a micropump with two pump chambers in series [101]. Unlike Smits' triple-series-chamber design, Shoji et al.'s design requires check valves. However, the two-chamber design was reported to operate effectively at higher frequencies than an otherwise-similar single-chamber micropump. Shoji et al.'s micropump is piezoelectrically driven and fabricated from glass and silicon; its size is

$S_p \cong 4.0 \text{ cm}^3$. $Q_{\max} = 18 \text{ }\mu\text{L min}^{-1}$ and $\Delta p_{\max} = 10.7 \text{ kPa}$ operating at $f = 25 \text{ Hz}$ and $V = 100 \text{ V}$. Yun et al. reported a reciprocating displacement micropump with two chambers in series driven by electrowetting-induced oscillation of a mercury plug [102]. For this micropump, $Q_{\max} = 70 \text{ }\mu\text{L min}^{-1}$ and $\Delta p_{\max} = 700 \text{ Pa}$ operating at $f = 25 \text{ Hz}$ and $V = 2.3 \text{ V}$. Power consumption is $P = 0.17 \text{ mW}$ and $\eta_{\text{est}} = 0.12 \%$. Berg et al. [103] demonstrated that pressure and flow can be generated by phased actuation of two chambers in series without use of check valves.

Shoji et al. also reported reciprocating displacement micropumps with two pump chambers arranged in parallel [101]. This configuration was intended to reduce oscillations in the pump output due to the periodic action of the micropump driver. A micropump with this parallel-chamber configuration pumps water with $Q_{\max} = 42 \text{ }\mu\text{L min}^{-1}$ operating at $f = 50 \text{ Hz}$ and $V = 100 \text{ V}$; Δp_{\max} was not reported. Olsson et al. reported double-parallel-chamber reciprocating displacement micropumps with piezoelectric drivers attached to both the top and bottom surfaces of each pump chamber [104, 105]. A precision-machined brass micropump ($S_p \cong 1.6 \text{ cm}^3$) with this four-driver design pumps water with $Q_{\max} = 16 \text{ mL min}^{-1}$ and $\Delta p_{\max} = 16.2 \text{ kPa}$ operating at $f = 540 \text{ Hz}$ and $V = 130 \text{ V}$. Performance improvements realized with multi-chamber designs must be balanced against associated increases in fabrication complexity and overall size. A recent study suggests two-chamber micropump designs are particularly effective when combined with fixed-geometry valves (discussed further below) [86].

Materials and fabrication techniques

The most common method for fabricating micropumps is micromachining of silicon, combined with glass bonding layers, as seen in van Lintel et al.'s and Smits'

micropumps. While these early micropumps are relatively large (each occupying an entire 2 inch silicon wafer), silicon micromachining is suitable for producing much smaller micropumps, as exemplified by an electrostatically driven reciprocating displacement micropump reported by Zengerle et al. in 1995 [106]. With four-layer construction and efficient arrangement of the pump components, this micropump's size is $S_p \cong 0.1 \text{ cm}^3$. Operating at $f = 300 \text{ Hz}$, this micropump pumps water with $Q_{\max} = 850 \text{ }\mu\text{L min}^{-1}$ —corresponding to a self-pumping frequency $f_{sp} \cong 1.6$ —over two orders of magnitude higher than for van Lintel et al.'s and Smits' micropumps. Pressure generation is $\Delta p_{\max} = 29 \text{ kPa}$.

A number of reciprocating displacement micropumps have been fabricated through means other than traditional silicon/glass micromachining. Piezo-driven micropumps made by precision machining of brass were reported by Stemme and Stemme in 1993 [107]. These micropumps are $S_p \cong 2.5 \text{ cm}^3$ in size. Two micropumps (with different valves) were reported. The first pumps water with $Q_{\max} = 4.4 \text{ mL min}^{-1}$ and $\Delta p_{\max} = 20.6 \text{ kPa}$ operating at $f = 110 \text{ Hz}$ and $V = 20 \text{ V}$. For the other, $Q_{\max} = 15.5 \text{ mL min}^{-1}$ and $\Delta p_{\max} = 4.9 \text{ kPa}$ for $f = 310 \text{ Hz}$. The two-chamber reciprocating displacement micropumps reported by Olsson et al. [104] was made by precision machining of brass, but with planar geometries rather than the three-dimensional geometries of the Stemme and Stemme micropumps.

Improvements in techniques for fabricating precision components from plastic have led to increasing use of plastics in reciprocating displacement micropumps. Indeed, the only micropump currently in widespread commercial distribution, produced by thinXXS GmbH of Germany (a spin-off company of IMM, the Institut für Mikrotechnik

Mainz GmbH) is made from microinjection molding of plastic [108, 109]. The size of this micropump is $S_p \cong 4.6 \text{ cm}^3$; it produces $Q_{\max} = 2 \text{ mL min}^{-1}$ and $\Delta p_{\max} = 35 \text{ kPa}$ at $V = 450 \text{ V}$ and $f = 20 \text{ Hz}$. A number of other plastic reciprocating displacement pumps have been reported. Bohm et al. reported a very compact $S_p \cong 0.3 \text{ cm}^3$ plastic reciprocating displacement micropump [110]. Carrozza et al. [111] reported a micropump fabricated by stereolithography of an ultraviolet-photocurable polymer. The size of this micropump is $S_p \cong 1.3 \text{ cm}^3$; it is partially made of brass. It pumps water with $\Delta p_{\max} = 25 \text{ kPa}$ and $Q_{\max} = 2.7 \text{ mL min}^{-1}$ operating at $V = 300 \text{ V}$ and $f = 70 \text{ Hz}$. A reciprocating displacement micropump made from printed circuit boards has been reported [112].

As discussed in section 2.1, ΔV is partially a function of the mechanical properties of the pump diaphragm, making the choice of pump diaphragm material particularly important. For micropumps driven by low-frequency and/or low-force actuators, a low-modulus diaphragm material generally allows ΔV to be maximized, favorably impacting performance. Mylar [110] and silicone rubber [113] pump diaphragms have been used in thermopneumatically driven reciprocating displacement micropumps for this reason. Since the pump diaphragm comes into contact with the working fluid, however, the stability of soft polymer diaphragms is a concern. A micropump commercially produced by Debiotech S.A. of Switzerland and targeted for implanted drug delivery has a glass diaphragm, even though its operating frequency is low enough ($f < 1 \text{ Hz}$) to permit use of low-modulus materials [114, 115]. This micropump produces flow rates of up to a few $\mu\text{L min}^{-1}$, suitable for therapeutic agent dispensation. For drivers that can operate at high frequency and produce ample force, the fast mechanical response of a stiff diaphragm

generally yields the best performance. For this reason, silicon and glass are the most common diaphragm materials in piezo-driven reciprocating displacement micropumps.

Diaphragm geometry

Among reciprocating displacement micropumps with planar, circular diaphragms, d_d and t_d vary widely. Moreover, several micropumps with noncircular and nonplanar diaphragm geometries have been reported. Piezoelectrically driven reciprocating displacement micropumps reported by Esashi et al. [116], Shoji et al. [101], and Stehr et al. [117] have diaphragms with bosses at the center. The diaphragm in a high-performance reciprocating displacement micropump reported by Li et al. [118] and discussed further below is made from two layers of silicon with interior center bosses to yield piston-like behavior.

Drivers

Figure 2.6 shows the five most common reciprocating displacement micropump driver designs: lateral-configuration piezoelectric, axial-configuration piezoelectric, thermopneumatic, electrostatic, and pneumatic. The use of piezoelectrics to drive micropumps can be traced to a class of ink jet printheads developed in the 1970s, illustrated schematically in figure 2.7. A piezoelectric actuator contracts a chamber in the printhead, causing a droplet of ink to be ejected from the nozzle. During expansion, a vacuum in the main liquid chamber fills it with ink from the ink supply, while the pressure difference associated with surface tension at the ejector orifice prevents air from entering the chamber. In this way, surface tension and capillary pressure are used as an inherent check valve with no solid moving parts. IBM was issued a U.S. patent for this

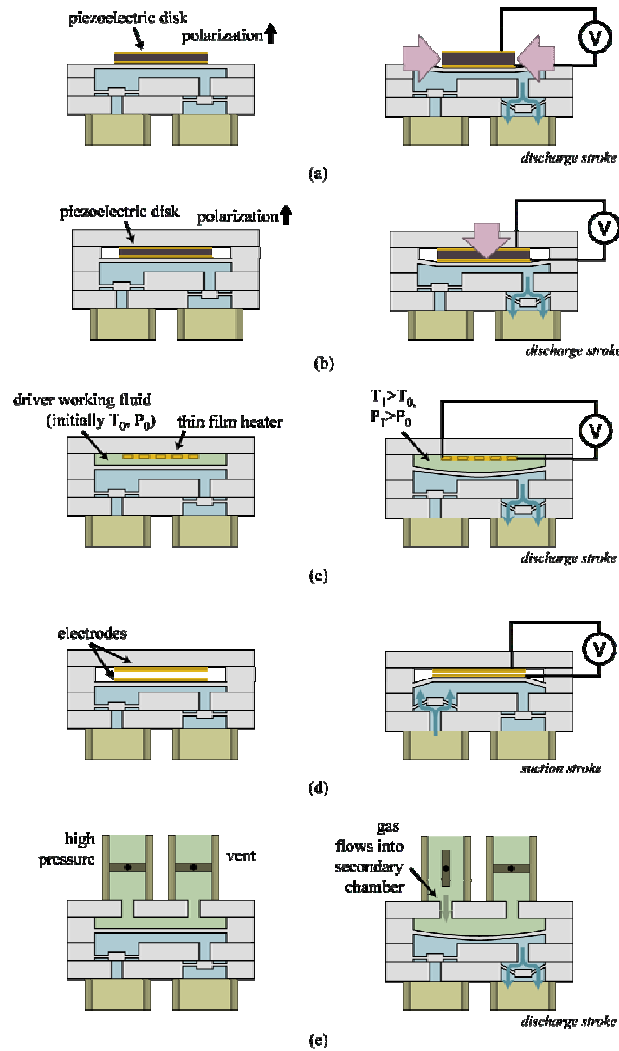


Figure 2.6: Drivers for reciprocating displacement micropumps. (a) Piezoelectric driver in the lateral-strain configuration. The bottom surface of the piezoelectric disk is bonded to the pump diaphragm; the top surface is unconstrained. During operation, the pump diaphragm deflects under a bending moment produced by radial strain in the piezoelectric disk. An axial electric field is applied to the disk. (b) Piezoelectric driver in the axial-strain configuration, where a piezoelectric disk is mounted between the pump diaphragm and a rigid frame. During operation, the pump diaphragm deflects primarily as a result of axial strain in the piezoelectric disk. As in (a), an axial electric field is applied to the disk. (c) Thermopneumatic driver, in which a thin-film resistive element heats fluid in a secondary chamber above the pump chamber. The heated fluid expands, exerting pressure on the pump diaphragm. (d) Electrostatic driver, in which the pump diaphragm deflects upward when an electric potential difference is applied between parallel electrodes. Electrostatically-driven reciprocating displacement micropumps typically have a powered suction stroke and an unpowered discharge stroke. Insulating coatings prevent shorting. (e) External pneumatic driver, in which active valves alternately pressurize and vent a secondary chamber above the pump diaphragm. Illustrations capture key features of reported micropumps with each type of driver; see text for specific examples and citations.

design in 1974 [119]. Researchers later conceived of fabricating the ink chamber using then-nascent silicon micromachining technology [120, 121].

Figures 2.6(a) and (b) illustrate piezoelectric drivers in lateral and axial configurations. The free strain that can be produced in the driver places an upper limit on the stroke volume of a piezoelectric-driven micropump. The available driving voltage and the polarization limit of the piezoelectric material, in turn, determine the maximum piezoelectric free strain. PZT-5H, a high-performance piezoceramic, has a d_{31} strain coefficient of $-274 \times 10^{-12} \text{ C N}^{-1}$ (for strain normal to the polarization direction) and a d_{33} strain coefficient of $593 \times 10^{-12} \text{ C N}^{-1}$ (for strain parallel to the polarization direction). Piezoelectrics can be driven at frequencies over 1 kHz by electric fields on the order of 10 kV cm^{-1} or higher. The efficiency of electromechanical conversion in piezoelectrics is typically between 10 and 30% (excluding the finite efficiency of the voltage conversion and AC voltage control) [122].

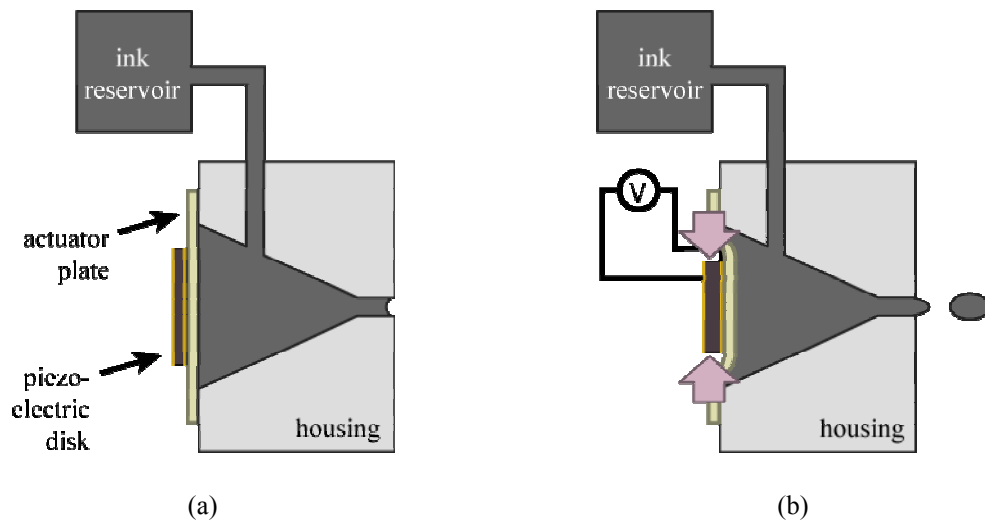


Figure 2.7: IBM ink jet printhead schematic. To eject an ink droplet, a piezoelectric disk actuator deflects the plate sealing the back side of the chamber, decreasing the chamber volume. Surface tension at the ejector orifice acts as a check valve, rectifying the flow. From U.S. patent no. 4,266,232 [121].

In piezoelectric inkjet printheads, chamber actuation results from lateral strain induced in the piezoelectric disk. In many piezo-driven micropumps, including van Lintel et al.'s [81] and Smits' [16], piezoelectric actuators are employed in a similar manner. As shown in figure 2.6(a), one face of a piezoelectric disk is bonded to the chamber diaphragm (typically using epoxy); the other face of the disk is unconstrained. The piezoelectric disk is polarized in the axial direction, and each face is covered with an electrode. Applying an axial electric field across the piezoelectric disk produces both a lateral and an axial response in the disk, described by the d_{31} and d_{33} piezoelectric strain coefficients, respectively. For this configuration, the chamber diaphragm bows to balance the lateral stress in the piezoelectric disk. If the induced lateral stress in the disk is compressive, the diaphragm bows into the chamber; if tensile, it bows away from the chamber. In some micropumps, the piezoelectric actuators are driven bidirectionally to maximize stroke volume [16]. Progress has been made recently on the development of analytical solutions for the mechanical response of piezo-bonding layer-diaphragm structures [123]. Morris and Forster used numerical simulations to identify optimal diaphragm and piezoelectric disk geometries for lateral-strain piezo-driven reciprocating displacement micropumps [88]. Other researchers have also used numerical methods to study lateral-strain piezo-driven reciprocating displacement micropumps [84, 124]. Stroke volume can be increased by using multiple electrodes to apply a spatially-varying field across the piezoelectric disk [100].

Micropumps that rely on piezoelectric coupling parallel to the applied field (described by the d_{33} piezoelectric strain coefficient), as shown in figure 2.6(b), have also been reported. In this configuration, both faces of the piezoelectric disk are

constrained—one by a rigid support and one by the pump diaphragm. The axial strain induced in the disk by applying an external axial electric field causes the pump diaphragm to deflect, expanding and contracting the pump chamber. Esashi et al. [116] reported the first reciprocating displacement micropump driven by a piezoelectric actuator in this configuration. This micropump was fabricated from two layers of silicon with an intermediate layer of sputtered glass. A glass housing fixes a piezoelectric actuator above a 2 mm square bossed silicon diaphragm. The pump size is $S_p \cong 0.8 \text{ cm}^3$; it pumps water with $Q_{\max} = 15 \text{ } \mu\text{L min}^{-1}$ and $\Delta p_{\max} = 6.4 \text{ kPa}$ at $f = 30 \text{ Hz}$ and $V = 90 \text{ V}_{\text{p-p}}$.

Many reported piezo-driven reciprocating displacement micropumps operate at very high frequencies, taking advantage of the fast temporal response of piezoelectric actuators. A two-chamber piezo-driven reciprocating displacement micropump reported by Olsson et al. [125, 126] operates at $f = 3 \text{ kHz}$ and pumps water with $Q_{\max} = 2.3 \text{ mL min}^{-1}$. Fluid dynamic effects rather than mechanical check valves are used to produce net flow through this micropump, an approach discussed in more detail below. Li et al. [118] reported an axial-configuration piezo-driven reciprocating displacement micropump driven by multiple stacks of high-performance piezoelectric materials. This micropump, intended for microrobotics and shoe strike power conversion, has an $S_p \cong 3.2 \text{ cm}^3$ and pumps silicone oil (in a closed, pressurized system) with $Q_{\max} = 3 \text{ mL min}^{-1}$ and $\Delta p_{\max} = 300 \text{ kPa}$ operating at $f = 3.5 \text{ kHz}$ and $V = 1.2 \text{ kV}$. A number of other piezoelectric-driven reciprocating displacement micropumps have been reported [127, 128].

Inserting and attaching piezoelectric actuators may increase manufacturing costs relatively to a fully batch process. Koch et al. sought to address this limitation by screen-

printing a PZT thick film to function as a lateral-strain-configuration reciprocating displacement micropump driver [129-131]. This micropump produced $Q_{max} = 120 \mu\text{L min}^{-1}$ and $\Delta p_{max} = 1.7 \text{ kPa}$ operating at 200 Hz and 600 V_{p-p}; an otherwise-identical micropump with a bulk piezoelectric driver produced $Q_{max} = 150 \mu\text{L min}^{-1}$ and $\Delta p_{max} = 3.5 \text{ kPa}$ operating at $f = 200 \text{ Hz}$ and $V = 200 \text{ V}_{p-p}$. A modified version of this micropump with a bulk piezoelectric driver produced $Q_{max} = 1.5 \text{ mL min}^{-1}$ and $\Delta p_{max} = 1 \text{ kPa}$ [132]. Stehr et al. [117] reported a reciprocating displacement micropump driven by a piezoelectric actuator with a bimorphic piezoelectric cantilever structure attached to the center of the pump diaphragm. This micropump pumps water with $Q_{max} = 1.5 \text{ mL min}^{-1}$ and $\Delta p_{max} = 17 \text{ kPa}$ operating at $f = 190 \text{ Hz}$ and $V = 200 \text{ V}$. Further discussion of the design and performance of piezoelectric drivers and their applications in reciprocating displacement micropumps can be found in several recent papers [133-137].

Figure 2.6(c) illustrates the design of a typical thermopneumatically driven reciprocating displacement micropump. A chamber opposite the primary pump chamber holds a secondary working fluid (typically a gas, although liquids are also used). Heating the secondary working fluid, usually with an integrated thin-film resistive heater, causes it to expand. The expanding secondary working fluid deflects the pump diaphragm, discharging primary working fluid through the pump outlet. The intake stroke occurs when the heater is deactivated and the diaphragm relaxes. The secondary chamber is usually vented to reduce relaxation time. The first thermopneumatically-driven reciprocating displacement micropump was reported by van de Pol et al. in 1989 [138, 139]. This relatively large micropump ($S_p \cong 4 \text{ cm}^3$) consists of three layers of silicon and two layers of glass with an evaporated aluminum thin film heater element. With air as

the secondary working fluid, it pumps water with $Q_{\max} = 34 \mu\text{L min}^{-1}$ and $\Delta p_{\max} = 5 \text{ kPa}$ operating at $f = 1 \text{ Hz}$ and $V = 6 \text{ V}$; $\eta_{\text{th}} = 3.6 \times 10^{-5} \%$ (i.e., less than one part in 1,000,000 of the input power is converted to work on the fluid).

The temporal response of thermopneumatic actuators is limited by the rate of heat transfer into and out of the secondary working fluid. As a result, thermopneumatically driven reciprocating displacement micropumps typically operate at relatively low frequencies ($f < 5 \text{ Hz}$). Elwenspoek et al. sought to maximize f with a design that minimizes heat transfer into the substrate (instead of the secondary working fluid) during the heating step [140]. This micropump pumps water with $Q_{\max} = 55 \mu\text{L min}^{-1}$ operating at $f = 5 \text{ Hz}$; Δp_{\max} was not reported.

Low-modulus pump diaphragm materials are often used in thermopneumatically-driven reciprocating displacement micropumps in order to maximize ΔV . Schomburg et al. [141] reported a thermopneumatically driven reciprocating displacement micropump with a $2.5 \mu\text{m}$ thick polyimide pump diaphragm. This micropump was fabricated by polymer injection molding; the heater is titanium. With air as the secondary working fluid, this micropump pumps air with $Q_{\max} = 44 \mu\text{L min}^{-1}$ and $\Delta p_{\max} = 3.8 \text{ kPa}$ operating at $f = 5 \text{ Hz}$ and $V = 15 \text{ V}$; $\eta_{\text{est}} = 1.6 \times 10^{-4} \%$. S_p was not reported, but the lateral dimensions of the pump are $7 \text{ mm} \times 10 \text{ mm}$. Grosjean and Tai reported a thermopneumatically driven reciprocating displacement micropump with a $120 \mu\text{m}$ thick silicone rubber diaphragm [142]. The silicone rubber is coated with a thin layer of parylene, which functions as a vapor barrier. With air as the secondary working fluid, this device pumps water with $Q_{\max} = 4.2 \mu\text{L min}^{-1}$ and $\Delta p_{\max} = 3 \text{ kPa}$ at $f = 2 \text{ Hz}$. Power consumption is 0.3 W ($\eta_{\text{est}} = 3 \times 10^{-4} \%$). Jeong and Yang [143] reported a

thermopneumatically driven reciprocating displacement micropump with a corrugated silicon pump diaphragm. The corrugations are intended to increase diaphragm deflection (and therefore stroke volume) for a given secondary chamber pressure. This micropump produces $Q_{\max} = 14 \mu\text{L min}^{-1}$ operating at $f = 4 \text{ Hz}$ and $V = 8 \text{ V}$; Δp_{\max} was not reported. Sim et al. [144] attempted to increase the thermopneumatic actuator force through phase change of the secondary working fluid. This micropump is highly compact ($S_p = 0.070 \text{ cm}^3$), has a $30 \mu\text{m}$ thick silicone rubber diaphragm and aluminum flap valves, and uses water as the secondary working fluid. Operating at $f = 0.5 \text{ Hz}$ and $P = 0.6 \text{ W}$, this micropump pumps water with $Q_{\max} = 6 \mu\text{L min}^{-1}$ and $\Delta p_{\max} = 100 \text{ Pa}$. Maximum thermodynamic efficiency was reported to be $\eta = 3.6 \times 10^{-7}\%$. Advantages of thermopneumatic actuation include ready fabrication using standard micromachining processes and low operating voltages. Whereas the stroke lengths of piezoelectrically- and electrostatically-driven micropumps are typically limited to a few microns, the stroke lengths of thermopneumatically-driven micropumps can be much larger, limited only by the available driver force and the mechanical properties of the diaphragm. The diaphragm in the pump reported by Schomburg et al. deflects $100 \mu\text{m}$ during operation, yielding a compression ratio large enough to pump gases [141]. Schomburg et al.'s plastic micropump, for example, is bonded to a silicon heat sink for this reason. A number of papers discuss thermopneumatically-driven reciprocating displacement micropumps (including heat transfer aspects) in detail [145-147].

A subset of thermopneumatically driven reciprocating displacement micropumps are so-called “bubble” pumps, in which phase change of the primary working fluid, rather than of a secondary working fluid in a separate chamber, is induced. Tsai and Lin

reported a thermal bubble-driven reciprocating displacement micropump fabricated from only two layers of material [148]. This micropump pumps isopropyl alcohol with $Q_{\max} = 45 \mu\text{L min}^{-1}$ and $\Delta p_{\max} = 400 \text{ Pa}$ operating at $f = 400 \text{ Hz}$ and $V = 20 \text{ V}$; power consumption is $P = 0.5 \text{ W}$ ($\eta_{\text{est}} = 1.4 \times 10^{-6}\%$). Zimmermann et al. [149] reported a thermal bubble micropump in which the heated chamber is offset from the main flow path, reducing heating of the working fluid. This micropump pumps isopropyl alcohol with $Q_{\max} = 9 \mu\text{L min}^{-1}$ and $\Delta p_{\max} = 16 \text{ kPa}$ operating at $f = 10 \text{ Hz}$; power consumption is $P = 0.18 \text{ W}$.

Electrostatic forces are widely used for actuation in MEMS devices. Electrostatically driven reciprocating displacement micropumps typically have the parallel-plate actuator design shown in figure 2.6(d). The large-displacement comb-drive configuration that is widely used to increase the range of electrostatically actuated MEMS devices [150] is difficult to implement in reciprocating displacement micropumps. The micropump diaphragm (and therefore the bottom electrode) typically bows during pump operation, but the driver force can be easily determined at the very beginning of the pump stroke when both electrodes are flat plates. The capacitance between a pump diaphragm of diameter d_d and a counterelectrode of equal size separated by a distance s is

$$C = \frac{\varepsilon\pi d_d^2}{4s} \quad (2.5)$$

The electrostatic force F_e between the two plates is therefore

$$F_e = \frac{1}{2} \frac{\partial C}{\partial s} V^2 = -\frac{\varepsilon\pi d_d^2}{8s^2} V^2 \quad (2.6)$$

where ε is the permittivity of the medium separating the plates and V is the potential difference between them [151]. To generate an initial driver force per unit diaphragm area p_a of 100 kPa with an electrostatic driver operating in a vacuum or in air ($\varepsilon = 8.85 \times 10^{-12} \text{ C}^2 \text{ J}^{-1} \text{ m}^{-1}$) requires a voltage-separation distance ratio V/s of $150 \text{ V } \mu\text{m}^{-1}$. With adequate control over out-of-plane feature size during fabrication, therefore, electrostatic drivers can produce appreciable forces at moderate voltages. They offer the further advantage of increasing driver force as the diaphragm deflects (and stiffens). The highly compact ($S_p \cong 0.1 \text{ cm}^3$) reciprocating displacement micropump reported by Zengerle et al. and discussed above is electrostatically driven [106, 152]. This micropump exemplifies several favorable features electrostatic drivers: it is fully micromachined, highly compact, and capable of operating at high frequency. With $s = 5 \text{ } \mu\text{m}$, it pumps water with $Q_{\max} = 850 \text{ } \mu\text{L min}^{-1}$ and $\Delta p_{\max} = 29 \text{ kPa}$ operating at $V = 200 \text{ V}$ and $f = 800 \text{ Hz}$. Power consumption is $P = 5 \text{ mW}$ ($\eta_{\text{est}} = 0.39\%$). Richter et al. [96] compared the performance of two similar reciprocating displacement micropumps, one with an electrostatic driver and one with a lateral-configuration piezoelectric driver. The electrostatically driven micropump pumps water with $Q_{\max} = 260 \text{ } \mu\text{L min}^{-1}$ operating at $f = 400 \text{ Hz}$, compared to $Q_{\max} = 700 \text{ } \mu\text{L min}^{-1}$ for the piezo-driven micropump operating at $f = 220 \text{ Hz}$. Cabuz et al. reported a electrostatically driven triple-series-chamber micropump [153]. Further analysis and review of the performance of electrostatically driven reciprocating displacement micropumps can be found in several recent papers [85, 154-157].

Reciprocating displacement micropumps driven pneumatically, as shown in Figure 2.6(e), have also been reported. These pumps require an external pneumatic

supply and one or more high-speed valve connections and therefore are not strictly comparable to micropumps with fully integrated actuators. In settings where the necessary infrastructure is available, however, pneumatically-driven reciprocating displacement micropumps can be effective. A pneumatically-driven reciprocating displacement micropump fabricated using LIGA techniques was reported by Rapp et al. [158]. The three-chamber (series configuration) reciprocating displacement micropump reported by Grosjean et al. and described above exhibited much better performance when driven pneumatically than thermopneumatically ($Q_{\max} = 100 \mu\text{L min}^{-1}$ with pneumatic actuation vs. $Q_{\max} = 4.2 \mu\text{L min}^{-1}$ with thermopneumatic actuation) [142].

As with thermopneumatic drivers, low-modulus diaphragm materials are widely used in pneumatically-driven reciprocating displacement micropumps. Unger et al. reported a class of pneumatically-driven series multi-chamber reciprocating displacement micropumps made by lithographically patterning multiple layers of a soft elastomeric substrate [159]. Individual layers of elastomer are first spun onto molds made from patterned photoresist, then stacked to form chambers and channels. The channels and chambers made using this “soft” lithography technique have cross-sectional dimensions between 10-100 μm . The soft elastomer chambers are actuated by pneumatic pressure of order 100 kPa; separate, individually-controlled valves of centimeter scale or larger are required for these chambers. Pressure performance for these devices was not reported, but Q_{\max} is of order 100 nL min^{-1} . Mathies and coworkers have performed extensive work on pneumatically-driven reciprocating displacement micropumps for microchip-based laboratory systems for performing biological and chemical analysis [30, 160]. A

representative micropump with a 3.0 mm diameter PDMS diaphragm was reported to pump water with $Q_{\max} = 2.8 \mu\text{L min}^{-1}$ and $\Delta p_{\max} = 30 \text{ kPa}$.

Other, less common micropump drivers have been reported. A version of the piezoelectrically-driven reciprocating displacement micropump reported by Bohm et al. was produced with an electromagnetic driver resembling a solenoid [110]. The choice of actuator has little impact on pump performance ($Q_{\max} = 2 \text{ mL min}^{-1}$, $\Delta p_{\max} = 12.5 \text{ kPa}$ operating at $V = 350 \text{ V}_{\text{p-p}}$ and $f = 50 \text{ Hz}$), but the micropump with the electromagnetic driver is substantially larger than the piezoelectrically-driven version ($S_p = 8 \text{ cm}^3$ vs. $S_p = 2.9 \text{ cm}^3$). Dario et al. reported a smaller ($S_p \cong 2.5 \text{ cm}^3$) electromagnetically-driven reciprocating displacement micropump made by thermoplastic molding [161]. Water is pumped with $Q_{\max} = 780 \text{ mL min}^{-1}$ and $\Delta p_{\max} = 4.6 \text{ kPa}$ operating at $V = 14 \text{ V}$ and $f = 264 \text{ Hz}$. Meng et al. reported high-flow-rate micropumps with pneumatic and solenoid drivers [162]. In handheld electronic medical diagnostic devices marketed by i-STAT Corporation, a solenoid actuates a rubber diaphragm to pump samples [163]. Gong et al. analyzed the theoretical performance of an optimized electromagnetically-actuated reciprocating displacement micropump [164]. Santra et al. reported a reciprocating displacement pump driven by the interaction of a stationary electromagnet with a permanent magnet diaphragm [165]. Bernard et al. reported reciprocating displacement micropumps driven by shape-memory alloy actuators [166]. An SMA-driven micropump made of five layers of micromachined silicon with a polyimide diaphragm and sputter-deposited titanium nickel pumps water with $Q_{\max} = 50 \mu\text{L min}^{-1}$ and $\Delta p_{\max} = 0.5 \text{ kPa}$ operating at $f = 0.9 \text{ Hz}$. Power consumption is $P = 0.63 \text{ W}$ ($\eta_{\text{est}} = 1.7 \times 10^{-5}\%$). The use of shape-memory alloys in reciprocating displacement

micropumps is discussed further by Makino et al. [167]. As discussed above, Yun et al. reported a reciprocating displacement micropump driven by electrowetting [102]. Micropump designs with bimetallic drivers [168-170] and magnetoelastic drivers [171] have also been reported.

Valves

The performance of check valves at the inlet and outlet of the pump chamber is critical to the operation of reciprocating displacement micropumps. Microvalves have been reviewed recently [72, 172]. Figures of merit for check valves include diodicity, or the ratio between the forward and reverse pressure drop across the valve; maximum operating pressure; ease of fabrication; and reliability. Most micropumps incorporate some sort of normally-closed, passive (non-actuated), mechanical flap structure. The valves in the reciprocating displacement micropump reported by van Lintel et al. consist of a flexible, circular diaphragm with an opening at the center surrounded by a stiffening “ring mesa” [81]. A number of other reciprocating displacement micropumps use this valve structure [108, 110, 118, 139]. Flap valves based on cantilever structures are easily fabricated and widely used in micropumps [96, 97, 106]. Several micropumps incorporating check valves with a tethered-plate structure (similar to that shown in figure 2.1) have been reported [101, 116, 166]. The dynamic response of passive flap valves can be important for high-frequency pumps, and the flow can reverse direction above a mechanical resonance of the valves [106, 173]. Several recent papers discuss passive flap valves [157, 164, 174-176]. The stereolithographically-fabricated reciprocating displacement micropump reported by Carrozza et al. has ball-type check valves [111]. Ball valves for micropumps are further discussed by Accoto et al. [177].

Active valves—opened and closed by an actuating force—offer improved performance at the expense of fabrication and operational complexity. Active valves with bimetallic [178], electrostatic [179-182], thermopneumatic [183-186], piezoelectric [116, 187], and other actuators [172, 188-194] have been reported.

Fluid flow through reciprocating displacement micropumps can also be rectified by leveraging fluid dynamic effects in inlet and outlet channels with suitable geometries. Pumps with flow-rectifying channels instead of more traditional valves are referred to as having “fixed-geometry” or “no-moving-parts” valves, or, occasionally, as “valveless” pumps. The brass micropumps reported in 1993 by Stemme and Stemme have nozzle-diffuser inlet and outlet channel geometries that function as fixed-geometry valves [107]. Flow separation in these structures causes pressure drop to be a function of flow direction. A micropump with 4 mm long nozzles with small and large diameters of 230 μm and 600 μm , respectively, pumps water with $Q_{\text{max}} = 4.4 \text{ mL min}^{-1}$ and $\Delta p_{\text{max}} = 20.6 \text{ kPa}$ at $f = 110 \text{ Hz}$ and $V = 20 \text{ V}$. An otherwise-identical micropump with 3 mm long nozzles with small and large diameters of 530 μm and 1.1 mm, respectively, pumps water with $Q_{\text{max}} = 15.5 \text{ mL min}^{-1}$ and $\Delta p_{\text{max}} = 4.9 \text{ kPa}$ at $f = 310 \text{ Hz}$.

Olsson et al. reported a brass micropump with planar nozzle-diffuser elements [104]. A pump with this design and two pumping chambers produced $Q_{\text{max}} = 16 \text{ mL min}^{-1}$ and $\Delta p_{\text{max}} = 100 \text{ kPa}$. In 1995, Gerlach reported a nozzle-diffuser micropump produced by micromachining silicon [195]. Much smaller than the brass pumps that preceded it ($S_p \cong 0.2 \text{ cm}^3$), this piezo-driven micropump pumps water with $Q_{\text{max}} = 400 \mu\text{L min}^{-1}$ and $\Delta p_{\text{max}} = 3 \text{ kPa}$ at $f = 3 \text{ kHz}$ and $V = 50 \text{ V}$. Forster et al. [196] reported reciprocating displacement micropumps in which Tesla valves, rather than the more widely-used

nozzle-diffuser structures, rectify the flow. A number of other micropumps with fixed-geometry valves have been reported, including those of Koch et al. [129-131] and Jeong and Yang [143].

The absence of moving structures in fixed-geometry valves may be advantageous when the working fluid contains cells or other materials prone to damage or clogging. In 1999, Jang et al. [197] reported pumping suspensions of polystyrene beads as large as 20 μm through piezo-driven reciprocating displacement micropumps with Tesla-type fixed-geometry valves. Andersson et al. [198] subsequently reported pumping liquid samples containing beads through a piezo-driven reciprocating displacement micropump with nozzle-diffuser valves. Several recent studies discuss fixed-geometry valves [91, 199-203].

Intriguing alternatives to the traditional valves used in micropumps have been proposed. Liu et al. reported using hydrogel swelling in response to changes in environmental chemistry to restrict flow through microchannels or close them off entirely [204]. Matsumoto et al. reported a piezo-driven micropump in which temperature-induced viscosity changes at the inlet and outlet rectify the flow [205]. Yun et al. proposed using electrohydrodynamic effects to improve the performance of fixed-geometry valves [206]. Kirby et al. [193] reported the use of in-situ polymerized plugs which act as check valve pistons [207]. These valves have an impressive open/closed flow ratio of 10^6 at pressures as high as 700 kPa.

Dynamic effects

While some reciprocating displacement micropumps are designed to operate exclusively in a quasi-static manner, dynamic effects are relevant to the operation of

others. As discussed above, micropumps with fixed-geometry valves rely on fluid dynamic effects to rectify fluid flow without traditional flap valves. Reciprocating displacement micropumps with high-frequency drivers often designed to operate at frequencies where dynamic effects lead to improved performance, particularly increased flow rate. Recent papers have suggested that this approach is particularly effective for micropumps with fixed-geometry valves [84, 90]. As mentioned earlier, dynamic effects often cause flow reversal in micropumps with flap valves operated at high frequencies [101, 106].

For dynamic effects to be relevant to the operation of a reciprocating displacement micropump, the operation of the micropump must such that (i) the operating frequency is on the order of (or greater than) the mechanical resonant frequency of the diaphragm, and/or (ii) inertial effects in the fluid are important [48]. Figure 2.8 shows the importance of dynamic effects in reported reciprocating displacement micropumps with simple diaphragm geometries. The ratio of the operating frequency f and the approximate diaphragm resonant frequency f_r (calculated from the reported diaphragm geometry and material properties using eqn 2.3) is plotted against the product of the Reynolds and Strouhal number. High values along either axis imply that the pump is operating in a regime where dynamic effects are important. A number of papers discuss dynamic effects in reciprocating displacement micropumps [84, 106, 152, 177].

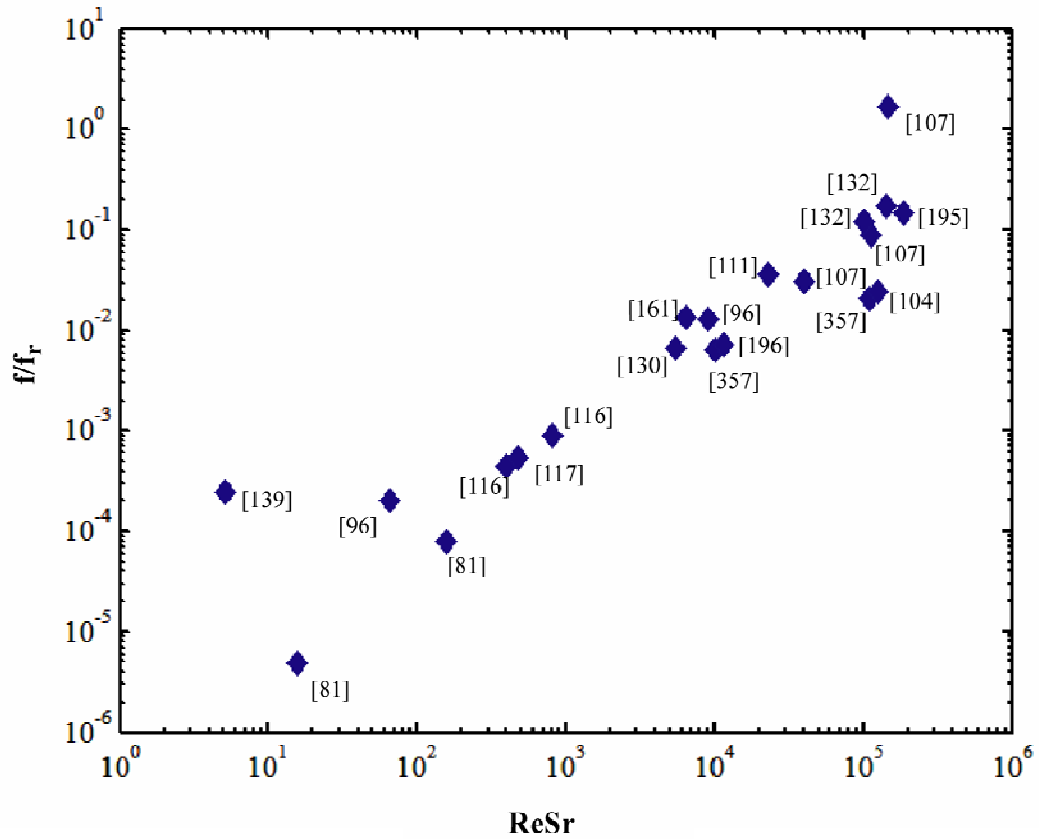


Figure 2.8.: Dynamic effects in reported reciprocating displacement micropumps. The product of the Reynolds number Re and the Strouhal number Sr indicates the importance of fluid inertia in low Re flows. The ratio of the operating frequency f and the diaphragm resonant frequency f_r indicates the extent to which dynamic effects are relevant in the membrane mechanical response. Higher values of f/f_r and lower $Re \cdot Sr$ is indicative of a micropump performance-limited by the mechanical time constant of the pump driver and/or diaphragm. Lower values of f/f_r and higher $Re \cdot Sr$ are associated with micropumps where fluid inertia is particularly important. Multiple data points shown for micropumps tested with more than one working fluid and/or at more than one operating frequency.

2.3. Other displacement micropumps

While most reported displacement micropumps employ a reciprocating surface to generate pressure and flow, rotary displacement micropumps and aperiodic displacement micropumps have also been reported.

Rotary Displacement Micropumps

The rotary displacement micropumps that have been reported are mostly micro gear pumps. Dopfer et al. [208] reported a gear micropump fabricated by LIGA and driven by a small electromagnetic motor. Two opposing in-line gears, 0.6 mm in diameter, pump a glycerin-water solution with $Q_{\max} = 180 \mu\text{L min}^{-1}$ and $\Delta p_{\max} = 100 \text{ kPa}$ operating at 2250 rpm. Minimizing the gaps between the gears and the housing through which backflow occurs is a major fabrication challenge. The back pressure against which a gear pump can operate generally scales with the inverse of viscosity, making these pumps best suited for use with moderately high-viscosity liquids. Dopfer et al. tested a slightly larger gear pump (gear diameter 1.2 mm) with both the glycerin-water solution and with pure water. With the glycerin-water solution, $Q_{\max} = 190 \mu\text{L min}^{-1}$ and $\Delta p_{\max} = 100 \text{ kPa}$, while for pure water $Q_{\max} = 5.5 \mu\text{L min}^{-1}$ and $\Delta p_{\max} = 2.4 \text{ kPa}$. A gear micropump made of PMMA and also fabricated by LIGA was reported by Dewa et al. [209]. The use of external motors with gear pumps limits the prospects for true miniaturization; the gear pump reported by Dopfer et al., for example, is $S_p = 3 \text{ cm}^3$ in size. As an alternative to using an external motor, a planetary gear micropump driven by surface micromachined electrostatic comb drives has been proposed [210].

Terray et al. reported a highly novel gear micropump based on optically trapping $3 \mu\text{m}$ diameter colloidal silica [211]. Several microspheres are arranged into a two-lobe

gear within a fluid chamber. The microspheres are controlled individually by rapidly scanning a laser between the microspheres, and the mechanism produces a flow rate of around 1 nL per hour.

Gad el Hak and co-workers have studied an alternative rotary displacement micropump design based flow generation through eccentric rotation of a cylinder in a microchannel [212, 213]. Hatch et al. reported a rotary displacement micropump based on manipulating a ferrofluidic plug with an external magnet [214]. The plug pushes the working fluid in front of it as it circulates through a closed path; inlet and outlet ports along the path produce net flow of the working fluid. This manner of operation resembles that of macroscale vane pumps. Key issues for such pumps include ensuring the immiscibility of the ferrofluidic plug and liquid being pumped; degradation of ferrofluid over time; and the need to incorporate an external controller for the magnet.

Aperiodic Displacement Micropumps

A number of micropumps have been reported in which a moving surface or boundary exerts pressure on the working fluid, but in which the movement of the pressure surface is not generally reciprocating or otherwise periodic. These aperiodic displacement micropumps tend to be suitable only for pumping finite volumes of fluid. Aperiodic displacement pumping with compressed gas reservoirs is used in Minimed implanted insulin delivery systems [23]. Electronically controlled solenoid-driven valves control the release of insulin from the secondary chamber; through a tube, and into the diabetic's intraperitoneal cavity. The implanted device occupies a volume of over 50 cm³. Sefton et al. discuss implanted pumps in detail [215]. A valved pressure source is also the basis of a flow cytometry system under development by Cabuz et al. of the Honeywell Corporation [216]. This device includes a 2 cm³ pressurized chamber and

produces regulated flow with $Q \approx 50 \mu\text{L min}^{-1}$ against unspecified back pressure. The Honeywell device exemplifies both the advantages and the disadvantages of pneumatic aperiodic displacement pumps. The pump is inherently low power and robust, but requires closed-loop control because the driving pressure varies over time. A means of recharging the pressure source is required for long term use. The inherently unidirectional flow produced by the pressure source is converted to bidirectional flow using active valves—increasing the versatility of the pump, but at a substantial cost in complexity.

Pneumatically-driven aperiodic displacement pumping is readily implemented at the microscale. Interfacial tension effects often take the place of traditional moving surfaces for applying pressure on working fluids [13]. Tas et. al. reported an aperiodic displacement micropump based on injecting bubbles into a microchannel through a port midway along its length [217]. Axial variations in surface tension due to discontinuities in the microchannel height produce net flow. Producing bidirectional flow at the microscale with valved pressure reservoirs is discussed by Jen and Lin [218].

Aperiodic displacement micropumps based on thermal or electrochemical phase change have been widely reported. Evans et al. [206] demonstrated an aperiodic displacement micropump based on locally boiling the liquid in a closed-end microchannel [219]. A similar approach was taken by Handique et al. [220], producing $Q_{\text{max}} = 20 \text{ nL min}^{-1}$. Jun et al. [221] and Song et al. [222] reported using an array of heating elements to generate flow in a channel open on both ends. Several other aperiodic displacement micropumps based on phase change have been reported [223-

225]. Lin et al. discuss thermal bubble formation in micromachined devices in detail [226].

Electrical control of interfacial tension was proposed as a microscale pumping mechanism by Matsumoto and Colgate [227, 228]. Electrowetting-driven aperiodic displacement micropumps and other electrowetting-based microfluidic devices have since been developed [229, 230]. A related class of micropumps based on thermocapillary effects has also been reported [231, 232]. Osmosis has been used as an aperiodic displacement pumping mechanism in microfluidic systems [233, 234]. Aperiodic pumping based on the interaction of local electric fields with DNA has been reported [235].

2.4. Dynamic micropumps

Centrifugal pumps are the most common type of traditional dynamic pump. Extensive miniaturization of centrifugal pumps has been precluded, however, by typically unfavorable scaling of efficiency with decreasing Reynolds number [236] and the limitations of microfabrication technologies. Microturbines with $S_p < 1 \text{ cm}^3$ have been explored for applications such as microrocketry [237-240]. Axial flow pumps may generally be favored for other applications, particularly in space exploration, involving primarily gas phases. Miniature axial flow pumps are also being developed for certain biological applications [241].

There are a variety of alternatives to rotating machinery for continuously adding momentum (or directly imparting Lorentz forces into the fluid volume) at the microscale. Electrohydrodynamic, electroosmotic, and magnetohydrodynamic micropumps are all based on interactions between the working fluid and an electromagnetic field. An

additional category of dynamic micropumps are those which generate flow through acoustic effects. Key features and the performance of reported dynamic micropumps are summarized in table A-2.

Electrohydrodynamic micropumps

Electrohydrodynamic (EHD) micropumps are based on the interaction of electrostatic forces with ions in dielectric fluids. Ion drag—which is related to ionic mobility—results in bulk fluid flow and pressure. The electric body force density F_e associated with an applied electric field E is given by

$$F_e = qE + P \cdot \nabla E - \frac{1}{2} E^2 \nabla \varepsilon + \frac{1}{2} \nabla \left[E^2 \left(\frac{\partial \varepsilon}{\partial \rho} \right)_T \rho \right] \quad (2.7)$$

where q is the charge density, ε is the fluid permittivity, ρ is the fluid density, T is the fluid temperature, and P is the polarization vector [242]. Micropumps based on Coulomb forces acting on free charges in a field (the first term in equation 2.7) and on dielectric forces in a fluid containing a permittivity gradient (the third term in equation 2.7) have been reported. Coulomb force-based EHD micropumps generally require the existence of space charge in a dielectric fluid. Space charge can be produced because of inhomogeneities in the fluid, or through dissociation or direct charge injection. These three mechanisms for space charge generation are associated with *induction*, *conduction*, and *injection* EHD pumping, respectively.

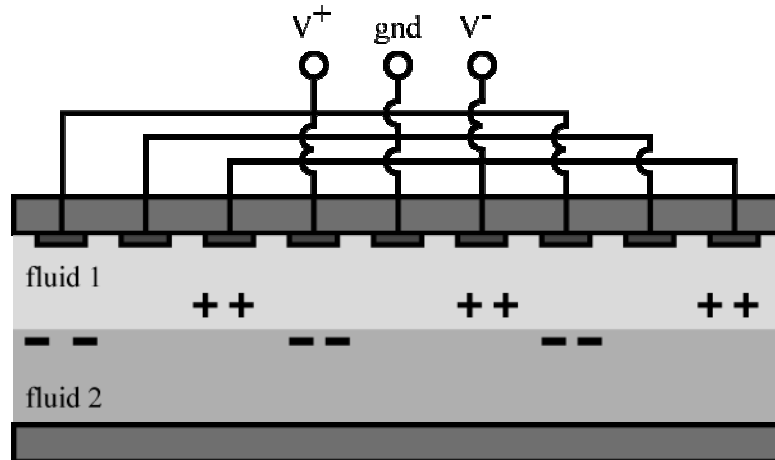


Figure 2.9: One type of traveling-wave (induction) electrohydrodynamic pump. Arrays of electrodes capacitively induce mirror charges at the interface between two fluids. Sequential switching of the electrode arrays results in net fluid flow. After Ahn and Kim [243].

In *induction* EHD micropumps, space charge is induced in an inhomogeneous working fluid through the application of an electric field with a component transverse to the flow direction, as shown in figure 2.9. Applying phased driving voltages to the electrode array results in net fluid flow as the space charge is accelerated by the axial component of the electric field. Bart et al. reported an induction EHD micropump that pumps silicone oil [244]. Quantitative performance measures were not reported.

Fuhr et al. reported an EHD micropump based on electric field interactions with dipoles in a polarized medium [245]. Like a typical Coulomb force-based induction EHD micropump, this micropump operates by means of traveling waves applied to arrays of electrodes. This micropump generates $Q_{\max} = 2 \mu\text{L min}^{-1}$ operating at $V = 40 \text{ V}$. Darabi et al. reported a polarization-based EHD micropump intended for microelectronics cooling applications. This micropump operates at relatively low voltages (150 V) and with a nondielectric working fluid (R-134a, chosen for its thermal properties). The

working fluid was reported to be pumped through a 250 Pa pressure difference; further details of pump performance were not reported. [246].

Applying a weak electric field (much less than 100 kV cm^{-1}) between electrodes immersed in a dielectric fluid causes dissociation of ionizable groups at the electrode/fluid interface. Coulomb forces acting on these ions result in the transport of small amount of charge through the bulk liquid. *Conduction* EHD pumps rely on ion drag associated with this bipolar conduction [247, 248]. Micropumps based on conduction EHD pumping have not yet been reported, although Jeong and Seyed-Yagoobi reported conduction EHD pumps with high voltage-ground electrode modules 2.2 cm in diameter by 4 cm long [247].

EHD micropumps based on the injection of ions from electrodes into the working fluid have also been reported. Whereas electrode charge transfer usually occurs through oxidation/reduction reactions, ion injection can occur at certain electrode/liquid interfaces (typically a metal electrode with sharp features in contact with a dielectric liquid) at very high electric fields ($> 100 \text{ kV cm}^{-1}$). The Coulomb force acts on the injected charges; differential ion drag can thereby generate bulk flow. Richter et al. reported a charge injection EHD micropump with mesh electrodes fabricated by wet etching and metallizing single-crystal silicon [249]. The electrode grid openings are on the order of $100 \mu\text{m}$; the electrode separation distance is approximately $350 \mu\text{m}$. Reported performance with ethyl alcohol as the working fluid and a potential difference of $V = 600 \text{ V}$ is $Q_{\text{max}} = 14 \text{ mL min}^{-1}$ and $\Delta p_{\text{max}} = 2.5 \text{ kPa}$. An injection EHD micropump with a similar electrode design was reported by Wong [250]. This micropump produces $\Delta p_{\text{max}} = 290 \text{ Pa}$ operating at $V = 120 \text{ V}$ with isopropyl alcohol as the working fluid. Ahn

and Kim reported an injection EHD micropump with 30 pairs of electrodes arrayed in the direction of flow [243]. This micropump produces $Q_{\max} = 40 \mu\text{L min}^{-1}$ and $\Delta p_{\max} = 300 \text{ Pa}$ operating at $V = 100 \text{ V}$ with ethyl alcohol as the working fluid. Darabi et al. reported a paired-electrode-array injection EHD micropump with saw-tooth electrode geometries to reduce power consumption [251]. The gap between the two electrodes in each pair is $50 \mu\text{m}$; the pairs are spaced at $100 \mu\text{m}$ intervals. For this micropump, $S_p = 640 \text{ mm}^2$. With 3M HFE-7100 ($\epsilon_r = 7.4$) as the working fluid, this micropump produced $\Delta p_{\max} = 2.5 \text{ kPa}$; flow rate data was not reported. Other papers discuss EHD pumping [252, 253].

Electroosmotic micropumps

Silicon electroosmotic micropumps are discussed in detail in the ensuing chapters. A number of non-silicon electroosmotic micropumps have been reported. The most basic EO pumps are single capillaries or microchannel sections with electrodes submerged within end-channel reservoirs and a flow resistance in series with the channel [62, 254, 255]. The flow rates produced by such pumps are typically very small ($Q_{\max} < 1 \mu\text{L min}^{-1}$). For example, Ramsey and Ramsey applied a 350 V cm^{-1} electric field to a portion of a microchannel network etched on a glass slide to produce a flow rate of 90 nL min^{-1} [62].

To increase flow rate, most electroosmotic micropumps incorporate some sort of porous structure rather than a simple channel. The pores act as a bundle of n capillaries for generating EO flow [61, 256, 257]. An EO micropump incorporating a $75 \mu\text{m}$ ID fused silica capillary packed with silica beads was reported by Paul et al. [60, 258]. This pump produces only $Q_{\max} = 200 \text{ nL min}^{-1}$, but exceptionally high pressures—reportedly up to 20 MPa —at an applied voltage of $V = 6.75 \text{ kV}$.

A few special metrics are sometimes useful in comparing electroosmotic micropumps. Dividing Q_{\max} by the product of applied voltage and flow cross-sectional area yields a normalized maximum flow rate $Q_{\max,V,A}$ ($\mu\text{L min}^{-1} \text{V}^{-1} \text{cm}^{-2}$). Dividing Δp_{\max} by the applied voltage yields a normalized maximum back pressure, $\Delta p_{\max,V}$ (kPa V^{-1}). Gan et al. reported $\Delta p_{\max,V} = 0.3 \text{ kPa V}^{-1}$ and $Q_{\max,V,A} = 0.6 \mu\text{L min}^{-1} \text{V}^{-1} \text{cm}^{-2}$ with a 3.5 cm inner diameter (ID) pump using a bed of sintered glass beads as the EO porous structure [259]. Zeng et al. used large-diameter (500-700 μm) capillaries packed with silica particles to produce $\Delta p_{\max,V} = 1 \text{ kPa V}^{-1}$ and $Q_{\max,V,A} = 1 \mu\text{L min}^{-1} \text{V}^{-1} \text{cm}^{-2}$ [256]. Maximum thermodynamic efficiency is $\eta = 1.3\%$. An EO micropump in which the EO porous structure is a bed of silica particles held in place by a 1 cm diameter porous polymer frit produces $\Delta p_{\max,V} = 0.2 \text{ kPa V}^{-1}$ and $Q_{\max,V,A} = 1 \mu\text{l min}^{-1} \text{V}^{-1} \text{cm}^{-2}$ [260]. Yao et al. reported an EO pump in which the porous structure is a 4 cm diameter (1 mm thick) sintered glass frit [61]. Operating at $V = 100 \text{ V}$, this pump produces $\Delta p_{\max,V} = 1.3 \text{ kPa V}^{-1}$ and $Q_{\max,V,A} = 26 \mu\text{L min}^{-1} \text{V}^{-1} \text{cm}^{-2}$. The absolute Δp_{\max} and Q_{\max} for the latter pump are 130 kPa and 33 mL min^{-1} ; maximum thermodynamic efficiency is $\eta = 0.3\%$.

Chen and Santiago used glass micromachining to fabricate an EO micropump in which electroosmotic flow is generated in a channel 4 cm wide and 1 micron deep and 1 mm long in the flow direction [63, 261]. The channel is subdivided across its width by narrow structural ribs. Operating at $V = 1 \text{ kV}$, this micropump produces $\Delta p_{\max,V} = 0.03 \text{ kPa V}^{-1}$ and $Q_{\max,V,A} = 42 \mu\text{L min}^{-1} \text{V}^{-1} \text{cm}^{-2}$ (corresponding to absolute Δp_{\max} and Q_{\max} of 33 kPa and 15 $\mu\text{L min}^{-1}$). The maximum thermodynamic efficiency is

$\eta = 0.49\%$. Other implementations of EO pumping at the microscale have been reported [262-270].

Magnetohydrodynamic micropumps

Several micropumps have been reported in which current-carrying ions in aqueous solutions are subjected to a magnetic field. The magnetic field imparts a Lorentz force on the liquid, thereby inducing flow. A typical magnetohydrodynamic pump is shown in figure 2.10. In a rectangular channel with transverse current density j_y and perpendicular transverse magnetic flux density B_x , the maximum pressure is

$$P_{\max,MHD,th} = j_y B_x l \quad (2.8)$$

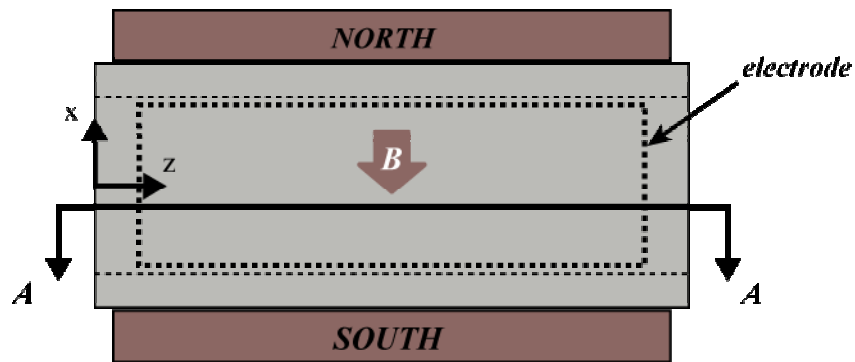
and the maximum flow rate is on the order of

$$Q_{\max,MHD,th} = j_y B_x \frac{\pi D_h^4}{128\mu} \quad (2.9)$$

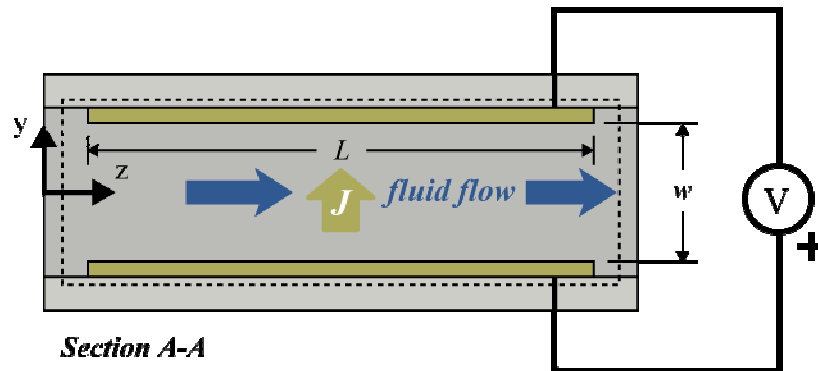
where l and D_h are the length and hydraulic diameter (cross-sectional area multiplied by four and divided by the perimeter) of the pumping channel. The performance of magnetohydrodynamic pumps is typically limited by the magnetic flux density (up to approximately 1 Tesla for miniature permanent magnets or 0.1 Tesla for miniature electromagnetic coils); the scaling of flow rate with the fourth power of hydraulic diameter makes miniaturization challenging. Thermal effects can also limit current density.

Jang and Lee reported a magnetohydrodynamic micropump with a 40 mm long pumping channel hydraulic with hydraulic diameter on the order of 1 mm [271]. With permanent magnets producing a magnetic flux density of 0.44 T and total current between 1 and 100 μA , this pump produces $Q_{\max} = 63 \mu\text{L min}^{-1}$ and $\Delta p_{\max} = 170 \text{ Pa}$. To avoid electrolysis associated with DC operation, Lemoff and Lee used a miniature

electromagnetic coil operating (along with the electric field) at 1 kHz [272]. This micropump pumps a 1 M NaCl solution with $Q_{\max} = 18 \mu\text{L min}^{-1}$. Several papers have discussed microscale applications of magnetohydrodynamic effects [273-277].



(a)



(b)

Figure 2.10: Top view (a) and section view (b) schematics of a simple magnetohydrodynamic micropump. A transverse magnetic field exerts a Lorentz force on current-carrying ions flowing across the channel, producing net flow in the axial direction. After Jang and Lee [271]

Other dynamic micropumps

Net fluid flow can be induced by flexural waves propagating through a membrane with which the fluid is in contact. A micropump based on ultrasonic flexural plate waves

was reported by Luginbuhl et al. [278]. Piezoelectric actuators in this pump operate at 2-3 MHz and actuate regions of a 2 x 8 mm membrane. A flow rate of $Q_{\max} = 255 \text{ nL min}^{-1}$ was reported. Black and White reported an ultrasonic flexural wave pump with a 2 x 8 mm membrane that produces $Q_{\max} = 1.5 \text{ }\mu\text{L min}^{-1}$ [279]. Ultrasonic flexural wave pump design and optimization is further discussed in recent papers [280, 281]. Dynamic micropumps based on thermal transpiration have been reported [282, 283].

CHAPTER 3: ESTABLISHED MODELS OF ELECTRIFIED INTERFACES AND ELECTROSMOTIC FLOW

As with all electrokinetic phenomena, the existence of an equilibrium ionic concentration gradient at a solid-liquid interface is a prerequisite for electroosmotic flow. A well-established model of equilibrium interface electrification, the Gouy-Chapman-Grahame-Stern (GCGS) model, is presented in this chapter. Based on the GCGS equations describing concentration and potential gradients in a fluid phase near a planar surface and following the work of Burgreen and Nakache [284], a model is developed of electroosmotic flow in an idealized conduit geometry of particular relevance to silicon electroosmotic micropumps: the slit capillary. The treatment of interface electrification and electroosmotic flow is applicable to solid phases and aqueous solutions with a wide range of properties. The last section in this chapter covers phenomena of particular relevance to silicon electroosmotic micropumps: nonequilibrium charge at semiconductor-electrolyte interfaces. Several excellent texts provide more exhaustive discussion of the material in this chapter, including Probstein [59], Hunter [285], Bockris et al. [52], and Adamson and Gast [286] for equilibrium interface electrification and electroosmotic flow and Morrison [287] for semiconductor-electrolyte interfaces.

3.1. The Gouy-Chapman-Grahame-Stern electrified interface model

Concentration gradients of liquid-phase ions near a solid surface, such as the interior of a capillary or the interior of the pores in a bed of clay, tend to arise due to exergonic reactions occurring when two phases first come into contact. The layers of opposite-polarity charge in the two components of an interface are collectively referred to as the electric double layer, or EDL. The distribution of charge within the fluid phase of

the electric double layer determines the direction and magnitude of the electroosmotic flow which results from applying an electric field.

In this section, solid-liquid interface electrification is considered in the context of a particular solid phase of interest, silicon oxide. Silicon oxides, both bulk and thin-film, feature prominently in electrokinetics. The interface between a slightly basic aqueous electrolyte and bulk silicon oxide has been extensively studied and is a suitable vehicle for developing a widely used model of the electric double layer, the Gouy-Chapman-Grahame-Stern (GSGS) model. This model—particularly when combined with the Debye-Hückel approximation—provides a highly tractable and reasonably accurate basis for analyzing many electroosmotic flows.

Qualitative description of the silicon oxide-electrolyte interface

Silicon oxide surfaces in contact with an aqueous electrolyte are generally terminated by oxygen and hydrogen. Hydroxyls and protons in solution bind to exposed silicon and oxygen atoms, respectively. For an aqueous electrolyte with pH of approximately 3 or higher, hydroxyl group adsorption onto the oxide surface is thermodynamically favored over proton adsorption, such that the net surface charge is negative. The hydroxyl group surface density is between 1.4 and 4.6 per nm², depending on the extent to which hydroxyl groups are arranged in pairs (as opposed to isolated) [288]. The paired hydroxyl group structure is illustrated in figure 3.1. Near-interface charge build-up likewise occurs in other types of solid phases, although it might take different forms; in a semiconductor, for example, electrons might accumulate in or be depleted from a nanometer-scale region near the interface.

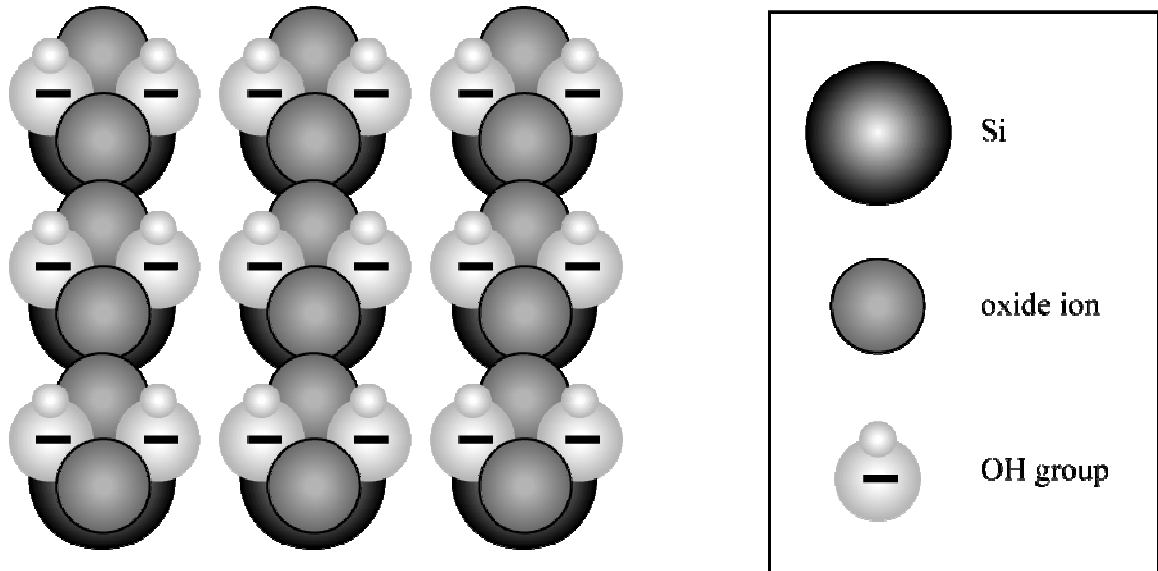


Figure 3.1: Perspective schematic illustration of an oxide surface with paired hydroxyl groups. After Furlong et al. [288].

Charge buildup in the solid phase is accompanied by nonuniform charge distributions in the liquid phase. Electrostatic forces exerted on liquid-phase ions by surface charges are balanced at equilibrium by diffusion. In the case of silicon oxide in a pH-basic solution, cations are present at a higher concentration near the surface than in the bulk liquid and anions at a lower concentration. A layer of ions adjacent to the wall, the Stern layer, is considered to be immobile. Ions in the diffuse Gouy-Chapman layer just beyond the Stern layer, in contrast, tend to drift in the presence of an externally imposed electric field. This is the Gouy-Chapman-Grahame-Stern model of the electric double layer, illustrated in figure 3.2. The electrical potential in the liquid phase can increase or decrease across the Stern layer, depending on specific adsorption, and decays from its value at the outer Helmholtz plane (negative, for a pH neutral-to-basic solution) toward a nominal value (usually taken to be zero) in the bulk [288].

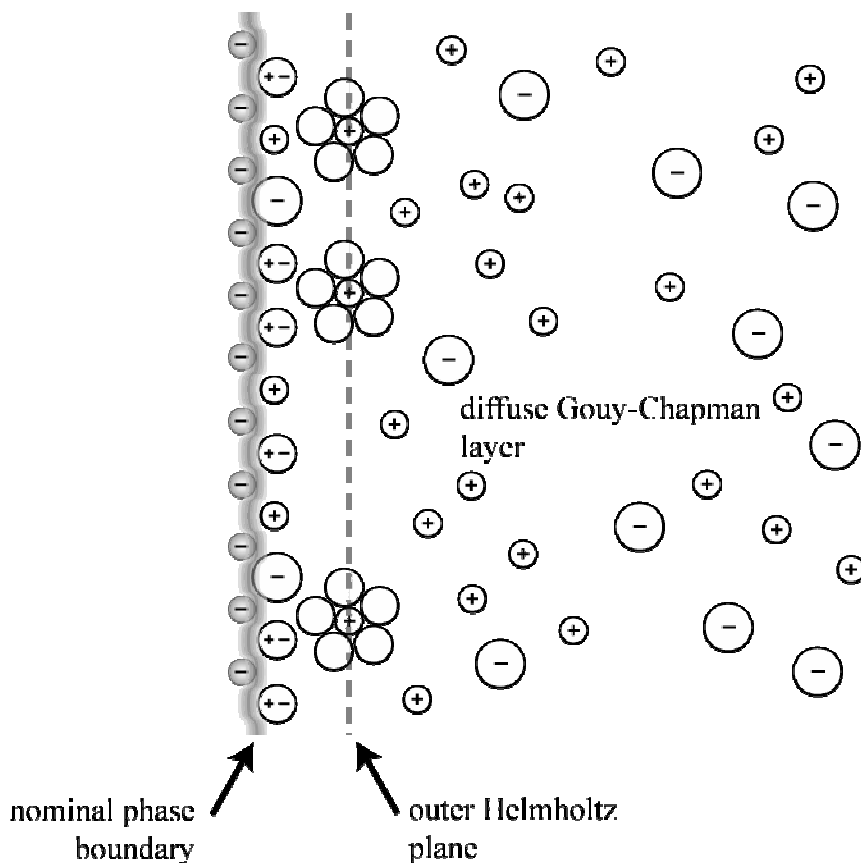


Figure 3.2: Schematic of the Gouy-Chapman-Grahame-Stern model of the electric double layer (EDL) at the interface between a silicon oxide surface and a pH-neutral or basic aqueous electrolyte. Interface equilibrium is characterized by charge buildup at the oxide surface and adsorption of ions and water molecules. The outer Helmholtz plane is defined by the point of closest approach to the interface of hydrated ions. Beyond the outer Helmholtz plane is the diffuse Gouy-Chapman layer, where counterions are found at greater concentration than in the bulk and co-ions at lesser concentration.

Modeling ionic concentration and electrical potential in the liquid phase of the EDL

While experimental techniques for determining the precise distribution of ions in the liquid phase of the EDL have not yet been developed, numerous models have been developed to explain experimental data associated with the EDL. The Gouy-Chapman-Grahame-Stern (GCGS) EDL model described qualitatively above is the most prominent of these models. Under this model, the potential energy associated with each double layer ion is assumed to be small compared with its kinetic energy. Overbeek [289]

analyzed charge distribution in the liquid phase of the EDL under the GCGS model. The starting point for this analysis is the Nernst-Planck equation for the molar flux \vec{j}_i^* of a dilute solution of species i [59]:

$$\vec{j}_i^* = -v_i z_i F c_i \nabla \varphi - D_i \nabla c_i + c_i \bar{v} \quad (3.1)$$

Here c_i , v_i , z_i , and D_i are the concentration (molar density), mobility, valence number, and diffusion constant, respectively, of the ionic species i in solution; φ is the spatially-varying electrical potential; and \bar{v} is the mass average velocity. At equilibrium, there is no net mass flux and the ensemble-averaged ion velocity is zero. Accordingly, the Nernst-Planck equation reduces to a balance between electromigration and diffusion:

$$v_i z_i F c_i \nabla \varphi_{DL} = D_i \nabla c_i \quad (3.2).$$

Under the GCGS model, the only electrical potential considered is that associated with interface charges, termed φ_{DL} . Considering a flat surface with in-plane dimensions sufficiently large that $\varphi_{DL} = \varphi_{DL}(y)$ and $\rho = \rho(y)$ (coordinate axes as shown in figure 3.3), eqn 3.2 reduces to

$$v_i z_i F c_i \frac{d\varphi_{DL}}{dy} = D_i \frac{d\rho_i}{dy} \quad (3.3)$$

The Nernst-Einstein model (treating ions as solid spheres) relates D_i and v_i in terms of the solution temperature T , the Boltzmann constant k , and the electron charge e :

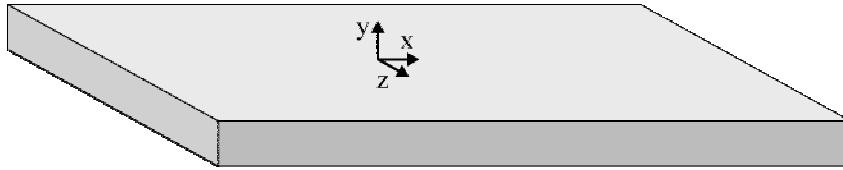


Figure 3.3: Flat-plate geometry showing coordinate axes used in EDL model.

$$D_i = \frac{kTF}{e} v_i.$$

Accordingly, eqn 3.3 becomes

$$\frac{z_i e}{kT} \frac{d\varphi_{DL}}{dy} = \frac{1}{c_i} \frac{dc_i}{dy} \quad (3.4)$$

The dy terms in eqn 3.4 cancel, allowing the two sides to be integrated separately. This leads to a straightforward exponential relationship between the density and the potential:

$$c_i(y) = A \exp\left(-\frac{z_i e}{kT} \varphi_{DL}(y)\right)$$

With the boundary conditions

$$c_i(\infty) = c_{i,\infty} \quad \varphi_{DL}(\infty) = 0$$

(i.e. assuming that the electrical potential in the bulk solution to be neutral and for bulk concentration $c_{i,\infty}$), A is found to be equal to $c_{i,\infty}$, yielding the Boltzmann distribution of ions as a function of electrical potential:

$$c_i(y) = c_{i,\infty} \exp\left(-\frac{z_i e}{kT} \varphi_{DL}(y)\right) \quad (3.5)$$

Equivalently, the Boltzmann distribution in terms of number density n_i is

$$n_i(y) = n_{i,\infty} \exp\left(-\frac{z_i e}{kT} \varphi_{DL}(y)\right) \quad (3.6)$$

In eqn 3.5, both the concentration c_i and the electrical potential φ_{DL} are variables. The starting point for obtaining a second equation relating these two variables is the Poisson equation:

$$\nabla^2 \varphi = -\frac{1}{\varepsilon} \rho_E \quad (3.7)$$

where ρ_E and ε are the charge density and electrical permittivity, respectively, of the solution. For the infinite flat plate in fig 3.7, eqn 3.14 reduces to a one-dimensional form:

$$\frac{d^2 \varphi_{DL}(y)}{dy^2} = -\frac{1}{\varepsilon} \rho_E(y) \quad (3.8)$$

For an electrolyte containing N species, the charge density at any point is the sum of the molar densities of the constituent species at that point multiplied by each species' valence number and the Faraday constant:

$$\rho_E(y) = F \sum_{i=1}^N z_i c_i \quad (3.9)$$

Combining eqns 3.8, 3.9, and 3.3 yields the Poisson-Boltzmann equation for the variation in the double layer potential φ_{DL} as function of y :

$$\frac{d^2 \varphi_{DL}}{dy^2} = -\frac{F}{\varepsilon} \sum_{i=1}^N z_i c_{i,\infty} \exp\left(-\frac{z_i e}{kT} \varphi_{DL}\right) \quad (3.10)$$

Eqn 3.10 is difficult to solve for many geometries. For an flat plate, however, Hunter showed that it can be manipulated to yield [290]

$$\tanh\left(\frac{ze\varphi_{DL}}{4kT}\right) = \tanh\left(\frac{ze\zeta}{4kT}\right) \exp[-\kappa y], \quad (3.11)$$

having applied boundary conditions for an electrically neutral bulk electrolyte:

$$\left. \frac{d\varphi_{DL}}{dy} \right|_{y \rightarrow \infty} = 0 \quad \varphi_{DL} \Big|_{y \rightarrow \infty} = 0.$$

An additional boundary condition used to obtain eqn 3.11 is the value of the electrical potential at the wall. The relevant potential is that at the outer Helmholtz plane (see figure 3.2); since ions in the Stern layer are immobile, they can be considered to be part of the solid surface for the purposes of modeling the EDL. The electrical potential at the wall is referred to as the zeta potential, ζ :

$$\varphi_{DL}|_{y=0} = \zeta .$$

The zeta potential is an important parameter in the study of EOF. The electrical potential may rise, fall, or be constant in the region between the outer Helmholtz plane and the solid; such potential gradients affect the transverse charge distribution in the diffuse layer, but with the ions in this Stern layer immobile, there is essentially no further influence on flow tangential to the surface. Zeta potential is discussed further in section 3.2 below.

In eqn 3.11, the term κ is the Debye-Hückel parameter:

$$\kappa = \left[\frac{Fe \sum_{i=1}^N z_i c_{\infty,i}}{\varepsilon kT} \right]^{\frac{1}{2}} . \quad (3.12)$$

Many other solutions for and simplifications of the EDL relations (including the Debye-Hückel approximation detailed below) involve κ .

Figures 3.4 and 3.5 illustrate the potential and concentration gradients, calculated using eqn 3.11, associated with EDL chemistries similar to those typically found in electroosmotic micropumps. A univalent, room-temperature electrolyte with permittivity $\varepsilon_R = 78.3$ is assumed in all cases. In figure 3.4, the bulk concentration $c_{i,\infty}$ is taken to be 0.2 mM. Figure 3.4(a) illustrates the dependence of double layer electrical potential on y for $\zeta = -10$ mV and $\zeta = -50$ mV. In figure 3.4(b), the counter-ion (cation) and co-ion (anion) concentrations are plotted vs. y for the same two assumed values of ζ .

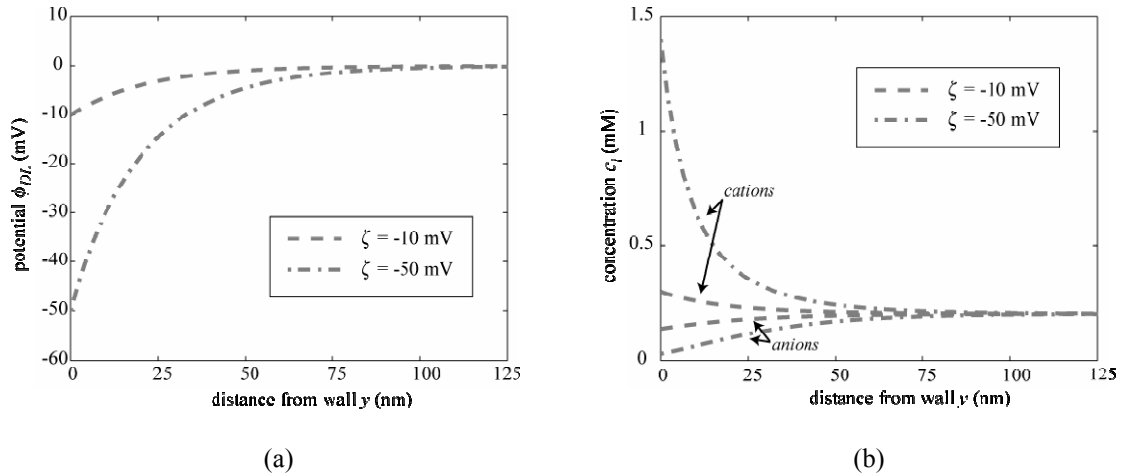


Figure 3.4: Electrical potential and ionic concentration in the Gouy-Chapman layer for common chemistries and ζ values of -10 mV and -50 mV. (a) The electrical potential ϕ_{DL} decays with increasing y to zero in the bulk. (b) Counterion and co-ion concentrations approach their bulk values over the same lengthscale. Values calculated using the Hunter solution (eqn. 3.11) to the Poisson-Boltzmann equation assuming a room-temperature univalent, symmetrical electrolyte with $c_{i,\infty} = 0.2$ mM.

Figure 3.5 shows the influence of bulk concentration $c_{i,\infty}$ on double layer thickness. The zeta potential ζ is assumed to be -50 mV. The concentrations of anions and cations at the shear plane are each a constant multiple of the bulk concentration. In the diffuse layer, however, the ionic concentrations approach $c_{i,\infty}$ more rapidly at higher $c_{i,\infty}$ (fig 3.5(b)). Electrical potential likewise decays to zero more rapidly at higher $c_{i,\infty}$ (fig 3.5(a)).

The Poisson-Boltzmann description of the EDL is considered to be imperfect [290]. Errors associated with the Poisson-Boltzmann description of the EDL have been estimated by Levine and Bell to be minimal for electrolyte concentrations up to 0.1 M and potentials up to 75 mV for 1:1 electrolytes [291]. Blum discusses several alternative electric double layer models [292].

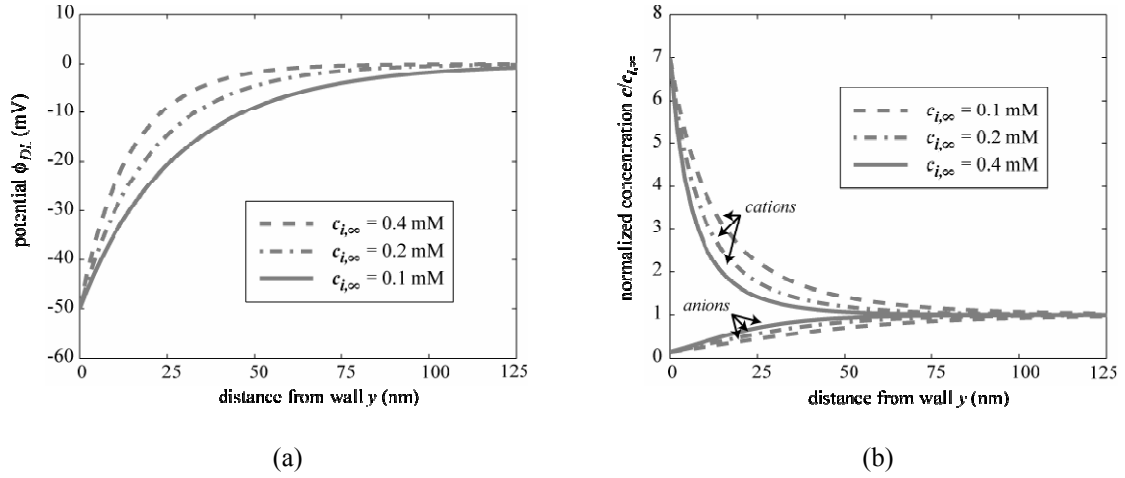


Figure 3.5: Electrical potential and ionic concentration in the Gouy-Chapman layer for a range of bulk concentrations ($c_{i,\infty} = 0.1, 0.2, 0.4$ mM) – (a) potential ϕ_{DL} ; (b) counterion and co-ion concentration, normalized by dividing by the bulk concentration $c_{i,\infty}$. Values calculated from the Hunter solution (eqn. 3.11) to the Poisson-Boltzmann equation assuming a room-temperature univalent, symmetrical electrolyte and $\zeta = -50$ mV.

The Debye-Hückel approximation

For small values of the exponential term, eqn 3.10 can be simplified by invoking the Debye-Hückel approximation:

$$\exp(-x) \cong 1 - x \quad (x \ll 1) \quad (3.13).$$

With this approximation, eqn 3.10 reduces to

$$\frac{d^2 \phi_{DL}}{dy^2} = \kappa^2 \phi_{DL} \quad (3.14).$$

This is simply the homogeneous form of the undamped harmonic oscillator equation with the Debye-Hückel parameter (seen above in eqn 3.11) emerging as the positive eigenvalue. Applying the same boundary conditions as were used to derive eqn 3.11, the electrical potential ϕ_{DL} is found to decay exponentially as function of y , with the rate of decay described by κ :

$$\phi_{DL} = \zeta \exp(-\kappa y) \quad (3.15).$$

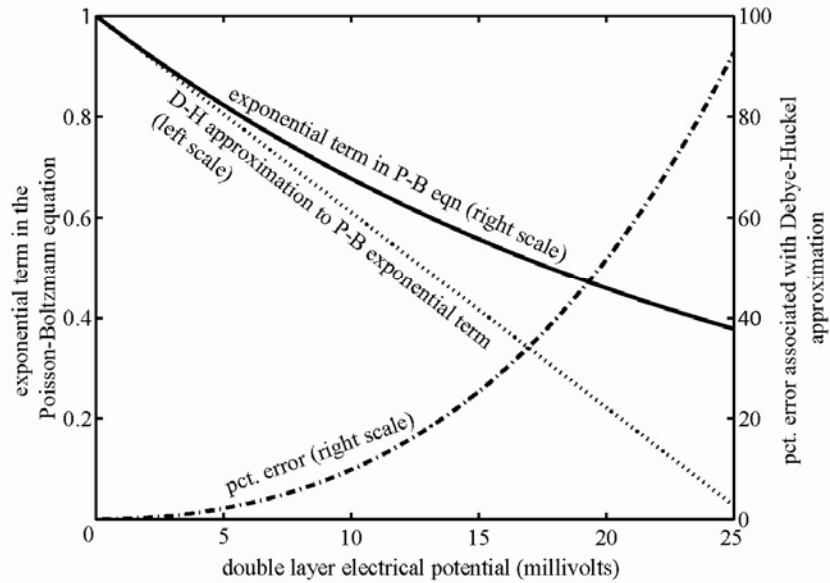


Figure 3.6: Debye-Hückel approximation for the exponential term in the Poisson-Boltzmann equation. The error in this term grows rapidly as the zeta potential increases past a few millivolts.

The inverse of κ is the distance from the wall at which the electrical potential has decayed to $1/e$ of its value at the wall; this distance is known as the Debye shielding length λ_D .

The argument of the exponential term in eqn 3.10 equals 1 at $\varphi_{DL} = 8.6 \times 10^{-5} T$, i.e. $\varphi_{DL} = 25.7$ mV at room temperature. Therefore, as shown in figure 3.6, the Debye-Hückel approximation significantly underestimates the value of the exponential term in eqn 3.10 for potentials greater than a few millivolts and is unphysical for $\varphi_{DL} \geq 8.6 \times 10^{-5} T$.

Notwithstanding the potentially substantial error introduced by applying eqn 3.13, the Debye-Hückel solution of the Poisson-Boltzmann equation yields accurate results for many chemistries of interest. This is due, in large part, to equivalency of eqns 3.11 and 3.15 in the limit of $\varphi_{DL} \rightarrow \zeta$. As shown in figure 3.7, the maximum error at any point in the diffuse layer in the ionic concentrations calculated using eqn 3.15 is only a few percent even for $\zeta = -50$ mV.

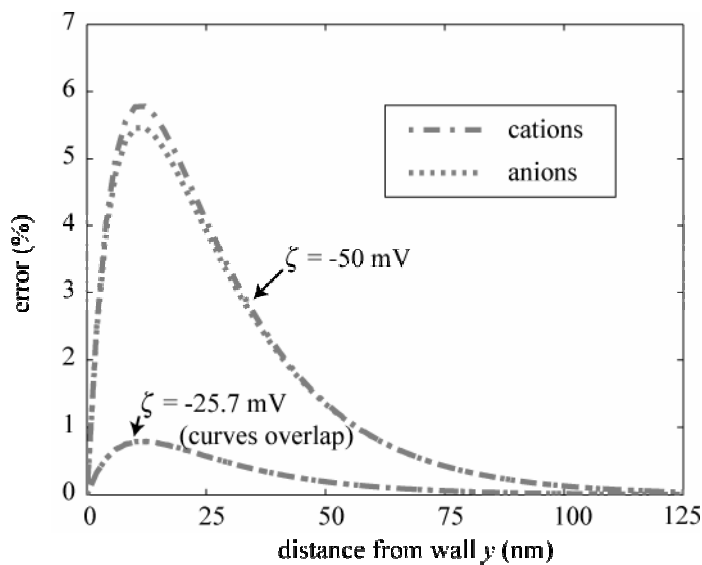


Figure 3.7: Error in concentration values determined by using the Debye-Hückel approximation for the exponential term in the Poisson-Boltzmann equation. Values calculated for a symmetrical, univalent electrolyte at room temperature, where the argument of the exponential term equals 1 at $\varphi_{DL} = 25.7$ mV.

3.2. Electroosmotic flow in slit capillaries

Models of EOF must take into account coupled electrochemical and fluidic phenomena. In this section, the GCGS model of ion concentration and electrical potential in the liquid phase of the electric double layer is used to derive a set of equations describing electroosmotic flow in a specific geometry of interest, the slit capillary. The concept of zeta potential, the electrical potential at the surface of shear in an electrokinetic system, is a key component of this model.

Modeling electroosmotic flow

Applying a field to a liquid phase causes ions in the liquid to be accelerated until an equilibrium velocity is reached where the force exerted by the electric field is balanced by molecular forces. Although this ionic current is associated with energy transfer into

the bulk, the transferred energy may be manifested only as joule heating—not necessarily as net fluid flow. As discussed in chapter 2, among the circumstances under which an electric field can cause net flow (referred to as electrohydrodynamic flow) is when ionic concentration gradients are present. As shown in the preceding section, pronounced concentration gradients are found in the liquid phase of the electric double layer. Counterions concentrated in the liquid phase of the EDL drift when an electric field is applied parallel to a surface; their momentum tends to propagate into the bulk. For conduits with large cross-sections, the effect of the drifting EDL counterions can be dwarfed by other phenomena, such as the presence of externally imposed pressure gradients. If at least one cross-sectional dimension is within a few orders of magnitude of the EDL thickness, however, EDL counterion drift can be an important or even dominant effect. Bulk flow resulting from the interaction of an applied electric field and mobile

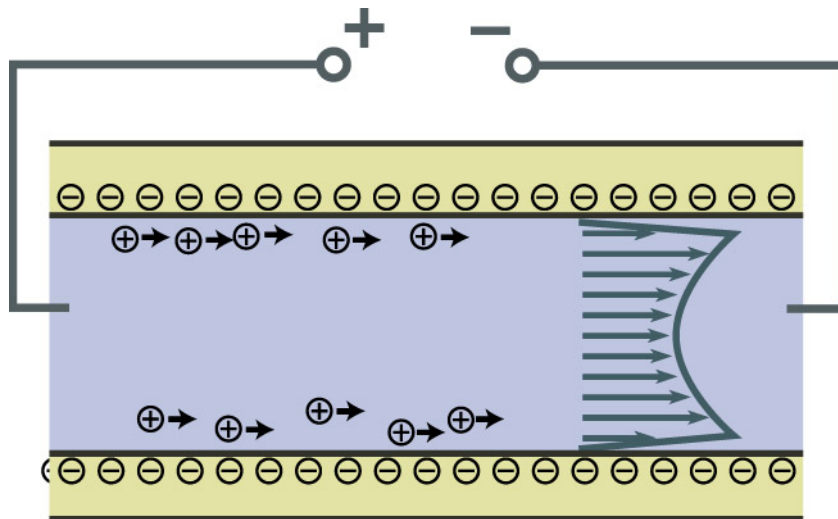


Figure 3.8: Schematic of electroosmotic flow in a capillary. An externally-applied electric field exerts force on ions near the charged wall. Ion drag forces the fluid to flow against a pressure gradient.

ions in the liquid phase of the electroosmotic double layer, as illustrated schematically in figure 3.8, is referred to as electroosmotic flow, or EOF.

Models have been developed of electroosmotic flow in conduits with various geometries. Perhaps the foremost geometry is the cylindrical capillary, for which a Rice and Whitehead published a groundbreaking solution in 1965 [293]. Another important geometry for EOF is the slit capillary, an orthogonal capillary with one cross-sectional dimension much larger than the other. EOF in slit capillaries was first analyzed in detail by Burgreen and Nakache in 1964 [284]. Because slit capillary-like structures can be formed in single-crystal silicon substrates with relative ease using micromachining technologies (as will be seen in chapter 4), the slit capillary is a particularly relevant geometry for silicon electroosmotic micropumps.

Figure 3.9 shows the coordinate axes and relevant dimensions used in the analysis of EOF in slit capillaries. The convention used here is to refer to the smaller of the two cross-sectional dimensions as the slit width; the distance from either wall to the center of the channel is then the slit half-width a_l . The larger of the two slit capillary cross-sectional dimensions is referred to as the slit depth b_l . It should be noted that some authors use different naming conventions when describing slit capillary dimensions; a_l , for example (a very important dimension for the analysis of electrokinetic phenomena in slit capillary-like geometries) is referred to by some authors as the slit half-height. The manner in which the terms *width* and *depth* are used in this text is consistent with standard terminology for microchannels, taking into account the orientation relative to the substrate surface of the slit capillaries in most silicon electroosmotic micropumps.

For modeling EOF, the slit capillary is assumed to be completely filled with a liquid phase. Also assumed is the existence of an axial electric field and an end-to-end pressure difference as shown in figure 3.9(b). Although the axial electric field E_x is assumed to be temporally uniform, extending the analysis below to encompass temporal

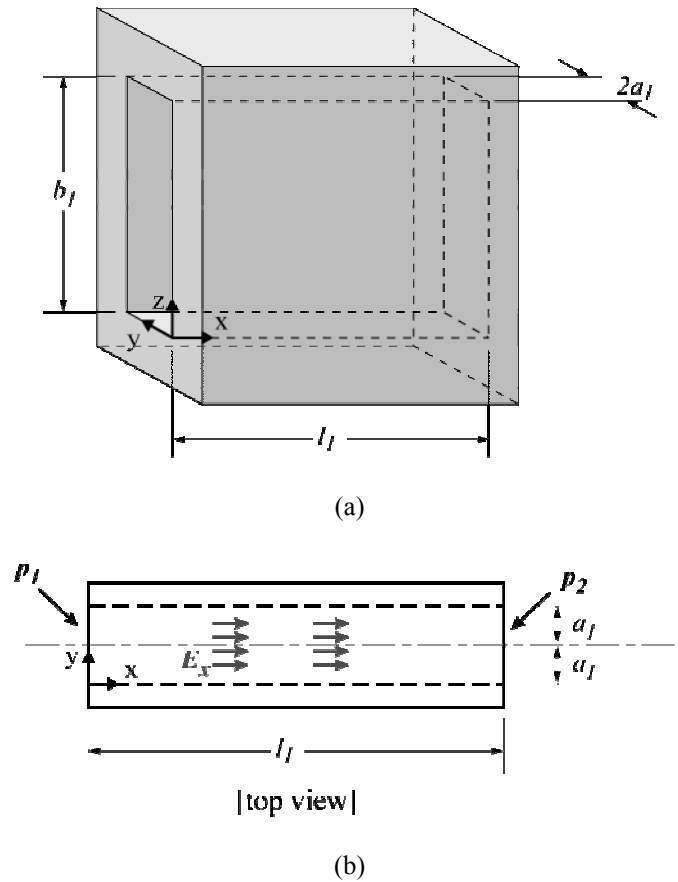


Figure 3.9: A rectangular cross-section fluid conduit in which one cross-sectional dimension is much larger than the other is referred to as a slit capillary. (a) Notation and coordinate axes used in slit capillary EOF analysis. The dimension a_I is one-half of the smaller of the two cross-sectional dimensions; it is referred to as the slit half-width. (b) Top view, showing the spatially constant one-dimensional electric field E_x and the pressures at left and right ends of slit, p_1 and p_2 .

variation in E_x is straightforward, as shown in chapter 5 for a step change in E_x . The fluid pressure is taken to be uniformly p_1 at the left end of the capillary and uniformly p_2 at the right end.

The Burgreen-Nakache model

The starting point for analyzing EOF in a slit capillary (or in any other geometry) is the continuity equation

$$\frac{1}{\rho} \frac{D\rho}{Dt} + \nabla \cdot \bar{u} = 0 \quad (3.16)$$

where the operator D/Dt (the material derivative) is defined as

$$\frac{D}{Dt} = \frac{\partial}{\partial t} + \bar{u} \cdot \nabla$$

Assuming $\rho^{-1} D\rho/Dt$ to be small [93], the continuity equation reduces to

$$\nabla \cdot \bar{u} = 0$$

The momentum equation for an incompressible Newtonian fluid, in index notation, is

$$\rho \frac{Du_i}{Dt} = b_i - \frac{\partial p}{\partial x_i} + \frac{\partial}{\partial x_j} \left\{ \mu \left(\frac{\partial u_i}{\partial x_j} + \frac{\partial u_j}{\partial x_i} \right) \right\}. \quad (3.17)$$

This is based on the expression for stress in a Newtonian fluid as

$$\sigma_{ij} = -p\delta_{ij} + \mu \left[\frac{\partial u_i}{\partial x_j} + \frac{\partial u_j}{\partial x_i} \right].$$

In eqn 3.17, body forces per unit volume are collected in the term \bar{b} . Next, viscosity μ is assumed to be uniform. Fluid temperature variations due to Joule heating require validation of this assumption on a case-by-case basis. The x component of eqn 3.17 becomes:

$$\rho \left(\frac{\partial u_x}{\partial t} + u_x \frac{\partial u_x}{\partial x} + u_y \frac{\partial u_x}{\partial y} + u_z \frac{\partial u_x}{\partial z} \right) = b_x - \frac{\partial p}{\partial x} + \mu \left(2 \frac{\partial^2 u_x}{\partial x^2} + \frac{\partial^2 u_x}{\partial y^2} + \frac{\partial^2 u_y}{\partial x \partial y} + \frac{\partial^2 u_x}{\partial z^2} + \frac{\partial^2 u_z}{\partial x \partial z} \right).$$

Grouping terms yields

$$\rho \left(\frac{\partial u_x}{\partial t} + u_x \frac{\partial u_x}{\partial x} + u_y \frac{\partial u_x}{\partial y} + u_z \frac{\partial u_x}{\partial z} \right) = \rho b_x - \frac{\partial p}{\partial x} + \mu \left(\frac{\partial^2 u_x}{\partial x^2} + \frac{\partial^2 u_x}{\partial y^2} + \frac{\partial^2 u_x}{\partial z^2} \right) + \mu \frac{\partial}{\partial x} \left(\frac{\partial u_x}{\partial x} + \frac{\partial u_y}{\partial y} + \frac{\partial u_z}{\partial z} \right) \quad (3.18)$$

Continuity requires the last term on the right-hand side of eqn 3.18 and the comparable terms in the y and z components of the momentum equation to be zero.

Therefore, the momentum equation reduces to (in vector form)

$$\rho \frac{D\vec{u}}{Dt} = -\nabla p + \mu \nabla^2 \vec{u} + \vec{b}. \quad (3.19)$$

The inertial term is neglected based on an assumption of low Reynolds number, which is appropriate for a working fluid with properties similar to water at atmospheric pressure and temperature flowing through a slit capillary with $2a_l \leq 10 \mu\text{m}$ at an average velocity on the order of 1 cm sec^{-1} or below. Gravity is assumed to be negligible. The body force is the electrostatic Lorentz force, $F_i = qE_i$. Charge density is related to electrical potential by the Poisson equation (as in section 3.1):

$$\nabla^2 \phi = \frac{\rho_E}{\epsilon} \quad (3.20)$$

Accordingly, the momentum equation with a Poisson term is

$$\mu \nabla^2 \vec{u} = \nabla p - \epsilon \nabla^2 \phi \vec{E} \quad (3.21)$$

For unidirectional flow ($u_y = u_z = 0$), continuity requires $\partial u_x / \partial x$ to be zero. For $l_l \gg a_l$, entrance and exit effects can be ignored (i.e. the partial derivative of u_x with respect to y and the second derivative of ϕ with respect to x can be taken as zero). The same assumption dictates that the second derivative of ϕ with respect to x , the externally

imposed potential difference, with respect to y is zero (although $\partial^2\phi_{DL}/\partial y^2 \neq 0$). For $b_l \gg a_l$, velocity and electric field variations at the top and bottom of the slit capillary are minimal ($\partial u_x/\partial z = 0$, $\partial^2\phi/\partial z^2 = 0$). For steady (time-invariant) flow, the x component of eqn 3.21 then becomes:

$$\mu \frac{\partial^2 u_x}{\partial y^2} - \frac{\partial p}{\partial x} = \varepsilon \frac{\partial^2 \phi_{DL}}{\partial y^2} E_x. \quad (3.22)$$

The boundary conditions are no-slip at the surface of shear and symmetry at the slit channel centerline:

$$u_x|_{y=0} = 0 \quad \left. \frac{\partial u_x}{\partial y} \right|_{y=a_l} = 0.$$

Eqn 3.22 can be solved for the flow velocity $u_x(y)$ in terms of the double layer potential, the pressure gradient, the applied axial electric field, the slot geometry, and electrochemical and material parameters:

$$u_x(y) = \frac{1}{2\mu} (y^2 - 2a_l y) \frac{\partial p}{\partial x} + \frac{\varepsilon}{\mu} E_x \left(1 - \frac{\phi_{DL}}{\zeta} \right). \quad (3.23)$$

Eqn 3.23 describes the superposition two flow profiles—a parabolic flow profile associated with the axial pressure gradient and an electroosmotic flow profile in which the velocity increases across the double layer toward a constant value in the bulk—which was introduced qualitatively in figure 3.8. Integrating u_x over the slit capillary half-width and dividing by a_l yields the average velocity:

$$\bar{v} = -\frac{a_l^2}{3\mu l_1} \Delta p_1 + \frac{\varepsilon \zeta}{\mu} E_x [1 - G(\alpha, \kappa a_l)] \quad (3.24)$$

Here the properties of the fluid within the capillary and of the capillary surface are assumed to be invariant with x , such that the internal pressure gradient is constant and

$\partial p/\partial x$ has been replaced with $\Delta p/l_1$ (where Δp_1 is the entrance-to-exit pressure increase in the capillary) The analysis which follows is applicable even if the assumption of axial uniformity does not hold; a spatially variable pressure gradient can be accounted for in many cases simply by considering axial sections of the slit capillary individually and matching boundary conditions. The term G in eqn 3.31 ranges from 0 to 1 and takes into account the finite width of the electric double layer relative to a_1 :

$$G(\alpha, \kappa a_1) = \frac{\bar{\varphi}}{\zeta} \quad (3.25)$$

where $\bar{\varphi}$ is the mean potential over the slit capillary cross-section. The term α on which G depends is the ionic energy parameter, which reflects the magnitude of the potential relative to the thermal energy of the ions:

$$\alpha = \frac{ez\zeta}{kT}$$

For small potentials ($\alpha \ll 1$, i.e. in the regime where the Debye-Huckel electric double layer model is valid), G is

$$G = \frac{\tanh \kappa a_1}{\kappa a_1} \quad (3.26)$$

This expression for G monotonically decreases from one to zero moving from the thick double layer limit to the thin double layer limit (figure 3.10).

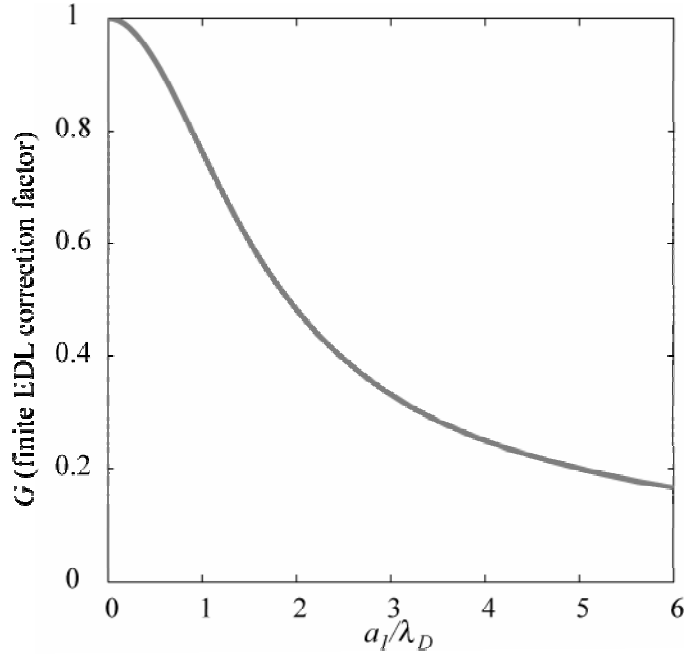


Figure 3.10: Variation of the finite EDL correction factor with double layer thickness relative to slit capillary half-width a_1 .

Eqn 3.24 encapsulates, in a highly tractable form, much of the physics underlying the operation of silicon electroosmotic micropumps. It conveys a negative linear relationship between pressure and average flow velocity

$$\bar{v} = \left(-\frac{\Delta p}{\Delta p_{\max}} + 1 \right) \bar{v}_{\max}$$

where the two constants in the linear relationship are the average velocity in the limit of zero back pressure (effectively a normalized flow rate)

$$\bar{v}_{\max} = \frac{\varepsilon \zeta}{\mu} E_x [1 - G(\alpha, \kappa a_1)]$$

and the back pressure in the limit of zero net flow

$$\Delta p_{\max} = \frac{3\varepsilon \zeta l_1}{a_1^2} E_x [1 - G(\alpha, \kappa a_1)].$$

Figure 3.11 illustrates the scaling with slit half-height a_1 of back pressure at zero net flow Δp_{\max} and normalized flow rate at zero back pressure \bar{v}_{\max} . The plotted values are for Debye lengths λ_D of 10 nm and 100 nm. In the thin EDL regime, Δp_{\max} scales favorably with decreasing a_1 , while \bar{v}_{\max} is independent of a_1 in this regime.

Zeta potential

From inspection of the slit capillary EOF relations, it is readily apparent that the zeta potential ζ at a solid-liquid interface critically impacts electroosmotic flow at that

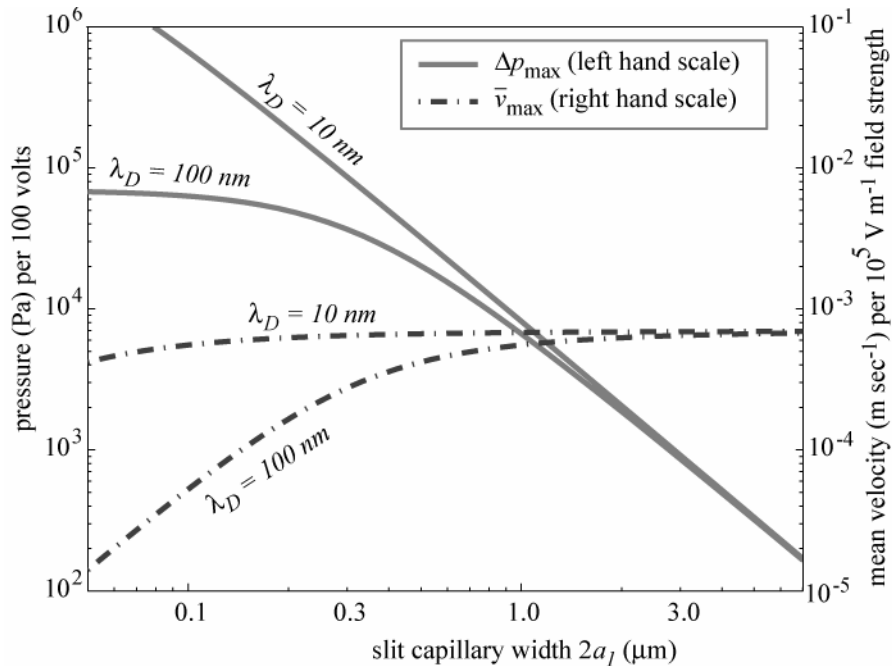


Figure 3.11: Scaling relations for electroosmotic flow in slit capillaries. Back pressure at zero net flow Δp_{\max} and mean flow velocity at negligible back pressure \bar{v}_{\max} are calculated for Debye lengths $\lambda_D = 10$ nm and 100 nm assuming working fluid properties similar to those of water and a modest value for zeta potential, $\zeta = -10$ mV. Δp_{\max} and \bar{v}_{\max} are linear functions of applied potential and applied field strength, respectively; the values shown are per 100 V and per 10^5 V m⁻¹, respectively. \bar{v}_{\max} is independent of a_1 for $a_1 \gg \lambda_D$ and decreases with decreasing a_1 in the finite EDL regime. Δp_{\max} is proportional to the inverse square of a_1 for $a_1 \gg \lambda_D$.

interface. Whereas little opportunity exists to tune EOF by manipulating material parameters such as permittivity and viscosity, zeta potential of common liquid-solid interfaces vary appreciably. Zeta potential is a strong function of pH, with negative zeta potentials increasing in magnitude as pH increases until some saturation pH value is reached [285]; zeta potential is also a weaker function of ion density. A simple relation for zeta potential, based on fitting the experimental data reported by Scales et al. [294] to the detailed model for silica surfaces presented by Yates et al. [295], is presented by Yao et al. [296]. Revil et al. [297] and others have noted that for silica surfaces, zeta potential appears to scale linearly with the logarithm of concentration, with an offset attributed to specific ionic adsorption onto the surface. In all cases, current increases monotonically with increasing ion density.

Several references provide further discussion of zeta potential and certain other aspects of electroosmotic flow. Santiago developed models of vorticity production and analyzed other inertial effects relevant to EOF in microchannels, including those with arbitrary geometry [298]. Burgreen and Nakache's slit capillary EOF model was extended and further analyzed by Hildreth [299]. Electroosmotic flow in specific geometries other than cylindrical capillaries and slit capillaries has been studied to a limited extent [300]. Finite EDL effects are discussed by Dutta and Beskok [301]. Electrokinetic phenomena of the second kind are discussed by Dukhin [302]. Ghosal recently reviewed certain important aspects of EO flow, particularly in the context of capillary electrophoresis [303]. Kirby and Hasselbrink recently reviewed published data on the zeta potential of silicon-based materials [304] and of polymers [305].

3.3. Models of equilibrium and nonequilibrium processes in silicon-electrolyte interfaces

The model of the oxide-electrolyte interface at equilibrium developed in section 3.1 provides a basis for analyzing many electrokinetic effects, including EOF in insulating capillaries. To model the operation of silicon electrokinetic devices, however, the possibility of *nonequilibrium* charge transfer at the silicon-electrolyte interface must also be taken into account, as silicon structures in electroosmotic pumps are a potentially significant electrical conduction path. This section covers the prevailing theories of semiconductor bulk charge transport and electrode behavior, considering first the relevant properties of silicon and a bare silicon-electrolyte interface and then the effect of placing an insulating layer between the silicon and the electrolyte. The physical models reviewed here apply to semiconductor-insulator-electrolyte systems generally, but the treatment focuses on single-crystal silicon substrates and the two most common insulating films used in silicon processing, silicon nitride and silicon oxide. Relevant properties of these three materials are listed in table 3.1.

Table 3.1: Material properties of silicon and silicon films

	Young's modulus (GPa)	Poisson ratio	density ($\times 10^3 \text{ kg m}^{-3}$)	stress state	relative permittivity	dielectric breakdown strength (V cm^{-1})
silicon (100)	190 [75]	0.25	2.3 [75]	none	11.8 [306]	n/a
silicon nitride	146 [76] 222 [307]	0.28 [307]	3.1 [308]	tensile, 200-2000 GPa [308]	6-7 [308]	10^7 [308]
silicon oxide (thermal, wet, 900 C)			2.21 [309]	compressive	4 [310]	10^7 [310]

Further discussion of the electrochemistry of silicon and other semiconductors can be found in Morrison [287] and Pierret [306]; of thin-film dielectrics such as silicon oxide and silicon nitride, in Campbell and Morley [311] and O'Dwyer [312].

Single-crystal silicon and bare silicon-electrolyte interfaces

In crystalline silicon, all four valence electrons are involved in covalent bonds with neighboring atoms. With the gap between the valence band and the conduction band only 1.12 eV (at room temperature), electrons are readily excited into the conduction band. As a result, even undoped (intrinsic) silicon is moderately conductive ($G_{Si} = 4 \mu\text{S cm}^{-1}$ at room temperature) [306]. Doping introduces additional carriers to the silicon crystal—electrons in the case of *n*-type substrates (e.g. phosphorus-doped) and holes for *p*-type substrates (e.g. boron-doped).

Upon contacting an electrolyte, any mismatch which might exist between the silicon Fermi energy and the oxidation-reduction potential of the solution will tend to drive redox reactions at the interface. The redox potential scale (E^*) is related to the electron energy scale E by [313]

$$E^* = q(-4.5eV - E).$$

The efficiency of redox reactions at the interface depends on the degree of overlap between the quantum states in the energy bands of the semiconductor and the donor or acceptor levels in the reactants of the electrolyte [310]. Silicon-electrolyte redox reactions tend to result in the formation of a space-charge layer in the silicon through a process analogous to Fermi energy level matching at metal-silicon interfaces. A representative example of Fermi energy level matching, for an *n*-type silicon substrate in contact with a high-work-function metal such as copper, is illustrated by the energy band

diagram in figure 3.12(a). Electrons tend to flow from the silicon into the metal, where the Fermi energy level is nominally lower. The loss of electrons to the metal, however, causes a surface depletion region to form in the silicon. The electric field in the depletion region prevents further nonequilibrium charge transfer. Fermi energy level matching is manifested in the energy band diagram as bending of the conduction and valence bands on the silicon side of the interface [287].

Energy band bending at silicon-electrolyte interfaces is mitigated by surface states, as shown in figure 3.12(b). The silicon surface is normally terminated by some combination of oxygen and hydrogen (with hydrogen and oxygen termination associated with hydrophobic and hydrophilic behavior, respectively). Differences between the

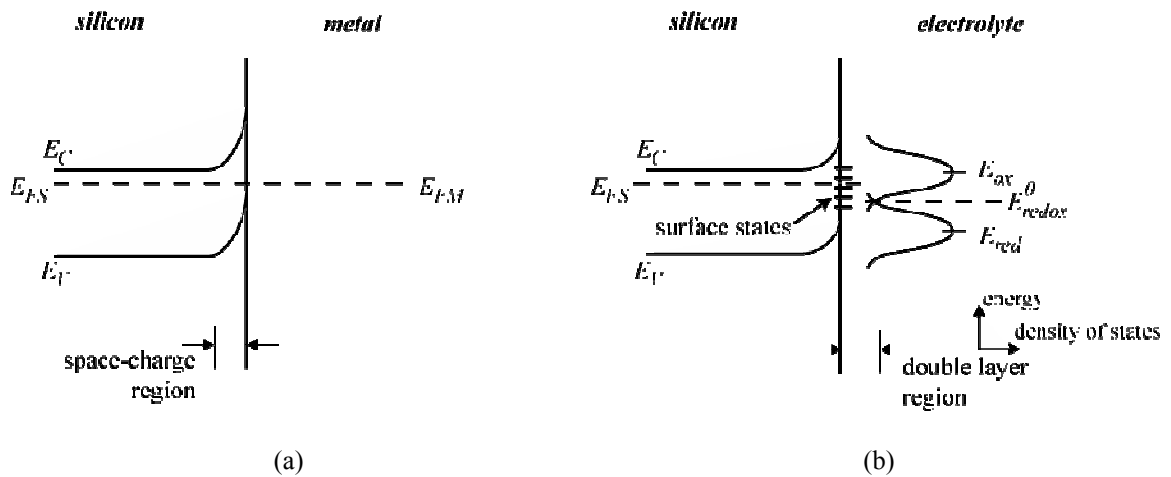


Figure 3.12: Comparison of unbiased silicon-metal and silicon-electrolyte interfaces using energy band diagrams. (a) At a semiconductor-metal interface, the Fermi energies of the two materials are matched through band bending (space charge layer formation) in the semiconductor; in the case shown here, the metal workfunction is greater than the semiconductor workfunction and the space charge region is a depletion layer. (b) At a semiconductor-electrolyte interface with an equivalent energetic relation ($E_{redox}^0 < E_{FS}$), band bending is partially mitigated by ionization of surface states and by double layer effects. Note that the x -axis in the electrolyte-side profiles is the density of states, not the spatial location. Energy bands shown are for n-type silicon. After Pierret [306] and Morrison [287].

silicon Fermi level and the redox potential can also be supported by Helmholtz and Gouy-Chapman layer effects [314, 315].

Non-equilibrium charge transfer at semiconductor-electrolyte interfaces

Biasing a substrate relative to an adjoining electrolyte tends to drive nonequilibrium processes at the silicon-electrolyte interface. Figure 3.13 illustrates the effects of biasing a semiconductor-electrolyte system for an *n*-type semiconductor. Under bias, carriers in the silicon rapidly drift toward the electrolyte interface (the mobility of holes and electrons in the lattice-scattering-dominated regime, for dopant concentrations below $\sim 10^{16} \text{ cm}^{-3}$, is $\mu_p \approx 450 \text{ cm}^2 \text{ V}^{-1} \text{ sec}$ and $\mu_n \approx 1350 \text{ cm}^2 \text{ V}^{-1} \text{ sec}$ [306]). The silicon becomes degenerate (quasimetallic) near its surface and a potential

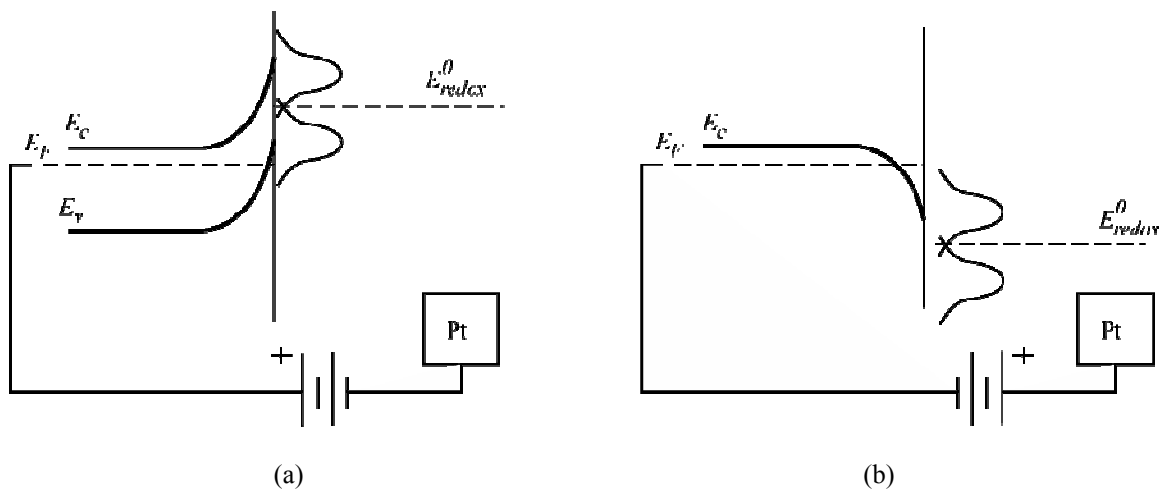


Figure 3.13: Effect of biasing a semiconductor-electrolyte interface (*n*-type shown). (a) A strong anodic bias (of the electrolyte relative to the semiconductor) drives the semiconductor into a degenerate (deep depletion) state near the interface, leading to metallic behavior and the movement of electrons from reducing agent in the electrolyte into the semiconductor valence band. (b) With the semiconductor at cathodic bias, an inversion layer forms in the semiconductor. After Morrison [287].

drop develops across the interface. For the electrolyte at anodic bias, the region near the silicon surface becomes deeply depleted, with the Fermi level within the valence band as shown in figure 3.13(a). The quasimetallic semiconductor surface readily removes electrons from the reducing agent. The semiconductor likewise becomes degenerate at a large cathodic bias (of the electrolyte relative to the silicon) with the formation of an inversion layer, as shown in figure 3.13(b). Analogous effects occur upon biasing a *p*-type semiconductor.

At anodic potentials greater than a few volts, silicon surfaces tend to react with aqueous media to form a solid-phase silicon oxide layer [310]:



The increasingly thick oxide layer acts as a barrier to further interface charge transfer, such that anodic current tends to decrease over time. Zhang [310] summarizes experiments on anodic silicon oxidation at potentials ranging from 0-15 V in a range of electrolytes, which show that the oxide layer reaches a final thickness between 2 and 40 Å per volt over a timescale of minutes. Drift of oxidant anions across the oxide is believed to be the rate-limiting process in anodic oxide formation [316]. Reported values for oxidation current density vary somewhat with electrode size as well as electrolyte composition. Bardwell et al. [317], found $j \approx 10 \text{ mA cm}^{-2}$ after 1 second for *p*-type silicon electrodes ranging in size from $10^{-4} - 10^{-1} \text{ cm}^2$ cathodically biased at 10 V anodic silicon oxidation in 0.1 M HCl, results which are somewhat typical. Constant-current oxidation studies indicate that the maximum anodization potential is around 200 V in acids and around 500 V in organic solutions; at higher potentials, the oxide breaks down [318]. Anodic silicon oxides formed at constant potential, as when a step voltage input is

applied to a silicon-walled electrolytic cell, have a higher hydroxyl content than those formed under gradually increasing voltage and are less effective dielectrics [317].

At a cathodic silicon surface, water molecules are reduced to yield hydrogen gas and hydroxyls. The exchange current density i_0 depends on electrolyte composition and illumination and ranges from $10^{-6} - 10^{-11}$ A cm⁻² [310, 319]. The native oxide layer which tends to form on silicon surfaces exposed to aqueous solutions containing dissolved oxygen is generally less than 10 Å thick; because electrons can readily tunnel through this thickness of oxide, the native oxide layer does not significantly impact hydrogen evolution at cathodic silicon surfaces [287, 320].

Effect of an intermediate insulating layer

The presence of one or more dielectric layers at a silicon-electrolyte interface can significantly affect interface charge transfer. Energy band diagrams for a silicon-insulator-electrolyte system at zero bias and for the semiconductor surface at cathodic

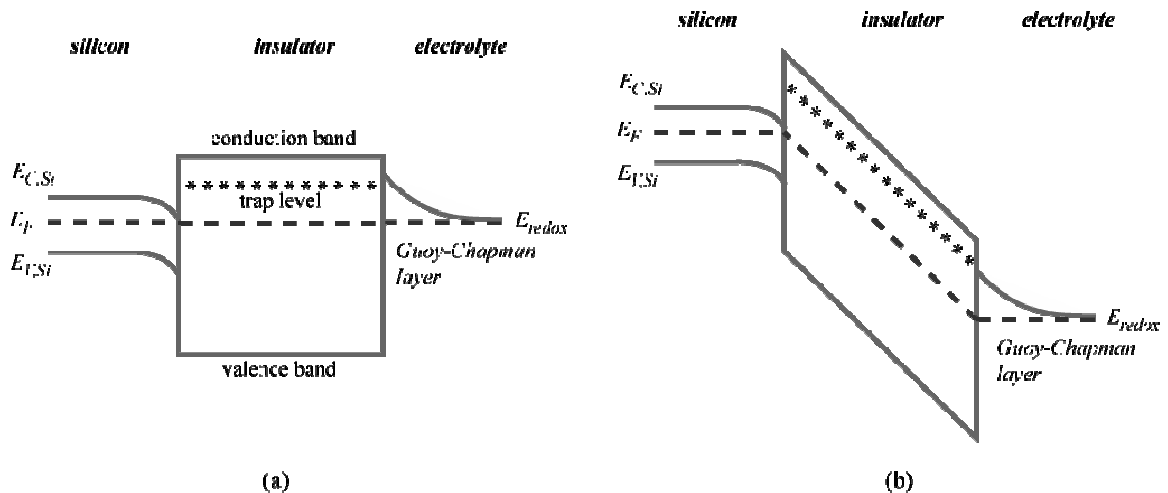


Figure 3.14: Energy band diagrams for a silicon-insulator-electrolyte interface, unbiased (a) and with the silicon at cathodic potential (b). As in the uninsulated silicon case (fig 3.12), band bending occurs in the silicon. After Morrison [287].

potential are shown in figure 3.14. The insulator nominally acts as a barrier to charge transfer, with an electric field developing in the insulator in proportion to the applied voltage.

A sufficiently large field can result in the flow of significant currents through the insulator. Conduction within insulators can be ionic and/or electronic. Ionic transport (e.g. of sodium ions in oxide films) is interstitial. Electronic conduction into and through a dielectric thin film can occur through a variety of mechanisms, illustrated in figure 3.15. Carriers must first surmount the potential barrier at the interface, which can occur

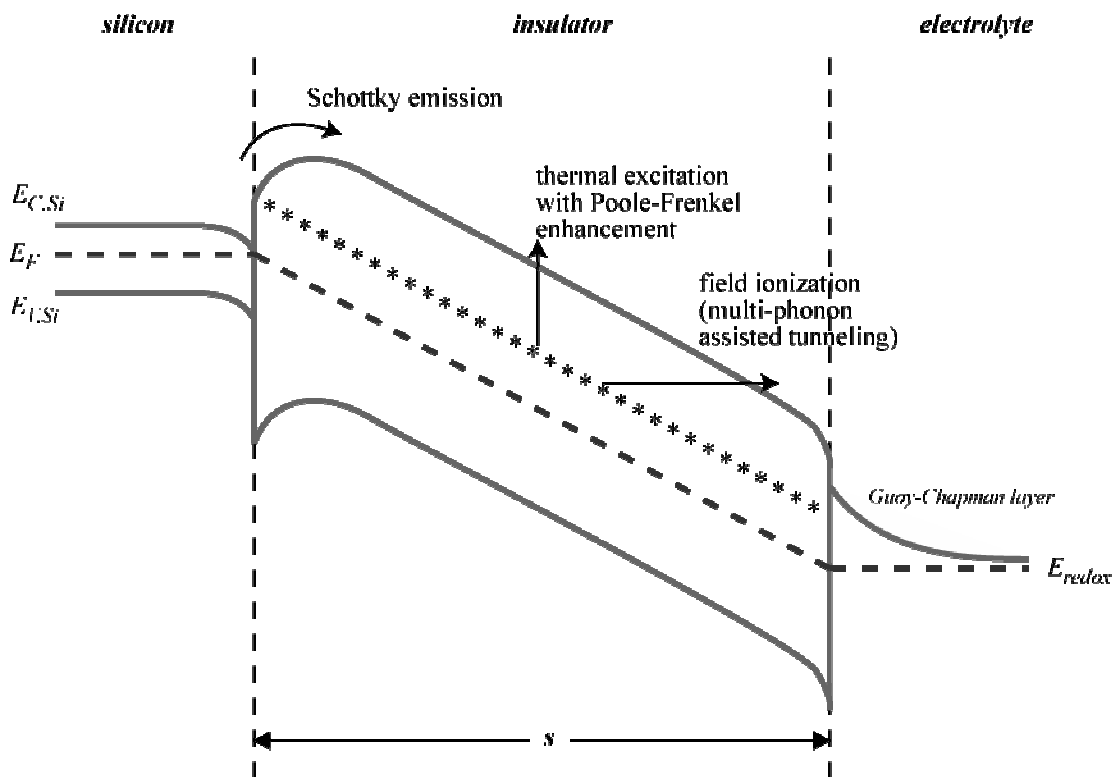


Figure 3.15: Energy band diagram illustrating mechanisms of charge transport into and through dielectric films. After Campbell and Morley [311].

through either Fowler-Nordheim emission or Schottky emission. Carrier transport within the insulator is generally controlled by ionizable irregularities in the film, called traps. Trap-controlled bulk transport processes include Poole-Frenkel conduction and field ionization. Tunneling into the insulator conduction band or from the insulator valence band is an additional conduction mechanism. Carriers can tunnel all the way through dielectric layers less than 50 Å thick [311].

Fowler-Nordheim emission is a quantum mechanical tunneling phenomenon well known as the temperature-independent mechanism of electron emission from a metal into a vacuum. Fowler-Nordheim emission for insulators is electron tunneling across a metal-insulator or semiconductor-insulator interface energy barrier into the bulk dielectric. It is often current limiting in silicon oxide films in solid-state devices [321]. In electrolyte systems, highly mobile alkali ions dominate conduction in silicon oxide films, limiting the effectiveness of oxide as an insulating layer when an aqueous medium is present [322, 323]. Schottky emission is a thermionic process – the temperature of the charge carriers is sufficiently high that a subset can surmount the interface energy barrier, the height of which is diminished by a strong field. The log of Schottky emission current is characteristically linear with square root of field [311].

Poole-Frenkel conduction is bulk (trap-controlled) thermionic emission comparable to the Schottky effect at an interface. A high electric field strength reduces the energy barrier height in the vicinity of forbidden-band traps, such that more electrons escape into the insulator's conduction band [312]. Poole-Frenkel conduction has historically been thought to dominate in silicon nitride films, which resist ionic penetration from liquid phases. Field ionization involves hopping of electrons between

impurities in the insulator. Gap states in silicon nitride films deposited through chemical vapor deposition have been found to be around 3 eV [324]. Multiphonon-assisted tunneling from deep traps, described for semiconductors by Markam-Ebeid and Lannoo [325], is another possible conduction mechanism in insulating films. Models of insulator conduction are developed in chapter 6 in the context of measured currents in silicon electroosmotic micropumps.

CHAPTER 4: CORE DESIGN CONSIDERATIONS

This chapter contemplates the design of electroosmotic micropumps in which the principal solid phase is single-crystal silicon. The design process is informed by chapter 3's models of the electric double layer, electroosmotic flow, and nonequilibrium semiconductor-electrolyte charge transfer as well as by the strengths and limitations of silicon micromachining. Particular attention is paid to processes for fabricating capillaries and arrays of capillaries and for depositing dielectric thin films resistant to penetration by fluid phase ions. The critical issue of process yield is addressed in section 4.3. Additional fabrication details are set forth in appendix B.

4.1 Silicon electroosmotic micropump components and modeling

A basic silicon electroosmotic micropump design is illustrated in figure 4.1. The major components are a structure in which electroosmotic flow is generated (the EOF element); inlet and outlet manifolds/ports, electrodes; and a quantity of working fluid. The following parameters are used to describe the geometry: l_1 and A_1 are the length and total cross-sectional area, respectively, of the EOF element; A_2 is the cross-sectional area of the manifold regions flanking the EOF structure (and is equal to the product of the manifold width w and depth b); l_2 is the electrode separation distance; and l_3 is the distance between the inlet and outlet ports.

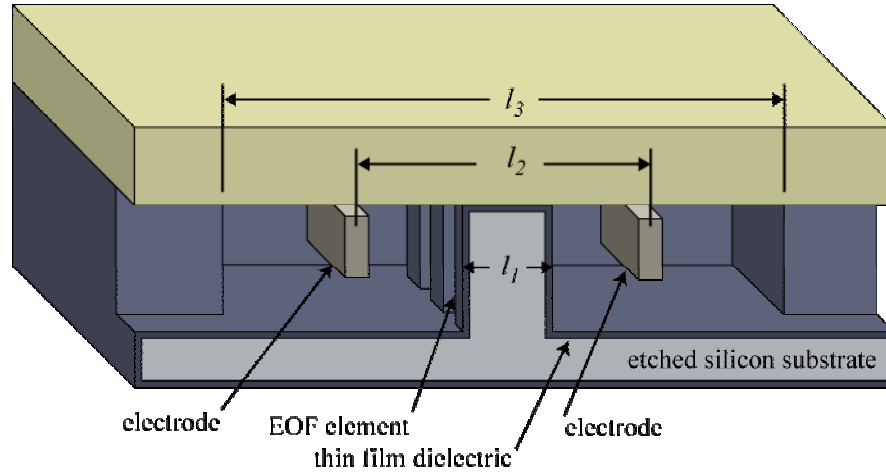


Figure 4.1: Schematic (section view) of a basic silicon electroosmotic micropump design. The EOF element is a structure with features conducive to generating electroosmotic flow, such as an array of fine pores. Biasing the electrodes on either side of the EOF element causes an axial electric field to develop in the EOF element. Fluid manifolds connect the EOF element with inlet and outlet ports. Silicon surfaces exposed to the electrolyte are coated with dielectric thin films.

Internal pressure losses

The passage of fluid through the pump manifolds is associated with a finite pressure drop, which diminishes the pump-external pressure drop. For manifolds which are much wider than they are deep, manifold flow is well modeled using the laminar-regime parallel plate solution which relates pressure drop to flow rate as [326]

$$\Delta p_2 = \frac{12\mu l_3}{wb^3} Q \quad (4.1).$$

Here Δp_2 includes the manifold pressure drop as well as any other pressure drops occurring within the pump but external to the slit capillary array. The parameter w is the effective width of the manifold, taking into account contractions at the inlet and outlet ports. For minimal flow disturbance in the transitional regions between the slit capillary array and the manifolds, the pressure drop Δp_2 simply subtracts from the inlet-to-outlet pressure rise generated by the pump, as shown in figure 4.2.

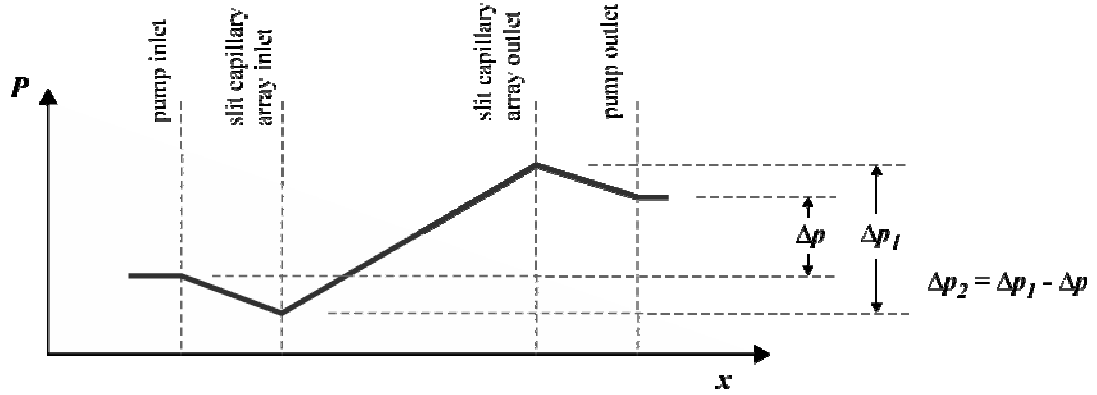


Figure 4.2: Schematic of approximate pressure gradients within silicon electroosmotic micropumps.

Electromigration current

A nondimensional electrical resistance parameter A^* can be defined as

$$A^* = \frac{l_2 A_1}{(l_2 - l_1) A_2 + l_1 A_1}, \quad 0 < A^* \leq 1 \quad (4.2).$$

This parameter captures the extent to which the EOF flow generation structure dominates the electrical resistance of the entire cell. With the electrodes located a finite distance $0.5(l_2 - l_1)$ from the slit capillary array, V_1 is a fraction of the bias applied across the electrodes V_2 , given by

$$V_1 = \frac{A^* A_2 l_1}{A_1 l_2} V_2. \quad (4.3)$$

The molar flux \vec{j}_i^* of species i under an electric field \vec{E} (absent field dependence of the fluid properties) is [59]:

$$\vec{j}_i^* = v_i z_i F c_i \vec{E} \quad (4.4)$$

Here v_i is the species mobility (in $\text{mol N}^{-1} \text{m s}^{-1}$), which depends primarily on the viscosity of the fluid medium, the ion hydrodynamic (Stokes) radius, and the ion valence

number. Multiplying both sides of eqn 4.4 by the valence number z_i and F yields the contribution of species i to current density i_i (in A m^{-2}):

$$i_i = \nu_i z_i^2 F^2 c_i \bar{E} \quad (4.5)$$

The current-voltage relationship is therefore ohmic, and the product of the terms multiplying the electric field is the contribution of species i to the conductivity σ of the solution. The mobilities of common ions range from $4.1 \times 10^{-13} \text{ mol N}^{-1} \text{ m s}^{-1}$ for Li^+ to $3.8 \times 10^{-12} \text{ mol N}^{-1} \text{ m s}^{-1}$ for H^+ [51], corresponding to molar conductivities λ_i ($\lambda_i = \nu_i z_i^2 F^2$) of $3.8 \times 10^{-3} \text{ S m}^2 \text{ mol}^{-1}$ and $3.5 \times 10^{-2} \text{ S m}^2 \text{ mol}^{-1}$, respectively.

Assuming the current path to be one-dimensional and the fluid to be homogeneous, the conductance of the fluid between the electrodes can be approximated as

$$G = \frac{\sigma A_2 A^*}{l_2} \quad (4.6)$$

where σ reflects the contributions of all ionic charge carriers in solution as described by eqn 4.5.

4.2 Forming slit capillary arrays in silicon

Trenches are ubiquitous in integrated circuit and microelectromechanical systems fabrication, with oxide-filled trenches providing electrical isolation in nearly all integrated circuits and trench etching used to define the features of most electrostatic comb drives and other surface micromachined devices. Indeed, it is because tools and techniques for forming trenches—including high-aspect-ratio trenches—in silicon are so well established that the slit capillary is a highly relevant geometry for silicon EOF devices.

Silicon trench etching techniques

An abundance of tools and techniques are available for etching micron-scale trenches in silicon substrates: Etch mechanisms can be physical, chemical, or both; etchants are found in liquid and gas phases; etc. Wet silicon etchants include ethylene diamine pyrocatechol (EDP), potassium hydroxide (KOH), and tetra methyl ammonium hydroxide (TMAH) [76]. EDP, KOH, and TMAH are anisotropic etchants, meaning that etching is selective with respect to silicon crystal planes. This crystal plane dependence usually precludes high channel depth-to-width aspect ratios ($r_{dw} \gg 1$). Wet etching of high-aspect-ratio channels in $\langle 110 \rangle$ silicon has been explored with limited success [327]. Anisotropic wet etching is discussed in detail by Hines [328].

Plasma etching of silicon is widely used in integrated circuit fabrication [329]. A process known as time-multiplexed inductively coupled plasma (TMICP) etching was developed in the early 1990s specifically for etching high-aspect-ratio structures [330]. The silicon substrate is alternately etched with SF_6 ion-enhanced plasma and passivated with C_4F_8 . This alternating etch-passivation process yields silicon:photoresist selectivity of 50:1 or higher, etch rates over $2 \mu\text{m min}^{-1}$, and aspect ratios over 40. In contrast, typical plasma etchers using temporally constant fluorine chemistries etch silicon at a rate of only $0.35 \mu\text{m min}^{-1}$ with silicon:photoresist selectivity of 7:1 [331]. The availability of the TMICP etching tools has played an important role in the proliferation of micromachined devices in commercial products, particularly inertial sensors (such as accelerometers and gyroscopes) and telecommunications equipment.

Chow compiled extensive data on narrow-channel silicon etching with a TMICP tool manufactured by Surface Technology Systems (STS) at the Stanford Nanofabrication Facility (SNF), a public cleanroom facility on the campus of Stanford University [332].

Process parameters for three common etch recipes used at SNF, along with average silicon and photoresist etch rates, are shown in table 4.1. For small features, the TMICP etch rate generally decreases with decreasing feature size and with increasing depth. Figure 4.3 shows etch rate for the recipe DEEP is plotted as a function of trench depth for 2 μm and 5 μm trenches. Data similar to that compiled by Chow for the SNF machine is available for other publicly accessible TMICP tools [333, 334].

Table 4.1: TMICP etch recipe parameters and etch rates. After Chow [332].

Etch recipe	DEEP	SMOODEEP	SMOOSHALL
SF ₆ flow rate (sccm)	130	130	130
SF ₆ active time (sec)	11	8	7
etch electrode power (W)	12	8	12
C ₄ F ₈ flow rate (sccm)	85	85	120
C ₄ F ₈ active time (sec)	8	6	7
passivate electrode power (W)	0	0	0
coil power (W)	600	600	600
APC angle (°)	70	70	55
silicon etch rate ($\mu\text{m min}^{-1}$)*	3.8	2.9	1.2
photoresist etch rate (\AA min^{-1})*	370	239	288
silicon/photoresist selectivity*	103	123	42

*average over 80 minute etch

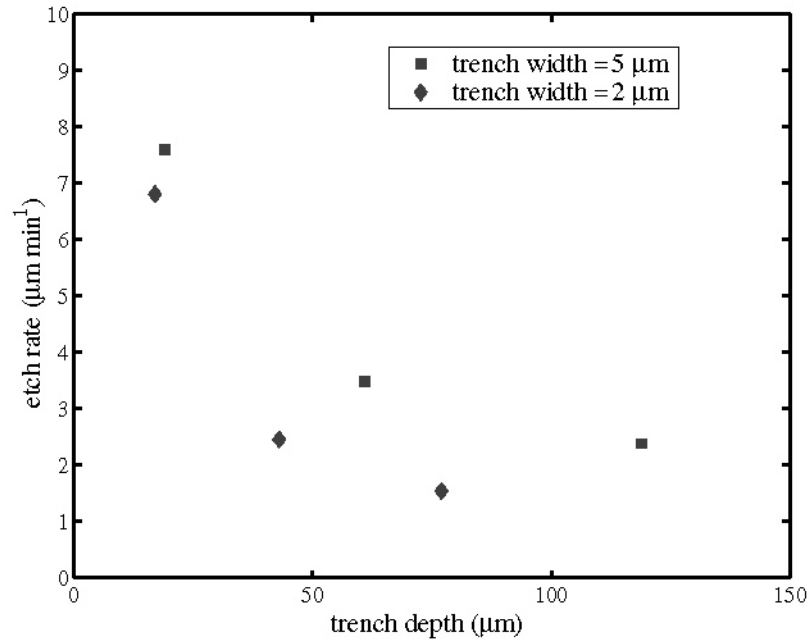


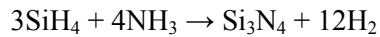
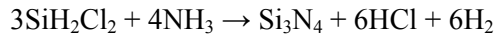
Figure 4.3: TMICP etch rate dependence on trench width and depth. After Chow [332].

Anodic silicon dissolution is an alternative approach to TMICP etching for producing arrays of high-aspect ratio channels [335, 336]. Anodic silicon dissolution is a wet-chemistry-based process well suited to etching through-wafer channels (as opposed to channels parallel to the wafer surface). Efforts have recently begun to use porous silicon structures formed in this manner for EOF generation [337]. Additive techniques, such as electroplating, are another means of producing slit capillaries and other types of fluid conduits in silicon.

Thin film dielectric deposition

In light of the prospect of significant interface charge transfer at a bare silicon-electrolyte interface, silicon surfaces which will contact the electrolyte in an electrolytic cell are usually coated with one or more thin layers of insulating material during manufacturing. Because silicon electroosmotic micropumps almost invariably use

aqueous salt solutions as the working fluid, silicon nitride's tendency to resist ionic diffusion (as discussed in section 3.3) makes it a good choice for the primary dielectric layer (the layer immediately atop the silicon substrate). Silicon nitride films are nominally composed of Si and N at a 3:4 ratio, although the elemental ratio varies considerably depending on the fabrication method and conditions. High-quality silicon nitride films can be produced by deposition at low pressure using a combination of ammonia and either dichlorosilane or silane [338]:



Silicon nitride films fabricated through this process, known as low-pressure chemical vapor deposition (LPCVD), are generally moderately tensile and high-strength (see table 3.1).

As discussed in chapter 3, the high mobility of alkali ions in silicon oxide makes this material generally unsuitable as the sole component of a dielectric thin film in a silicon-electrolyte system. Oxide can, however, be effective as a component of a multilayer dielectric film—particularly when used as the outermost layer, because of its tendency to develop a relatively high zeta potential (discussed further below). Direct oxidation of silicon nitride is practical only to a very limited extent [339]. Thermally grown oxides generally exhibit the best dielectric properties. Oxide films can also be deposited directly through plasma-enhanced processes a technique which is usually used when high-temperature processing would be detrimental. However, plasma-enhanced chemical vapor deposition of oxide is generally associated with poor step coverage. Silicon oxide films, whether grown in steam or dry heat, deposited, or formed anodically,

are amorphous, with a density of approximately 2.21 g cm^{-3} (compared to 2.65 g cm^{-3} for the crystalline form, quartz) [309].

Slit capillary array formation

As shown in figure 3.11, the Burgreen-Nakache slit capillary EOF model indicates that a_l on the order of or less than $1 \mu\text{m}$ will, in general, produce finite EOF against relatively large back pressures with modest applied voltages (e.g. $\Delta p_{\text{max}} > 1 \text{ kPa}$ for $a_l = 1 \mu\text{m}$ assuming $V = 100 \text{ V}$, working fluid properties similar to those of water, and $\zeta = -10 \text{ mV}$). Both Δp_{max} and \bar{v}_{max} are independent of slit depth b , while total flow rate

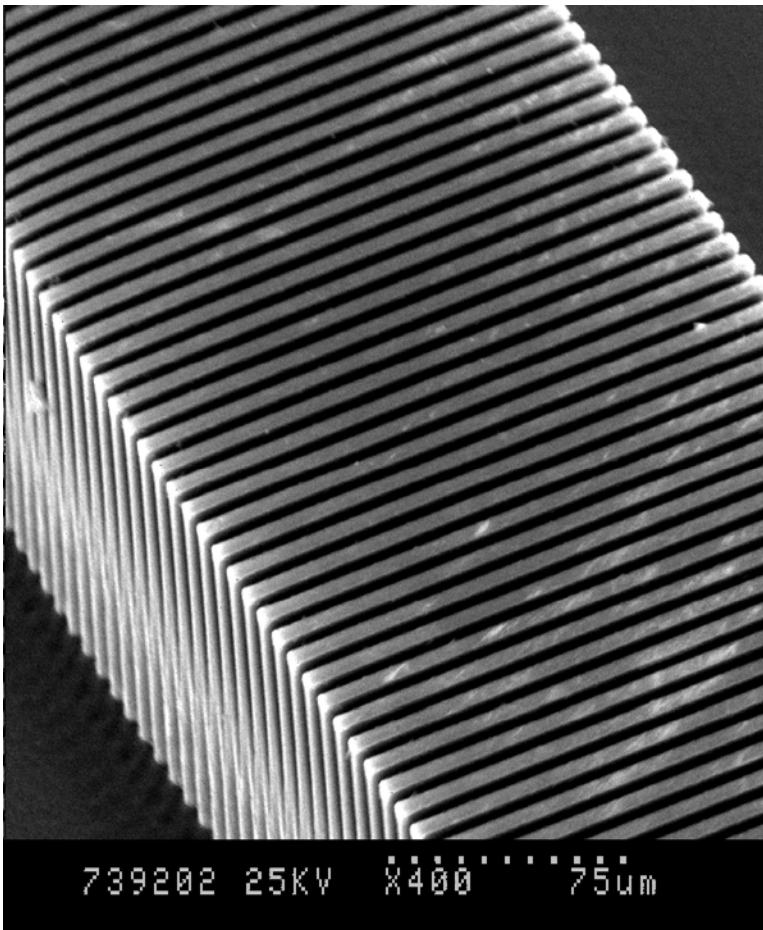
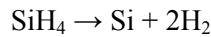


Figure 4.4: Scanning electron micrograph of a slit capillary array. The trenches are $3 \mu\text{m}$ wide and spaced at a pitch of $10 \mu\text{m}$.

scales linearly with b . From the standpoint of geometry, therefore, the goal in fabricating an EOF element comprising a parallel array of trenches is to maximize b and minimize trench centerline-to-centerline spacing s_{cc} for $a_l \approx 1 \mu\text{m}$. A further objective is to rigorously control process steps which affect a_l , since small variations in this parameter have a pronounced effect on Δp_{max} (and therefore on the entire pressure-flow rate curve). An electron micrograph of a slit capillary array is shown in figure 4.4.

The lower limit on trench spacing $s_{cc,\text{min}}$ depends on how the wafer is handled during processing. Accordingly, $s_{cc,\text{min}}$ is treated as an empirical parameter and considered in the context of process yield in section 4.3. The maximum trench depth b_{max} is, because of TMICP feature size dependence illustrated in figure 4.3, a strong function of a_l for small a_l . A further consideration for b , as well as for a_l , is dielectric thin film conformality, discussed earlier in this section. The parameters a_l^* , b^* , and a_l' are introduced to facilitate study of these fabrication process issues. The nondimensional parameter b^* takes into account the feature size dependence of TMICP etch depth, such that the actual slit capillary depth is usually less than the depth b of the manifolds. The parameter a_l' has units of length and is the slit half-width as photolithographically defined during pump fabrication. The nondimensional parameter a_l^* takes into account the reduction in slit capillary half-width, relative to a_l' due to the application of one or more passivation layer(s) as well as any z -dependence of slit half-width arising from the etch process. Both a_l^* and b^* approach unity for an orthogonal slit capillary array with negligible feature size dependence of etch depth and for negligible dielectric film thickness.

TMICP feature size dependence and dielectric film uniformity were studied by patterning arrays of 3 μm and 4 μm lines in 7 μm thick layer Shipley SPR-220-7 photoresist (which has similar properties to the AZ4260 photoresist used in Chow's work [332]), exposing 4 times for 1.6 seconds at 15 second intervals, and etching for 80 minutes with the recipe DEEP. The photoresist was then removed and the etched test structures coated with an oxide-on-nitride film (nominal thickness 250 nm/450 nm, measured on an unpatterned portion of the wafer surface using a Nanospec non-contact, spectro-reflectometry system, Nanometrics, Milpitas, CA). A novel process was developed to conformally deposit double-layer film with this composition, which (as described in chapter 5) has favorable properties for generating electroosmotic flow in silicon-based devices. A near-stoichiometric nitride layer is first deposited as described above. Next, a layer of polycrystalline silicon (polysilicon) is first deposited by LPCVD at 620° C through the decomposition of silane [329]:



At this temperature, polysilicon deposition is highly conformally because the probability of attachment upon a collision of a silane molecule with the surface is sufficiently small that (given silane's relatively long mean free path) the molecules tend to bounce repeatedly in the hole, nearly eliminating position dependence of attachment [340]. The polysilicon deposition also smoothes rough silicon surfaces left by deep etching processes. After deposition of the polysilicon layer, the wafers are heated in a steam ambient in order to oxidize the polysilicon layer in its entirety.

Scanning electron micrographs of etched and coated slit capillary arrays are shown in figure 4.5. Measured trench depth variations with width are plotted in

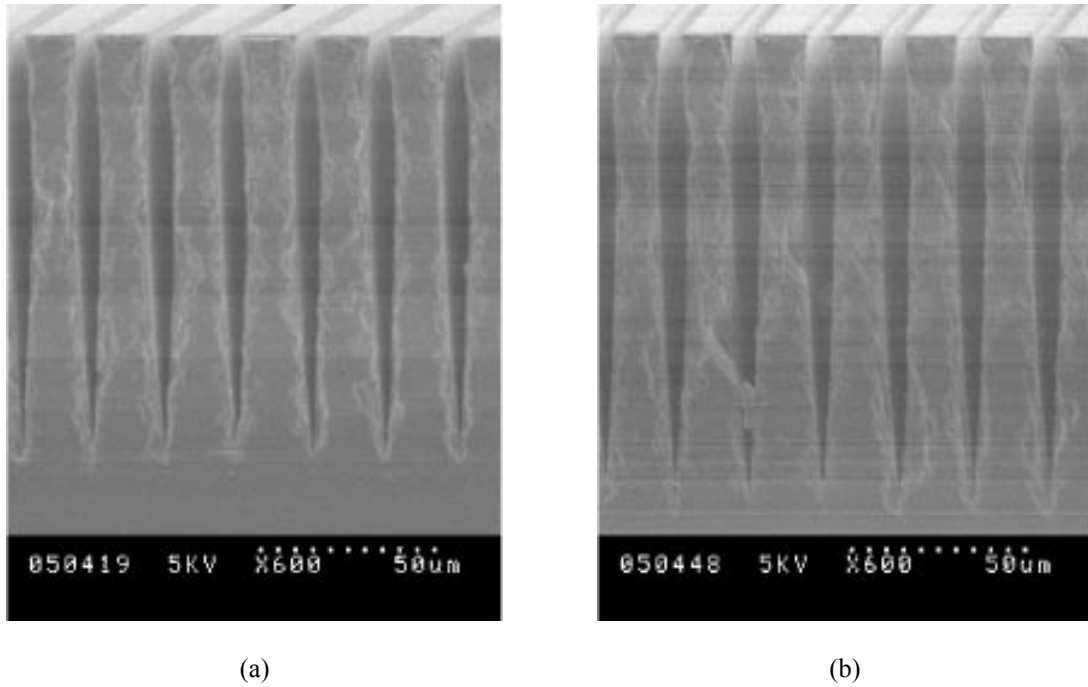


Figure 4.5: Dependence of trench depth b on photolithographically patterned trench width: (a) $2a' = 3 \mu\text{m}$; (b) $2a' = 4 \mu\text{m}$.

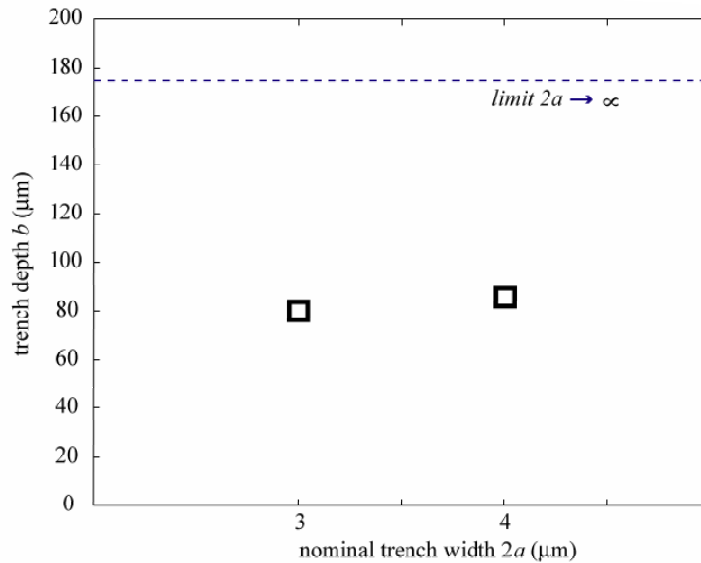


Figure 4.6: Trench depth variation as a function of trench width. Standard deviation is approximately $1.6 \mu\text{m}$ ($N = 9$) for both the $2a = 3 \mu\text{m}$ and $2a = 4 \mu\text{m}$ trenches.

figure 4.6. Trench depth b^*b increases monotonically with increasing width, approaching a saturation value which is the depth to which large ($>10\ \mu\text{m}$) features are etched.

Variation in the measured trench depths can be attributed to two factors: small,

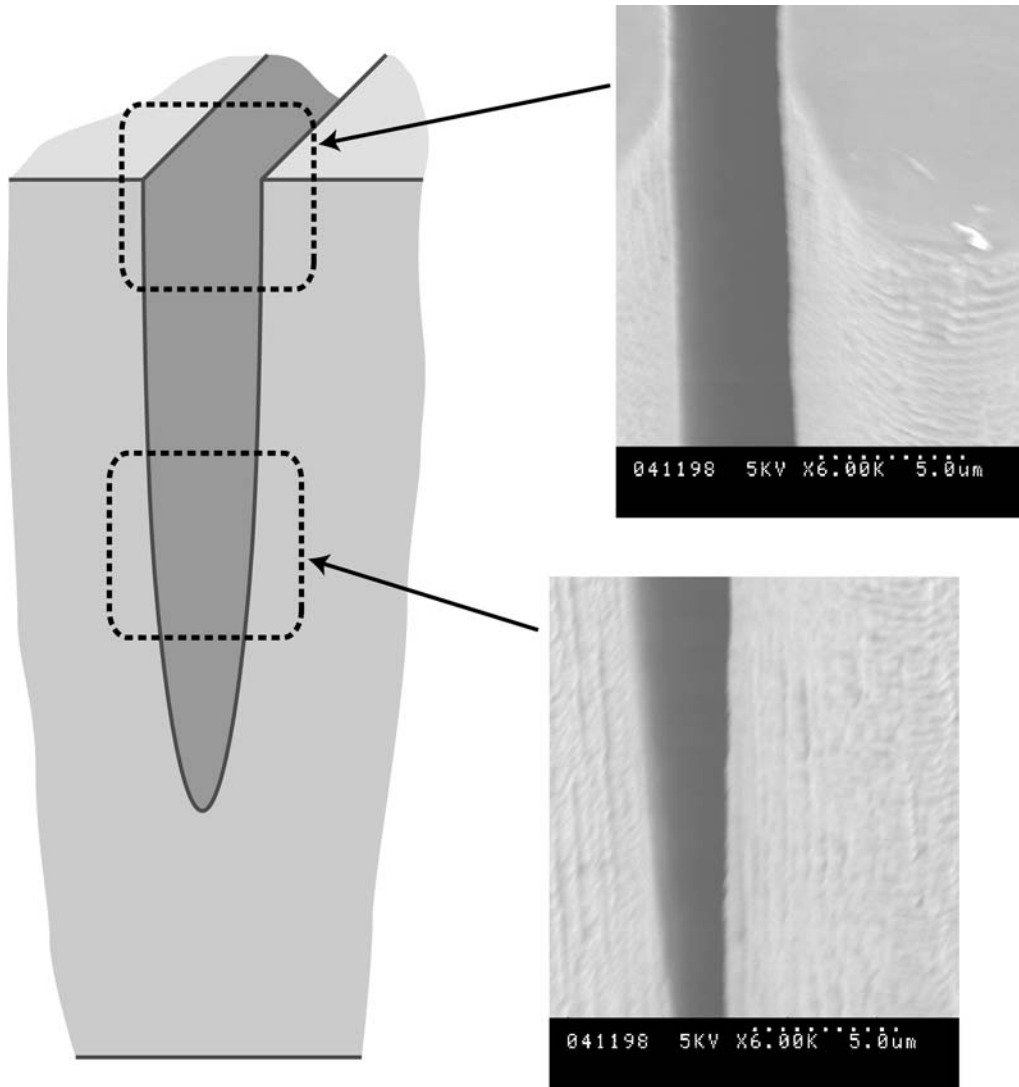


Figure 4.7: Deviation of TMICP-etched high-aspect-ratio silicon trenches from ideal slit capillary geometry. Trench width varies slightly as a function of distance from the substrate surface, bulging slightly near the top of the trench and contracting toward the trench bottom. The in-plane trench wall curvature is a mask feature.

unintended variations in the photolithographically defined trench width due to spatial nonuniformity (variation across the surface of the wafer) of the ultraviolet radiation used to expose the photoresist; and spatial nonuniformity of the TMICP etch process.

As shown in figure 4.7, TMICP-etched trenches can deviate from the ideal orthogonal slit capillary geometry illustrated in figure 3.9. In figure 4.8, trench width (as a fraction of the photolithographically defined width at the surface of the substrate) is plotted as a function of distance from the substrate surface for a sample of trenches with $2a' = 4 \mu\text{m}$ etched for 80 min using DEEP. All trench dimensions were determined from scanning electron micrographs using the National Institutes of Health's *Image* software (PC version from Scion Corporation, Frederick, MD).

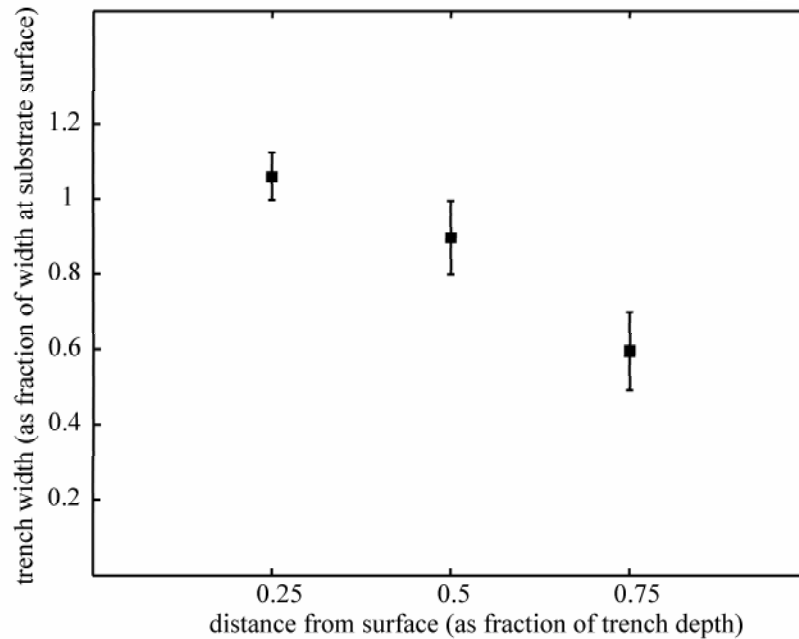


Figure 4.8: Trench width variation as a function of distance from substrate surface. Mean and standard deviation shown; $N = 9$.

4.3 Process yield

Economic considerations dictate that for new classes of microfabricated devices, fabrication yield is of great importance, often deciding—regardless of performance—whether the device enters widespread use or is of academic interest only.

Thin film dielectric failure

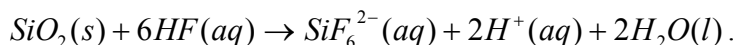
Failure of the thin film dielectric layer (evidenced by currents approximately an order of magnitude higher than the calculated current based on ionic conduction in the electrolyte) was the largest source of lost yield in early efforts to produce silicon electroosmotic micropumps. Two LPCVD nitride film compositions were evaluated. One film is silicon-rich and accordingly characteristically low stress, achieved by flowing ammonia at a relatively low rate. This film is widely used in the fabrication of MEMS devices. The other film is deposited with ammonia at a higher flow rate and is nearly stoichiometric. Complete deposition parameters for both films can be found in appendix B.

The issue of passivation layer performance during micropump operation is interwoven with a practical issue for silicon electroosmotic micropump production: the need to seal the silicon substrate with a cover plate. Anodic bonding with glass wafers is a straightforward, well established method of sealing silicon microfluidic devices. Glass covers offer optical access to the fluid chambers; anodic bonds are characteristically high strength and leak-free. However, anodic bonding to a nitride-coated silicon wafer occurs through polarization currents in the nitride—so the tendency of nitride films to resist bulk currents, which is vital to these films' function in silicon electroosmotic micropumps, tends to inhibit anodic bonding.

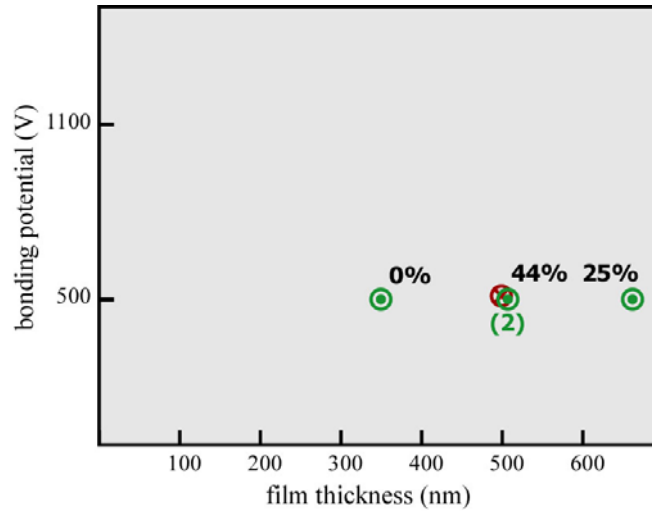
Yield data relating to the dielectric thin films is summarized in figure 4.9. The data encompasses films ranging in thickness from 250 nm to 680 nm. An electrode bias of 200 V was used as the standard for micropump operability. The low-stress nitride film was easy to bond but was found to offer inadequate insulation at any thickness, yielding virtually no operable devices, as shown in figure 4.9(a). The near-stoichiometric film at thicknesses greater than 400 nm thick was associated with consistently high yields, as shown in figure 4.9(b). A bonding voltage of 1100 V was required to anodically bond the glass cover onto wafers with these films. For very thick (>600 nm) near-stoichiometric films, even this very high bonding voltage did not consistently result in successful bonding.

Insulating thin films are susceptible to failure due to dielectric breakdown when subjected to high electric fields. Regardless of passivation layer composition or thickness, almost all devices failed when biased above 500 V. Some failed devices were subsequently recovered after being flushed with deionized water and allowed to sit for a few days, while others did not recover.

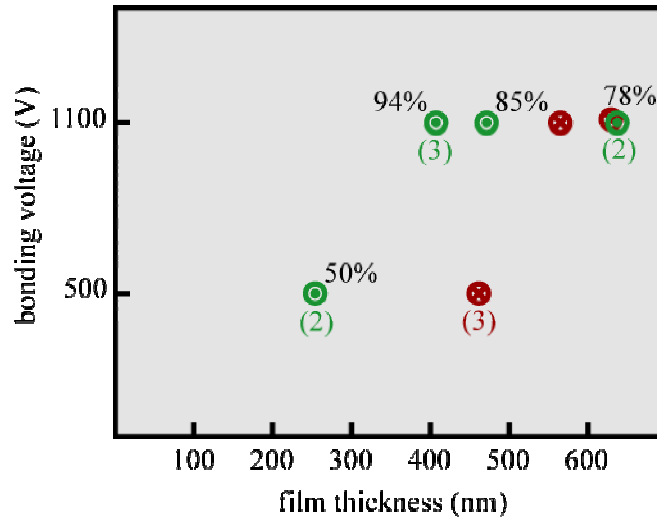
Dissolution is a concern with silicon oxide films exposed to aqueous solutions. Silicon oxide films tend to dissolve in the presence of HF:



Fluoride ion-containing working fluids have been avoided in testing silicon electroosmotic micropumps. The borate buffer solutions used in most testing are basic; a possible concern given that the solubility of silicon oxide in solution increases rapidly



(a)



(b)

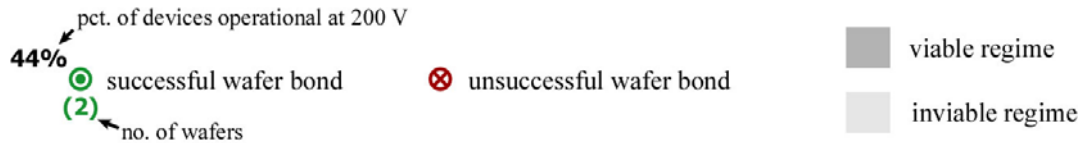


Figure 4.9: Yield data for dielectric thin films, taking into account both dielectric breakdown and anodic bonding failure. (a) Low-stress nitride films tend to fail at all thicknesses evaluated. (b) Dielectric failure is rare with near-stoichiometric nitride films, but anodic bonding can be inhibited. Consistently high yields were realized with near-stoichiometric films with thickness between 400-600 μm .

with solution alkalinity at $\text{pH} > 9$ [310]. However, no evidence of dissolution of the oxide passivation layer was seen during testing. All passivation layers tested also appeared to prevent corrosion of the silicon substrate, which prior work has shown to be a concern for semiconductor electrodes (particular *n*-type) [313].

An extensive discussion of the phenomena underlying anodic bonding can be found in Albaugh [341]. Lee et al. carried out experimental work on bonding with various thin-film-coated silicon substrates [342].

Slit capillary wall fracture during processing

The mechanical integrity of the slit capillary array walls was studied by tracking yields of micropumps undergoing similar fabrication processes but with different slit capillary wall geometries. For arrays of closely spaced slit capillaries, the slit capillary walls are susceptible to mechanical failure during processing. The walls resemble slab cantilevers, for which the maximum stress upon application of a transverse load W (as shown in figure 4.10) scales linearly with b_l and l_l^{-1} and with the inverse square of the wall half-thickness t_w [80]:

$$\sigma_{\max} = \frac{12Wb}{t_w^2 l}$$

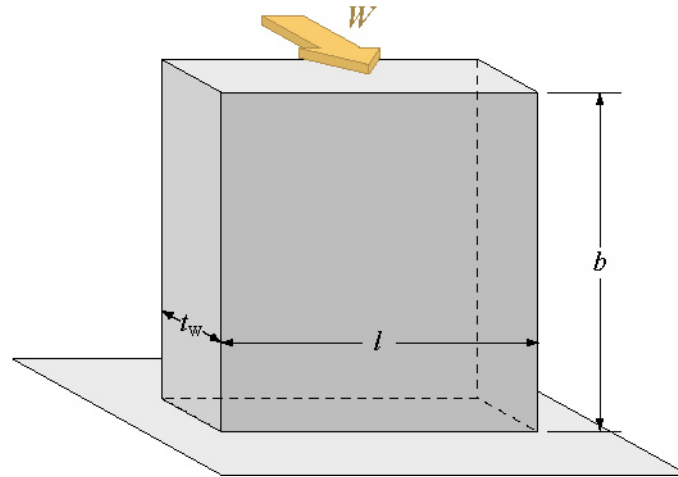


Figure 4.10: Slit capillary walls resemble slab cantilevers and are susceptible to mechanical failure when subjected to a transverse load, as shown, during processing.

Lost yield associated with the mechanical integrity of etched slit capillary arrays was thin film dependent. Lengths range from $50\ \mu\text{m}$ to $400\ \mu\text{m}$. The results of this study are shown in figure 4.11.

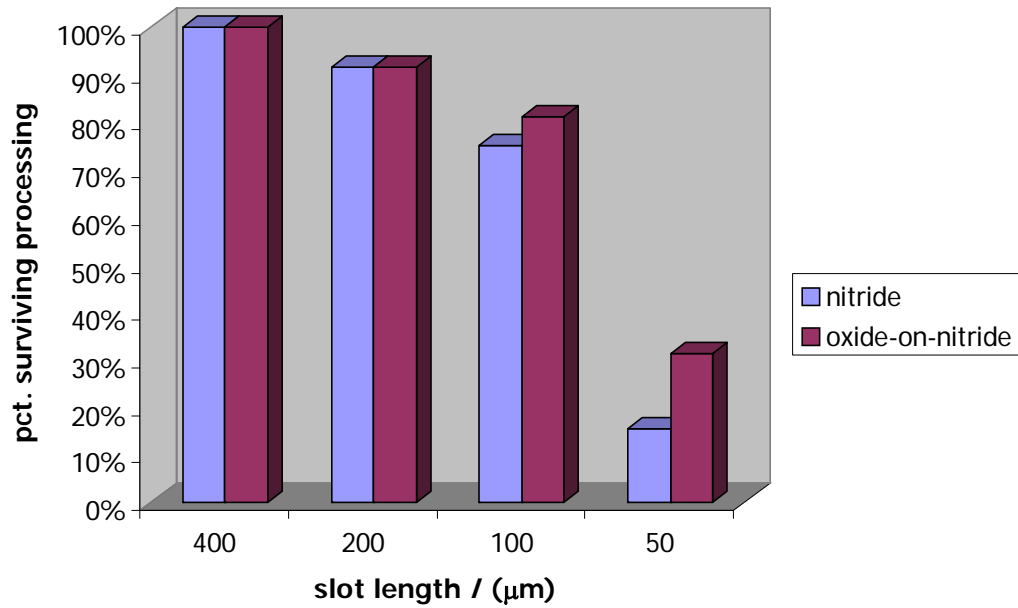


Figure 4.11: Mechanical integrity of microfabricated slit capillary arrays. Test arrays were 1 cm wide, with slots spaced at 20 μm intervals and etched for 80 minutes. For over half of the test arrays with 50 μm long slots, one or more walls broke during processing. Test array yield with an oxide-on-nitride coating is slightly higher than with a nitride coating only.

CHAPTER 5: DETAILED MODELING AND OPERATIONAL DATA

In this chapter, data on pressure, flow rate, current, and transient response are compared to the predictions of a silicon electroosmotic micropump model based on the Burgreen-Nakache solution for EOF in slit capillaries. The experimental regimen focused on a particular micropump design, with parametric variations introduced during both fabrication and testing. Observed quasi-steady-state operation of tested prototypes is consistent with predictions of the micropump model and have been used to estimate the zeta potential of silicon nitride and oxide-on-nitride dielectric films.

5.1 Standard silicon electroosmotic micropump design

To facilitate data collection and analysis, a standard silicon electroosmotic micropump design, illustrated in figure 5.1, was adopted. Approximately sixty micropump prototypes with variations on this basic design were fabricated and tested. The standard design is conducive to studying the influence on pump operation of dielectric film composition, geometric parameters such as a_1 and l_1 , and operating conditions such as V_2 and c . The complete fabrication process for micropumps with this design is set out in appendix B.

A critical feature of this design is the array of narrow, deep trenches arranged in parallel. Each trench resembles a slit capillary, for which an EOF model was set out in section 3.2. The standard design has $n = 500$ slit capillaries with centerline-to-centerline spacing $s_{cc} = 20 \mu\text{m}$, such that the entire array is 1 cm wide. The photolithographically defined slit capillary width is $2a_1' = 3 \mu\text{m}$ for approximately half of the prototype micropumps and $2a_1' = 4 \mu\text{m}$ for the remainder.

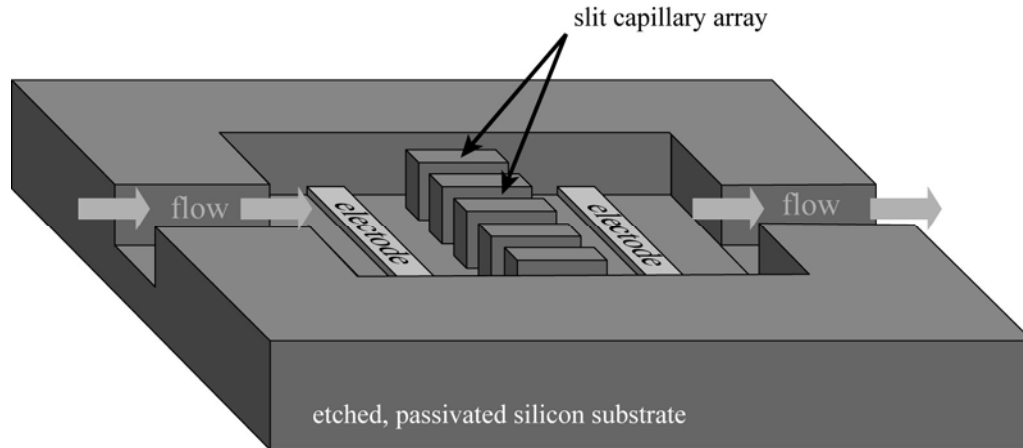


Figure 5.1. Standard silicon electroosmotic micropump design. The EOF element is an array of n narrow, deep trenches, each of which resembles a slit capillary. Platinum wires are inserted on either side of the slit capillary array causes an axial electric field to develop in the slit capillaries. The micropump is sealed with a glass cover (not shown).

The dielectric film on the $2a_1' = 3 \mu\text{m}$ micropumps is 400 nm thick silicon nitride. The film on the $2a_1' = 4 \mu\text{m}$ micropumps is 650 nm thick oxide-on-nitride. The flow cross-sectional area of the slit capillary array is $A_1 = 2na_1^*a_1'b^*b$.

Other salient features of the micropump design include in-plane manifolds connecting the slit capillary arrays to the fluid ports; a glass cover plate; and platinum electrodes. Individual micropumps are released by dicing the bonded glass-silicon wafer stacks at the conclusion of cleanroom processing. The dies are 1.2 cm x 1.3 cm. The electrodes are 0.1 mm diameter platinum wires inserted into the manifolds through channels opening at the edge of the die; after insertion, the electrodes are held in place with epoxy. Although electrodes made of platinum or other materials could be deposited onto internal pump surfaces during the fabrication process, the post-cleanroom method proved to be reliable and effective.

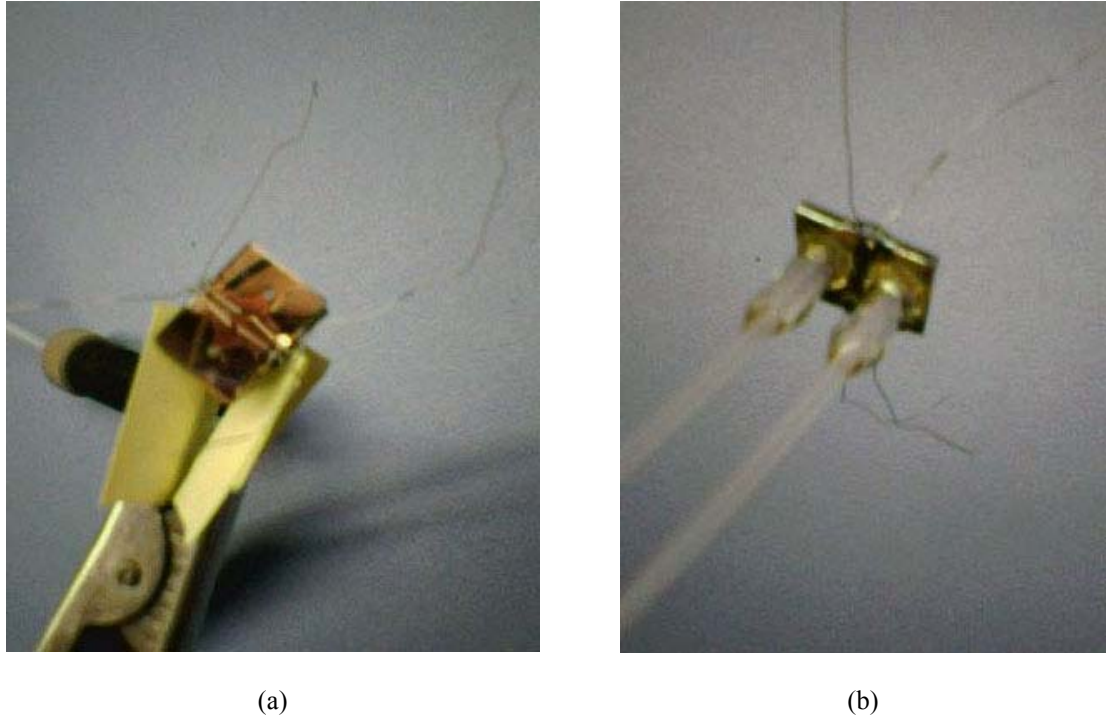


Figure 5.2: Silicon electroosmotic micropump, fixtured for testing. (a) Showing glass cover and platinum electrodes. (b) Showing fluid interconnects.

The working fluid enters and exits through ports on the back side of the die. The fluid interconnects are 0.6 cm long, 1/16" ID glass pipes attached to the dies using Loctite 352 UV cure adhesive. Standard 1/16" OD tubing is easily inserted into the glass interconnects. A fixtured micropump is shown in figure 5.2.

5.2 Experimental methods

Micropump operational testing apparatus

Primary micropump operational figures of merit—flow rate, back pressure, and power consumption—were determined using the experimental setup illustrated in figure 5.3. Applied voltages are produced by a Tektronics PS5010 programable power supply connected to a Burleigh PZ-70 high voltage DC operational amplifier. The maximum voltage for the Burleigh amplifier is 500 V.

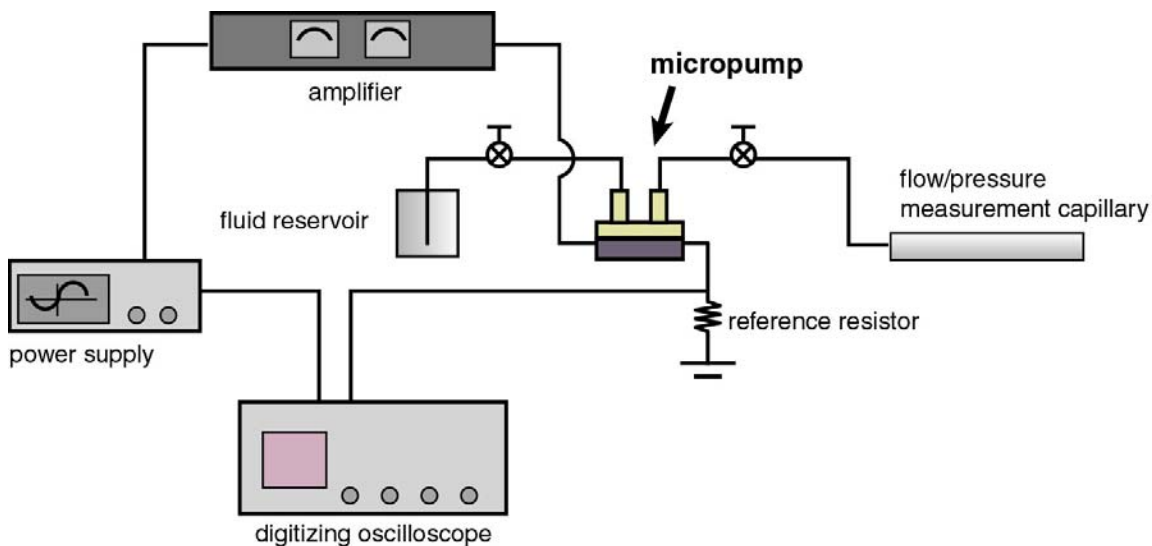


Figure 5.3: Schematic of standard experimental setup used for silicon electroosmotic micropump testing.

Pump current is monitored by measuring the potential drop across a 30 k Ω reference resistor in series with the micropump. All voltages are monitored using an Infiniium four-channel 1.5 GHz digitizing oscilloscope (Agilent Technologies, Inc., Palo Alto, CA).

A 10 cm length of 1/16" OD ethylene-tetrafluoroethylene (ETFE, ID 500 μm +/- 25 μm , Upchurch Scientific,) tubing connects the working fluid reservoir and the micropump inlet port. A second length of tubing is connected to the micropump outlet. Measurements of Q are made by monitoring the position of the flow front in the outlet tube at regular time intervals. To minimize transient effects, Q is generally measured over the course of thirty seconds of pump operation. The margin of error for measurements of Q with only fluidic resistances is approximately 1 $\mu\text{L min}^{-1}$ at flow rates below 5 $\mu\text{L min}^{-1}$ and 10% at higher flow rates. The fluidic resistance per meter of ID 0.20" ETFE tubing for laminar flow and $\mu = 10^{-3}$ N sec m $^{-2}$ is approximately 10 $^{-3}$

$^3 \text{ Pa } (\mu\text{L min}^{-1})^{-1}$. For measurements of flow rate as a function of back pressure, the outlet tube is connected to a closed capillary containing a fixed quantity of room air. Back pressure is calculated from measurements of air column volume changes. Q vs. Δp measurements are associated with a higher margin of error, estimated at 15%, primarily due to uncertainty as to the initial volume of air in the closed column.

As discussed in section 5.4 below, micropumps with integrated pressure-sensing diaphragms were produced for testing fast transient response. The experimental apparatus used in this testing is illustrated in figure 5.4. A Polytec OFV 502 fiber interferometer with OFV-5000 vibrometer controller (Polytec, Inc., Tustin, CA) is used to make noncontact measurements of diaphragm position and velocity. During measurements, the vibrometer head is positioned 10 cm from the moving surface. At this distance, the vibrometer has a minimum spot size of approximately $25 \mu\text{m}$. The OFV-5000 controller outputs a voltage signal in proportion to the measured velocity; it has a maximum frequency of 250 kHz.

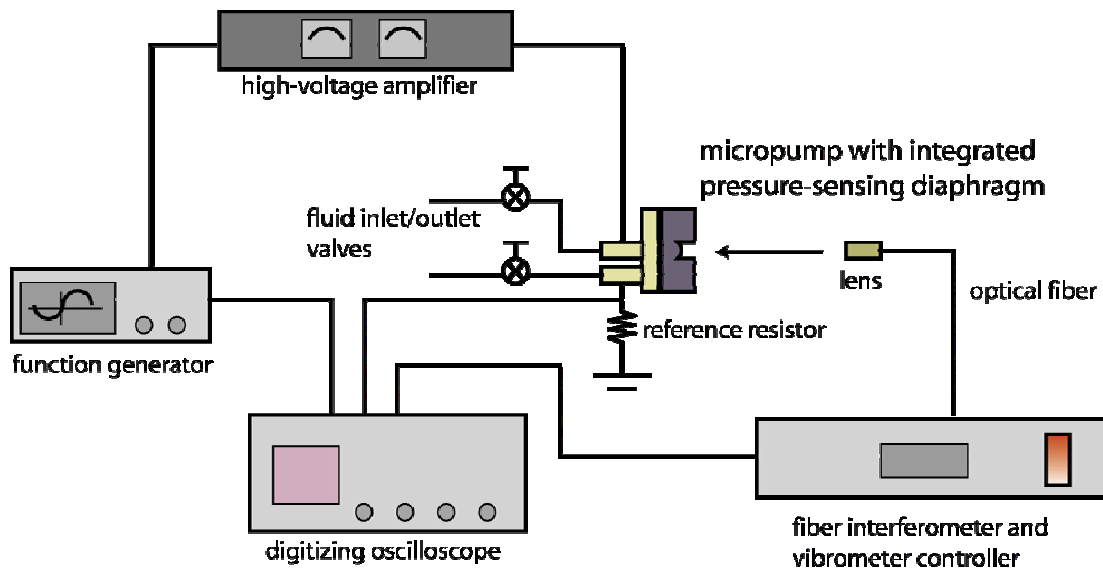
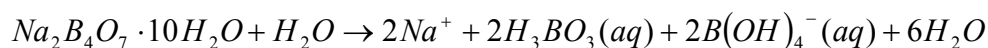


Figure 5.4: Schematic of test apparatus for measuring silicon EO micropump transient response.

Working fluids

Table 5.1 lists the working fluids used in micropump testing. Working fluid conductivity and pH were measured using an Oakton pH/CON 510 meter with a 1.0 cm⁻¹ plastic body conductivity/temperature probe and a single junction epoxy body pH probe. The concentrations of aqueous salt solutions chosen were intended to provide sufficient charge carriers as to avoid excessive charge build-up at electrodes while minimizing bulk currents. Borate buffer solutions were prepared by mixing powdered sodium tetraborate decahydrate (Na₂B₄O₇·10H₂O, Sigma-Aldrich) with purified deionized water (Fisher Scientific):



Boric acid (H₃BO₃) is also reduced in water to yield additional metaborate ion B(OH)₄⁻. The H₃BO₃-B(OH)₄⁻ conjugate acid-base pair minimizes pH changes resulting from acidic and basic products of electrolysis (at the anode and cathode, respectively) [343]. The pH of the borate buffer solutions used is sufficiently low that silicon oxide dissolution is minimal [310].

Table 5.1: Working fluids used for micropump testing

working fluid	pH	conductivity (μS cm ⁻¹)
deionized water	5.4 – 7.0	
borate buffer (Na ₂ B ₄ O ₇ , 0.2 mM*)	9.2	15
borate buffer (Na ₂ B ₄ O ₇ , 0.4 mM*)	9.2	28

**based on Na⁺*

Activity coefficients of sodium tetraborate as a function of molarity were taken from Platford [344]. Prior to all experiments, working fluids were outgassed in a vacuum chamber. The chamber is pumped down, held at vacuum for five minutes, and then vented. This process is then repeated a second time. Working fluids were used within four hours of outgassing.

In general, silicon electroosmotic micropump operational parameters have been observed to fluctuate slightly day to day and over the course of repeated testing during a particular day. Some variation in micropump performance for low buffer concentration experiments may be due to unstable pH conditions. Also, at very low concentrations, ionic impurities from surfaces and gases in contact with the buffer (e.g., carbonic acid) can significantly affect working fluid conductivity. At times, measurements of buffers conductivity several hours or days after preparation revealed significant deviation (+/- 25%) from the nominal values. This was particularly the case for the 0.2 mM buffer. Preliminary testing with borate buffers at concentrations below 0.2 mM produced erratic results, confirming that 0.2 mM is a practical lower limit on borate buffer concentration for silicon electroosmotic micropumps.

5.3 Pressure, flow rate, and power consumption

A model of silicon electroosmotic micropump operation taking into account manifold geometry and other factors has been developed. Experimental pressure and flow rate data for micropumps with a range of geometrical parameters and two different dielectric films (nitride only, oxide-on-nitride) substantiate this model.

Thin EDL silicon electroosmotic micropump model

In section 3.2, the average velocity associated with EOF in a slit capillary was shown to be a function of the slit geometry, the working fluid chemistry, the fluid-solid surface chemistry, the back pressure, and the applied electrical field:

$$\bar{v} = -\frac{a_1^2}{3\mu l_1} \Delta p_1 + \frac{\varepsilon \zeta}{\mu} E_x [1 - G(\alpha, \kappa a_1)] \quad (3.24)$$

As discussed in chapter 4, the limitations of photolithographic feature definition and TMICP etching, along with mechanical integrity considerations, generally preclude fabrication of slit capillary arrays with $a_1 < 0.5 \mu\text{m}$. Accordingly, the thin EDL assumption is appropriate for silicon electroosmotic micropumps with essentially any choice of working fluid. The flow rate-pressure relationship for an array of n slit capillaries is then

$$Q = 2a_1 b^* b n \left[-\frac{a_1^2}{3\mu l_1} \Delta p_1 - \frac{\varepsilon \zeta}{\mu l_1} V_1 \right], \quad (5.1)$$

Axial field variations have been assumed to be negligible, such that the voltage V_1 (introduced in section 4.1) can be substituted for $E_x \times l_1$. The impact of manifold pressure losses Δp_2 (introduced in chapter 4) on Q can be represented by a linear scaling factor, defined as γ :

$$\gamma = \left[1 + \frac{4A_1 a_1^2 l_3}{w b^3 l_1} \right]^{-1} \quad (5.2)$$

In figure 5.2, calculated values of γ as a function of a_1 are plotted for $b = 100 \mu\text{m}$, $50 \mu\text{m}$, and $10 \mu\text{m}$. Typical values have been assumed for the other parameters in eqn 5.2 ($A_2 = 0.25 \times b \times w$; $l_1/l_3 = 0.1$).

Combining eqns 5.1, 5.2, and 4.3, the pressure-flow rate relation for slit capillary array-based silicon electroosmotic micropumps can be expressed as

$$Q = -A_1 \gamma \frac{(a_1^* a_1')^2}{3\mu l_1} \Delta p - \gamma \frac{\varepsilon \zeta}{\mu} \frac{A_2}{A^* l_2} V_2. \quad (5.3)$$

This compact expression is used in the ensuing analysis of silicon electroosmotic micropump operational data.

Minimal-back-pressure data

Data on Q_{\max} , Q vs. P , I , etc. was collected for most of the sixty silicon electroosmotic micropump prototypes fabricated. To rigorously characterize the dependence of pump operation on geometry, dielectric film composition, and operating

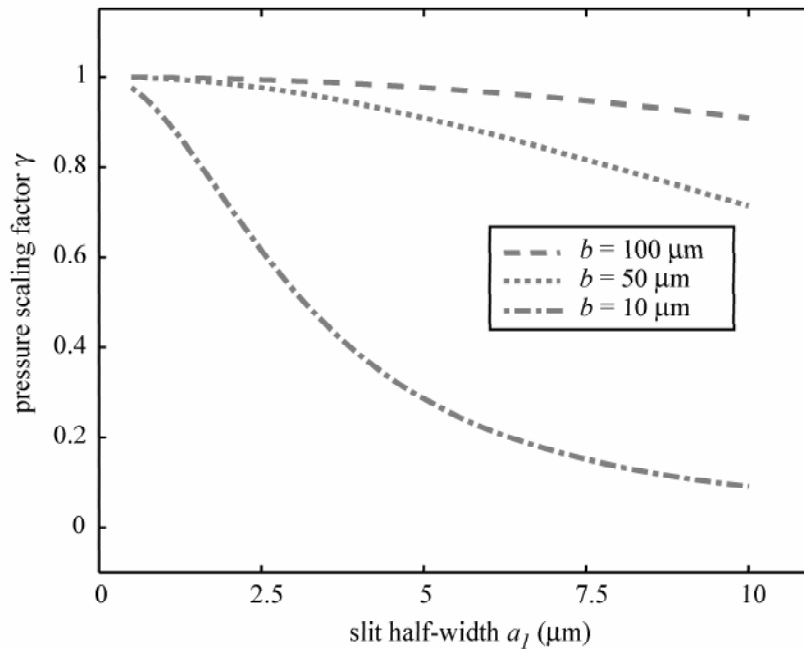


Figure 5.5: Pressure scaling factor γ (calculated using eqn 5.2) as a function of slit half-width a_1 for various manifold depths b . Assumptions: $A_2 = 0.25 \times b \times w$; $l_1/l_3 = 0.1$.

conditions, intensive testing was carried out with sixteen micropumps: three with a nitride-only film and $l_l = 100 \mu\text{m}$, two with an oxide-on-nitride film and $l_l = 100 \mu\text{m}$; three with a nitride-only film and $l_l = 200 \mu\text{m}$, three with an oxide-on-nitride film and $l_l = 200 \mu\text{m}$; three with a nitride-only film and $l_l = 400 \mu\text{m}$; and two with an oxide-on-nitride film and $l_l = 400 \mu\text{m}$. The substrate is (100) p -type silicon (boron-doped, $\rho = 10\text{-}20 \Omega \text{ cm}$). All pumps with the same dielectric film were taken from the same wafer. The micropumps all have $n = 500$ and $s_{cc} = 20 \mu\text{m}$.

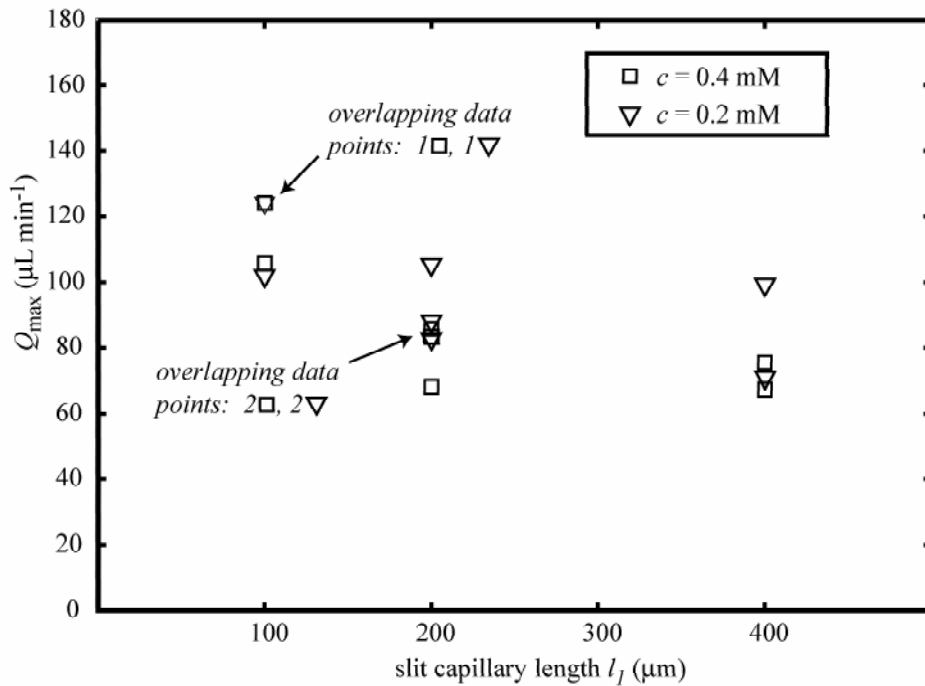


Figure 5.6: Minimal-back-pressure flow rate for seven micropumps with three different slit capillary lengths. Each data point is the mean Q_{\max} value for several tests of a particular micropump with each working fluid (7 pumps total). All micropumps have oxide-on-nitride surfaces. Working fluid is borate buffer ($\text{Na}_2\text{B}_4\text{O}_7$, $\text{pH}=9.2$) with concentrations (based on Na^+) as shown. The operating voltage is $V_2 = 200 \text{ V}$.

Measured values of Q_{max} at $V_2 = 200$ V for the seven oxide-on-nitride micropumps are plotted in figure 5.6. The slit capillary array parameters for these micropumps are $a_l' = 4$ μm , $b = 120$ μm , $a_l^* = 0.6$, $b^* = 0.8$. The nitride and oxide layers thicknesses are $t_n = 450$ nm, $t_{ox} = 250$ nm. The micropumps were tested with 0.2 mM and 0.4 mM borate buffers. Each plotted value is the arithmetic mean of measured Q_{max} values from at least two experiments. From the plotted data, an increase in Q_{max} with decreasing l_l is readily apparent. Eqn 5.3 in the minimum back pressure limit is

$$Q_{max} = -\gamma \frac{\varepsilon \zeta}{\mu} \frac{A^* A_2}{l_2} V_2. \quad (5.4)$$

The parameters ε , ζ , μ , and A_2 are constant for all prototypes. Figure 5.7 was produced by dividing the measured values of Q_{max} by the remaining parameters on the right-hand side of eqn 5.4, which are functions of the pump geometry (although constant for a given l_l). Normalized in this manner, the Q_{max} collapse to single values (for each chemistry) across the range of l_l . These results support the silicon electroosmotic micropump model developed at the beginning of this section.

Also shown in figure 5.7 are normalized Q_{max} data ($V_2 = 200$ V; $c = 0.4$ mM) for the nine micropumps with nitride-only dielectric films. The slit capillary array parameters for these micropumps are $a_l = 1.5$ μm , $b = 120$ μm , $a_l^* = 0.67$, $b^* = 0.7$. The nitride and oxide layers thicknesses are $t_n = 450$ nm, $t_{ox} = 250$ nm. With 0.4 mM buffer,

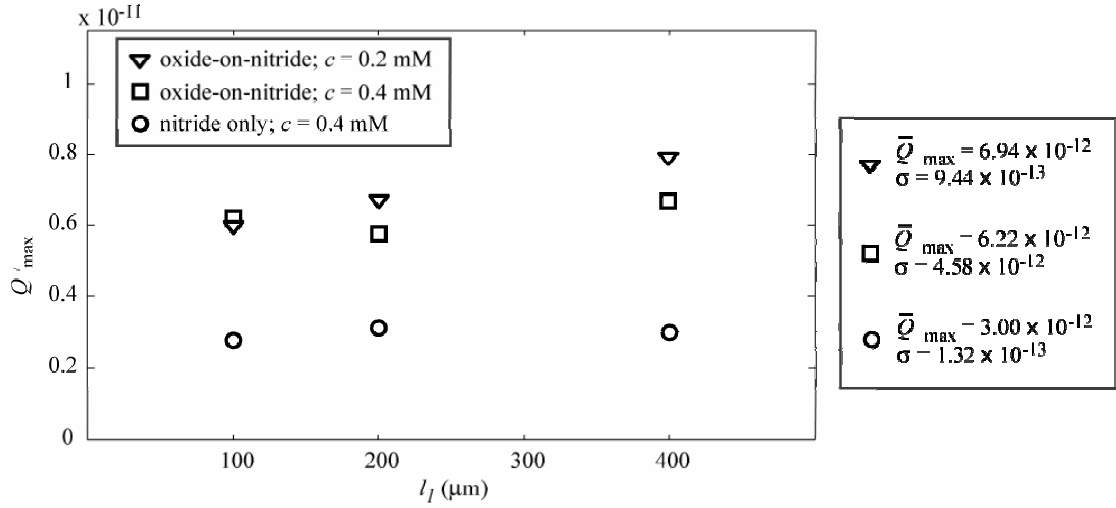


Figure 5.7: Normalized minimal-back-pressure flow rates Q'_{\max} for the oxide-on-nitride flow rate data in figure 5.6 and comparable data (not shown) for nitride-only micropumps. The normalization collapses Q_{\max} to a single value across all l_l for each surface composition/buffer chemistry combination.

the mean Q_{\max} produced by these nitride-only micropumps was $32.0 \mu\text{L min}^{-1}$, $40.9 \mu\text{L min}^{-1}$, and $51.1 \mu\text{L min}^{-1}$ for $l_l = 400 \mu\text{m}$, $200 \mu\text{m}$, and $100 \mu\text{m}$.

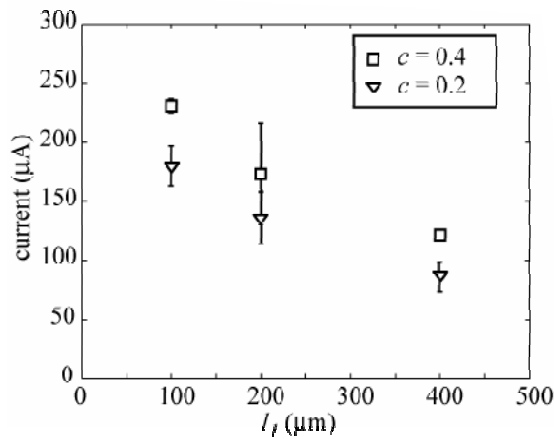


Figure 5.8: Measured current drawn during operation of micropumps with oxide-on-nitride surfaces. Working fluid is borate buffer ($\text{Na}_2\text{B}_4\text{O}_7$, $\text{pH}=9.2$) with concentrations (based on Na^+) as indicated in figure; test conditions as described in text. Error bars show standard deviation.

Current drawn by oxide-on-nitride micropumps during minimal-back-pressure testing is plotted in figure 5.8. Micropump current is discussed in detail in chapter 6.

Zeta potential, buffer chemistry, and surface composition

The zeta potential for a particular fluid-solid interface can be estimated from silicon electroosmotic micropump experimental data for Q_{\max} , Δp_{\max} , or both. Q_{\max} data for silicon electroosmotic micropumps tends to be more repeatable than data for pump operation at finite Δp , probably because pH changes near the electrodes are less pronounced when the fluid in the manifold is turned over frequently by high flow rates. Values of zeta potential for oxide-on-nitride and nitride-only dielectric films with borate buffers were calculated directly from the normalized Q_{\max} data. To obtain ζ , the normalized Q_{\max} were multiplied by $(\mu / \varepsilon \times A_2 \times V_2)$. The calculated values of ζ are shown in table 5.2.

Table 5.2: Calculated zeta potentials for dielectric thin film-coated silicon surfaces and borate buffers

dielectric	buffer concentration c	zeta potential ζ
oxide-on-nitride	0.2 mM	-42 mV
oxide-on-nitride	0.4 mM	-37 mV
nitride only	0.4 mM	-18 mV

The measured ζ are of the same order as reported data for bulk oxides, although reports of higher ζ values for oxides are not uncommon [304]. Electrolyte interfaces with thin nitride have not been studied extensively, so there are fewer points of comparison for the nitride values of ζ . Exposed silicon atoms on the nitride surface are

generally believed to react with water molecules, causing the surface to resemble oxide to some extent. Studies on electrophoresis with nitride beads support this model, as the nitride appears to become negatively charge in neutral-to-basic solutions and positively charged in acidic solutions, but with a lower surface charge density than oxide. A surface-site model for silicon nitride was advanced by Haramé et al. [345]. Bousse et al. reported ζ for silicon nitride of approximately -25 mV with an NaCl-based electrolyte of unspecified composition at pH 9.22 [346]. Additional discussion of the electrochemical properties of silicon nitride films can be found in works on ion-sensing field effect transistors, such as recent publications by Dubbe [347] and Bergveld [348].

Pressure vs. flow rate

Measured pressure-flow rate curves are plotted in figure 5.9 for an oxide-on-nitride micropump with $l_l = 100 \mu\text{m}$ ($c = 0.2 \text{ mM}$). Pressure-flow rate results were repeatable within +/- 30% over the course of repeated testing of this micropump at each V_2 and for tests of a second identical pump. Also plotted are Q vs. Δp curves calculated using the value for zeta potential found previously for the oxide-on-nitride/0.2 mM borate buffer interface ($\zeta = -42 \text{ mV}$). Measured Q vs. Δp is approximately linear as predicted by eqn 5.3. The Q vs. Δp curve shifts up in proportion to V_2 , also as predicted. Deviation of measured data from the predicted Q vs. Δp curves is attributable to measurement uncertainty and to buffer instability. As discussed in section 5.2, buffer instability is exacerbated at low Q , a condition which necessarily arises during Q vs. Δp testing.

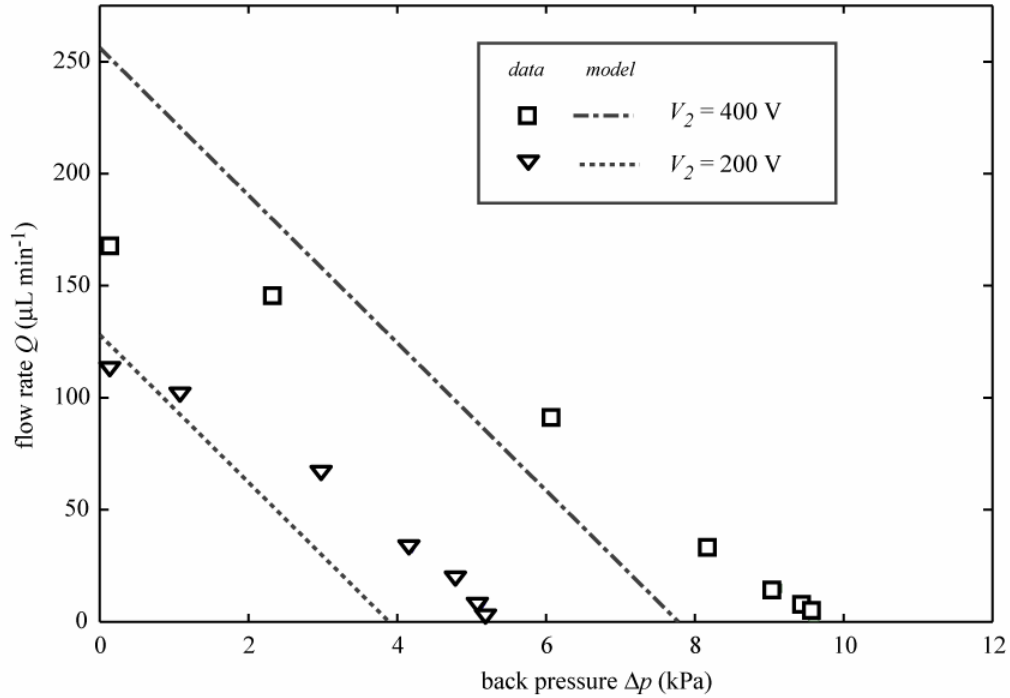


Figure 5.9: Pressure-flow rate data for an oxide-on-nitride micropump with $l_l = 100 \mu\text{m}$. Working fluid is borate buffer ($\text{Na}_2\text{B}_4\text{O}_7$, $\text{pH}=9.2$), concentrations (based on Na-) 0.2 mM; operating voltage as shown.

Measured power consumption for the Q vs. Δp micropump tests was 150 mW for $V_2 = 400$ V and 40 mW for $V_2 = 200$ V. The corresponding thermodynamic efficiency (determined using the midpoint of the measured pressure-flow rate curves per eqn 1.2) is below 0.05%. This relatively low thermodynamic efficiency is attributable in part to substrate currents, discussed in chapter 6, and in part to a_l 's large size relative to λ_D . Practical considerations may preclude significant reduction of a_l in silicon electroosmotic micropumps of this design. Many photolithography-based micromachining techniques are ill-suited to forming nanometer-scale trenches. Moreover, for very small a_l , achieving total flow rates Q high enough for practical applications can be difficult even if \bar{v}_{max} is large. To the extent to which producing trenches with a_l on the order of 100 nm

or less is feasible, the prospect of unfavorable scaling in the finite EDL regime suggests seeking to minimize λ_D . However, the primary tool for decreasing λ_D is increasing the ion density of the solution—which, in turn, increases the ionic current through the pump, lowering thermodynamic efficiency. The tradeoff between Debye length and thermodynamic efficiency is a major consideration for all practical implementations of electroosmotic flow. Further discussion of thermodynamic efficiency in electroosmotic micropumps can be found in Chen and Santiago [63], Yao et al. [296], and Min et al. [349].

5.4 Transient response

Given that electrolysis is an inherently nonequilibrium process, the operation of electroosmotic pumps can be expected to vary with time. An understanding of the transient aspects of silicon electroosmotic micropump operation is vital to assessing the suitability of these devices for particular applications. The time required for a silicon EO micropump to reach a pseudo-steady state (the fast transient response) is limited by factors including polarization currents and the finite rate of momentum diffusion from the EDL to the bulk. Over a much longer timescale, electrolytic gas generation can inhibit EOF by reducing the effective electrode area.

Micropump design for measurement of fast transient response

The standard silicon electroosmotic micropump design was modified as shown in figure 5.10 to permit measurement of fast transient response. In this design, the slit capillary is in an annular, rather than linear, configuration. A diaphragm is located at the center of the annulus. The interior face of the diaphragm is subjected to the

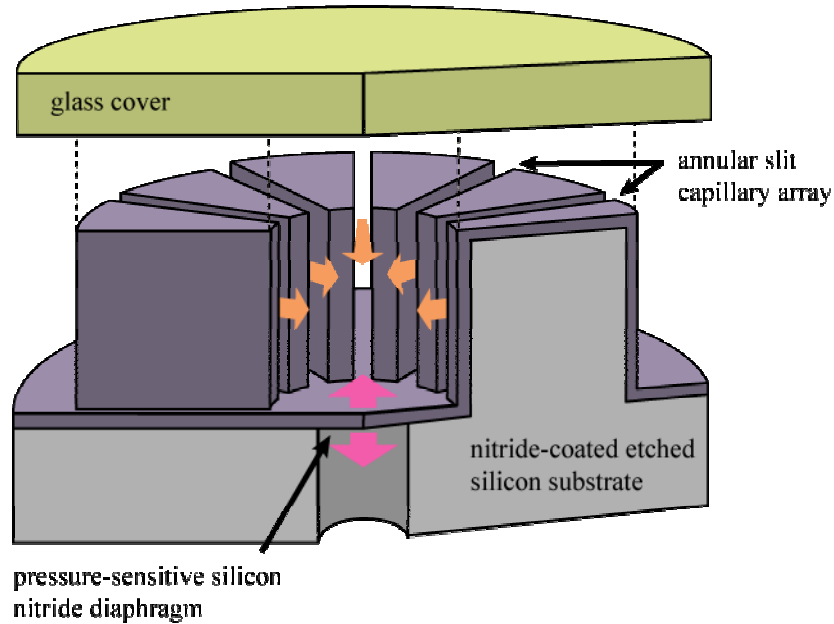


Figure 5.10: Silicon electroosmotic micropump design with an integrated pressure-sensitive diaphragm.

internal pump pressure and the exterior face to the ambient pressure. Measuring the diaphragm deflection therefore provides information about the pressure differential. Silicon nitride was chosen for the diaphragm material because of its favorable mechanical properties and for fabrication convenience (because a silicon nitride layer is deposited as part of the standard silicon electroosmotic micropump fabrication process).

Micropumps were fabricated with pressure-sensing diaphragms with $d_d = 250 \mu\text{m}$ and $d_d = 500 \mu\text{m}$. The standard micropump fabrication process is modified for these devices by including a backside etch immediately after dielectric thin film deposition. The dielectric thin film in these micropumps is silicon nitride with $t_d = 0.65 \mu\text{m}$. For the micropumps tested, $n = 360$, $2a_1' = 4 \mu\text{m}$. The inner annulus radius is 1mm. The devices are fabricated on 1 cm x 2 cm dies. After dicing, a 300 \AA layer of gold with a 50 \AA

chrome adhesion layer is evaporatively deposited on the back side of each die to increase the reflectivity of the silicon nitride diaphragm. For fixturing, fluid ports are drilled in the glass cover. Figure 5.11 shows scanning electron micrographs of an annular slit capillary array and a $d_d = 250 \mu\text{m}$ pressure-sensitive diaphragm.

Film thickness measurements during processing indicate that the silicon nitride diaphragm thickness is spatially uniform to within 5%. Assuming the internal and external pressure on the diaphragm is spatially uniform, the diaphragm model developed in chapter 2 for reciprocating displacement micropumps applies, with maximum deflection, maximum stress, and resonant frequency given by eqns 2.1, 2.2, and 2.3, respectively. Pressure-centerline displacement curves calculated using these relations and the material properties in table 4.1 are shown in figure 5.12. Finite element analysis with ANSYS showed that residual tensile stress in the nitride (estimated at 150 MPa) has

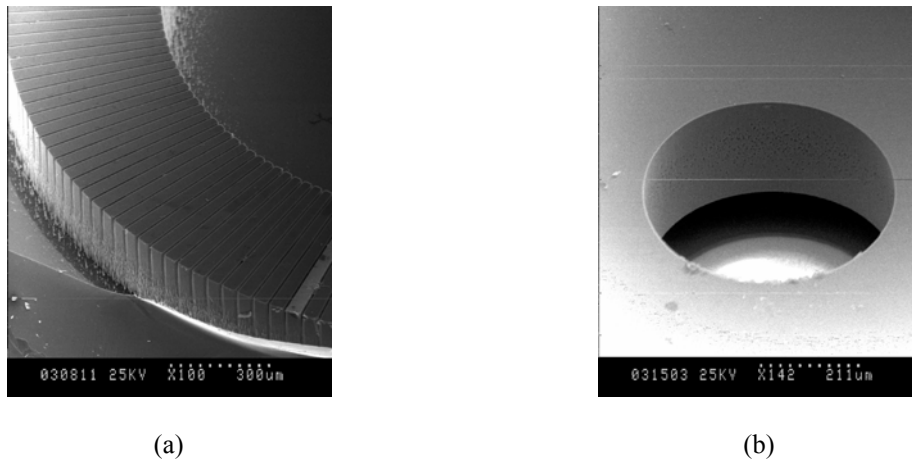


Figure 5.11: (a) Scanning electron micrograph of the top side of the silicon substrate (prior to bonding of the glass cover) showing a portion of etched annular pump structure. (b) SEM showing the released circular diaphragm.

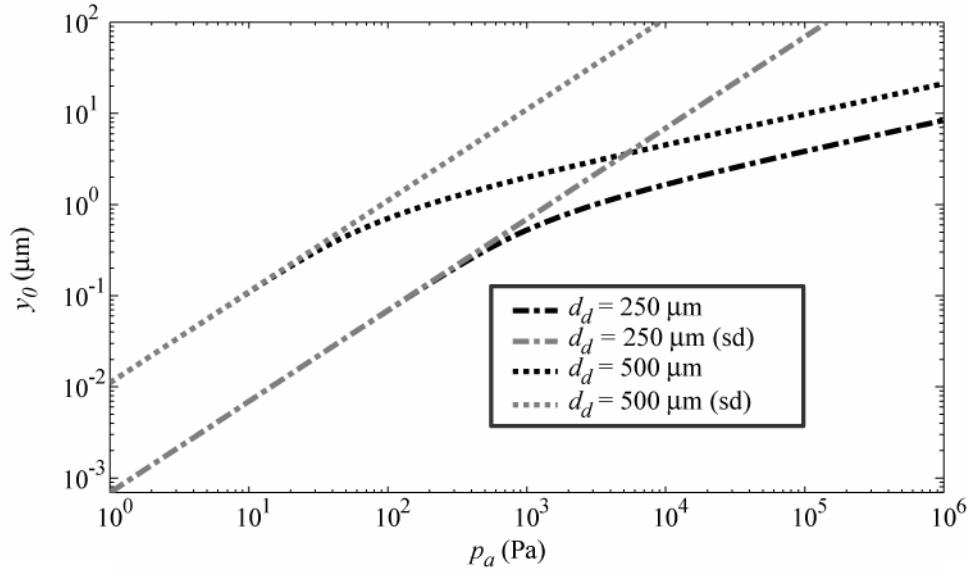


Figure 5.12: Predicted static response of silicon nitride pressure sensing diaphragms. Full-model curves calculated using eqn 2.1; linear small-displacement model curves calculated using a linearized form of eqn 2.1.

a negligible effect on the p_a - y_0 curves. The pressure sensors are linear to within 5% for $p_a < 300$ Pa ($d_d = 250$ μm) and $p_a < 20$ Pa ($d_d = 500$ μm). The first resonance of the 500 μm and 250 μm diaphragms (calculated using eqn 2.3) are 43 kHz and 170 kHz.

Fast transient response data

The measured Q - Δp curve for one of the annular slit capillary array micropump is shown in figure 5.13. The curve is approximately linear, as predicted by eqn 5.3, with $\Delta p_{\text{max}} = 5.5$ kPa. Repeated Q - Δp testing of this micropump yielded comparable results, as did tests of other micropumps with the same geometry. A micropump with a 250 μm diaphragm was then driven by a $V_{p-p} = 400$ V sinusoidal voltage while the diaphragm

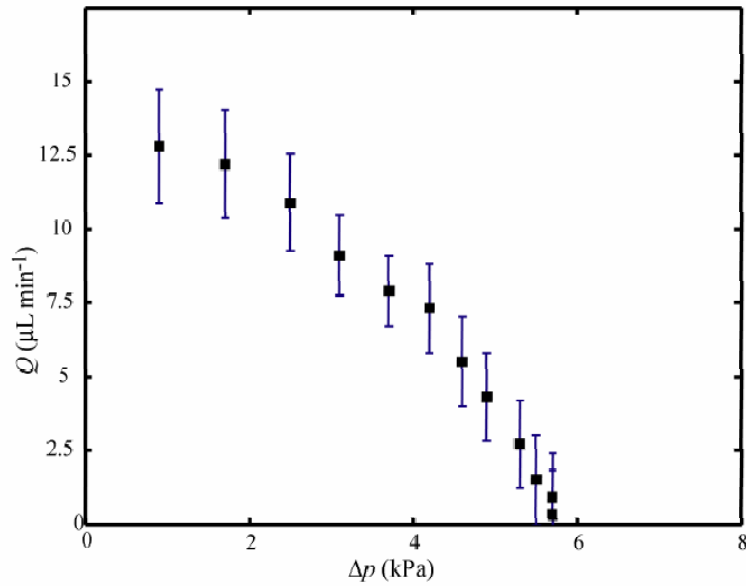


Figure 5.13: Flow rate-back pressure curve (quasistatic operation), $V_2 = 400$ V. Maximum back pressure for this micropump is approximately 5.5 kPa

velocity was measured using the laser velocimetry apparatus described in section 5.2.

The frequency response is shown in figure 5.14.

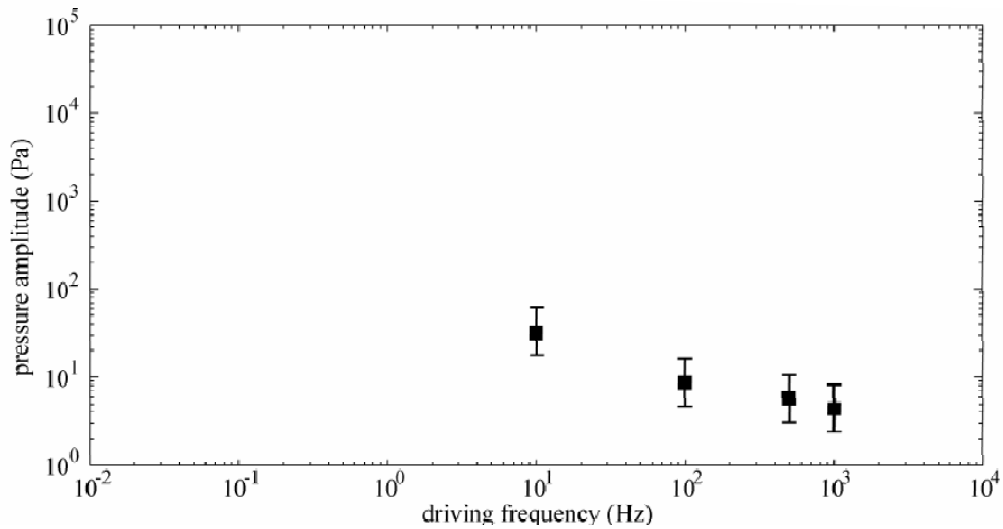


Figure 5.14: Measured diaphragm amplitude (centerline deflection) as a function of driving frequency.

The micropump transient response was also tested by applying step function voltage inputs. Individual measurements were too noisy to resolve a step response, so a large number of curves (obtained by applying a 20% duty cycle square wave) were ensemble averaged. Figure 5.15 shows the step velocity and displacement response for both positively and negatively biased center well electrode, corresponding to negative and positive center well relative pressure.

The fast transient response measurements shown in figures 5.13 and 5.14, as well as the results of other tests under various operating conditions, suggest that silicon electroosmotic micropumps develop Δp_{\max} over a timescale of tens of seconds or longer. One factor limiting the fast transient response of electroosmotic pumps is the finite time required for momentum to diffuse from the double layer into the bulk liquid. Momentum

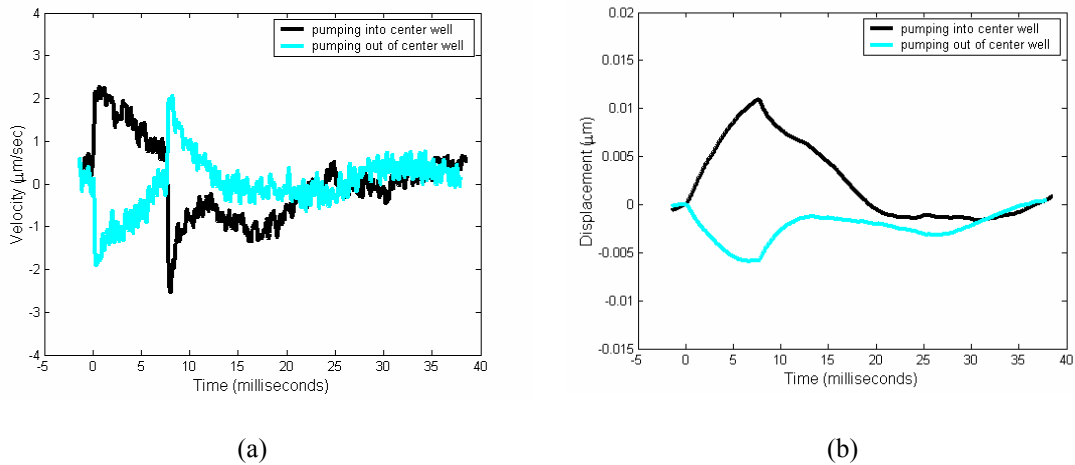


Figure 5.14: Micropump response (500 μm diaphragm) for a 25 Hz, 400 volt square-wave input with a duty cycle of 20%. Data is ensemble averaged over 1,280 cycles. Plots show (a) diaphragm velocity and (b) diaphragm displacement (found by integrating velocity). Curves shown for both positive and negative center electrode bias. Positive velocities and displacements correspond to outward deflection of the membrane.

diffusion-limited transient response can be modeled by analogy to Stokes' second problem, in which a flat surface oscillates within a liquid medium. The momentum equation in this case can be reduced to

$$\frac{\partial u}{\partial t} = -\frac{1}{\rho} \frac{dp}{dx} + \nu \left(\frac{\partial^2 u}{\partial y^2} + \frac{\partial^2 u}{\partial z^2} \right)$$

By changing variables as:

$$u' = u + \int \frac{1}{\rho} \frac{dp}{dx} dt$$

the momentum equation takes the form of the homogeneous heat equation:

$$\frac{\partial u'}{\partial t} = \nu \left(\frac{\partial^2 u'}{\partial y^2} + \frac{\partial^2 u'}{\partial z^2} \right) \quad 5.5$$

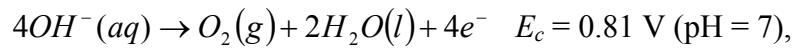
For a step velocity input at the wall $u(0)(t < t_0) = 0$, $u(0)(t > t_0) = U_0$, the solution to eqn 5.5 is [326]

$$\frac{u(y)}{\bar{v}} = 1 - \operatorname{erfc} \left(\frac{y}{2\sqrt{\nu t}} \right)$$

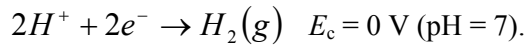
For slit capillary arrays with $a_l < 10 \mu\text{m}$ and typical working fluids, u/\bar{v} at the slit capillary midpoint can be expected approach unity on a timescale of milliseconds. The presence of bubbles is a possible explanation for the relatively slow observed transient response. However, silicon electroosmotic micropumps in routine testing appear to reach a static pressure faster than the transient response data suggests. One or both of two factors unrelated to the EOF—possible misalignment of the vibrometer and higher than expected nitride residual stresses—may have caused the transient response to appear slower than it really is.

Slow transients—EOF retardation due to electrolytic gas generation

Applying an electrical potential difference across a volume of aqueous solution causes gases to be generated at the electrode-liquid interface. The volume of gas generated is generally proportional to current and may be a function of other factors. Ionization of platinum electrodes is assumed to be negligible. In addition to the oxidation and reduction of water, electroosmotic micropump overpotentials can drive secondary electrode reactions, including the oxidation of hydroxyl groups at the anode:



and the reduction of hydronium ions at the cathode:



For both cathode reactions, one mole of hydrogen gas is formed for every two moles of electrons produced. Hydrogen gas generation as a function of current is therefore

$$\dot{V}_{H_2(g)} = \frac{1 \text{ mol } e^- \text{ sec}^{-1}}{F} \cdot \frac{0.5 \text{ mol } H_2}{1 \text{ mol } e^-} \cdot \frac{22.41 \text{ L}}{1 \text{ mol } H_2}.$$

Per 100 μA of current flowing through the pump, therefore, hydrogen gas will be generated at a rate of approximately $0.7 \mu\text{L min}^{-1}$ (ignoring any elevation in pressure within the manifold). In testing of micropumps with $\sim 10 \mu\text{L}$ manifold volumes, flow rate is observed to diminish over a timescale on the order of 100 sec, slightly shorter than would be expected based solely on electrolytic gas generation. Developing pH gradients in the liquid phase and polarization of the solid phase may be contributing factors.

CHAPTER 6: SUBSTRATE CURRENT

As discussed briefly in section 4.1, electrical current in electroosmotic pumps is generally associated with (though not necessarily limited by) the movement of ions from one electrode to the other through the liquid phase. In silicon electroosmotic micropumps, however, the substrate represents a second current path. For many silicon electroosmotic micropumps, liquid phase ionic current models substantially underpredict pump current draw, suggesting that substrate current is significant. A substrate current model, focusing on high-field trap-controlled hole conduction through silicon nitride films, is proposed in this chapter.

Equivalent circuit model

Figure 6.1 illustrates a proposed equivalent circuit model for a silicon electroosmotic micropump with an ungrounded silicon substrate. This circuit is a modified version of the standard Randles electrochemical cell with Warburg impedance [53]. The resistance R_{Q1} accounts for the requirement that, with the silicon substrate ungrounded, all current pass through the interface of each platinum electrode with the working fluid and is carried by ions for a finite distance. Some or all of the cell current may pass exclusively through the liquid phase as ionic current; this current path is represented by the resistance R_{Q2} . Current may pass from the working fluid to the silicon substrate, traversing the silicon-electrolyte interface by means of one or more of the mechanisms outlined in section 3.3. This charge travels through the silicon substrate, encountering the resistance R_{Q3} , and passes back into the working fluid. In the model, $C_{edl,Pt}$ represents the platinum electrode double layer capacitance; $R_{ct,Pt}$ and $Z_{w,Pt}$ the

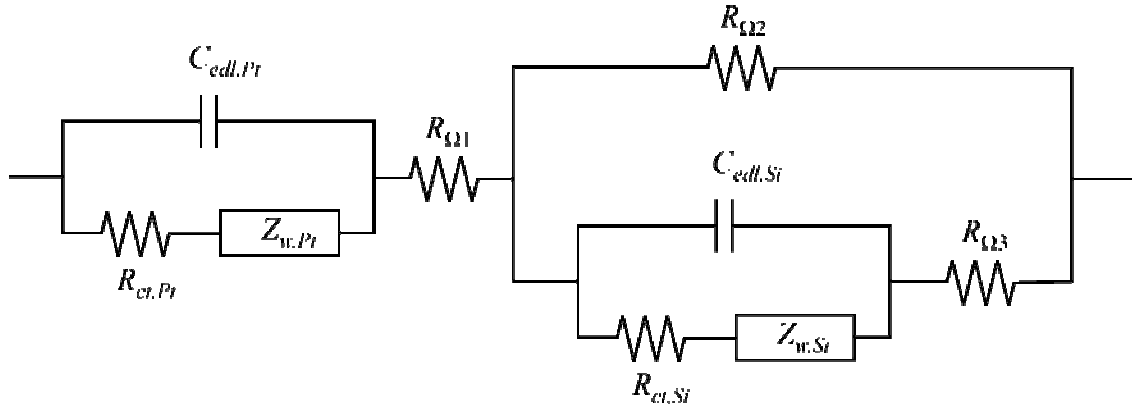


Figure 6.1: Proposed silicon electroosmotic micropump equivalent circuit model.

platinum electrode Faradic impedance; $C_{edl,Si}$ the silicon-electrolyte double layer capacitance; and $R_{ct,Si}$ and $Z_{w,Si}$ the silicon-electrolyte Faradic impedance. Note that this model lumps all silicon-electrolyte charge transfer into a single set of equivalent circuit components. The validity of this approximation is examined later.

For silicon electroosmotic micropumps with nearly one-dimensional fluid phase current paths and a homogenous working fluid, eqn 4.6 can be used to estimate $(R_{\Omega 1} + R_{\Omega 2})$. Double layer concentration gradients are a potential source of inaccuracy in this calculation. In figure 6.2, the error associated with ignoring double layer effects in calculating electromigration current in a slit capillary is plotted as a function a_1 . With a_1 in silicon electroosmotic micropumps almost invariably greater than $1 \mu\text{m}$, this analysis indicates that double layer conductivity gradients have a negligible effect on silicon electroosmotic micropump current.

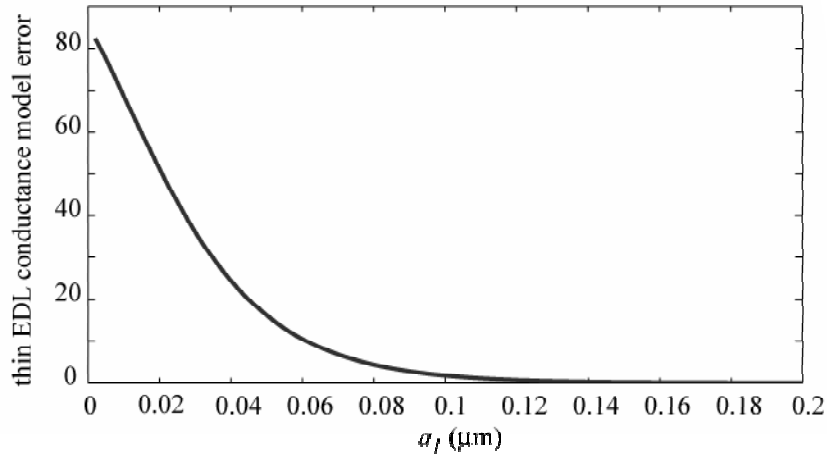


Figure 6.2: Estimated error in slit capillary conductance calculations based on assuming the EDL to be negligibly thin. EDL ionic concentration calculated using eqn 3.11; symmetric electrolyte with $v_i = 5.4 \times 10^{-13} \text{ mol N}^{-1} \text{ m s}^{-1}$ assumed.

Figure 6.3 was produced by using eqn 4.6 to estimate $(R_{Q1} + R_{Q2})$ and subtracting the estimated ionic current from the measured current values during the Q_{max} testing of 16 micropumps described in section 5.3. Measured current consistently exceeded current predicted using eqn 4.6.

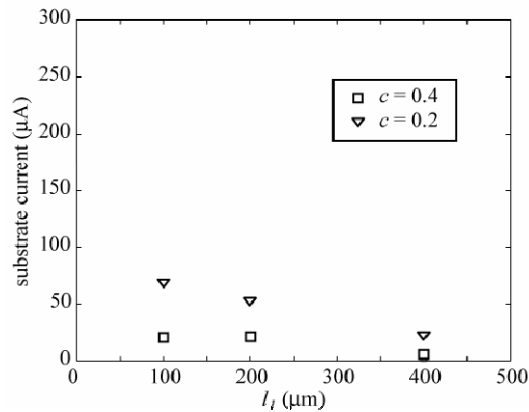


Figure 6.3: Current unaccounted for by liquid phase ionic conduction during operation of micropumps with oxide-on-nitride surfaces. Working fluid is borate buffer ($\text{Na}_2\text{B}_4\text{O}_7$, $\text{pH}=9.2$) with concentrations (based on Na^+) as indicated in figure; test conditions as described in text.

The magnitude of surplus current appears to be inversely related to electrolyte concentration. While this apparent inverse relationship may be spurious, the absence of a proportional relationship to c suggests that the extra current is flowing through the substrate. The tendency of the extra current to increase with decreasing l_l is consistent with the substrate current explanation, as smaller l_l is associated with higher electric fields within the slit capillary array structure.

Figure 6.4 shows measured pump currents after application of a step voltage input to the electrodes of a particular micropump. Individual current measurements tend to be noisy, so a large number of cycles were averaged (1,280 in this case). An initial current spike after the voltage is applied is clearly visible. A corresponding dip occurs immediately after the bias is removed. After the initial current spike, the current can be seen to decay slightly on a timescale of tens of milliseconds.

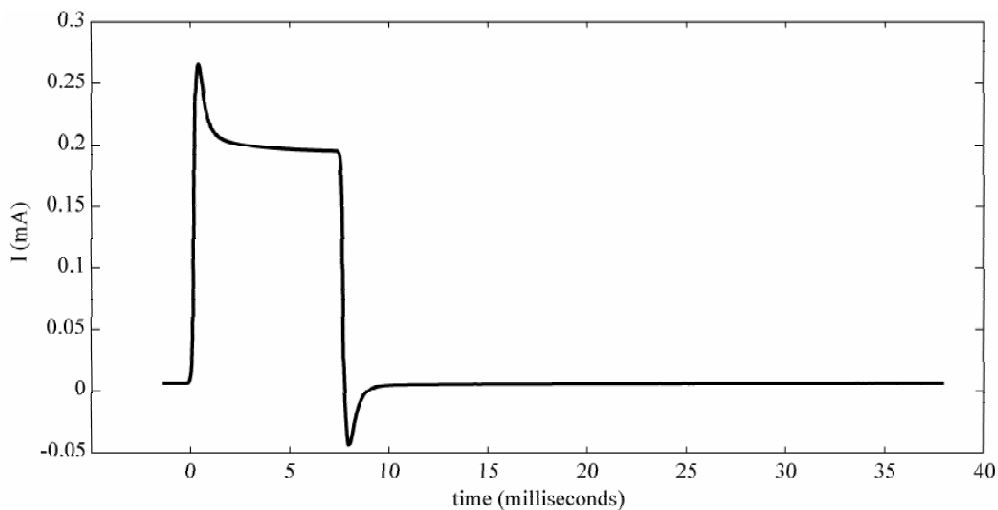


Figure 6.4: Micropump current with step voltage bias input.

As further means of studying substrate current in silicon electroosmotic micropumps, the slit capillary array, electrodes, and manifolds of a prototype micropump were imaged during operation through the glass cover using a CCD camera and an optical microscope. Six images spanning 30 seconds of micropump operation are shown in figure 6.5. The visualization shows that hydrogen gas evolution is taking place at the cathodic substrate (the portion near the platinum anode). No gas generation is visible at the substrate which is at anodic potential, which is consistent with a hypothesis of solid phase oxide formation.

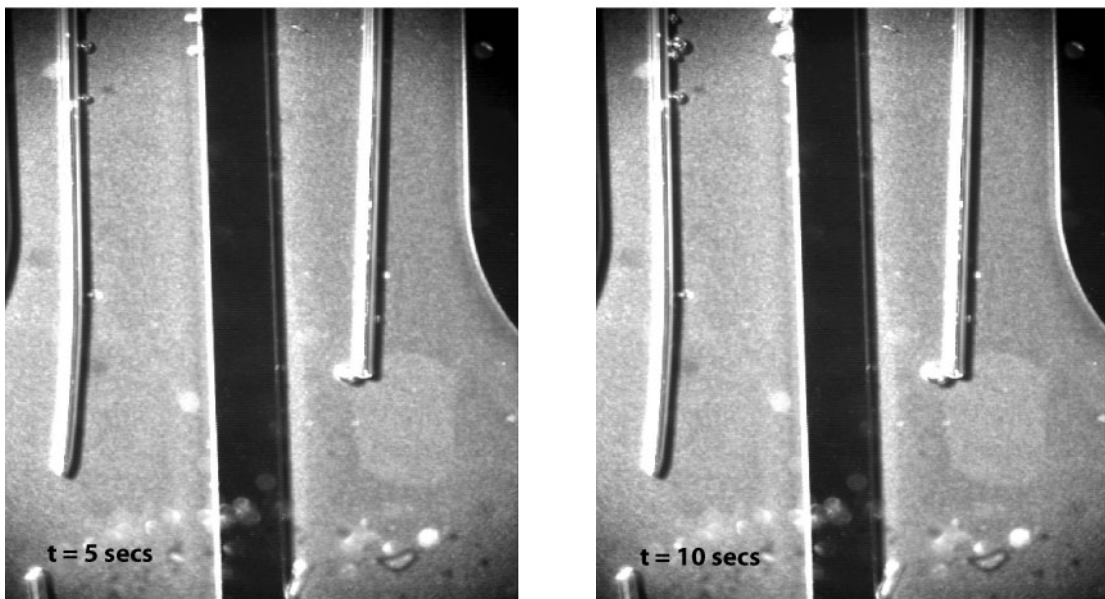


Figure 6.5 (continued on next page)

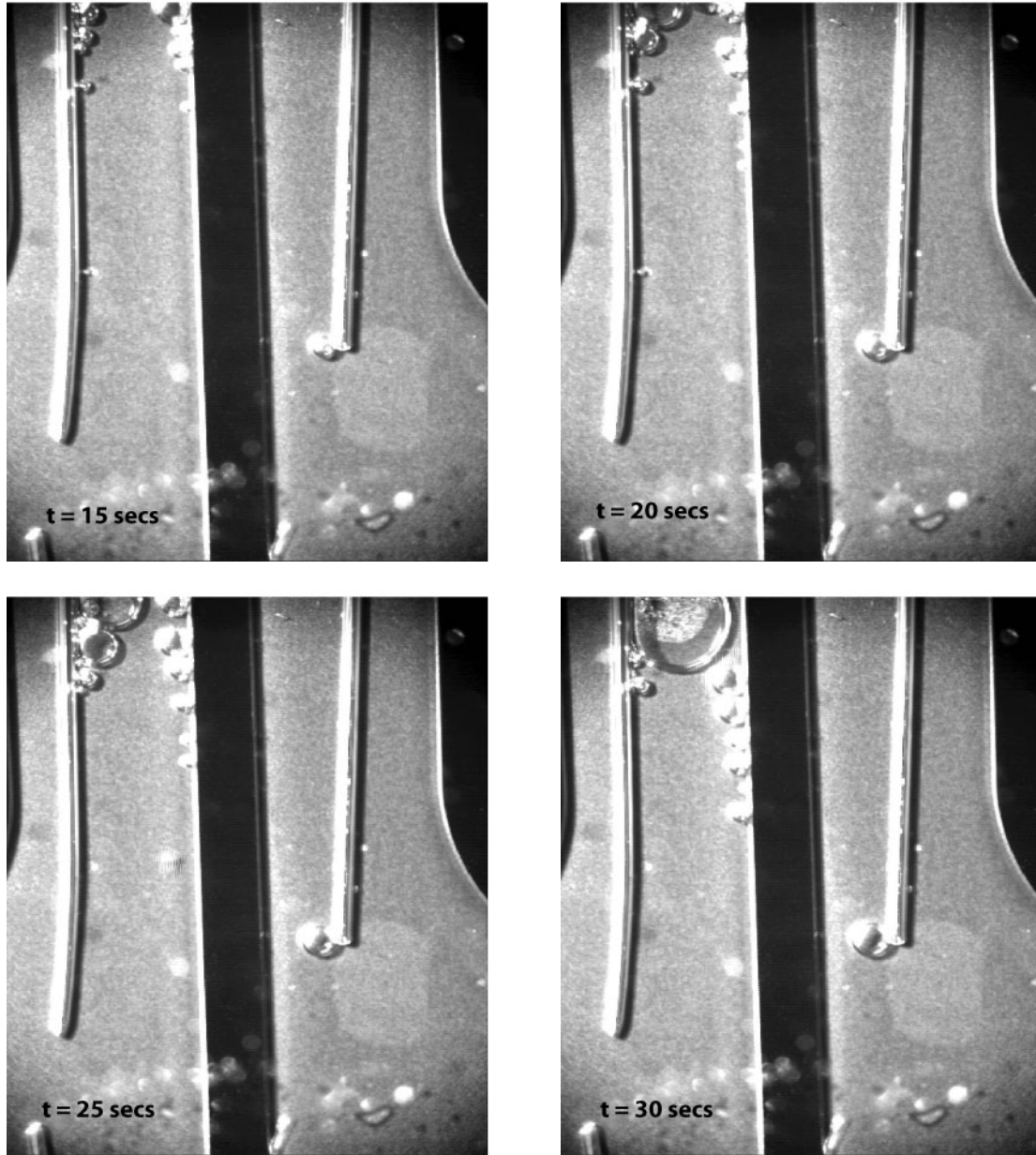


Figure 6.5: Visualization of micropump operation. Direction of flow is left to right.

Discussion of substrate current mechanisms

Based on current measurements during micropump testing and observed bubble formation, substrate current in silicon electroosmotic micropumps with oxide-on-nitride dielectric films is proposed to occur through the mechanisms illustrated in figure 6.6.

Where the silicon substrate is at cathodic potential, water is reduced within the oxide layer (penetrating interstitially and/or through pinholes), with the reduction current limited by Poole-Frenkel conduction through the nitride layer. Holes are almost certainly the dominant carriers in the nitride, having been shown to carrier three orders of magnitude more current than electrons at room temperature [350]. Where the silicon is at anodic potential, anodic oxide formation occurs at the oxide-nitride interface, supported again by conduction through the nitride layer. Both the lack of bubble formation at the anodic silicon (figure 6.5) and the decay in current over time (figure 6.4) are consistent with oxide formation at the anodic silicon. The current spike in figure 6.4 could be associated with polarization currents in either the fluid or solid phases, or both.

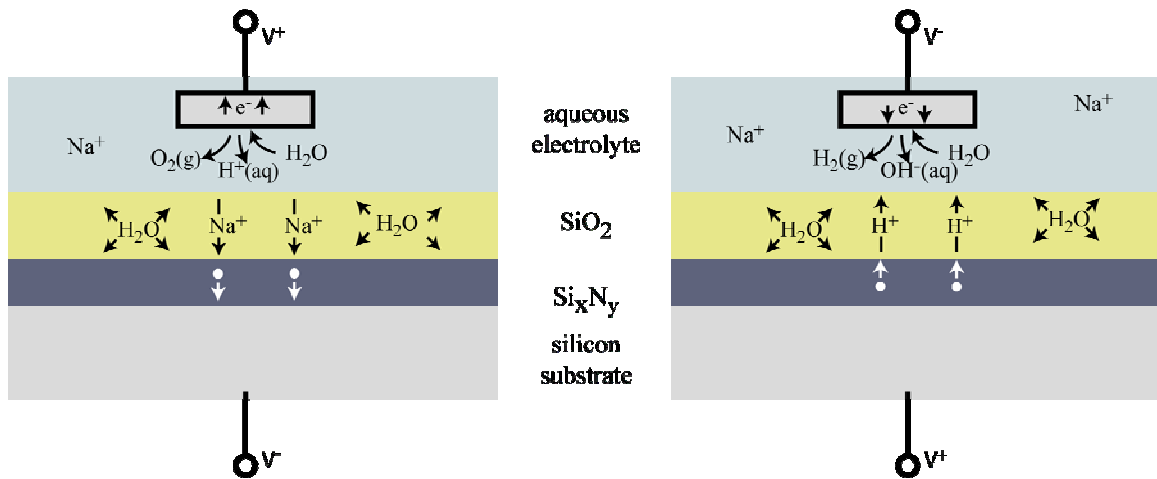


Figure 6.6: Proposed conduction models for an electrolyte-oxide-nitride-silicon system. With the silicon at cathodic potential (left), holes are the dominant carrier in the nitride and are injected from the oxide/electrolyte. Sodium ions tend to migrate through the oxide toward the oxide-nitride interface, where they may sediment. With the silicon at anodic potential (right), holes are injected into the nitride from the silicon and migrate toward the oxide interface, where they recombine with electrons released during oxidation processes. Such processes could include anodic oxide (oxynitride) formation on the surface of the silicon-rich nitride.

Although the presence of an oxide layer has been shown to affect ζ , because of the presence of alkali ions such as Na^+ in the electrolyte, the oxide is expected to have a negligible effect on substrate current. In addition to ionic currents in the oxide, water easily penetrates the oxide through micropores or by interstitial diffusion ($D = 10^{-13} \text{ cm}^2 \text{ sec}^{-1}$ or higher in the presence of Na^+) [322]. Measured currents in prototype micropumps with oxide-only dielectric films exceed predictions based on fluid conduction models by over an order of magnitude, confirming that substantial currents tend to flow through oxide films in contact an aqueous electrolyte.

As discussed in section 3.3, charge can be injected into a nitride layer by either Fowler-Nordheim or thermionic emission; the injection process is not rate-limiting [351]. With the mobility of ions in silicon nitride generally low [338, 352], electrons and holes are the primary charge carriers in nitride films. Electrical conduction is largely controlled by traps located within the nitride forbidden energy band. The electric field dependence of silicon nitride thin film conduction was shown by Sze to be described by the superposition of three components:

$$j_{N1} = C_1 E \exp\left[-\frac{q}{kT} \left(\varphi_{N1} - \sqrt{\frac{qE}{\pi \epsilon_0 \epsilon_r}} \right)\right]$$

$$j_{N2} = C_2 E^2 \exp\left(-\frac{E_2}{E}\right)$$

$$j_{N3} = C_3 E \exp\left(-\frac{q\varphi_{N3}}{kT}\right)$$

Sze attributed j_{n1} to Poole-Frenkel conduction. Recent studies have suggested that multiphonon-assisted tunneling from deep traps in the nitride is a more plausible mechanism for the j_{n1} component of silicon nitride thin film conduction than the Poole-

Frenkel effect [353]. Regardless of the precise nature of this component in nitride films, it is reasonably well described assuming values of 0.1 for C_t , the trap density parameter; 1.3 V for ϕ_{NI} , a barrier height; and 5.5 for ϵ_d , the dynamic dielectric constant. The other components of nitride conduction are field ionization (j_{n2}) and impurity-based hopping conduction (j_{n3}) [351].

The effect on an insulated semiconducting substrate of an electrolyte potential gradient can be approximated by a series of electrodes and a voltage divider network, illustrated in figure 6.7. For an n -type semiconductor, electrons accumulate in the portion of the substrate immediately below the most positively biased electrode; immediately below the most negatively biased electrode, the substrate is depleted of majority carriers and (for a bias greater than a few volts) becomes inverted. In an electrolytic cell with insulated silicon walls, comparable in-plane substrate polarization forces portions of the insulating layer to sustain potential drops equal to a significant fraction of the total bias voltage.

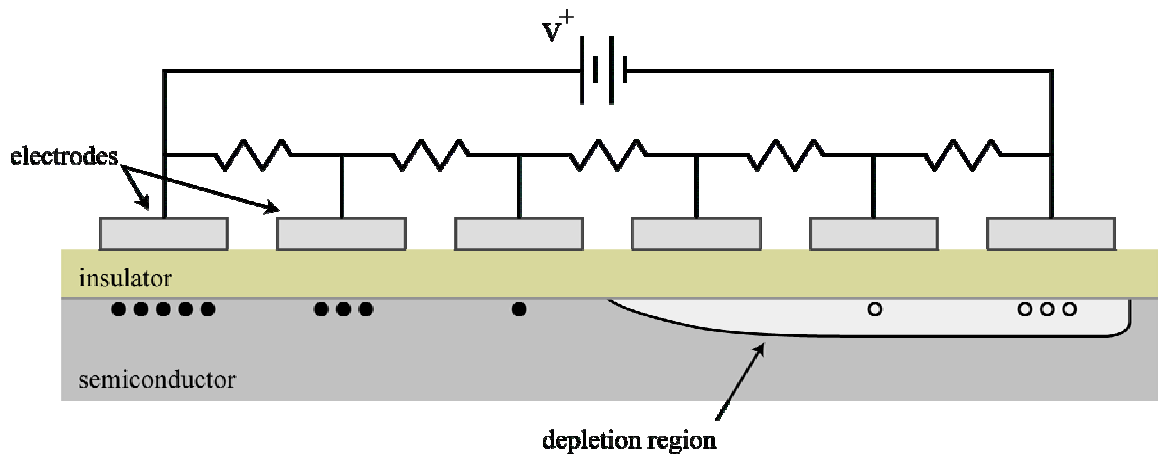


Figure 6.7: Schematic of accumulation, depletion, and inversion regions in an insulated n -type semiconducting substrate subjected to a linear electrical potential gradient (represented by a voltage divider). Filled and open circles represent electrons and holes, respectively. Similar effects can be expected to occur in electrolytic cells with thin-film-insulated silicon walls.

Assuming the silicon to be an equipotential surface, therefore, for a silicon electroosmotic with a 450 μm thick nitride film, the upper limit on the electric field for $V_2 = 200$ is approximately 4 MV cm^{-1} . As shown in figure 6.8, conduction in nitride films at field strengths greater than approximately $3\text{-}4 \text{ MV cm}^{-1}$ is dominated by Poole-Frenkel conduction (or multiphonon tunneling processes with similar scaling). Based on the first-order estimate of field strength in the pump nitride, only a slight increase in nitride conductivity is expected. Localized field enhancing effects in the nitride may explain the apparent early onset of the high-field nitride conduction regime. The slit capillary arrays contain numerous corner regions—totaling over 10 cm in length for a typical device—where field lines converge and where the nitride film may be slightly nonconformal. The nitride in these regions may also be at a different stress state than

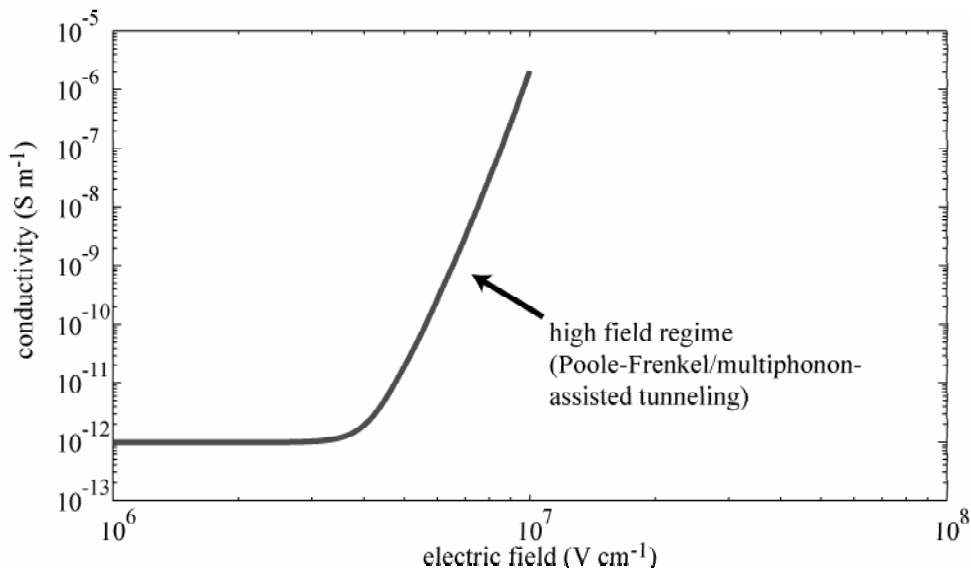


Figure 6.8: Field dependence of conduction in silicon nitride thin films, believed to limit substrate conduction in silicon electroosmotic micropumps. The high-field regime is associated with either Poole-Frenkel conduction or multiphonon-assisted tunneling.

elsewhere; spatial variations in nitride film stress have recently been suggested to influence Poole-Frenkel conduction [354].

Substrate current is deleterious in two respects. It increases total cell current, decreasing electroosmotic pump thermodynamic efficiency. It also diminishes the field strength in the fluid channel—where the field is needed to induce EOF—by causing the electrolyte regions outside the channel to account for a greater fraction of the total cell resistance. Further substrate current mitigation is a major focus of ongoing silicon electroosmotic micropump research.

CHAPTER 7: SILICON ELECTROOSMOTIC MICROPUMPS IN PRACTICE

With silicon electroosmotic micropumps operation well modeled, a cogent analysis is possible of the prospects for using these pumps in real-world applications. Comparisons to other reported micropumps are one means of evaluating the usefulness of these new devices. The pump capabilities are also evaluated in the context of two particular applications discussed in chapter 1, microelectronics cooling and biological fluids analysis.

7.1 Comparison with other reported micropumps

The data in the preceding chapters on pressure, flow rate, power consumption, etc. for silicon electroosmotic micropumps can be compared directly to the data for reported micropumps in appendix A. Comparing the silicon electroosmotic micropumps to subsets of reported micropumps in terms of specific characteristics shows the strengths and weaknesses of these new pumps more clearly, taking into account factors such as package size and operating requirements.

Comparison with other dynamic micropumps

As with reciprocating displacement micropumps, various factors other than pressure and flow rate performance are relevant to the selection of a dynamic micropump. The magnitude of the electrical potential difference required to operate these field-driven micropumps is one important factor which can be compared directly and which varies widely. In figure 7.1, Q_{\max} is plotted as a function of operating voltage for reported field-driven dynamic micropumps. Electroosmotic pumps as a group produce higher flow rates at lower operating voltages than do EHD or MHD pumps. Silicon electroosmotic micropumps produce substantially lower flow rates than frit pumps.

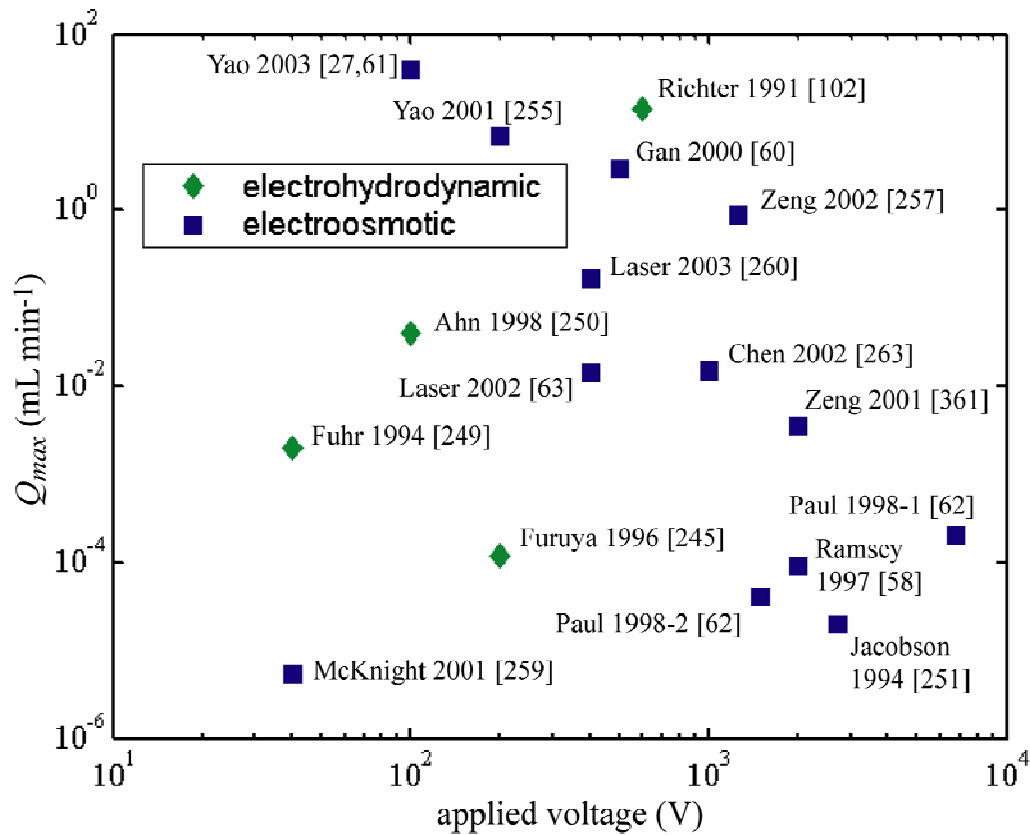


Figure 7.1: Q_{max} for reported electrohydrodynamic and electroosmotic micropumps, plotted as a function of operating voltage V.

Working fluid properties are also relevant in the selection of a dynamic micropump. Electroosmotic pumps can handle a wide range of working fluids, including many that are widely used in chemical and biological analysis such as deionized water and chemical buffers. In contrast, most EHD pumps require dielectric fluids. Electrolytic gas generation which occurs at the electrodes of many field-driven dynamic micropumps is a concern for some applications. Lastly, current passing through the working fluid used in electrohydrodynamic, electroosmotic, and magnetohydrodynamic pumps may, in some cases, cause significant Joule heating.

7.2 Silicon electroosmotic micropumps for integrated circuit thermal management

Continued performance improvements for many integrated circuit devices may require new cooling solutions incorporating liquid or two-phase forced convection. As discussed above, miniature sintered glass frit electroosmotic pumps have been developed to provide two-phase convective cooling for high-power-density integrated circuits [61]. These pumps generate over one atmosphere of pressure at 100 V and can pump liquids at flow rates as high as 33 mL min^{-1} .

While silicon electroosmotic micropumps are unlikely to be suitable for producing the very high flow rates needed to cool entire chips, they may be suitable for certain IC thermal management applications. One such application is reducing the temperature of small, high-power-density regions of microchips through single-phase forced-convective cooling. Systems-on-a-chip (SoC) and high-performance ICs that contain a mix of high- and low-power devices are prone to developing hot spots during operation. Even with chip-scale heat sinking adequate for a microchip's overall power dissipation, the thermal resistance associated with solid-state conduction to the heat sink may cause hot spots to reach intolerably high temperatures. This is particularly true for chips with multiple active layers in a 3-D configuration [355]. A single-phase forced-convection cooling system like the one illustrated in figure 7.3(a) is a possible solution. The system incorporates an integrated silicon electroosmotic micropump, avoiding the need for fluidic connections to the chip. Similar systems incorporating arrays of feedback-controlled silicon electroosmotic micropumps could provide on-demand forced convective cooling of spatially- and temporally-varying hot spots. Integrating the

micropumps in this manner is feasible because simply replacing the glass cover with silicon renders the micropump fabrication process CMOS-compatible process.

Zhang et al. showed that a flow rate of $100 \mu\text{L min}^{-1}$ is sufficient for cooling some hot spots [6]. A simple model of a single-phase microchannel heat sink allows estimation of micropump performance requirements for hot spot cooling generally [356]. This

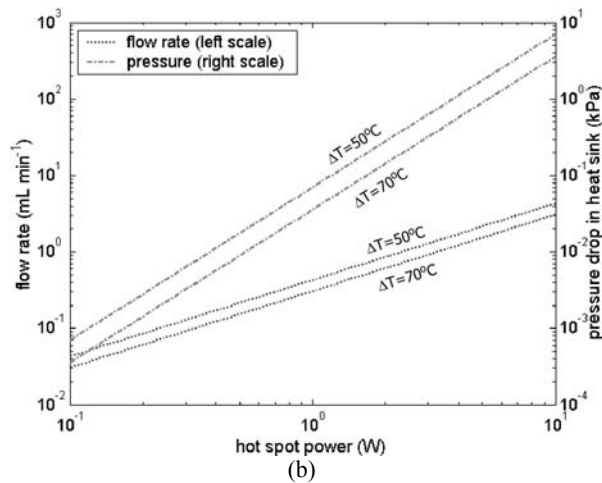
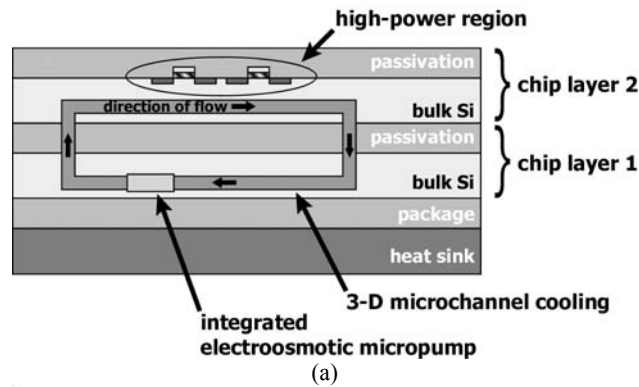


Figure 7.3. (a) Thermal management system for ICs based on integrated electroosmotic micropumps and microchannels. Single-phase, micropump-driven forced-convective cooling supplements heat conduction from high-power-density regions. In a two-layer 3-D IC, forced convection cools regions on the layer furthest from the heat sink. (b) Estimated flow rate required for single-phase forced-convective cooling of a 1 mm x 1 mm hot spot with a local microchannel heat sink. The pressure drop in the microchannel heat sink is also shown.

model assumes a very small thermal resistance in the solid (Biot number much less than one). In figure 7.3(b), the calculated flow rate required for single-phase forced-convective cooling of a 1 mm x 1 mm hot spot is plotted as a function of hot spot power. The corresponding pressure drop (across microchannel heat sink) is also plotted. These estimates were made using the properties of water at 30°C and a channel-to-chip cross-sectional area ratio of 0.25. The local microchannel heat sink is assumed to have been designed to minimize required pumping power. This analysis indicates that, for an allowed fluid temperature rise of 70°C, forced convective cooling of a 2 W hot spot requires a flow rate of approximately 620 $\mu\text{L min}^{-1}$. The corresponding pressure drop across the microchannel heat sink is approximately 0.14 kPa. Pressure losses in the rest of the system are estimated at 1-10 kPa. Silicon electroosmotic micropumps for hot spot cooling, therefore, must generate flow rates between one and two orders of magnitude greater than early prototypes while maintaining pressure performance.

7.3 Automating biological fluids analysis

Analysis of blood and other body fluids is an important component of the practice of modern medicine. Body fluid assays usually involve, at a minimum, either interaction between the sample and another phase (e.g. the chemical reaction of ketones in urine with a sodium nitroprusside-impregnated dipstick) or manipulating the sample (e.g. passing blood through a channel to determine its coagulatory properties). The outcome of some assays, such as the coagulation (prothrombin time) measurement, is determined by monitoring assay kinetics. For other assays, such as the urine ketone measurement, the outcome is determined after an endpoint is reached (e.g. the passage of a finite period of time). Silicon electroosmotic micropumps can be used in both types of assays.

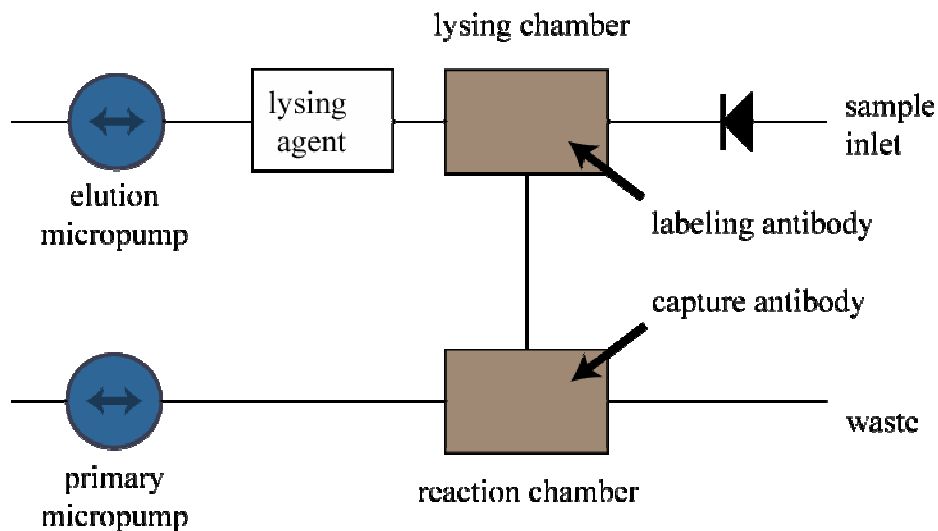


Figure 7.4: Schematic of sandwich assay automation using silicon electroosmotic micropumps.

Figure 7.4 shows a schematic of simple assay automated using two silicon electroosmotic micropumps. This is a generic immunoassay involving three primary steps: lysing the sample (to release proteins contained within cells and microorganisms); tagging proteins of interest (referred to as antigens) with labeled antibodies; and capturing the antibody-tagged proteins. The last two steps are usually accomplished by means of a so-called sandwich assay.

Lysing and tagging are combined with introducing the sample into the system through the use of a porous medium impregnated with lysate and labeled antibodies. After the sample is introduced, then, the lysate is pumped out of the sample pad. The concentration of labeled antigen in the released lysate is a function of the quantity of antigen initially present, the properties of the sample pad, the size of the antigen molecules, the composition of the lysate (size and quantity of molecules other than antigen), and the flow rate. The lysate is pumped into a reaction chamber, where the labeled antigen is captured by solid-phase antibodies. The antibodies are assumed to be

affixed to a planar surface. The capture rate depends on the concentration of antigen in the lysate; the surface density of the capture antibodies; the diffusivity of the antigen; and the reaction chamber geometry.

The most demanding aspect of this assay from the standpoint of micropump automation is pumping the lysate out of the sample pad. The fluidic resistance of a representative 3 mm x 15 mm sample pad is shown in figure 7.5. Existing silicon electroosmotic micropumps produce pressures nearly adequate for pumping analyte out of such a sample pad at $25 \mu\text{L min}^{-1}$.

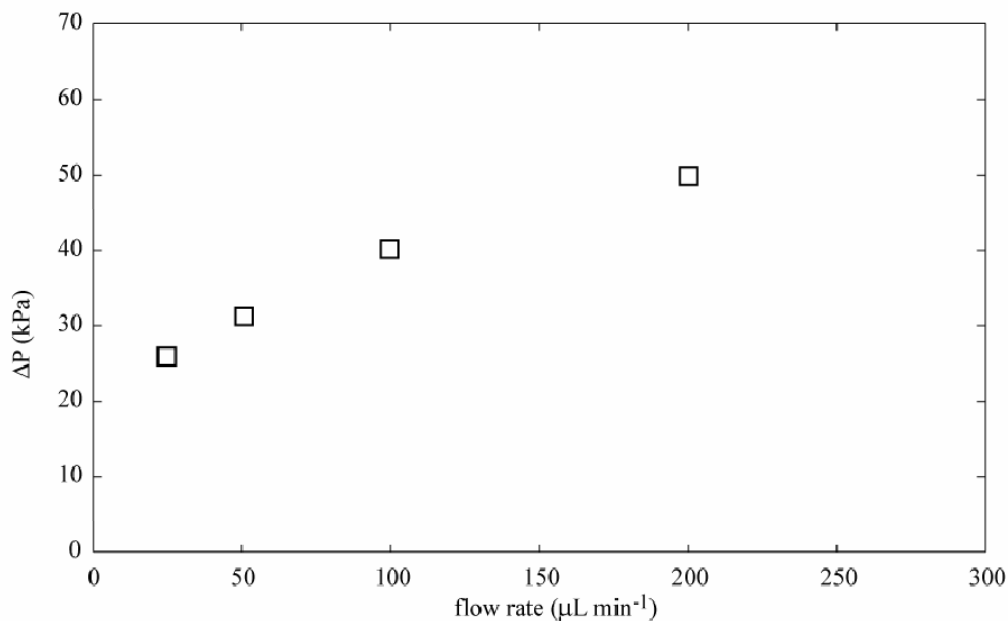


Figure 7.5: Measured pressure vs. flow rate for removing a lysed and labeled biological fluid sample from a porous sample pad.

CHAPTER 8: CONCLUSIONS

This dissertation describes a novel approach to addressing some of the challenges associated with active fluid transport at the microscale. Fundamental to this approach is the combination of the phenomenon of electroosmotic flow with silicon micromachining.

Among the major contributions from this work are:

- A comprehensive model of silicon electroosmotic micropump operation has been developed and experimentally validated, with data collected from over sixty electroosmotic micropump prototypes.
- Electroosmotic flow has been studied with new combinations of materials and geometries. Values for the zeta potential of silicon nitride and oxide-on-nitride films have been determined experimentally. Established theories of electroosmotic flow and electric double layers have been affirmed.
- Silicon fabrication techniques, particularly with relation to dielectric thin film deposition in deep trenches, have been characterized in detail.
- New insight has been gained on the electrochemical properties of silicon-insulator-electrolyte systems.
- Silicon electroosmotic micropumps have been shown to be suitable for certain applications.
- Dramatic performance gains have been realized. The development of the models and fabrication techniques set out in this text was accompanied by prototype micropump performance improvements including a 30-fold increase

in flow rate, a five-fold increase in pressure, and an 80% reduction in package size.

With recent data beginning to yield insight on the intriguing issue of substrate current, this is clearly a prominent area for further work. A variety of approaches to further mitigating substrate current can be readily conceived, including selective doping of the substrate during pump manufacturing or biasing during operation. Pump transient response is another area of ongoing interest.

APPENDIX A: DESIGN AND OPERATIONAL PARAMETERS OF REPORTED MICROPUMPS

Table A-1: Reciprocating Displacement Micropumps

author & year	driver	valves	construction	pump chambers	diaphragm material	S_p (approx.) (mm ³)	diaphragm thickness (mm)	working fluid	V (V)	f (Hz)	Δp_{\max} (kPa)	Q_{\max} (mL min ⁻¹)
van Lintel 1988 [81]	piezoelectric (lateral)	flap (diaphragm-ring mesa)	glass-Si-glass	1	glass	4,100	0.3	water	125	0.1	24	0.0006
							0.19	water	100	1	9.8	0.008
Smits 1990 [16]	piezoelectric (lateral)	none	glass-Si-glass	3 (S)	glass	1,500	n/r	water	100	15	5.9	0.1
Stemme 1993 [107]	piezoelectric (lateral)	fixed-geometry (nozzle-diffuser)	brass	1	brass	2,500	0.2	water	20	110	21	4.4
								water	20	310	4.9	16
								air	20	6,000	0.78	35
Gass 1994 [127]	piezoelectric (lateral)	flap (diaphragm-ring mesa)	glass-Si-glass	1	glass	11,800	0.3	water	250	40	9.0	0.55
Forster 1995 [196]	piezoelectric (lateral)	fixed-geometry	Si-glass	1	glass	n/r	0.15	water	150	114	n/r	0.038
Carrozza 1995 [111]	piezoelectric (lateral)	ball	polymer-brass	1	brass	1,270	0.1	water	300	70	25	2.7
Gerlach 1995 [195]	piezoelectric (lateral)	fixed-geometry (nozzle-diffuser)	Si-Si-glass	1	glass	200	0.12	water	50	3,000	3.2	0.39
								methanol	50	5,000	7	0.32
Olsson 1995 [104]	piezoelectric (lateral)	fixed-geometry (nozzle-diffuser)	brass	2 (P)	brass	1,600	0.35	water	130	540	16	16

Appendix A: Design and Operational Parameters of Reported Micropumps

author & year	driver	valves	construction	pump chambers	diaphragm material	S_p (approx.) (mm ³)	diaphragm thickness (mm)	working fluid	V (V)	f (Hz)	Δp_{\max} (kPa)	Q_{\max} (mL min ⁻¹)
Olsson 1996 [105]	piezoelectric (lateral)	fixed-geometry (nozzle-diffuser)	Si-glass	2 (P)	glass, silicon	270	0.3 (Si); 0.5 (glass)	methanol	n/r	1,318	17	0.23
Bardell 1997 [357]	piezoelectric (lateral)	fixed-geometry (tesla)	Si-glass	1	glass	n/r	0.15	water	300	100	2.3	0.085
						220	0.5	water	290	3000	47	0.75
Olsson 1997 [126]	piezoelectric (lateral)	fixed-geometry (nozzle-diffuser)	Si-glass	2 (P)	glass	260	0.5	water	200	3500	74	1.1
Kamper 1998 [108]	piezoelectric (lateral)	flap (diaphragm-ring mesa)	molded polycarbonate (two layers)	1	brass/poly-carbonate	500	0.15	water	n/r	70	200	0.4
								air	n/r	n/r	50	3.5
Koch 1998 [130]	piezoelectric (lateral)	flap (cantilever)	Si-Si-Si	1	silicon	n/r	0.07	ethanol	600	200	1.8	0.12
Linnemann 1998 [97]	piezoelectric (lateral)	flap (cantilever)	Si-Si-Si	1	silicon	110	0.04	water	160	220	n/r	1.2
Richter 1998 [96]	piezoelectric (lateral)	flap (cantilever)	Si-Si	1	silicon	n/r	0.04	water	160	220	n/r	0.7
								air	n/r	300	n/r	1.4
Bohm 1999 [110]	piezoelectric (lateral)	flap (diaphragm-ring mesa)	molded plastic	1	brass	290	0.075	water	350	50	12	1.9
Andersson 2001 [198]	piezoelectric (lateral)	fixed-geometry (nozzle-diffuser)	Si-glass bonded	1	silicon	n/r	n/r	water	97	700	n/r	0.0023
Schabmueller 2002 [132]	piezoelectric (lateral)	fixed-geometry (nozzle-diffuser)	Si-Si bonded	1	silicon	120	0.07	ethanol	190	2400	1.0	1.5
								air	190	3400	n/r	0.69

Appendix A: Design and Operational Parameters of Reported Micropumps

author & year	driver	valves	construction	pump chambers	diaphragm material	S_p (approx.) (mm ³)	diaphragm thickness (mm)	working fluid	V (V)	f (Hz)	Δp_{\max} (kPa)	Q_{\max} (mL min ⁻¹)
thinXXS2000 2003 [358]	piezoelectric (lateral)	flap (diaphragm-ring mesa)	micro-injection molded/laser welded plastic	1	plastic	4600	n/r	water	450	20	35	2.5
MIP Implantable 2003	piezoelectric (lateral)	flap (diaphragm-ring mesa)	glass-Si-glass-Si	1	silicon	360	n/r	water	150	0.2	57	0.0017
Stehr 1996 [359]	piezoelectric (lateral/cantilever)	none	Perspex-Si	1	silicon	n/r	.018 (bossed)	water	200	190	17	1.5
Esashi 1989 [117]	piezoelectric (axial)	flap (tethered plate)	Si-Si w/ spun-on glass layer	1	silicon	800	0.05	water	90	30	6.4	0.015
Shoji 1990 [116]	piezoelectric (axial)	flap (tethered plate)	glass-Si-glass	1	silicon	4000	0.05	water	100	50	n/r	0.022
				2 (P)	silicon	4000	0.05	water	100	50	n/r	0.042
				2 (S)	silicon	4000	0.05	water	100	25	10.7	0.018
Li 2000 [101]	piezoelectric (axial)	flap (diaphragm-ring mesa)	Si, glass (7 layers)	1	silicon	3300	0.025 (bossed)	silicone oil	1200	3500	304	3
Zengerle 1995 [118]	electrostatic	flap (cantilever)	Si	1	silicon	100	n/r	water	200	300	29	0.16
Richter 1998 [106]	electrostatic	flap (cantilever)	Si-Si bonded	1	silicon	n/r	n/r	water	n/r	400	n/r	0.26
van de Pol 1990 [96]	thermo-pneumatic (air)	flap (diaphragm-ring mesa)	glass-Si-Si-Si-glass	1	silicon	3000	0.018	water	6	1	5.1	0.034

Appendix A: Design and Operational Parameters of Reported Micropumps

author & year	driver	valves	construct- ion	pump chambers	dia- phragm material	S_p (approx). (mm ³)	dia- phragm thickness (mm)	working fluid	V (V)	f (Hz)	Δp_{\max} (kPa)	Q_{\max} (mL min ⁻¹)
Folta 1992 [139]	thermo- pneumatic (air)	none	Si-Si-Si fusion bonded	3 (S)	silicon	n/r	0.002	water	n/r	1	n/r	n/r
Elwenspoek 1994 [147]	thermo- pneumatic (air)	flap (diaphragm- ring mesa)	glass-Si- glass	1	silicon	n/r	n/r	Water	n/r	5	n/r	0.055
Schomburg 1994 [140]	thermo- pneumatic (air)	flap (diaphragm- ring mesa)	polymer (Polysulph one)	1	poly- imide	n/r	0.0025	air	15	5	3.8	0.044
Grosjean 1999 [141]	thermo- pneumatic (air)	none	acrylic, silicon, glass	3 (S)	Parylene/ silicone rubber	970	0.122	water	n/r	2	3.4	0.0063
Jeong 2000 [142]	thermo- pneumatic (air)	fixed-geometry (nozzle-diffuser)	glass-Si- glass	1	silicon	n/r	0.002	water	8	4	0	0.014
Wego 2001 [143]	thermo- pneumatic (air)	flap (diaphragm- ring mesa)	printed circuit board (4 layers)	1	poly- imide	780	0.0078	water		2	12	0.53
Sim 2003 [112]	thermo- pneumatic (water/phase- change)	flap (cantilever)	glass-Si- Si-Si	1	silicone rubber	72	0.03	water	10	0.5	0.10	0.006
Tsai 2002 [144]	thermo- pneumatic (bubble)	fixed-geometry (nozzle-diffuser)	glass-Si	1	n/a	n/r	n/a	isopropyl alcohol	20	400	0.38	0.0045

Appendix A: Design and Operational Parameters of Reported Micropumps

author & year	driver	valves	construction	pump chambers	dia-phragm material	S_p (approx.) (mm ³)	dia-phragm thickness (mm)	working fluid	V (V)	f (Hz)	Δp_{\max} (kPa)	Q_{\max} (mL min ⁻¹)
Zimmermann 2004 [148]	thermo-pneumatic (bubble)	flap (in-plane)	glass-Si	1	n/a	n/r	n/a	isopropyl alcohol	n/r	10	16	0.009
Rapp 1994 [149]	pneumatic	none	gold, polyimide, glass	3 (S)	titanium	n/a	0.003	water	n/a	5	2.3	n/r
Grosjean 1999 [158]	pneumatic	none	acrylic, silicon, glass	3 (S)	Parylene/silicone rubber	n/a	0.122	water	n/a	16	34.5	0.1
Meng 2000 [142]	pneumatic	flap (tethered plate)	Si, thermoplastic, silicone rubber	1	silicone rubber	n/a	0.14	water	n/a	5	5.9	3.5
Unger 2000 [162]	pneumatic	none	multi-layer elastomer	3 (S)	elastomer	n/a		water	n/a	75	n/r	0.00014
Grover 2003 [159]	pneumatic	flap (diaphragm)	glass-PDMS-glass	1	PDMS	n/a	0.254	water	n/a	< 1	30	0.0028
Berg 2003 [160]	pneumatic	none	PDMS, glass	2 (S)	PDMS	n/a	2.3	water	n/a	1	0.17	0.006
Benard 1998 [103]	shape-memory alloy	flap (tethered plate)	Silicon	1	TiNi	560	0.003	water	n/r	0.9	0.53	0.05

Appendix A: Design and Operational Parameters of Reported Micropumps

author & year	driver	valves	construction	pump chambers	diaphragm material	S_p (approx.) (mm ³)	diaphragm thickness (mm)	working fluid	V (V)	f (Hz)	Δp_{\max} (kPa)	Q_{\max} (mL min ⁻¹)
Dario 1996 [166]	electromagnetic	flap (double opposing cantilevers)	molded plastic	1	rubber	2,500	n/r	water	14	264	4.6	0.78
Bohm 1999 [161]	electromagnetic	flap (diaphragm-ring mesa)	molded plastic	1	silicone rubber	1,000	0.2	water	n/r	50	10	2.1
								air	n/r	400	n/r	40
Yun 2002 [110]	electrowetting	flap (cantilever)	glass-SU8-Si-Si	2	silicone rubber	n/r	0.08	water	2.3	25	0.70	0.07

Table A-2: Dynamic Micropumps

author & year	description	construction	working fluid	approx. size (mm ³)	operating voltage (V)	Δp_{\max} (kPa)	Q_{\max} (mL/min)
Richter 1991 [102]	electrohydrodynamic (injection)	Si-Si	ethanol	10	600	0.43	14
Fuhr 1994 [249]	electrohydrodynamic (induction)	Si-glass	water	n/r	40	n/r	0.002
Furuya 1996 [245]	electrohydrodynamic (injection)	polyimide	ethanol	n/r	200	n/r	0.00012
Wong 1996 [360]	electrohydrodynamic (injection)	Si-Si	propanol	70	120	0.29	

Appendix A: Design and Operational Parameters of Reported Micropumps

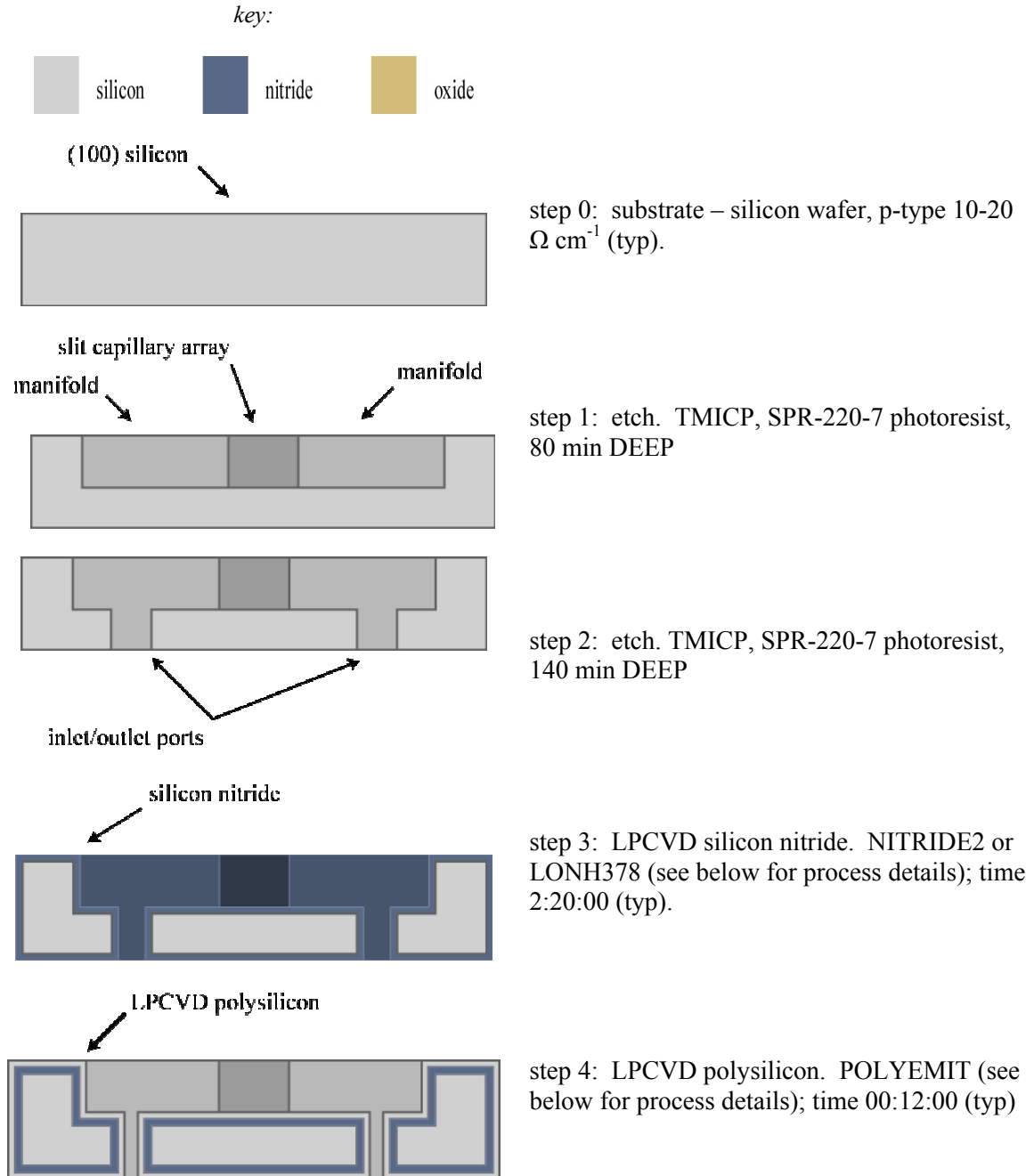
author & year	description	construction	working fluid	approx. size (mm ³)	operating voltage (V)	Δp_{\max} (kPa)	Q_{\max} (mL/min)
Ahn 1998 [250]	electrohydrodynamic (injection)	Si-glass	ethyl alcohol	90	100	0.25	0.04
Darabi 2001 [243]	electrohydrodynamic (polarization)	quartz	R-134a (refrigerant)	250	120	0.25	n/r
Darabi 2002 [246]	electrohydrodynamic (injection)	ceramic	3M HFE-7100	640	250	0.78	n/r
Jacobson 1994 [251]	electroosmotic (microchannel)	glass	water	n/a	2,700	n/a	0.00002
Ramsey 1997 [58]	electroosmotic (micromachined)	glass	water/methanol	1,250	2,000	n/r	0.00009
Paul 1998 [62]	electroosmotic (porous media)	packed silica particles	80:20 acetonitrile:water with 4 mM aqueous sodium tetraborate buffer	120	6,750	20,000	0.0002
			NH ₄ OH (0.35 mM)		500	150	3.0
Gan 2000 [60]	electroosmotic (porous media)	sintered glass beads	TBE buffer (Tris, boric acid, EDTA)	n/a	40	0	5.4x10 ⁻⁶
McKnight 2001 [259]	electroosmotic (microchannel)	PDMS-glass	borate buffer	3,800	200	250	7.0
Yao 2001 [255]	electroosmotic (porous media)	sintered glass frit	water	85	2,000	2000	0.0036
Zeng 2001 [361]	electroosmotic (porous media)	packed silica particles	phosphate buffer	n/r	40	5.0	n/r
Takamura 2001 [256]	electroosmotic (micromachined)	quartz					

Appendix A: Design and Operational Parameters of Reported Micropumps

author & year	description	construction	working fluid	approx. size (mm³)	operating voltage (V)	Δp_{\max} (kPa)	Q_{\max} (mL/min)
Chen 2002 [263]	electroosmotic (micromachined)	soda-lime glass	water	9,000	1,000	33	0.015
Laser 2002 [63]	electroosmotic (micromachined)	Si-glass	borate buffer	120	400	10	0.014
Zeng 2002 [257]	electroosmotic (porous media)	packed silica particles	water	1,200	1,250	250	0.9
Laser 2003 [260]	electroosmotic (micromachined)	Si-glass	borate buffer	120	400	10	0.17
Yao 2003 [27, 61]	electroosmotic (porous media)	sintered glass frit	borate buffer	9,500	100	130	33
Jang 2000 [61]	magnetohydrodynamic (DC)	Si-Si	seawater	n/r	n/a	0.17	0.063
Lemoff 2000 [271]	magnetohydrodynamic (AC)	glass-Si-glass	1 M NaCl solution	n/r	n/a	0	0.018

APPENDIX B: MICROPUMP FABRICATION PROCESS DETAILS

Process flow for two-layer thin film dielectric, backside inlet/outlet ports



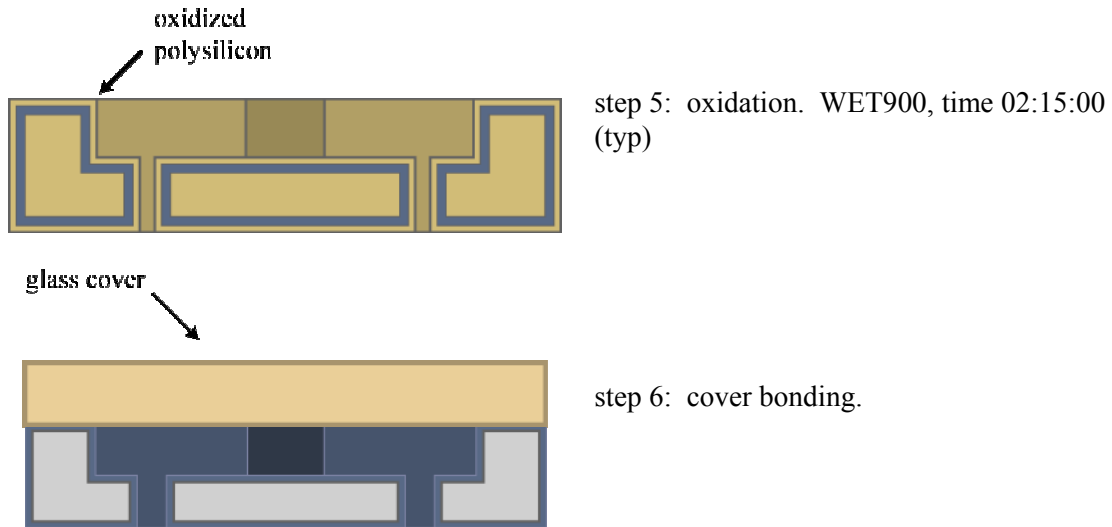


Figure B.1: Standard process flow for fabrication of silicon electroosmotic micropumps with oxide-on-nitride thin film dielectrics, backside inlet/outlet ports, anodically bonded glass covers, post-cleanroom electrode insertion.

Silicon nitride deposition recipe

```

PROCESS ID: NITRIDE2
DESCRIPTION: STD NITRIDE DEP ST
BANK: 3
TUBES: 10
REUSE: YES

0001.0000     IDLE
0001.0005     STEP N2PURG=3000
0001.0010     STEP TEMPL=585
0001.0015     STEP TEMPC=590
0001.0020     STEP TEMPS=590
0001.0025     STEP UNLOAD=OFF
0001.0030     STEP LOAD=ON
0001.0035     STEP SPEED=25

0005.0000     BOAT OUT
0005.0005     STEP TIME:00:00:00
0005.0010     STEP N2PURG=2800
0005.0015     STEP TEMPL=595
0005.0020     STEP TEMPC=600
0005.0025     STEP TEMPS=595
0005.0030     STEP LOAD=OFF
0005.0035     STEP UNLOAD=ON
0005.0040     STEP SPEED=25
0005.0045     STEP IF ALMACK=ON GOTO 0010
    
```

Appendix B: Fabrication Processes

```
0010.0000      BOAT IN
0010.0005      STEP TIME:00:00:00
0010.0010      STEP TEMPL=700
0010.0015      STEP TEMPC=700
0010.0020      STEP TEMPS=700
0010.0025      STEP UNLOAD=OFF
0010.0030      STEP LOAD=ON
0010.0035      STEP SPEED=25
0010.0040      STEP TCU CTLID=1
0010.0045      STEP IF DNTLK=ON GOTO 0015
0010.0050      STEP TCU LEARN=OFF

0015.0000      PRE PUMP STABILIZE TO +-5 DEG
0015.0005      STEP TIME:00:00:15
0015.0010      STEP N2PURG=1500
0015.0015      STEP TCU LEARN=OFF

0020.0000      INITIAL PUMPDOWN
0020.0005      STEP TIME:00:03:00
0020.0010      STEP N2PURG=110
0020.0015      STEP VACUUM=ON
0020.0020      STEP TEMPL=779
0020.0025      STEP TEMPC=785
0020.0030      STEP TEMPS=791
0020.0035      STEP TCU CTLID=2
0020.0040      STEP TCU LEARN=OFF

0025.0000      STABILIZE
0025.0005      STEP TIME:00:25:00
0025.0010      STEP N2PURG=100
0025.0015      STEP TCU CTLID=2
0025.0020      STEP TCU LEARN=OFF

0030.0000      PUMP DOWN
0030.0005      STEP TIME:00:02:00
0030.0010      STEP N2PURG=OFF
0030.0015      STEP N2PURG=0
0030.0020      STEP TCU CTLID=2
0030.0025      STEP TCU LEARN=OFF

0035.0000      PUMPDOWN AND GROSS LEAK CHECK
0035.0005      STEP TIME:00:03:00
0035.0010      STEP TCU CTLID=2
0035.0015      STEP PRCPR TOLERANCE=1.0
0035.0020      STEP IF PRCPR>500 GOTO 0105
0035.0025      STEP TCU LEARN=OFF

0040.0000      LEAK CHECK
0040.0005      STEP TIME:00:01:00
0040.0010      STEP TCU CTLID=2
0040.0015      STEP VACUUM=OFF
0040.0020      STEP IF PRCPR>60 GOTO 0105
0040.0025      STEP TCU LEARN=OFF
```

Appendix B: Fabrication Processes

```
0045.0000     REPUMP
0045.0005     STEP TIME:00:02:00
0045.0010     STEP VACUUM=ON
0045.0015     STEP TCU CTLID=2
0045.0020     STEP TCU LEARN=OFF
0045.0025     STEP IF TEMPC<700 GOTO 0075

0050.0000     START PURGE
0050.0005     STEP TIME:00:03:00
0050.0010     STEP N2PURG=100
0050.0015     STEP TCU LEARN=OFF

0055.0000     FINAL STABILIZATION
0055.0005     STEP TIME:00:15:00
0055.0010     STEP N2PURG=110
0055.0015     STEP TCU CTLID=2
0055.0020     STEP TCU LEARN=OFF
0055.0025     STEP IF PRCPR>1200 GOTO 0075

0060.0000     START AMMONIA FLOW
0060.0005     STEP TIME:00:03:00
0060.0010     STEP N2PURG=OFF
0060.0015     STEP N2PURG=0
0060.0020     STEP NH3=140
0060.0025     STEP TCU CTLID=2
0060.0030     STEP TCU LEARN=OFF

0065.0000     *DEPOSITION*
0065.0005     STEP TIME:VARIABLE
0065.0010     STEP DCS=40
0065.0015     STEP TCU CTLID=2
0065.0020     STEP TCU LEARN=OFF
0065.0025     STEP IF PRCPR>1200 GOTO 0075

0070.0000     AMMONIA PURGE
0070.0005     STEP TIME:00:03:00
0070.0010     STEP DCS=OFF
0070.0015     STEP DCS=0
0070.0020     STEP TEMPL=560
0070.0025     STEP TEMPC=560
0070.0030     STEP TEMPS=560
0070.0035     STEP TCU LEARN=OFF
0070.0040     STEP IF PRCPR>1200 GOTO 0075

0075.0000     1ST PUMPDOWN
0075.0005     STEP TIME:00:03:00
0075.0010     STEP NH3=OFF
0075.0015     STEP NH3=0
0075.0020     STEP DCS=OFF
0075.0025     STEP DCS=0
0075.0030     STEP TEMPS=560
0075.0035     STEP TEMPC=560
0075.0040     STEP TEMPL=560
0075.0045     STEP TCU LEARN=OFF
```

Appendix B: Fabrication Processes

```
0080.0000      1ST PURGE
0080.0005      STEP TIME:00:01:00
0080.0010      STEP N2PURG=300

0085.0000      2ND PUMP DOWN
0085.0005      STEP TIME:00:01:00
0085.0010      STEP N2PURG=300

0090.0000      2ND PURGE
0090.0005      STEP TIME:00:01:00
0090.0010      STEP N2PURG=100

0095.0000      FINAL PUMP DOWN
0095.0005      STEP TIME:00:01:00
0095.0010      STEP N2PURG=300

0100.0000      FINAL PURGE AND RAMPDOWN
0100.0005      STEP TIME:00:00:00
0100.0010      STEP N2PURG=715
0100.0015      STEP N2BKFL=50
0100.0020      STEP TEMPL TOLERANCE=1.0
0100.0025      STEP IF TEMPL<610 GOTO 0105
0100.0030      STEP TCU LEARN=OFF

0105.0000      SLOW BACKFILL AND ABORT STEP
0105.0005      STEP TIME:00:08:00
0105.0010      STEP VACUUM=OFF
0105.0015      STEP TEMPL=500
0105.0020      STEP TEMPC=500
0105.0025      STEP TEMPS=500
0105.0030      STEP N2PURG=2800
0105.0035      STEP N2BKFL=750
0105.0040      STEP TCU LEARN=OFF

0110.0000      BOAT OUT
0110.0005      STEP TIME:00:00:00
0110.0010      STEP N2BKFL=OFF
0110.0015      STEP N2BKFL=0
0110.0020      STEP N2PURG=2500
0110.0025      STEP TEMPL=500
0110.0030      STEP TEMPC=525
0110.0035      STEP TEMPS=550
0110.0040      STEP LOAD=OFF
0110.0045      STEP UNLOAD=ON
0110.0050      STEP SPEED=25
0110.0055      STEP IF ALMACK=ON GOTO 0115

0115.0000      END
0115.0005      STEP END PROCESS
```

PROCESS ID: LONH378

Appendix B: Fabrication Processes

DESCRIPTION: NEW LOW STRESS NITRIDE RECIPE (DCS/NH3=14)
BANK: 3
TUBES: 10
REUSE: YES

```
0001.0000     IDLE
0001.0005     STEP N2PURG=2500
0001.0010     STEP TEMPL=590
0001.0015     STEP TEMPC=595
0001.0020     STEP TEMPS=595
0001.0025     STEP UNLOAD=OFF
0001.0030     STEP LOAD=ON
0001.0035     STEP SPEED=25

0005.0000     BOAT OUT
0005.0005     STEP TIME:00:00:00
0005.0010     STEP N2PURG=2000
0005.0015     STEP N2BKFL=100
0005.0020     STEP TEMPL=585
0005.0025     STEP TEMPC=600
0005.0030     STEP TEMPS=595
0005.0035     STEP LOAD=OFF
0005.0040     STEP UNLOAD=ON
0005.0045     STEP SPEED=25
0005.0050     STEP IF ALMACK=ON GOTO 0010

0010.0000     BOAT IN
0010.0005     STEP TIME:00:00:00
0010.0010     STEP TEMPL=700
0010.0015     STEP TEMPC=700
0010.0020     STEP TEMPS=700
0010.0025     STEP UNLOAD=OFF
0010.0030     STEP LOAD=ON
0010.0035     STEP SPEED=25
0010.0040     STEP TCU CTLID=1
0010.0045     STEP IF DNTLK=ON GOTO 0015
0010.0050     STEP TCU LEARN=OFF
0010.0055     STEP N2PURG=650
0010.0060     STEP N2BKFL=45

0015.0000     PRE PUMP STABILIZE TO +-5 DEG
0015.0005     STEP TIME:00:00:05
0015.0010     STEP N2PURG=1500
0015.0015     STEP N2BKFL=OFF
0015.0020     STEP N2BKFL=0
0015.0025     STEP TCU LEARN=OFF

0020.0000     INITIAL PUMPDOWN
0020.0005     STEP TIME:00:04:00
0020.0010     STEP N2PURG=130
0020.0015     STEP VACUUM=ON
0020.0020     STEP TEMPL=779
0020.0025     STEP TEMPC=785
0020.0030     STEP TEMPS=791
```

Appendix B: Fabrication Processes

```
0020.0035 STEP TCU CTLID=2
0020.0040 STEP TCU LEARN=OFF

0025.0000 STABILIZE
0025.0005 STEP TIME:00:20:00
0025.0010 STEP N2PURG=145
0025.0015 STEP TCU CTLID=2
0025.0020 STEP TCU LEARN=OFF

0030.0000 PUMP DOWN
0030.0005 STEP TIME:00:03:00
0030.0010 STEP N2PURG=OFF
0030.0015 STEP N2PURG=0
0030.0020 STEP TCU CTLID=2
0030.0025 STEP TCU LEARN=OFF
0030.0030 STEP IF TEMPC <700 GOTO 0080

0035.0000 PUMPDOWN AND GROSS LEAK CHECK
0035.0005 STEP TIME:00:03:00
0035.0010 STEP TCU CTLID=2
0035.0015 STEP PRCPR TOLERANCE=1.0
0035.0020 STEP IF PRCPR>500 GOTO 0110
0035.0025 STEP TCU LEARN=OFF

0040.0000 LEAK CHECK
0040.0005 STEP TIME:00:01:00
0040.0010 STEP TCU CTLID=2
0040.0015 STEP VACUUM=OFF
0040.0020 STEP IF PRCPR>60 GOTO 0110
0040.0025 STEP TCU LEARN=OFF

0045.0000 REPUMP
0045.0005 STEP TIME:00:02:00
0045.0010 STEP VACUUM=ON
0045.0015 STEP TCU CTLID=2
0045.0020 STEP TCU LEARN=OFF

0050.0000 START PURGE
0050.0005 STEP TIME:00:02:00
0050.0010 STEP N2PURG=120
0050.0015 STEP TCU CTLID=2
0050.0020 STEP TCU LEARN=OFF

0055.0000 FINAL STABILIZE TO +-1 DEG
0055.0005 STEP TIME:00:25:00
0055.0010 STEP N2PURG=135
0055.0015 STEP TCU CTLID=2
0055.0020 STEP TCU LEARN=OFF
0055.0025 STEP IF PRCPR>1200 GOTO 0080

0060.0000 PUMP DOWN
0060.0005 STEP TIME:00:00:15
0060.0010 STEP TCU CTLID=2
0060.0015 STEP TCU LEARN=OFF
```

Appendix B: Fabrication Processes

```
0065.0000     START AMMONIA FLOW
0065.0005     STEP TIME:00:01:00
0065.0010     STEP N2PURG=OFF
0065.0015     STEP N2PURG=0
0065.0020     STEP LONH3=13.5
0065.0025     STEP TCU CTLID=2
0065.0030     STEP TCU LEARN=OFF
0065.0035     STEP IF PRCPR>1200 GOTO 0080

0070.0000     *DEPOSITION*
0070.0005     STEP TIME:VARIABLE
0070.0010     STEP DCS=189
0070.0015     STEP TCU CTLID=2
0070.0020     STEP TCU LEARN=OFF
0070.0025     STEP IF PRCPR>1200 GOTO 0080

0075.0000     AMMONIA PURGE
0075.0005     STEP TIME:00:01:00
0075.0010     STEP DCS=OFF
0075.0015     STEP DCS=0
0075.0020     STEP TCU LEARN=OFF
0075.0025     STEP IF PRCPR>1200 GOTO 0080

0080.0000     1ST PUMPDOWN
0080.0005     STEP TIME:00:02:00
0080.0010     STEP LONH3=OFF
0080.0015     STEP LONH3=0
0080.0020     STEP DCS=OFF
0080.0025     STEP DCS=0
0080.0030     STEP TCU LEARN=OFF

0085.0000     1ST PURGE
0085.0005     STEP TIME:00:01:00
0085.0010     STEP N2PURG=300
0085.0015     STEP TEMPL=560
0085.0020     STEP TEMPC=560
0085.0025     STEP TEMPS=560
0085.0030     STEP TCU LEARN=OFF

0090.0000     2ND PUMP DOWN
0090.0005     STEP TIME:00:01:00
0090.0010     STEP N2PURG=100

0095.0000     2ND PURGE
0095.0005     STEP TIME:00:01:00
0095.0010     STEP N2PURG=300

0100.0000     FINAL PUMP DOWN
0100.0005     STEP TIME:00:01:00
0100.0010     STEP N2PURG=100

0105.0000     FINAL PURGE AND RAMPDOWN
0105.0005     STEP TIME:00:00:00
```

Appendix B: Fabrication Processes

```
0105.0010 STEP N2PURG=650
0105.0015 STEP N2BKFL=45
0105.0020 STEP TEMPL TOLERANCE=1.0
0105.0025 STEP IF TEMPL<600 GOTO 0110
0105.0030 STEP TCU LEARN=OFF

0110.0000 SLOW BACKFILL AND ABORT STEP
0110.0005 STEP TIME:00:08:00
0110.0010 STEP VACUUM=OFF
0110.0015 STEP TEMPL=550
0110.0020 STEP TEMPC=550
0110.0025 STEP TEMPS=550
0110.0030 STEP N2PURG=2500
0110.0035 STEP N2BKFL=750
0110.0040 STEP TCU LEARN=OFF

0115.0000 BOAT OUT
0115.0005 STEP TIME:00:00:00
0115.0010 STEP N2BKFL=OFF
0115.0015 STEP N2BKFL=0
0115.0020 STEP N2PURG=2500
0115.0025 STEP TEMPL=500
0115.0030 STEP TEMPC=525
0115.0035 STEP TEMPS=550
0115.0040 STEP LOAD=OFF
0115.0045 STEP UNLOAD=ON
0115.0050 STEP SPEED=25
0115.0055 STEP IF ALMACK=ON GOTO 0120

0120.0000 END
0120.0005 STEP END PROCESS
```

Polysilicon deposition recipe

```
PROCESS ID: POLYEMIT
DESCRIPTION: POLY EMITTER DEP AT 400mT USING H2 ST
BANK: 3
TUBES: 9
REUSE: YES
```

```
0001.0000 IDLE
0001.0005 STEP VACUUM=OFF
0001.0010 STEP N2PURG=2000
0001.0015 STEP TEMPL=590
0001.0020 STEP TEMPC=590
0001.0025 STEP TEMPS=590
0001.0030 STEP UNLOAD=OFF
0001.0035 STEP LOAD=ON
0001.0040 STEP SPEED=25
0001.0045 STEP TCU LEARN=OFF

0005.0000 BOAT OUT
```

Appendix B: Fabrication Processes

```
0005.0005 STEP TIME:00:00:00
0005.0010 STEP N2PURG=3500
0005.0015 STEP TEMPL=580
0005.0020 STEP TEMPC=585
0005.0025 STEP TEMPS=590
0005.0030 STEP LOAD=OFF
0005.0035 STEP UNLOAD=ON
0005.0040 STEP SPEED=25
0005.0045 STEP IF ALMACK=ON GOTO 0010
0005.0050 STEP TCU LEARN=OFF

0010.0000 BOAT IN
0010.0005 STEP TIME:00:00:00
0010.0010 STEP TEMPL=600
0010.0015 STEP TEMPC=600
0010.0020 STEP TEMPS=600
0010.0025 STEP UNLOAD=OFF
0010.0030 STEP LOAD=ON
0010.0035 STEP SPEED=25
0010.0040 STEP TCU CTLID=1
0010.0045 STEP TCU LEARN=OFF
0010.0050 STEP IF DNTLK=ON GOTO 0015

0015.0000 INITIAL PUMPDOWN
0015.0005 STEP TIME:00:03:00
0015.0010 STEP N2PURG=300
0015.0015 STEP VACUUM=ON
0015.0020 STEP TEMPL=617.0
0015.0025 STEP TEMPC=620.0
0015.0030 STEP TEMPS=623.0
0015.0035 STEP TCU CTLID=2
0015.0040 STEP TCU LEARN=OFF

0020.0000 START PURGE
0020.0005 STEP TIME:00:01:00
0020.0010 STEP N2PURG=150
0020.0015 STEP H2=60
0020.0020 STEP TCU CTLID=2
0020.0025 STEP TCU LEARN=OFF

0025.0000 STABILZE
0025.0005 STEP TIME:00:05:00
0025.0010 STEP TCU CTLID=2
0025.0015 STEP TCU LEARN=OFF
0025.0020 STEP IF PRCPR>1200 GOTO 0075

0030.0000 PUMP DOWN
0030.0005 STEP TIME:00:02:00
0030.0010 STEP N2PURG=OFF
0030.0015 STEP N2PURG=0
0030.0020 STEP H2=0
0030.0025 STEP H2=OFF
0030.0030 STEP TCU CTLID=2
0030.0035 STEP TCU LEARN=OFF
```

Appendix B: Fabrication Processes

```
0030.0040  STEP IF TEMPC<580 GOTO 0075

0035.0000      PUMPDOWN AND GROSS LEAK CHECK
0035.0005  STEP TIME:00:01:00
0035.0010  STEP TCU CTLID=2
0035.0015  STEP PRCPR TOLERANCE=1.0
0035.0020  STEP IF PRCPR>500 GOTO 0115

0040.0000      LEAK CHECK
0040.0005  STEP TIME:00:01:00
0040.0010  STEP TCU CTLID=2
0040.0015  STEP VACUUM=OFF
0040.0020  STEP TCU LEARN=OFF
0040.0025  STEP IF PRCPR>60 GOTO 0115

0045.0000      REPUMP
0045.0005  STEP TIME:00:02:00
0045.0010  STEP VACUUM=ON
0045.0015  STEP N2PURG=200
0045.0020  STEP TCU CTLID=2
0045.0025  STEP TCU LEARN=OFF

0050.0000      START FLOW
0050.0005  STEP TIME:00:02:00
0050.0010  STEP N2PURG=135
0050.0015  STEP H2=80
0050.0020  STEP TCU CTLID=2
0050.0025  STEP TCU LEARN=OFF

0055.0000      PRCPR STABLIZE
0055.0005  STEP TIME:00:02:00
0055.0010  STEP PRCPR=400
0055.0015  STEP TCU CTLID=2
0055.0020  STEP TCU LEARN=OFF

0060.0000      FINAL STABILIZE TO +-1 DEG
0060.0005  STEP TIME:00:45:00
0060.0010  STEP H2=110
0060.0015  STEP TCU CTLID=2
0060.0020  STEP TCU LEARN=OFF
0060.0025  STEP IF PRCPR>1200 GOTO 0075

0065.0000      *DEPOSITION*
0065.0005  STEP TIME:VARIABLE
0065.0010  STEP N2PURG=OFF
0065.0015  STEP N2PURG=0
0065.0020  STEP SIH4=136
0065.0025  STEP H2=110
0065.0030  STEP TCU CTLID=2
0065.0035  STEP TCU LEARN=OFF
0065.0040  STEP IF PRCPR>1200 GOTO 0075

0070.0000      H2 PURGE
0070.0005  STEP TIME:00:00:30
```

Appendix B: Fabrication Processes

```
0070.0010 STEP SIH4=0
0070.0015 STEP SIH4=OFF
0070.0020 STEP TCU CTLID=3
0070.0025 STEP TCU LEARN=OFF
0070.0030 STEP IF PRCPR>1200 GOTO 0075
```

```
0075.0000 1ST PUMP DOWN
0075.0005 STEP TIME:00:03:00
0075.0010 STEP SIH4=OFF
0075.0015 STEP SIH4=0
0075.0020 STEP H2=OFF
0075.0025 STEP H2=0
0075.0030 STEP PRCPR=OFF
0075.0035 STEP PRCPR=0
0075.0040 STEP TEMPL=500
0075.0045 STEP TEMPC=500
0075.0050 STEP TEMPS=500
0075.0055 STEP TCU LEARN=OFF
```

```
0080.0000 1ST PURGE
0080.0005 STEP TIME:00:01:00
0080.0010 STEP N2PURG=300
0080.0015 STEP TCU LEARN=OFF
```

```
0085.0000 2ND PUMPDOWN
0085.0005 STEP TIME:00:01:00
0085.0010 STEP N2PURG=OFF
0085.0015 STEP N2PURG=0
0085.0020 STEP TCU LEARN=OFF
```

```
0090.0000 2ND PURGE
0090.0005 STEP TIME:00:01:00
0090.0010 STEP N2PURG=350
0090.0015 STEP TCU LEARN=OFF
```

```
0095.0000 PUMP DOWN
0095.0005 STEP TIME:00:01:00
0095.0010 STEP N2PURG=OFF
0095.0015 STEP N2PURG=0
0095.0020 STEP TCU LEARN=OFF
```

```
0100.0000 3RD PURGE
0100.0005 STEP TIME:00:01:00
0100.0010 STEP N2PURG=350
0100.0015 STEP TCU LEARN=OFF
```

```
0105.0000 FINAL PUMP DOWN
0105.0005 STEP TIME:00:01:00
0105.0010 STEP N2PURG=OFF
0105.0015 STEP N2PURG=0
0105.0020 STEP TCU LEARN=OFF
```

```
0110.0000 FINAL PURGE AND RAMPDOWN
0110.0005 STEP TIME:00:00:00
```

Appendix B: Fabrication Processes

```
0110.0010 STEP N2PURG=400
0110.0015 STEP TEMPL TOLERANCE=1.0
0110.0020 STEP IF TEMPL<600 GOTO 0115
0110.0025 STEP TCU LEARN=OFF

0115.0000 SLOW BACKFILL AND ABORT STEP
0115.0005 STEP TIME:00:08:00
0115.0010 STEP VACUUM=OFF
0115.0015 STEP TEMPL=550
0115.0020 STEP TEMPC=550
0115.0025 STEP TEMPS=550
0115.0030 STEP N2PURG=2250
0115.0035 STEP N2BKFL=750
0115.0040 STEP TCU LEARN=OFF

0120.0000 BOAT OUT
0120.0005 STEP TIME:00:00:00
0120.0010 STEP N2BKFL=OFF
0120.0015 STEP N2BKFL=0
0120.0020 STEP N2PURG=3500
0120.0025 STEP TEMPL=500
0120.0030 STEP TEMPC=525
0120.0035 STEP TEMPS=550
0120.0040 STEP LOAD=OFF
0120.0045 STEP UNLOAD=ON
0120.0050 STEP SPEED=25
0120.0055 STEP IF ALMACK=ON GOTO 0125
0120.0060 STEP TCU LEARN=OFF

0125.0000 END
0125.0005 STEP END PROCESS
```

Wet oxidation recipe

```
PROCESS ID: WET900
DESCRIPTION: PYROGENIC STEAM AT 900 DEG ST
BANK: 1
TUBES: 1,2,3,4,7
REUSE: YES
```

```
0001.0000 IDLE
0001.0005 STEP N2=2.5
0001.0010 STEP O2HI=OFF
0001.0015 STEP O2HI=0
0001.0020 STEP TEMPL=800
0001.0025 STEP TEMPC=800
0001.0030 STEP TEMPS=800
0001.0035 STEP UNLOAD=OFF
0001.0040 STEP LOAD=ON
0001.0045 STEP SPEED=10
0001.0050 STEP TCU LEARN=OFF
```

Appendix B: Fabrication Processes

```
0005.0000      BOAT PULL
0005.0005      STEP TIME:00:00:00
0005.0010      STEP N2=5.0
0005.0015      STEP TEMPL=700
0005.0020      STEP TEMPC=750
0005.0025      STEP TEMPS=800
0005.0030      STEP LOAD=OFF
0005.0035      STEP UNLOAD=ON
0005.0040      STEP SPEED=8
0005.0045      STEP TCU LEARN=OFF
0005.0050      STEP IF ALMACK=ON GOTO 0010

0010.0000      BOAT IN
0010.0005      STEP TIME:00:20:00
0010.0010      STEP TEMPL=800
0010.0015      STEP TEMPC=800
0010.0020      STEP TEMPS=800
0010.0025      STEP UNLOAD=OFF
0010.0030      STEP LOAD=ON
0010.0035      STEP SPEED=10
0010.0040      STEP TCU CTLID=1
0010.0045      STEP TCU LEARN=OFF

0015.0000      RAMP UP TO 900 DEG +- 1.0
0015.0005      STEP TIME:00:20:00
0015.0010      STEP N2=2.4
0015.0015      STEP TEMPL=900
0015.0020      STEP TEMPC=900
0015.0025      STEP TEMPS=900
0015.0030      STEP O2LO=100
0015.0035      STEP TCU CTLID=3
0015.0040      STEP TCU LEARN=OFF

0020.0000      DRY OX
0020.0005      STEP TIME:00:10:00
0020.0010      STEP N2=OFF
0020.0015      STEP N2=0
0020.0020      STEP O2LO=OFF
0020.0025      STEP O2LO=0
0020.0030      STEP O2HI=2500
0020.0035      STEP TCU CTLID=3
0020.0040      STEP TCU LEARN=OFF

0025.0000      STEAM
0025.0005      STEP TIME:VARIABLE
0025.0010      STEP H2/O2=150
0025.0015      STEP O2HI=1000
0025.0020      STEP TCU CTLID=22
0025.0025      STEP TCU LEARN=OFF

0030.0000      DRY OX
0030.0005      STEP TIME:00:10:00
0030.0010      STEP H2/O2=OFF
0030.0015      STEP H2/O2=0
```

Appendix B: Fabrication Processes

```
0030.0020 STEP O2HI=2500
0030.0025 STEP TCU CTLID=3
0030.0030 STEP TCU LEARN=OFF

0035.0000 RAMP DOWN
0035.0005 STEP TIME:00:20:00
0035.0010 STEP O2HI=OFF
0035.0015 STEP O2HI=0
0035.0020 STEP N2=5.0
0035.0025 STEP TEMPL=750
0035.0030 STEP TEMPC=750
0035.0035 STEP TEMPS=750
0035.0040 STEP TCU LEARN=OFF

0040.0000 BOAT OUT
0040.0005 STEP TIME:00:00:00
0040.0010 STEP TEMPL=700
0040.0015 STEP TEMPC=750
0040.0020 STEP TEMPS=775
0040.0025 STEP TCU LEARN=OFF
0040.0030 STEP LOAD=OFF
0040.0035 STEP UNLOAD=ON
0040.0040 STEP SPEED=10
0040.0045 STEP IF ALMACK=ON GOTO 0045

0045.0000 END
0045.0005 STEP END PROCESS
```

REFERENCES

- [1] A. Manz, D. J. Harrison, E. Verpoorte, J. C. Fettinger, A. Paulus, H. Ludi, and H. M. Widmer, "Planar Chips Technology for Miniaturization and Integration of Separation Techniques into Monitoring Systems: Capillary Electrophoresis on a Chip," *Journal of Chromatography A*, vol. 593, pp. 253-258, 1992.
- [2] A. T. Woolley, D. Hadley, P. Landre, A. J. deMello, R. A. Mathies, and M. A. Northrup, "Functional Integration of PCR Amplification and Capillary Electrophoresis in a Microfabricated DNA Analysis Device," *Analytical Chemistry*, vol. 68, pp. 4081-4086, 1996.
- [3] J. Khandurina, T. E. McKnight, S. C. Jacobson, L. C. Waters, R. S. Foote, and J. M. Ramsey, "Integrated System for Rapid PCR-Based DNA Analysis in Microfluidic Devices," *Analytical Chemistry*, vol. 72, pp. 2995-3000, 2000.
- [4] M. T. Taylor, P. Nguyen, J. Ching, and K. E. Petersen, "Simulation of Microfluidic Pumping in a Genomic DNA Blood-Processing Cassette," *J. Micromech. Microeng.*, vol. 13, pp. 201-208, 2003.
- [5] D. B. Tuckerman and R. F. W. Pease, "High-Performance Heat Sinking for VLSI," *Electron Device Letters*, vol. 2, pp. 126-129, 1981.
- [6] L. Zhang, J. M. Koo, L. Jiang, M. Asheghi, K. E. Goodson, J. G. Santiago, and T. W. Kenny, "Measurements and Modeling of Two-Phase Flow in Microchannels with Nearly Constant Heat Flux Boundary Conditions," *Journal of Microelectromechanical Systems*, vol. 11, pp. 12-19, 2002.
- [7] L. Jiang, J. Mikkelsen, J.-M. Koo, D. E. Huber, S. Yao, L. Zhang, P. Zhou, J. G. Maveety, R. Prasher, J. G. Santiago, T. W. Kenny, and K. E. Goodson, "Closed-Loop Electroosmotic Microchannel Cooling System for VLSI Circuits," *IEEE Transactions on Components and Packaging Technologies*, vol. 25, pp. 347-355, 2002.
- [8] Therasense Inc., "Freestyle product literature, www.therasense.com/freestyle," 2003.
- [9] S.-K. Fan, P.-P. d. Guzman, and C. J. Kim, "EWOD Driving of Droplet on NxM Grid Using Single-Layer Electrode Patterns," presented at Solid-State Sensor, Actuator, and Microsystems Workshop, Hilton Head Island, S.C., 2002.

References

- [10] E. D. Hobbs and A. P. Pisano, "Micro Capillary-Force Driven Fluidic Accumulator/Pressure Source," presented at 12th International Conference on Solid-State Sensors, Actuators, and Microsystems (Transducers '03), Boston, MA, 2002.
- [11] Y.-C. Su and L. Lin, "Geometry and Surface Assisted Flow Discretization," presented at 12th International Conference on Solid-State Sensors, Actuators, and Microsystems, Boston, MA, 2003.
- [12] J. L. Selam, P. Micossi, F. L. Dunn, and D. M. Nathan, "Clinical Trial of Programmable Implantable Insulin Pump for Type I Diabetes," *Diabetes Care*, vol. 15, pp. 877-885, 1992.
- [13] M. A. Burns, B. N. Johnson, S. N. Brahmasandra, K. Handique, J. R. Webster, M. Krishnan, T. S. Sammarco, P. M. Man, D. Jones, D. Heldsinger, C. H. Mastrangelo, and D. T. Burke, "An Integrated Nanoliter DNA Analysis Device," *Science*, vol. 282, pp. 484-487, 1998.
- [14] M. Kanai, H. Abe, T. Munaka, Y. Fujiyama, D. Uchida, A. Yamayoshi, H. Nakanishi, A. Murakami, and S. Shoji, "Integrated Micro Chamber for Living Cell Analysis with Negligible Dead Volume Sample Injector," presented at 12th International Conference on Solid-State Sensors, Actuators, and Microsystems (Transducers '03), Boston, MA, 2003.
- [15] M. T. Blom, E. Chmela, F. H. J. van der Heyden, R. E. Oosterbroek, R. Tijssen, M. Elwenspoek, and A. van den Berg, "A Micro Viscosity Detector for Use in Miniaturized Chemical Separation Systems," presented at 6th International Conference on Micro Total Analysis Systems (MicroTAS), Nara, Japan, 2002.
- [16] J. G. Smits, "Piezoelectric Micropump with 3 Valves Working Peristaltically," *Sensors and Actuators A-Physical*, vol. 21, pp. 203-206, 1990.
- [17] A. K. Dash and G. C. Cudworth, "Therapeutic Applications of Implantable Drug Delivery Systems," *Journal of Pharmacological and Toxicological Methods*, vol. 40, pp. 1-12, 1998.
- [18] J.-L. Coll, P. Chollet, E. Brambilla, D. Desplanques, J.-P. Behr, and M. Favrot, "In Vivo Delivery to Tumors of DNA Complexed with Linear Polyethylenimine," *Human Gene Therapy*, vol. 10, pp. 1659-1666, 1999.
- [19] J. C. Pickup, H. Keen, J. Parsons, and K. Alberti, "Continuous Subcutaneous Insulin Infusion: An Approach to Achieving Normoglycemia," *Br J Med*, vol. 1, pp. 204-207, 1978.

References

- [20] D. G. Allen and M. V. Sefton, "A Model of Insulin Delivery by a Controlled Release Micropump," *Annals of Biomedical Engineering*, vol. 14, pp. 257-276, 1986.
- [21] H. Hanairebrouin, C. Broussolle, N. Jeandidier, E. Renard, B. Guerci, M. J. Haardt, V. Lassmannvague, M. Pinget, J. P. Tauber, J. Bringer, P. Vague, D. Raccach, P. Drouin, O. Ziegler, J. L. Selam, G. Slama, and F. Gilly, "Feasibility of Intraperitoneal Insulin Therapy with Programmable Implantable Pumps in IDDM - A Multicenter Study," *Diabetes Care*, vol. 18, pp. 388-392, 1995.
- [22] J. L. Selam, "External and Implantable Insulin Pumps: Current Place in the Treatment of Diabetes," *Experimental and Clinical Endocrinology & Diabetes*, vol. 109, pp. S333-S340, 2001.
- [23] Medtronic, "MiniMed 2007 Implantable Insulin Pump System product information, www.minimed.com."
- [24] A. C. Richards Grayson, R. S. Shawgo, A. M. Johnson, N. T. Flynn, Y. Li, M. J. Cima, and R. Langer, "A BioMEMS Review: MEMS Technology for Physiologically Integrated Devices," *Proc. IEEE*, vol. 92, pp. 6-21, 2004.
- [25] Semiconductor Industry Association, "International Technology Roadmap for Semiconductors," 2001.
- [26] E. N. Wang, L. Zhang, L. Jiang, J.-M. Koo, K. E. Goodson, J. G. Maveety, E. A. Sanchez, and T. W. Kenny, "Micromachined Jet Arrays for Liquid Impingement Cooling of VLSI Chips," presented at 2002 Solid State Sensors and Actuators and Microsystems Workshop, Hilton Head, S.C., 2002.
- [27] D. J. Laser, A. M. Myers, S. Yao, K. E. Goodson, J. G. Santiago, and T. W. Kenny, "Silicon Electroosmotic Micropumps for IC Thermal Management," presented at 12th International Conference on Solid-State Sensors, Actuators and Microsystems (Transducers '03), Boston, MA, 2003.
- [28] A. Manz and H. Becker, *Microsystems Technology in Chemistry and Life Science*. Berlin; New York: Springer, 1998.
- [29] S. C. Jakeway, A. J. de Mello, and E. L. Russell, "Miniaturized Total Analysis Systems for Biological Analysis," *Fresenius J Anal Chem*, vol. 366, pp. 525-539, 2000.
- [30] R. A. Mathies, E. T. Lagally, T. Kamei, W. H. Grover, C. N. Liu, J. R. Scherer, and R. A. Street, "Capillary Array Electrophoresis Bioprocessors," presented at

References

- Technical Digest of the 2002 Solid-State Sensor, Actuator, and Microsystems Workshop, Hilton Head Island, S.C., 2002.
- [31] B. H. van der Schoot, S. Jeanneret, A. van den Berg, and N. F. de Rooij, "A Silicon Integrated Miniature Chemical Analysis System," *Sensors and Actuators B-Chemical*, vol. 6, pp. 57-60, 1992.
- [32] C. C. Wong, J. H. Flemming, and D. R. Adkins, "Evaluation of Mini/Micro-Pumps for Micro-Chem-Lab," presented at 2002 ASME International Mechanical Engineering Congress and Exposition, New Orleans, 2002.
- [33] R. A. Clark, P. B. Hietpas, and A. G. Ewing, "Electrochemical Analysis in Picoliter Microvials," *Analytical Chemistry*, vol. 69, pp. 259-263, 1997.
- [34] A. L. Grosvenor, A. Feltus, R. C. Conover, S. Daunert, and K. W. Anderson, "Development of Binding Assays in Microfabricated Picoliter Vials: An Assay for Biotin," *Analytical Chemistry*, vol. 72, pp. 2590-2594, 2000.
- [35] P. C. H. Li and D. J. Harrison, "Transport, Manipulation, and Reaction of Biological Cells On-Chip Using Electrokinetic Effects," *Analytical Chemistry*, vol. 69, pp. 1564-1568, 1997.
- [36] P. A. Limbach and Z. Meng, "Integrating Micromachined Devices with Modern Mass Spectrometry," *Analyst*, vol. 127, pp. 693-700, 2002.
- [37] S. C. Terry, J. H. Jerman, and J. B. Angell, "Gas-Chromatographic Air Analyzer Fabricated on a Silicon Wafer," *IEEE Transactions on Electron Devices*, vol. 26, pp. 1880-1886, 1979.
- [38] C. H. Mastrangelo, M. A. Burns, and D. T. Burke, "Microfabricated Devices for Genetic Diagnostics," *Proceedings of the IEEE*, vol. 86, pp. 1769-1787, 1998.
- [39] B. Feldman, G. McGarraugh, A. Heller, N. Bohannon, J. Skyler, E. DeLeeuw, and D. Clarke, "FreeStyle: A Small-Volume Electrochemical Glucose Sensor for Home Blood Glucose Testing," *Diabetes Technology and Therapeutics*, vol. 2, 2000.
- [40] M. H. Craig, B. L. Bredenkamp, C. H. Williams, E. J. Rossous, V. J. Kelly, I. Kleinschmidt, A. Martineau, and G. F. Henry, "Field and Laboratory Comparative Evaluation of Ten Rapid Malaria Diagnostic Tests," *Transactions of the Royal Society of Tropical Medicine and Hygiene*, vol. 96, pp. 258-265, 2002.

References

- [41] Centers for Disease Control and Prevention, "Identification and Diagnosis of Parasites of Public Health Concern: Diagnostic Procedures for Blood Specimens."
- [42] D. Wiberg, B. Eyre, K. Shcheglov, V. White, and V. Garkanian, "Progress Toward Highly Miniaturized Vacuum Pumps," presented at 2nd Workshop on Harsh-Environment Mass Spectrometry, St. Petersburg, FL, 2001.
- [43] T. J. Watson, *Introduction to Mass Spectrometry*. Philadelphia: Lippincott-Raven, 1997.
- [44] U.S. Defense Advanced Research Projects Agency, "DARPA Mesoscale Machines program documentation."
- [45] M. M. Micci and A. D. Ketsdever, "Micropropulsion for Small Spacecraft." Reston, Va.: American Institute of Aeronautics and Astronautics, 2000.
- [46] P. Bruschi, A. Diligenti, and M. Piotta, "Micromachined Gas Flow Regulator for Ion Propulsion Systems," *IEEE Transactions on Aerospace and Electronic Systems*, vol. 38, pp. 982-988, 2002.
- [47] W. C. Krutzch and P. Cooper, "Introduction: Classification and Selection of Pumps," in *Pump Handbook*, I. J. Karassik, Ed.: McGraw-Hill, 2001.
- [48] W. M. Deen, *Analysis of Transport Phenomena*. New York: Oxford University Press, 1998.
- [49] W. W. Beck, "Pump Testing," in *Pump Handbook*, I. J. Karassik, Ed.: McGraw-Hill, 2001.
- [50] A. J. Bard, R. Parsons, and J. Jordan, "Standard Potentials in Aqueous Solutions." New York and Basel: Marcel Dekker, Inc., 1985.
- [51] P. Atkins and J. d. Paula, *Physical Chemistry*. New York: W.H. Freeman and Company, 2002.
- [52] J. O. M. Bockris, A. K. N. Reddy, and M. Gamboa-Aldeco, *Modern Electrochemistry*, vol. 2A: Kluwer Academic/Plenum, 2000.
- [53] A. J. Bard and L. R. Faulkner, *Electrochemical Methods: Fundamentals and Applications*: John Wiley & Sons, Inc., 2001.

References

- [54] V. Pretorius, B. J. Hopkins, and J. D. Schieke, "Electro-Osmosis: New Concept for High-Speed Liquid-Chromatography," *Journal of Chromatography*, vol. 99, pp. 23-30, 1974.
- [55] S. Liu and P. K. Dasgupta, "Flow-Injection Analysis in the Capillary Format using Electroosmotic Pumping," *Analytica Chimica Acta*, vol. 268, pp. 1-6, 1992.
- [56] D. J. Harrison, K. Fluri, K. Seiler, Z. Fan, C. S. Effenhauser, and A. Manz, "Micromachining a Miniaturized Capillary Electrophoresis-Based Chemical Analysis System on a Chip," *Science*, vol. 261, pp. 895-897, 1993.
- [57] A. Manz, C. S. Effenhauser, N. Burggraf, D. J. Harrison, K. Seiler, and K. Fluri, "Electroosmotic Pumping and Electrophoretic Separations for Miniaturized Chemical-Analysis Systems," *Journal of Micromechanics and Microengineering*, vol. 4, pp. 257-265, 1994.
- [58] S. C. Jacobson, R. Hergenroder, L. B. Koutny, and J. M. Ramsey, "Open-Channel Electrochromatography on a Microchip," *Analytical Chemistry*, vol. 66, pp. 2369-2373, 1994.
- [59] R. F. Probstein, *Physicochemical Hydrodynamics*. New York: Wiley, 1994.
- [60] P. H. Paul, D. W. Arnold, and D. J. Rakestraw, "Electrokinetic Generation of High Pressures using Porous Microstructures," presented at Micro Total Analysis Systems, Banff, Canada, 1998.
- [61] S. Yao, D. E. Hertzog, S. L. Zeng, J. C. Mikkelsen, and J. G. Santiago, "Porous Glass Electroosmotic Pumps: Design and Experiments," *Journal of Colloid and Interface Science*, vol. 268, pp. 143-153, 2003.
- [62] R. S. Ramsey and J. M. Ramsey, "Generating Electrospray from Microchip Devices Using Electroosmotic Pumping," *Analytical Chemistry*, vol. 69, pp. 1174-1178, 1997.
- [63] C.-H. Chen and J. G. Santiago, "A Planar Electroosmotic Micropump," *Journal of Microelectromechanical Systems*, vol. 11, pp. 672-683, 2002.
- [64] S. Shoji and M. Esashi, "Microflow Devices and Systems," *Journal of Micromechanics and Microengineering*, vol. 4, pp. 157-171, 1994.
- [65] P. Woias, "Micropumps - Summarizing the First Two Decades," presented at Microfluidics and BioMEMS, San Francisco, 2001.

References

- [66] N. T. Nguyen, X. Y. Huang, and T. K. Chuan, "MEMS-micropumps: A review," *Journal of Fluids Engineering-Transactions of the Asme*, vol. 124, pp. 384-392, 2002.
- [67] P. Woias, "Micropumps--past, progress and future prospects," *Sensors and Actuators B - Chemical*, vol. 105, pp. 28-38, 2005.
- [68] D. R. Reyes, D. Iossifidis, P. A. Auroux, and A. Manz, "Micro Total Analysis Systems. 1. Introduction, Theory, and Technology," *Analytical Chemistry*, vol. 74, pp. 2623-2636, 2002.
- [69] P. A. Auroux, D. Iossifidis, D. R. Reyes, and A. Manz, "Micro Total Analysis Systems. 2. Analytical Standard Operations and Applications," *Analytical Chemistry*, vol. 74, pp. 2637-2652, 2002.
- [70] P. Gravesen, J. Branebjerg, and O. S. Jensen, "Microfluidics - A Review," *Journal of Micromechanics and Microengineering*, vol. 3, pp. 168-182, 1993.
- [71] A. van den Berg and T. S. J. Lammerink, "Micro Total Analysis Systems: Microfluidic Aspects; Integration Concept and Applications," *Topics in Current Chemistry*, vol. 194, pp. 21-49, 1998.
- [72] M. Koch, A. Evans, and A. Brunnschweiler, *Microfluidic Technology and Applications*. Hertfordshire, England: Baldock, 2000.
- [73] N. A. Polson and M. A. Hayes, "Microfluidics: Controlling Fluids in Small Places," *Analytical Chemistry*, vol. 73, pp. 312A-319A, 2001.
- [74] N. T. Nguyen and S. Wereley, *Fundamentals and Applications of Microfluidics*: Artech House, International, 2002.
- [75] K. E. Petersen, "Silicon as a Mechanical Material," *Proceedings of the IEEE*, vol. 70, pp. 420-457, 1982.
- [76] G. T. A. Kovacs, *Micromachined Transducers Sourcebook*. Boston, MA: WCB, 1998.
- [77] J. W. Judy, "Microelectromechanical Systems (MEMS): Fabrication, Design and Applications," *Smart Mater. Struct.*, vol. 10, pp. 2001, 2001.
- [78] M. J. Madou, *Fundamentals of Microfabrication: The Science of Miniaturization*. Boca Raton: CRC Press, 2002.

References

- [79] M. Gad-el-Hak, "The MEMS Handbook." Boca Raton: CRC Press, 2002.
- [80] D. J. Laser and J. G. Santiago, "A Review of Micropumps," *Journal of Micromechanics and Microengineering*, vol. 14, pp. R35-R64, 2004.
- [81] H. T. G. van Lintel, F. C. M. van de Pol, and S. Bouwstra, "A Piezoelectric Micropump Based on Micromachining of Silicon," *Sensors and Actuators*, vol. 15, pp. 153-167, 1988.
- [82] H. T. G. van Lintel, "Micropump Having a Constant Output." U.S.: Westonbridge International Limited, 1992.
- [83] H. T. G. van Lintel, "Micropump with Improved Priming." U.S.: Westonbridge International, Ltd., 1993.
- [84] C. J. Morris and F. K. Forster, "Low-Order Modeling of Resonance for Fixed-Valve Micropumps Based on First Principles," *Journal of Microelectromechanical Systems*, vol. 12, pp. 325-334, 2003.
- [85] T. Bourouina, A. Bosseboeuf, and J. P. Grandchamp, "Design and Simulation of an Electrostatic Micropump for Drug-Delivery Applications," *Journal of Micromechanics and Microengineering*, vol. 7, pp. 186-188, 1997.
- [86] A. Olsson, G. Stemme, and E. Stemme, "A Numerical Design Study of the Valveless Diffuser Pump using a Lumped-Mass Model," *Journal of Micromechanics and Microengineering*, vol. 9, pp. 34-44, 1999.
- [87] W. A. Moussa and U. F. Gonzalez, "Simulation of MEMS Piezoelectric Micropump for Biomedical Applications," presented at ASME International Mechanical Engineering Congress and Exposition, New Orleans, LA, 2002.
- [88] C. J. Morris and F. K. Forster, "Optimization of a Circular Piezoelectric Bimorph for a Micropump Driver," *Journal of Micromechanics and Microengineering*, vol. 10, pp. 459-465, 2000.
- [89] T. Gerlach, "Microdiffusers as Dynamic Passive Valves for Micropump Applications," *Sensors and Actuators A-Physical*, vol. 69, pp. 181-191, 1998.
- [90] A. Ullman and I. Fono, "The Piezoelectric Valve-Less Pump - Improved Dynamic Model," *Journal of Microelectromechanical Systems*, vol. 11, pp. 655-664, 2002.

References

- [91] L. S. Pan, T. Y. Ng, X. H. Wu, and H. P. Lee, "Analysis of Valveless Micropumps with Inertial Effects," *J. Micromech. Microeng.*, vol. 13, pp. 390-399, 2003.
- [92] A. R. Gamboa, C. J. Morris, and F. Forster, "Optimized Fixed-Geometry Valves for Laminar Flow Micropumps," presented at ASME International Mechanical Engineering Congress and Exposition, Washington, D.C., 2003.
- [93] P. K. Kundu and I. M. Cohen, *Fluid Mechanics*: Academic Press, 2002.
- [94] W. C. Young and R. C. Budynas, *Roark's Formulas for Stress and Strain*, Seventh Edition ed. New York: McGraw-Hill, 2002.
- [95] M. Geradin and D. Rixen, *Mechanical Vibrations: Theory and Applications to Structural Dynamics*, 2nd ed. ed. Chichester, NY: John Wiley, 1997.
- [96] M. Richter, R. Linnemann, and P. Woias, "Robust Design of Gas and Liquid Micropumps," *Sensors and Actuators A-Physical*, vol. 68, pp. 480-486, 1998.
- [97] R. Linnemann, P. Woias, C.-D. Senfft, and J. A. Ditterich, "A Self-Priming and Bubble-Tolerant Piezoelectric Silicon Micropump for Liquids and Gases," presented at The Eleventh Annual International Workshop on Micro Electro Mechanical Systems, Heidelberg, Germany, 1998.
- [98] R. Zengerle and M. Richter, "Simulation of Microfluid Systems," *Journal of Micromechanics and Microengineering*, vol. 4, pp. 192-204, 1994.
- [99] T. T. Veenstra, J. W. Berenschot, J. G. E. Gardeniers, R. G. P. Sanders, M. C. Elwenspoek, and A. van den Berg, "Use of Selective Anodic Bonding to Create Micropump Chambers with Virtually No Dead Volume," *Journal of the Electrochemical Society*, vol. 148, pp. G68-G72, 2001.
- [100] J. G. Smits, "Piezoelectric Micropump with Microvalves." U.S., 1990.
- [101] S. Shoji, S. Nakagawa, and M. Esashi, "Micropump and Sample-Injector for Integrated Chemical Analyzing Systems," *Sensors and Actuators A-Physical*, vol. 21, pp. 189-192, 1990.
- [102] K.-S. Yun, I.-J. Cho, J.-U. Bu, C.-J. Kim, and E. Yoon, "A Surface-Tension Driven Micropump for Low-Voltage and Low-Power Operations," *Journal of Microelectromechanical Systems*, vol. 11, pp. 454-461, 2002.

References

- [103] J. M. Berg, R. Anderson, M. Anaya, B. Lahlouh, M. Holtz, and T. Dallas, "A Two-Stage Discrete Peristaltic Micropump," *Sensors and Actuators A-Physical*, vol. 104, pp. 6-10, 2003.
- [104] A. Olsson, G. Stemme, and E. Stemme, "A Valve-Less Planar Fluid Pump with 2 Pump Chambers," *Sensors and Actuators A-Physical*, vol. 47, pp. 549-556, 1995.
- [105] A. Olsson, P. Enoksson, G. Stemme, and E. Stemme, "A Valve-less Planar Pump Isotropically Etched in Silicon," *Journal of Micromechanics and Microengineering*, vol. 6, pp. 87-91, 1996.
- [106] R. Zengerle, J. Ulrich, S. Kluge, M. Richter, and A. Richter, "A Bidirectional Silicon Micropump," *Sensors and Actuators A-Physical*, vol. 50, pp. 81-86, 1995.
- [107] E. Stemme and G. Stemme, "A Valveless Diffuser/Nozzle-Based Fluid Pump," *Sensors and Actuators A-Physical*, vol. 39, pp. 159-167, 1993.
- [108] K.-P. Kamper, J. Dopfer, W. Ehrfeld, and S. Oberbeck, "A Self-Filling Low-Cost Membrane Micropump," presented at Eleventh Annual International Workshop on Micro Electro Mechanical Systems, Heidelberg, Germany, 1998.
- [109] thinXXS Microtechnology, "thinXXS XXS2000 data sheet."
- [110] S. Bohm, W. Olthuis, and P. Bergveld, "A Plastic Micropump Constructed with Conventional Techniques and Materials," *Sensors and Actuators A-Physical*, vol. 77, pp. 223-228, 1999.
- [111] M. C. Carrozza, N. Croce, B. Magnani, and P. Dario, "A Piezoelectric-Driven Stereolithography-Fabricated Micropump," *Journal of Micromechanics and Microengineering*, vol. 5, pp. 177-179, 1995.
- [112] A. Wego and L. Pagel, "A Self-Filling Micropump Based on PCB Technology," *Sensors and Actuators A-Physical*, vol. 88, pp. 220-226, 2001.
- [113] H. J. Yoon, W. Y. Sim, and S. S. Yang, "The Fabrication and Test of a Phase-Change Micropump," presented at 2001 ASME International Mechanical Engineering Congress and Exposition, New York, NY, 2001.
- [114] D. Maillefer, H. T. G. van Lintel, G. Rey-Mermet, and R. Hirschi, "A High-Performance Silicon Micropump for an Implantable Drug Delivery System," presented at Twelfth IEEE International Micro Electro Mechanical Systems Conference, Orlando, FL, 1999.

References

- [115] Debiotech, "MIP Implantable product literature."
- [116] M. Esashi, S. Shoji, and A. Nakano, "Normally Closed Microvalve and Micropump Fabricated on a Silicon-Wafer," *Sensors and Actuators*, vol. 20, pp. 163-169, 1989.
- [117] M. Stehr, S. Messner, H. Sandmaier, and R. Zengerle, "The VAMP: A New Device for Handling Liquids or Gases," *Sensors and Actuators A-Physical*, vol. 57, pp. 153-157, 1996.
- [118] H. Q. Li, D. C. Roberts, K. T. Steyn, J. A. Turner, O. Carretero, Y.-H. Yahlioglu, L. Su, N. W. Saggere, S. M. Spearing, M. A. Schmidt, R. Mlcak, and K. S. Breuer, "A High Frequency High Flow Rate Piezoelectrically-Driven MEMS Micropump," presented at 2000 Solid-State Sensor and Actuator Workshop, Hilton Head, S.C., 2000.
- [119] F. M. Demer, "Ink Jet Printer." U.S.: International Business Machines Corporation, 1974.
- [120] E. Bassous, L. Kuhn, and H. H. Taub, "Jet Nozzle Structure for Electrohydrodynamic Droplet Formation and Ink Jet Printing System Therewith." U.S.: International Business Machines Corporation, 1976.
- [121] A. Juliana, R. W. Koepcke, R. N. Mills, and F. E. Talke, "Voltage Modulated Drop-On-Demand Ink Jet Method and Apparatus." U.S.: International Business Machines Corporation, 1981.
- [122] J. Fraden, *Handbook of Modern Sensors: Physics, Designs, and Applications*. New York, NY: Springer-Verlag, 1996.
- [123] S. Li and S. Chen, "Analytical Analysis of a Circular PZT Actuator for Valveless Micropumps," *Sensors and Actuators A-Physical*, vol. 104, pp. 151-161, 2003.
- [124] S. H. Chang and B. C. Du, "Optimization of Asymmetric Bimorphic Disk Transducers," *J. Acoust. Soc. Am.*, vol. 109, pp. 194-202, 2001.
- [125] A. Olsson, G. Stemme, and E. Stemme, "Diffuser-Element Design Investigation for Valve-less Pumps," *Sensors and Actuators A-Physical*, vol. 57, pp. 137-143, 1996.
- [126] A. Olsson, P. Enoksson, G. Stemme, and E. Stemme, "Micromachined Flat-Walled Valveless Diffuser Pumps," *Journal of Microelectromechanical Systems*, vol. 6, pp. 161-166, 1997.

References

- [127] V. Gass, B. H. Vanderschoot, S. Jeanneret, and N. F. Derooij, "Integrated Flow-Regulated Silicon Micropump," *Sensors and Actuators A-Physical*, vol. 43, pp. 335-338, 1994.
- [128] J. H. Park, S. Yokota, and K. Yoshida, "A Piezoelectric Micropump using Resonance Drive with High Power Density," *JSME International Journal Series C-Mechanical Systems Machine Elements and Manufacturing*, vol. 45, pp. 502-509, 2002.
- [129] M. Koch, N. Harris, R. Maas, A. G. R. Evans, N. M. White, and A. Brunnschweiler, "A Novel Micropump Design with Thick-Film Piezoelectric Actuation," *Measurement Science & Technology*, vol. 8, pp. 49-57, 1997.
- [130] M. Koch, N. Harris, A. G. R. Evans, N. M. White, and A. Brunnschweiler, "A Novel Micromachined Pump based on Thick-Film Piezoelectric Actuation," *Sensors and Actuators A-Physical*, vol. 70, pp. 98-103, 1998.
- [131] M. Koch, A. G. R. Evans, and A. Brunnschweiler, "The Dynamic Micropump Driven with a Screen Printed PZT Actuator," *Journal of Micromechanics and Microengineering*, vol. 8, pp. 119-122, 1998.
- [132] C. G. J. Schabmueller, M. Koch, M. E. Mokhtari, A. G. R. Evans, A. Brunnschweiler, and H. Sehr, "Self-Aligning Gas/Liquid Micropump," *Journal of Micromechanics and Microengineering*, vol. 12, pp. 420-424, 2002.
- [133] N. N. Rogacheva, *The Theory of Piezoelectric Shells and Plates*: CRC Press, Inc., 1994.
- [134] A. B. Dobrucki and P. Pruchnicki, "Theory of Piezoelectric Axisymmetric Bimorph," *Sensors and Actuators A-Physical*, vol. 58, pp. 203-212, 1997.
- [135] Y. H. Mu, N. P. Hung, and K. A. Ngoi, "Optimisation Design of a Piezoelectric Micropump," *Int J Adv Manuf Technol*, vol. 15, pp. 573-576, 1999.
- [136] B. E. Williams and F. K. Forster, "Micropump Design for Optimum Pressure/Flow Characteristics," presented at 2001 ASME International Mechanical Engineering Congress and Exposition, New York, 2001.
- [137] D. C. Roberts, J. L. Steyn, H. Q. Li, K. T. Turner, R. Mlcak, L. Saggere, S. M. Spearing, M. A. Schmidt, and N. W. Hagood, "A High-Frequency, High-Stiffness Piezoelectric Micro-Actuator for Hydraulic Applications," presented at Transducers '01, Munich, Germany, 2001.

References

- [138] F. C. M. van de Pol, H. T. G. van Lintel, M. Elwenspoek, and J. H. J. Fluitman, "A Thermopneumatic Micropump Based on Micro-Engineering Techniques," presented at 5th International Conference on Solid-State Sensors and Actuators/Eurosensors III, 1989.
- [139] F. C. M. van de Pol, H. T. G. van Lintel, M. Elwenspoek, and J. H. J. Fluitman, "A Thermopneumatic Micropump Based on Micro-Engineering Techniques," *Sensors and Actuators A-Physical*, vol. 21, pp. 198-202, 1990.
- [140] M. Elwenspoek, T. S. J. Lammerink, R. Miyake, and J. H. J. Fluitman, "Towards Integrated Microliquid Handling Systems," *Journal of Micromechanics and Microengineering*, vol. 4, pp. 227-245, 1994.
- [141] W. K. Schomburg, J. Vollmer, B. Bustgens, J. Fahrenberg, H. Hein, and W. Menz, "Microfluidic Components in LIGA Technique," *Journal of Micromechanics and Microengineering*, vol. 4, pp. 186-191, 1994.
- [142] C. Grosjean and Y. C. Tai, "A Thermopneumatic Peristaltic Micropump," presented at The 1999 International Conference on Solid-State Sensors and Actuators (Transducers '99), Sendai, Japan, 1999.
- [143] O. C. Jeong and S. S. Yang, "Fabrication and Test of a Thermopneumatic Micropump with a Corrugated p+ Diaphragm," *Sensors and Actuators A-Physical*, vol. 83, pp. 249-255, 2000.
- [144] W. Y. Sim, Y. H.J., O. C. Jeong, and S. S. Yang, "A Phase-Change Type Micropump with Aluminum Flap Valves," *J. Micromech. Microeng.*, vol. 13, pp. 286-294, 2003.
- [145] M. C. Acero, J. A. Plaza, J. Esteve, M. Carmona, S. Marco, and J. Samitier, "Design of a Modular Micropump based on Anodic Bonding," *Journal of Micromechanics and Microengineering*, vol. 7, pp. 179-182, 1997.
- [146] M. Carmona, S. Marco, J. Samitier, and J. R. Morante, "Dynamic Simulations of Micropumps," *Journal of Micromechanics and Microengineering*, vol. 6, pp. 128-130, 1996.
- [147] J. A. Folta, N. F. Raley, and E. W. Hee, "Design, Fabrication, and Testing of a Miniature Peristaltic Membrane Pump," presented at Solid-State Sensor and Actuator Workshop, Hilton Head Island, SC, 1992.
- [148] J. H. Tsai and L. Lin, "A Thermal-Bubble-Actuated Micronozzle-Diffuser Pump," *Journal of Microelectromechanical Systems*, vol. 11, pp. 665-671, 2002.

References

- [149] S. Zimmermann, J. A. Frank, D. Liepmann, and A. P. Pisano, "A Planar Micropump Utilizing Thermopneumatic Actuation and In-Plane Flap Valves," presented at MEMS 2004: 17th IEEE International Conference on Micro Electro Mechanical Systems, Maastricht, The Netherlands, 2004.
- [150] W. C. Tang, T. C. H. Nguyen, and R. T. Howe, "Laterally Driven Polysilicon Resonant Microstructures," *Sensors and Actuators*, vol. 20, pp. 25-32, 1989.
- [151] D. J. Griffiths, *Introduction to Electrodynamics*. Upper Saddle River, N.J.: Prentice Hall, 1999.
- [152] R. Zengerle, W. Geiger, M. Richter, J. Ulrich, S. Kluge, and A. Richter, "Transient Measurements on Miniaturized Diaphragm Pumps in Microfluid Systems," *Sensors and Actuators a-Physical*, vol. 47, pp. 557-561, 1995.
- [153] C. Cabuz, E. I. Cabuz, W. R. Herb, T. Rolfer, and D. Zook, "Mesoscopic Sampler Based on 3D Array of Electrostatically Activated Diaphragms," presented at Transducers '99, Japan, 1999.
- [154] T. Bourouina and J. P. Grandchamp, "Modeling Micropumps with Electrical Equivalent Networks," *Journal of Micromechanics and Microengineering*, vol. 6, pp. 398-404, 1996.
- [155] O. Francais, I. Dufour, and E. Sarraute, "Analytical static modelling and optimization of electrostatic micropumps," *Journal of Micromechanics and Microengineering*, vol. 7, pp. 183-185, 1997.
- [156] O. Francais and I. Dufour, "Dynamic Simulation of an Electrostatic Micropump with Pull-In and Hysteresis Phenomena," *Sensors and Actuators A-Physical*, vol. 70, pp. 56-60, 1998.
- [157] P. Voigt, G. Schrag, and G. Wachutka, "Electrofluidic full-system modelling of a flap valve micropump based on Kirchhoffian network theory," *Sensors and Actuators A-Physical*, vol. 66, pp. 9-14, 1998.
- [158] R. Rapp, W. K. Schomburg, D. Maas, J. Schulz, and W. Stark, "Liga Micropump for Gases and Liquids," *Sensors and Actuators A-Physical*, vol. 40, pp. 57-61, 1994.
- [159] M. A. Unger, H. P. Chou, T. Thorsen, A. Scherer, and S. R. Quake, "Monolithic Microfabricated Valves and pumps by Multilayer Soft Lithography," *Science*, vol. 288, pp. 113-116, 2000.

References

- [160] W. H. Grover, A. M. Skelley, C. N. Liu, E. T. Lagally, and R. A. Mathies, "Monolithic Membrane Valves and Diaphragm Pumps for Practical Large-Scale Integration into Glass Microfluidic Devices," *Sensors and Actuators B-Chemical*, vol. 89, pp. 315-323, 2003.
- [161] P. Dario, N. Croce, M. C. Carrozza, and G. Varallo, "A Fluid Handling System for a Chemical Microanalyzer," *Journal of Micromechanics and Microengineering*, vol. 6, pp. 95-98, 1996.
- [162] E. Meng, X.-Q. Wang, H. Mak, and Y. C. Tai, "A Check-Valved Silicone Diaphragm Pump," presented at MEMS 2000: 13th Ann. International Conference on Micro Electro Mechanical Systems, Miyazaki, Japan, 2000.
- [163] C. Bisson, J. Campbell, R. Cheadle, M. Chomiak, J. Lee, C. Miller, C. Milley, P. Pialis, S. Shaw, W. Weiss, and C. Widrig, "A Microanalytical Device for the Assessment of Coagulation Parameters in Whole Blood," presented at Solid-State Sensor and Actuator Workshop, Hilton Head Island, S.C., 1998.
- [164] Q. L. Gong, Z. Y. Zhou, Y. H. Yang, and X. H. Wang, "Design, Optimization and Simulation on Microelectromagnetic Pump," *Sensors and Actuators A-Physical*, vol. 83, pp. 200-207, 2000.
- [165] S. Santra, P. Holloway, and C. D. Batich, "Fabrication and Testing of a Magnetically Actuated Micropump," *Sensors and Actuators B-Chemical*, vol. 87, pp. 358-364, 2002.
- [166] W. L. Benard, H. Kahn, A. H. Heuer, and M. A. Huff, "Thin-Film Shape-Memory Alloy Actuated Micropumps," *Journal of Microelectromechanical Systems*, vol. 7, pp. 245-251, 1998.
- [167] E. Makino, T. Mitsuya, and T. Shibata, "Fabrication of TiNi shape memory micropump," *Sensors and Actuators a-Physical*, vol. 88, pp. 256-262, 2001.
- [168] J. Pang, Q. Zou, Z. Tan, X. Qian, L. Liu, and Z. Li, "The Study of Single-Chip Integrated Microfluidic System," presented at IEEE 5th Int. Conf. on Solid-State and Integrated Circuit Technologies, Beijing, PRC, 1998.
- [169] Q. B. Zou, U. Sridhar, and R. M. Lin, "A Study on Micromachined Bimetallic Actuation," *Sensors and Actuators A-Physical*, vol. 78, pp. 212-219, 1999.
- [170] C. P. Hsu and W. S. Hsu, "A Two-Way Membrane-Type Micro-Actuator with Continuous Deflections," *Journal of Micromechanics and Microengineering*, vol. 10, pp. 387-394, 2000.

References

- [171] A. Beskok and A. R. Srinivasa, "Simulation and Analysis of a Magnetoelastically Driven Micro-Pump," *Journal of Fluids Engineering-Transactions of the ASME*, vol. 123, pp. 435-438, 2001.
- [172] P. K. Yuen, L. J. Kricka, and P. Wilding, "Semi-Disposable Microvalves for use with Microfabricated Devices or Microchips," *Journal of Micromechanics and Microengineering*, vol. 10, pp. 401-409, 2000.
- [173] M. Koch, A. G. R. Evans, and A. Brunnschweiler, "Characterization of Micromachined Cantilever Valves," *J. Micromech. Microeng.*, vol. 7, pp. 221-223, 1997.
- [174] M. Carmona, S. Marco, J. Samitier, M. C. Acero, J. A. Plaza, and J. Esteve, "An Analytical Model for Passive Microvalves," *Sensors and Materials*, vol. 13, pp. 373-383, 2001.
- [175] J. Voldman, M. L. Gray, and M. A. Schmidt, "An Integrated Liquid Mixer/Valve," *Journal of Microelectromechanical Systems*, vol. 9, pp. 295-302, 2000.
- [176] B. K. Paul and T. Terhaar, "Comparison of Two Passive Microvalve Designs for Microlamination Architectures," *Journal of Micromechanics and Microengineering*, vol. 10, pp. 15-20, 2000.
- [177] D. Accoto, M. C. Carrozza, and P. Dario, "Modelling of Micropumps Using Unimorph Piezoelectric Actuator and Ball Valves," *Journal of Micromechanics and Microengineering*, vol. 10, pp. 277-281, 2000.
- [178] H. Jerman, "Electrically-Activated, Normally-Closed Diaphragm Valves," *J. Micromech. Microeng.*, vol. 4, pp. 210-215, 1994.
- [179] K. Sato and M. Shikida, "An Electrostatically Actuated Gas Valve with an S-Shaped Film Element," *Journal of Micromechanics and Microengineering*, vol. 4, pp. 205-209, 1994.
- [180] X. Yang, A. Holke, and M. A. Schmidt, "An Electrostatic, On/Off MEMS Valve for Gas Fuel Delivery of a Microengine," presented at Solid-State Sensor, Actuator, and Microsystems Workshop, Hilton Head Island, S.C., 2002.
- [181] L. Yobas, M. A. Huff, F. J. Lisy, and D. M. Durand, "A Novel Bulk-Micromachined Electrostatic Microvalve with a Curved-Compliant Structure Applicable for a Pneumatic Tactile Display," *Journal of Microelectromechanical Systems*, vol. 10, pp. 187-196, 2001.

References

- [182] N. Vandelli, D. Wroblewski, M. Velonis, and T. Bifano, "Development of a MEMS Microvalve Array for Fluid Flow Control," *Journal of Microelectromechanical Systems*, vol. 7, pp. 395-403, 1998.
- [183] J. Fahrenberg, W. Bier, D. Maas, W. Menz, R. Ruprecht, and W. K. Schomburg, "A Microvalve System Fabricated by Thermoplastic Molding," *Journal of Micromechanics and Microengineering*, vol. 5, pp. 169-171, 1995.
- [184] C. Goll, W. Bacher, B. Bustgens, D. Maas, W. Menz, and W. K. Schomburg, "Microvalves with Bistable Buckled Polymer Diaphragms," *Journal of Micromechanics and Microengineering*, vol. 6, pp. 77-79, 1996.
- [185] W. K. Schomburg and C. Goll, "Design Optimization of Bistable Microdiaphragm Valves," *Sensors and Actuators A-Physical*, vol. 64, pp. 259-264, 1998.
- [186] D. Baechi, R. Buser, and J. Dual, "A High Density Microchannel Network with Integrated Valves and Photodiodes," *Sensors and Actuators A-Physical*, vol. 95, pp. 77-83, 2002.
- [187] I. Chakraborty, W. C. Tang, D. P. Bame, and T. K. Tang, "MEMS Micro-Valve for Space Applications," *Sensors and Actuators A-Physical*, vol. 83, pp. 188-193, 2000.
- [188] D. Bosch, B. Heimhofer, G. Muck, H. Seidel, U. Thumser, and W. Welser, "A Silicon Microvalve with Combined Electromagnetic/Electrostatic Actuation," *Sensors and Actuators A-Physical*, vol. 37-8, pp. 684-692, 1993.
- [189] P. W. Barth, "Silicon Microvalves for Gas Flow Control," presented at Transducers '95, The 8th International Conference on Solid-State Sensors and Actuators/Eurosensors IX, Stockholm, Sweden, 1995.
- [190] T. Otori, S. Shoji, K. Miura, and A. Yotsumoto, "Partly Disposable Three-Way Microvalve for a Medical Micro Total Analysis System (μ TAS)," *Sensors and Actuators A-Physical*, vol. 64, pp. 57-62, 1998.
- [191] M. Capanu, J. G. Boyd, and P. J. Hesketh, "Design; Fabrication; and Testing of a Bistable Electromagnetically Actuated Microvalve," *Journal of Microelectromechanical Systems*, vol. 9, pp. 181-189, 2000.
- [192] S. Bohm, G. J. Burger, M. T. Korthorst, and F. Roseboom, "A Micromachined Silicon Valve Driven by a Miniature Bi-Stable Electro-Magnetic Actuator," *Sensors and Actuators A-Physical*, vol. 80, pp. 77-83, 2000.

References

- [193] M. Kohl, D. Dittmann, E. Quandt, and B. Winzek, "Thin Film Shape Memory Microvalves with Adjustable Operation Temperature," *Sensors and Actuators A-Physical*, vol. 83, pp. 214-219, 2000.
- [194] K. Yoshida, M. Kikuchi, J. H. Park, and S. Yokota, "Fabrication of Micro Electro-Rheological Valves (ER valves) by Micromachining and Experiments," *Sensors and Actuators A-Physical*, vol. 95, pp. 227-233, 2002.
- [195] T. Gerlach and H. Wurmus, "Working Principle and Performance of the Dynamic Micropump," *Sensors and Actuators A-Physical*, vol. 50, pp. 135-140, 1995.
- [196] F. Forster, R. Bardell, M. Afromowitz, N. Sharma, and A. Blanchard, "Design, Fabrication, and Testing of Fixed-Valve Micropumps," presented at ASME International Mechanical Engineering Congress and Exposition, San Francisco, CA, 1995.
- [197] L.-S. Jang, C. J. Morris, N. R. Sharma, R. L. Bardell, and F. K. Forster, "Transport of Particle-Laden Fluids through Fixed-Valve Micropumps," presented at ASME 1999, MEMS-Vol. 1, Nashville, TN, 1999.
- [198] H. Andersson, W. van der Wijngaart, P. Nilsson, P. Enoksson, and G. Stemme, "A Valve-Less Diffuser Micropump for Microfluidic Analytical Systems," *Sensors and Actuators B-Chemical*, vol. 72, pp. 259-265, 2001.
- [199] M. Heschel, M. Mullenborn, and S. Bouwstra, "Fabrication and characterization of truly 3-D diffuser/nozzle microstructures in silicon," *Journal of Microelectromechanical Systems*, vol. 6, pp. 41-47, 1997.
- [200] X. N. Jiang, Z. Y. Zhou, X. Y. Huang, Y. Li, Y. Yang, and C. Y. Liu, "Micronozzle/Diffuser Flow and its Application in Micro Valveless Pumps," *Sensors and Actuators A-Physical*, vol. 70, pp. 81-87, 1998.
- [201] A. Olsson, G. Stemme, and E. Stemme, "Numerical and Experimental Studies of Flat-Walled Diffuser Elements for Valve-Less Micropumps," *Sensors and Actuators A-Physical*, vol. 84, pp. 165-175, 2000.
- [202] L. S. Pan, T. Y. Ng, G. R. Liu, K. Y. Lam, and T. Y. Jiang, "Analytical Solutions for the Dynamic Analysis of a Valveless Micropump: A Fluid-Membrane Coupling Study," *Sensors and Actuators A-Physical*, vol. 93, pp. 173-181, 2001.
- [203] T. T. Veenstra, N. R. Sharma, F. K. Forster, J. G. E. Gardeniers, M. C. Elwenspoek, and A. van den Berg, "The Design of an In-Plane Compliance

References

- Structure for Microfluidical Systems," *Sensors and Actuators B-Chemical*, vol. 81, pp. 377-383, 2002.
- [204] R. H. Liu, Q. Yu, and D. J. Beebe, "Fabrication and Characterization of Hydrogel-Based Microvalves," *Journal of Microelectromechanical Systems*, vol. 11, pp. 45-53, 2002.
- [205] S. Matsumoto, A. Klein, and R. Maeda, "Development of Bi-Directional Valve-Less Micropump for Liquid," presented at Twelfth IEEE International Micro Electro Mechanical Systems Conference, Orlando, FL, 1999.
- [206] Y. Yun, K. M. Lee, G. Lim, J. H. Lee, and Y. E. Pak, "Modeling of Diffuser/Nozzle Micropump under Electrohydrodynamic Backflow Control," presented at ASME FEDSM'00, Boston, Massachusetts, 2000.
- [207] B. J. Kirby, T. J. Shepodd, and E. F. Hasselbrink, Jr., "Voltage-Addressable On/Off Microvalves for High-Pressure Microchip Separations," *Journal of Chromatography A*, vol. 979, pp. 147-154, 2002.
- [208] J. Dopfer, M. Clemens, W. Ehrfeld, S. Jung, K. P. Kamper, and H. Lehr, "Micro Gear Pumps for Dosing of Viscous Fluids," *Journal of Micromechanics and Microengineering*, vol. 7, pp. 230-232, 1997.
- [209] A. S. Dewa, K. Degn, D. C. Ritter, C. Bonham, G. Guckel, and S. Massood-Ansari, "Development of LIGA-Fabricated, Self-Priming, In-Line Gear Pumps," presented at Transducers '97, Chicago, IL, 1997.
- [210] M. I. Kilani, P. C. Galambos, Y. S. Haik, and C.-J. Chen, "Electrostatically Actuated Surface Micromachined Offset Planetary Gear Pump Design," presented at 2001 ASME International Mechanical Engineering Congress and Exposition, New York, NY, 2001.
- [211] A. Terray, J. Oakey, and D. W. M. Marr, "Microfluidic Control using Colloidal Devices," *Science*, vol. 296, pp. 1841-1844, 2002.
- [212] M. Sen, D. Wajerski, and M. Gad el Hak, "A Novel Pump for MEMS Applications," *Journal of Fluids Engineering-Transactions of the ASME*, vol. 118, pp. 624-627, 1996.
- [213] D. DeCourtye, M. Sen, and M. Gad el Hak, "Analysis of Viscous Micropumps and Microturbines," *International Journal of Computational Fluid Dynamics*, vol. 10, pp. 13-25, 1998.

References

- [214] A. Hatch, A. E. Kamholz, G. Holman, P. Yager, and K. F. Bohringer, "A Ferrofluidic Magnetic Micropump," *Journal of Microelectromechanical Systems*, vol. 10, pp. 215-221, 2001.
- [215] M. V. Sefton, "Implantable Pumps," in *CRC Critical Reviews in Biomedical Engineering*, vol. 14, 1987, pp. 201-240.
- [216] E. Cabuz, J. Schwichtenberg, B. DeMers, E. Satren, A. Padmanabhan, and C. Cabuz, "MEMS-Based Flow Controller for Flow Cytometry," presented at 2002 Solid-State Sensors, Actuators, and Microsystems Workshop, Hilton Head, S.C., 2002.
- [217] N. R. Tas, J. W. Berenschot, T. S. J. Lammerink, M. Elwenspoek, and A. van den Berg, "Nanofluidic Bubble Pump using Surface Tension Directed Gas Injection," *Analytical Chemistry*, vol. 74, pp. 2224-2227, 2002.
- [218] C. P. Jen and Y. C. Lin, "Design and Simulation of Bi-Directional Microfluid Driving Systems," *Journal of Micromechanics and Microengineering*, vol. 12, pp. 115-121, 2002.
- [219] J. Evans, D. Liepmann, and A. P. Pisano, "Planar Laminar Mixer," presented at MEMS '97: IEEE 10th Annual International Workshop on Micro Electro Mechanical Systems, Nagoya, Japan, 1997.
- [220] K. Handique, D. T. Burke, C. H. Mastrangelo, and M. A. Burns, "On-Chip Thermopneumatic Pressure for Discrete Drop Pumping," *Analytical Chemistry*, vol. 73, pp. 1831-1838, 2001.
- [221] T. K. Jun and C. J. Kim, "Valveless Pumping using Traversing Vapor Bubbles in Microchannels," *Journal of Applied Physics*, vol. 83, pp. 5658-5664, 1998.
- [222] Y. J. Song and T. S. Zhao, "Modelling and Test of a Thermally-Driven Phase-Change Nonmechanical Micropump," *Journal of Micromechanics and Microengineering*, vol. 11, pp. 713-719, 2001.
- [223] S. Bohm, B. Timmer, W. Olthuis, and P. Bergveld, "A Closed-Loop Controlled Electrochemically Actuated micro-Dosing System," *Journal of Micromechanics and Microengineering*, vol. 10, pp. 498-504, 2000.
- [224] S. W. Lee, O. C. Jeong, and S. S. Yang, "The Fabrication of a Micro Injector Actuated by Boiling and/or Electrolysis," presented at Eleventh Annual International Workshop on Micro Electro Mechanical Systems, Heidelberg, Germany, 1998.

References

- [225] Z. X. Li, M. R. Wang, and L. Y. Tan, "Experimental Investigation on Phase Transformation Type Micropump," *Chinese Science Bulletin*, vol. 47, pp. 518-522, 2002.
- [226] L. W. Lin, A. P. Pisano, and V. P. Carey, "Thermal Bubble Formation on Polysilicon Micro Resistors," *Journal of Heat Transfer-Transactions of the ASME*, vol. 120, pp. 735-742, 1998.
- [227] J. E. Colgate and H. Matsumoto, "An Investigation of Electrowetting-Based Microactuation," *J. Vac. Sci. Technol. A*, vol. 8, pp. 3625-3633, 1990.
- [228] H. Matsumoto and J. E. Colgate, "Preliminary Investigation of Micropumping Based on Electrical Control of Interfacial Tension," presented at IEEE MEMS '90, Napa Valley, CA, 1990.
- [229] J. Lee and C. J. Kim, "Surface-Tension-Driven Microactuation Based on Continuous Electrowetting," *Journal of Microelectromechanical Systems*, vol. 9, pp. 171-180, 2000.
- [230] J. Lee, H. Moon, J. Fowler, T. Schoellhammer, and C. J. Kim, "Electrowetting and Electrowetting-on-Dielectric for Microscale Liquid Handling," *Sensors and Actuators A-Physical*, vol. 95, pp. 259-268, 2002.
- [231] D. E. Kataoka and S. M. Troian, "Patterning Liquid Flow on the Microscopic Scale," *Nature*, vol. 402, pp. 794-797, 1999.
- [232] T. S. Sammarco and M. A. Burns, "Thermocapillary Pumping of Discrete Drops in Microfabricated Analysis Devices," *AIChE Journal*, vol. 45, pp. 350-366, 1999.
- [233] S. J. Stolzenberg and W. H. Linkenheimer, "Osmotic Fluid Reservoir for Osmotically Activated Long-Term Continuous Injector Device." U.S.: American Cyanamid Company, 1971.
- [234] Y.-C. Su, L. Lin, and A. P. Pisano, "A Water-Powered Micro Drug Delivery System," presented at 2002 Solid-State Sensor, Actuator and Microsystem Workshop, Hilton Head, S.C., 2002.
- [235] L. Ying, A. Bruckbauer, A. M. Rothery, Y. E. Korchev, and D. Klenerman, "Programmable Delivery of DNA through a Nanopipet," *Analytical Chemistry*, vol. 74, pp. 1380-1385, 2002.

References

- [236] P. Cooper, "Centrifugal Pump Theory," in *Pump Handbook*, I. J. K. e. al., Ed. New York: McGraw-Hill, 2000.
- [237] L. G. Frechette, S. A. Jacobson, K. S. Breuer, F. F. Ehrich, R. Ghodssi, R. Khanna, C. W. Wong, X. Zhang, M. A. Schmidt, and A. H. Epstein, "Demonstration of a Microfabricated High-Speed Turbine Supported on Gas Bearings," presented at 2000 Solid-State Sensor and Actuator Workshop, Hilton Head, S.C., 2000.
- [238] A. P. London, A. H. Epstein, and J. L. Kerrebrock, "High-Pressure Bipropellant Microrocket Engine," *Journal of Propulsion and Power*, vol. 17, pp. 780-787, 2001.
- [239] A. Deux, "Design of a Silicon Microfabricated Rocket Engine Turbopump," MIT, 2001.
- [240] S. Pennathur, "Micro-Scale Turbopump Blade Cavitation," vol. Master's: MIT, 2001.
- [241] O. Marseille, N. Habib, H. Reul, and G. Rau, "Implantable Micropump System for Augmented Liver Perfusion," *Artificial Organs*, vol. 22, pp. 458-460, 1998.
- [242] J. R. Melcher, *Continuum Electromechanics*. Cambridge, MA: MIT Press, 1981.
- [243] S. H. Ahn and Y. K. Kim, "Fabrication and Experiment of a Planar Micro Ion Drag Pump," *Sensors and Actuators A-Physical*, vol. 70, pp. 1-5, 1998.
- [244] S. F. Bart, L. S. Tavrow, M. Mehregany, and J. H. Lang, "Microfabricated Electrohydrodynamic Pumps," *Sensors and Actuators a-Physical*, vol. 21, pp. 193-197, 1990.
- [245] G. Fuhr, T. Schnelle, and B. Wagner, "Traveling Wave-Driven Microfabricated Electrohydrodynamic Pumps for Liquids," *Journal of Micromechanics and Microengineering*, vol. 4, pp. 217-226, 1994.
- [246] J. Darabi, M. M. Ohadi, and D. DeVoe, "An Electrohydrodynamic Polarization Micropump for Electronic Cooling," *Journal of Microelectromechanical Systems*, vol. 10, pp. 98-106, 2001.
- [247] S. Jeong and J. Seyed-Yagoobi, "Experimental Study of Electrohydrodynamic Pumping through Conduction Phenomenon," *Journal of Electrostatics*, vol. 56, pp. 123-133, 2002.

References

- [248] P. Atten and J. Seyed-Yagoobi, "Electrohydrodynamically Induced Dielectric Liquid Flow Through Pure Conduction in Point/Plane Geometry," *IEEE Transactions on Dielectrics and Electrical Insulation*, vol. 10, pp. 27-36, 2003.
- [249] A. Richter, A. Plettner, K. A. Hofmann, and H. Sandmaier, "A Micromachined Electrohydrodynamic (EHD) Pump," *Sensors and Actuators A-Physical*, vol. 29, pp. 159-168, 1991.
- [250] C. C. Wong, D. R. Adkins, and D. Chu, "Development of a Micropump for Microelectronic Cooling," *Microelectromechanical Systems, ASME 1996*, vol. 59, 1996.
- [251] J. Darabi, M. Rada, M. Ohadi, and J. Lawler, "Design, Fabrication, and Testing of an Electrohydrodynamic Ion-Drag Micropump," *Journal of Microelectromechanical Systems*, vol. 11, pp. 684-690, 2002.
- [252] J. M. Crowley, G. S. Wright, and J. C. Chato, "Selecting a Working Fluid to Increase the Efficiency and Flow Rate of an EHD Pump," *IEEE Transactions on Industry Applications*, vol. 26, pp. 42-49, 1990.
- [253] M. Watanabe, J. Zheng, A. Hara, H. Shirai, and T. Hirai, "A Pumping Technique Using Electrohydrodynamic Flow inside a Gel," *IEEE Transactions on Dielectrics and Electrical Insulation*, vol. 10, pp. 181-185, 2003.
- [254] P. K. Dasgupta and S. Liu, "Auxiliary Electroosmotic Pumping in Capillary Electrophoresis," *Analytical Chemistry*, vol. 66, pp. 3060-3065, 1994.
- [255] T. E. McKnight, C. T. Culbertson, S. C. Jacobson, and J. M. Ramsey, "Electroosmotically Induced Hydraulic Pumping with Integrated Electrodes in Microfluidic Devices," *Analytical Chemistry*, vol. 73, pp. 4045-4049, 2001.
- [256] S. L. Zeng, C. H. Chen, J. C. Mikkelsen, and J. G. Santiago, "Fabrication and Characterization of Electroosmotic Micropumps," *Sensors and Actuators B-Chemical*, vol. 79, pp. 107-114, 2001.
- [257] D. J. Laser, K. E. Goodson, J. G. Santiago, and T. W. Kenny, "High-Frequency Actuation with Silicon Electroosmotic Micropumps," presented at 2002 Solid State Sensors and Actuators and Microsystems Workshop, Hilton Head, S.C., 2002.
- [258] P. H. Paul and D. J. Rakestraw, "Electrokinetic High Pressure Hydraulic System." U.S., 2000.

References

- [259] W. E. Gan, L. Yang, Y. Z. He, R. H. Zeng, M. L. Cervera, and M. delaGuardia, "Mechanism of Porous Core Electroosmotic Pump Flow Injection System and its Application to Determination of Chromium(VI) in Waste-Water," *Talanta*, vol. 51, pp. 667-675, 2000.
- [260] S. L. Zeng, C. H. Chen, J. G. Santiago, J. R. Chen, R. N. Zare, J. A. Tripp, F. Svec, and J. M. J. Frechet, "Electroosmotic Flow Pumps with Polymer Frits," *Sensors and Actuators B-Chemical*, vol. 82, pp. 209-212, 2002.
- [261] C.-H. Chen, S. L. Zeng, J. C. Mikkelsen, and J. G. Santiago, "Development of a Planar Electrokinetic Micropump," presented at 2000 ASME International Mechanical Engineering Congress and Exposition, Orlando, FL, 2000.
- [262] P. J. Kemery, J. K. Steehler, and P. W. Bohn, "Electric Field Mediated Transport in Nanometer Diameter Channels," *Langmuir*, vol. 14, pp. 2884-2889, 1998.
- [263] Y. Takamura, "Low-Voltage Electroosmotic Pump and Its Applications to On-Chip Linear Stepping Pneumatic Pressure Source," presented at Micro Total Analytical Systems, Monterey, California, 2001.
- [264] P. Selvaganapathy, Y.-s. Leung Ki, P. Renaud, and C. H. Mastrangelo, "Bubble-Free Electrokinetic Pumping," *Journal of Microelectromechanical Systems*, vol. 11, pp. 448-453, 2002.
- [265] A. Ajdari, "Electrokinetic "Ratchet" Pumps for Microfluidics," *Applied Physics A*, vol. 75, pp. 271-274, 2002.
- [266] W. E. Morf, O. T. Guenat, and N. F. de Rooij, "Partial Electroosmotic Pumping in Complex Capillary Systems, Part 1: Principles and General Theoretical Approach," *Sensors and Actuators B-Chemical*, vol. 72, pp. 266-272, 2001.
- [267] O. T. Guenat, D. Ghiglione, W. E. Morf, and N. F. de Rooij, "Partial Electroosmotic Pumping in Complex Capillary Systems, Part 2: Fabrication and Application of a Micro Total Analysis System (uTAS) Suited for Continuous Volumetric Nanotitrations," *Sensors and Actuators B-Chemical*, vol. 72, pp. 273-282, 2001.
- [268] B. P. Mosier, R. W. Crocker, J. L. Rognlien, and K. D. Patel, "High-Pressure Microhydraulic Actuator," presented at 2003 ASME International Mechanical Engineering Congress and Exposition, Washington, D.C., 2003.

References

- [269] V. Studer, A. Pepin, Y. Chen, and A. Ajdari, "An Integrated AC Electrokinetic Pump in a Microfluidic Loop for Fast and Tunable Flow Control," *The Analyst*, vol. 129, pp. 944-949, 2004.
- [270] T. T. Razunguzwa and A. T. Timperman, "Fabrication and Characterization of a Fritless Microfabricated Electroosmotic Pump with Reduced pH Dependence," *Analytical Chemistry*, vol. 76, pp. 1336-1341, 2004.
- [271] J. S. Jang and S. S. Lee, "Theoretical and Experimental Study of MHD (Magnetohydrodynamic) Micropump," *Sensors and Actuators A-Physical*, vol. 80, pp. 84-89, 2000.
- [272] A. V. Lemoff and A. P. Lee, "An AC Magnetohydrodynamic Micropump," *Sensors and Actuators B-Chemical*, vol. 63, pp. 178-185, 2000.
- [273] L. Huang, W. Wang, M. C. Murphy, K. Lian, and Z. G. Ling, "LIGA Fabrication and Test of a DC Type Magnetohydrodynamic (MHD) micropump," *Microsystem Technologies*, vol. 6, pp. 235-240, 2000.
- [274] J. H. Zhong, M. Q. Yi, and H. H. Bau, "Magneto Hydrodynamic (MHD) Pump Fabricated with Ceramic Tapes," *Sensors and Actuators A-Physical*, vol. 96, pp. 59-66, 2002.
- [275] N. Leventis and X. R. Gao, "Magnetohydrodynamic Electrochemistry in the field of Nd-Fe-B magnets. Theory; Experiment; and Application in Self-Powered Flow Delivery Systems," *Analytical Chemistry*, vol. 73, pp. 3981-3992, 2001.
- [276] H. H. Bau, J. H. Zhong, and M. Q. Yi, "A Minute Magneto Hydro Dynamic (MHD) Mixer," *Sensors and Actuators B-Chemical*, vol. 79, pp. 207-215, 2001.
- [277] H. H. Bau, "A Case for Magneto Hydro Dynamics (MHD)," presented at 2001 ASME International Mechanical Engineering Congress and Exposition, New York, NY, 2001.
- [278] P. Luginbuhl, S. D. Collins, G. A. Racine, M. A. Gretillat, N. F. deRoos, K. G. Brooks, and N. Setter, "Microfabricated Lamb wave device based on PZT sol-gel thin film for mechanical transport of solid particles and liquids," *Journal of Microelectromechanical Systems*, vol. 6, pp. 337-346, 1997.
- [279] J. Black and R. M. White, "Microfluidic Applications of Ultrasonic Flexural Plate Waves," presented at 2000 Solid-State Sensors and Actuators Workshop, Hilton Head, S.C., 2000.

References

- [280] N. T. Nguyen and R. M. White, "Design and Optimization of an Ultrasonic Flexural Plate Wave Micropump using Numerical Simulation," *Sensors and Actuators A-Physical*, vol. 77, pp. 229-236, 1999.
- [281] R. M. Moroney, R. M. White, and R. T. Howe, "Ultrasonically Induced Microtransport," presented at IEEE MEMS 91, Nara, Japan, 1991.
- [282] R. M. Young, "Analysis of a Micromachine Based Vacuum Pump on a Chip Actuated by the Thermal Transpiration Effect," *J. Vac. Sci. Technol. B*, vol. 17, pp. 280-287, 1999.
- [283] V. Namasivayam, R. G. Larson, D. T. Burke, and M. A. Burns, "Transpiration-Based Micropump for Delivering Continuous Ultra-Low Flow Rates," *J. Micromech. Microeng.*, vol. 13, pp. 261-271, 2003.
- [284] D. Burgreen and F. R. Nakache, "Electrokinetic Flow in Ultrafine Capillary Slits," *J. Phys. Chemistry*, vol. 68, pp. 1084-1091, 1964.
- [285] R. J. Hunter, *Zeta Potential in Colloid Science*. San Diego: Academic Press, Inc., 1981.
- [286] A. W. Adamson and A. P. Gast, *Physical Chemistry of Surfaces*. New York: Wiley, 1997.
- [287] S. R. Morrison, *Electrochemistry at Semiconductor and Oxidized Metal Electrodes*. New York: Plenum Press, 1980.
- [288] D. N. Furlong, D. E. Yates, and T. W. Healy, "Fundamental Properties of the Oxide/Aqueous Solution Interface," in *Electrodes of Conductive Metallic Oxides*, S. Trasatti, Ed.: Elsevier Scientific Publishing Company, 1981.
- [289] J. T. G. Overbeek, "Electrochemistry of the Double Layer," in *Irreversible Systems*, H. R. Kruyt, Ed. New York: Elsevier, 1952, pp. 115-193.
- [290] R. J. Hunter, *Foundations of Colloid Science*: Oxford University Press, 2001.
- [291] S. Levine and G. M. Bell, "Modified Poisson-Boltzmann Equation and Free Energy of Electrical Double Layers in Hydrophobic Clouds," *Discussions of the Faraday Society*, vol. 42, pp. 69-80, 1961.
- [292] L. Blum, "The Electric Double Layer - A Comprehensive Approach," in *Fluid Interfacial Phenomena*, C. A. Croxton, Ed.: John Wiley & Sons Ltd, 1986.

References

- [293] C. L. Rice and R. Whitehead, "Electrokinetic Flow in a Narrow Cylindrical Capillary," *J. Phys. Chemistry*, vol. 69, pp. 4017, 1965.
- [294] P. J. Scales, F. Grieser, and T. W. Healy, "Electrokinetics of the Silica-Solution Interface: A Flat Plate Streaming Potential Study," *Langmuir*, vol. 8, pp. 965-974, 1992.
- [295] D. E. Yates, S. Levine, and T. W. Healy, "Site-Binding Model of Electrical Double Layer at the Oxide/Water Interface," *Journal of the Chemical Society - Faraday Transactions I*, vol. 74, pp. 1807-1818, 1974.
- [296] S. Yao and J. G. Santiago, "Porous Glass Electroosmotic Pumps: Theory," *Journal of Colloid and Interface Science*, vol. 268, pp. 133-142, 2003.
- [297] A. Revil, P. A. Pezard, and P. W. J. Glover, "Streaming Potential in Porous Media, 1: Theory of Zeta Potential," *J. Geophysical Research*, vol. 104, pp. 20,021-20,031, 1999.
- [298] J. G. Santiago, "Electroosmotic Flows in Microchannels with Finite Inertial and Pressure Forces," *Analytical Chemistry*, vol. 73, pp. 2353-2365, 2001.
- [299] D. Hildreth, "Electrokinetic Flow in Fine Capillary Channels," *Analytical Chemistry*, vol. 74, pp. 2006-2015, 1970.
- [300] R. Sadr, M. Yoda, Z. Zheng, and A. T. Conlisk, "An Experimental Study of Electro-osmotic Flow in Rectangular Microchannels," *J. Fluid Mech.*, vol. 506, pp. 357-367, 2004.
- [301] P. Dutta and A. Beskok, "Analytical Solution of Combined Electroosmotic/Pressure Driven Flows in Two-Dimensional Straight Channels: Finite Debye Layer Effects," *Analytical Chemistry*, vol. 73, pp. 1979-1986, 2001.
- [302] S. S. Dukhin, "Electrokinetic Phenomena of the Second Kind and Their Applications," *Advances in Colloid and Interface Science*, vol. 35, pp. 173-196, 1991.
- [303] S. Ghosal, "Fluid Mechanics of Electroosmotic Flow and its Effect on Band Broadening in Capillary Electrophoresis," *Electrophoresis*, vol. 25, pp. 214-228, 2004.
- [304] B. J. Kirby and E. F. Hasselbrink, "Zeta Potential of Microfluidic Substrates: 1. Theory, Experimental Techniques, and Effects on Separations," *Electrophoresis*, vol. 25, pp. 187-202, 2004.

References

- [305] B. J. Kirby and E. F. Hasselbrink, "Zeta Potential of Microfluidic Substrates: 2. Data for Polymers," *Electrophoresis*, vol. 25, 2004.
- [306] R. F. Pierret, *Semiconductor Device Fundamentals*: Addison-Wesley, 1996.
- [307] J. J. Vlassak and W. D. Nix, "A New Bulge Test Technique for the Determination of Young Modulus and Poisson Ratio of Thin-Films," *J. Materials Research*, vol. 7, pp. 3242-3249, 1992.
- [308] A. Stoffel, A. Kovacs, W. Kronast, and B. Muller, "LPCVD against PECVD for Micromechanical Applications," *J. Micromech. Microeng.*, vol. 6, pp. 1-13, 1996.
- [309] S. M. Sze, *Semiconductor Devices: Physics and Technology*, 2nd ed: John Wiley & Sons, 2002.
- [310] X. G. Zhang, *Electrochemistry of Silicon and Its Oxide*. New York: Kluwer Academic, 2001.
- [311] D. S. Campbell and A. R. Morley, "Electrical Conduction in Thin Metallic, Dielectric and Metallic-Dielectric Films," *Rep. Prog. Phys.*, vol. 34, pp. 283-368, 1971.
- [312] J. J. O'Dwyer, *The Theory of Electrical Conductivity and Breakdown in Solid Dielectrics*. Oxford: Clarendon Press, 1973.
- [313] H. O. Finklea, "Semiconductor Electrode Concepts and Terminology," in *Semiconductor Electrodes*, H. O. Finklea, Ed. Amsterdam: Elsevier, 1988.
- [314] A. J. Bard, A. B. Bocarsly, F.-R. F. Fan, E. G. Walton, and M. S. Wrighton, "The Concept of Fermi Level Pinning at Semiconductor/Liquid Junctions. Consequences for Energy Conversion Efficiency and Selection of Useful Solution Redox Couples in Solar Devices," *J. Am. Chem. Soc.*, vol. 102, pp. 3671-3677, 1980.
- [315] N. S. Lewis and A. B. Bocarsly, "Silicon (Si) and Germanium (Ge)," in *Semiconductor Electrodes*, H. O. Finklea, Ed. Amsterdam: Elsevier, 1988.
- [316] K. Ghowsi and R. J. Gale, "Theoretical Model of the Anodic Oxidation Growth Kinetics of Si at Constant Voltage," *J. Electrochemical Society*, vol. 136, pp. 867-871, 1989.
- [317] J. A. Bardwell, E. M. Allegreto, J. Phillips, M. Buchanan, and N. Draper, "Influence of the Initial Electrochemical Potential on the Growth Mechanism and

References

- Properties of Anodic Oxides on (100) Si," *J. Electrochemical Society*, vol. 143, pp. 2931-2938, 1996.
- [318] P. F. Schmidt and M. W., "Anodic Formation of Oxide Films on Silicon," *J. Electrochemical Society*, vol. 104, pp. 230-236, 1957.
- [319] R. M. Candea, M. Kastner, R. Goodman, and N. Hickok, "Photoelectrolysis of water: Si in salt water," *J. Applied Physics*, vol. 47, pp. 2724-2726, 1976.
- [320] M. Morita, T. Ohmi, E. Hasegawa, M. Kawakami, and M. Ohwada, "Growth of Native Oxide on a Silicon Surface," *J. Applied Physics*, vol. 68, pp. 1272-1281, 1990.
- [321] M. Lenzlinger and E. H. Snow, "Fowler-Nordheim Tunneling into Thermally Grown SiO₂," *J. Applied Physics*, vol. 40, pp. 278-283, 1969.
- [322] G. L. Holmberg, A. B. Kuper, and F. D. Miraldi, "Water Contamination in Thermal Oxide on Silicon," *J. Electrochemical Society*, vol. 117, pp. 677-682, 1970.
- [323] E. H. Snow, A. S. Grove, B. E. Deal, and C. T. Sah, "Ion Transport Phenomena in Insulating Films," *J. Applied Physics*, vol. 36, pp. 1664-1673, 1965.
- [324] J. Robertson and M. J. Powell, "Gap States in Silicon Nitride," *Applied Physics Letters*, vol. 44, pp. 415-417, 1984.
- [325] S. Makram-Ebeid and M. Lannoo, "Quantum Model for Phonon-Assisted Tunnel Ionization of Deep Levels in a Semiconductor," *Physical Review B*, vol. 25, pp. 6406-6424, 1982.
- [326] F. M. White, *Viscous Fluid Flow*, 1991.
- [327] P. Krause and E. Obermeier, "Etch Rate and Surface Roughness of Deep Narrow U-grooves in (110)-oriented Silicon," *Journal of Micromechanics and Microengineering*, vol. 5, pp. 112-114, 1995.
- [328] M. A. Hines, "In Search of Perfection: Understanding the Highly Defect-Selective Chemistry of Anisotropic Etching," *Annual Review of Physical Chemistry*, vol. 54, pp. 29-56, 2003.
- [329] J. D. Plummer, M. Deal, and P. B. Griffin, *Silicon VLSI Technology: Fundamentals, Practice and Modeling*. Upper Saddle River, NJ: Prentice Hall, 2000.

References

- [330] F. Laermer and A. Schilp, "Method of Anisotropically Etching Silicon." U.S., 1996.
- [331] Stanford Nanofabrication Facility, "Drytek1 Processes, Recipes, and Etch Rates," 1996.
- [332] E. M. Chow, "Electrical Through-Wafer Interconnects and Microfabricated Cantilever Arrays using Through-Wafer Silicon Etching," in *Electrical Engineering*, vol. Ph.D.: Stanford University, 2001.
- [333] K.-S. Chen, A. A. Ayon, X. Zhang, and S. M. Spearing, "Effect of Process Parameters on the Surface Morphology and Mechanical Performance of Silicon Structures after Deep Reactive Ion Etching (DRIE)," *Journal of Microelectromechanical Systems*, vol. 11, pp. 264-275, 2002.
- [334] A. A. Ayon, R. Braff, C. C. Lin, H. H. Sawin, and M. A. Schmidt, "Characterization of a Time Multiplexed Inductively Coupled Plasma Etcher," *Journal of the Electrochemical Society*, vol. 146, pp. 339-349, 1999.
- [335] V. Lehmann, "Porous Silicon - A New Material for MEMS," presented at 9th IEEE International Workshop on Micro Electro Mechanical Systems (MEMS '96), San Diego, CA, 1996.
- [336] M. J. Theuniss, "Etch Channel Formation during Anodic Dissolution of N-Type Silicon in Aqueous Hydrofluoric Acid," *J. Electrochemical Society*, vol. 119, pp. 351-360, 1972.
- [337] A. Myers, "personal communication," 2004.
- [338] A. C. Adams, "Dielectric and Polysilicon Film Deposition," in *VLSI Technology*, S. M. Sze, Ed., 2nd ed: McGraw-Hill, Inc., 1988.
- [339] G. P. Kennedy, O. Bulu, and S. Taylor, "Oxidation of Silicon Nitride Films in an Oxygen Plasma," *J. Applied Physics*, vol. 85, pp. 3319-3326, 1999.
- [340] C. Kenney, S. Parker, J. Segal, and C. Storum, "Silicon Detectors with 3-D Electrode Arrays: Fabrication and Initial Test Results," *IEEE Trans. Nuclear Science*, vol. 46, pp. 1224-1236, 1999.
- [341] K. B. Albaugh, "Electrode Phenomena during Anodic Bonding of Silicon to Sodium Borosilicate Glass," *J. Electrochemical Society*, vol. 138, pp. 3089-3094, 1991.

References

- [342] T. M. H. Lee, D. H. Y. Lee, C. Y. N. Liaw, A. I. K. Lao, and I.-M. Hsing, "Detailed Characterization of Anodic Bonding Processes between Glass and Thin-Film Coated Silicon Substrates," *Sensors and Actuators A - Physical*, vol. 86, pp. 103-107, 2000.
- [343] R. J. Beynon and J. S. Easterby, *Buffer Solutions: The Basics*. New York: Oxford University Press, 1996.
- [344] R. F. Platford, "Osmotic and Activity Coefficients of Some Simple Borates in Aqueous Solutions at 25 degrees," *Canadian Journal of Chemistry*, vol. 47, pp. 2271-2273, 1969.
- [345] D. L. Hareme, L. J. Bousse, J. D. Shott, and J. D. Meindl, "Ion-Sensing Devices with Silicon Nitride and Borosilicate Glass Insulators," *IEEE Trans. Electron Devices*, vol. ED-34, pp. 1700-1707, 1987.
- [346] L. J. Bousse, S. Mostarshed, and D. Hafeman, "Combined Measurement of Surface Potential and Zeta Potential at Insulator/Electrolyte Interfaces," *Sensors and Actuators B - Chemical*, vol. 10, pp. 67-71, 1992.
- [347] A. Dubbe, "Fundamentals of Solid State Ionic Micro Gas Sensors," *Sensors and Actuators B - Chemical*, vol. 88, pp. 138-148, 2003.
- [348] P. Bergveld, "Thirty years of ISFETOLOGY: What happened in the past 30 years and what may happen in the next 30 years," *Sensors and Actuators B - Chemical*, vol. 88, pp. 1-20, 2003.
- [349] J. Min, E. Hasselbrink, and S. Kim, "On the Efficiency of Electrokinetic Pumping of Liquids through Nanoscale Channels," *Sensors and Actuators B - Chemical*, vol. 98, pp. 368-177, 2004.
- [350] S. Manzini and F. Volonte, "Charge Transport and Trapping in Silicon Nitride-Silicon Dioxide Dielectric Double Layers," *J. Applied Physics*, vol. 58, pp. 4300-4306, 1985.
- [351] S. M. Sze, "Current Transport and Maximum Dielectric Strength of Silicon Nitride Films," *J. Applied Physics*, vol. 38, pp. 2951-2956, 1967.
- [352] T. E. Burgess, J. C. Baum, F. M. Fowkes, R. Holmstrom, and G. A. Shirn, "Thermal Diffusion of Sodium in Silicon Nitride Shielded Silicon Oxide Films," *J. Electrochemical Society*, vol. 116, pp. 1005-1008, 1969.

References

- [353] K. A. Nasyrov, V. A. Gritsenko, M. K. Kim, H. S. Chae, S. D. Chae, W. I. Ryu, J. H. Sok, J.-W. Lee, and B. M. Kim, "Charge Transport Mechanism in Metal-Nitride-Oxide-Semiconductor Structures," *IEEE Electron Device Letters*, vol. 23, pp. 336-338, 2002.
- [354] S. Habermehl and C. Carmingnani, "Correlation of Charge Transport to Local Atomic Strain in Si-rich Silicon Nitride Thin Films," *Applied Physics Letters*, vol. 80, pp. 261-263, 2002.
- [355] K. Banerjee, S. J. Souri, P. Kapur, and K. C. Saraswat, "3-D ICs: A Novel Chip Design for Improving Deep-Submicrometer Interconnect Performance and System-on-Chip Integration," *Proc. IEEE*, vol. 89, pp. 602-633, 2001.
- [356] Y. Murakami and B. B. Mikic, "Parametric Optimization of Multichanneled Heat Sinks for VLSI Cooling," *IEEE Transactions on Components and Packaging Technologies*, vol. 24, pp. 2-9, 2001.
- [357] R. Bardell, N. Sharma, F. Forster, M. Afromowitz, and R. J. Penney, "Designing High-Performance Micro-Pumps Based on No-Moving-Parts Valves," presented at 1997 ASME Int. Mechanical Engineering Congress and Exposition, Dallas, TX, 1997.
- [358] IMM, "thinXXS XXS2000 data sheet, www.thinxxs.com."
- [359] "www.debiotech.sa."
- [360] A. Furuya, F. Shimokawa, T. Matsuura, and R. Sawada, "Fabrication of Fluorinated Polyimide Microgrids using Magnetically Controlled Reactive Ion Etching (MC-RIE) and their Applications to an Ion Drag Integrated Micropump," *Journal of Micromechanics and Microengineering*, vol. 6, pp. 310-319, 1996.
- [361] S. Yao, D. E. Huber, J. C. Mikkelsen, and J. G. Santiago, "A Large Flowrate Electroosmotic Pump with Micron Pores," presented at 2001 Int. Mechanical Engineering Congress and Exposition, New York, NY, 2001.